(NASA-CR-158522) THE EFFECTS OF DESIGN AND OPERATING VARIABLES ON THE RESPONSE OF AN AXIAL FLOW FAN TO INLET FLOW DISTORTIONS M.S. Thesis (Pennsylvania State Univ.) 228 p HC A11/MF A01 CSCL 21E G3/07

N79-22087

Unclas 18369

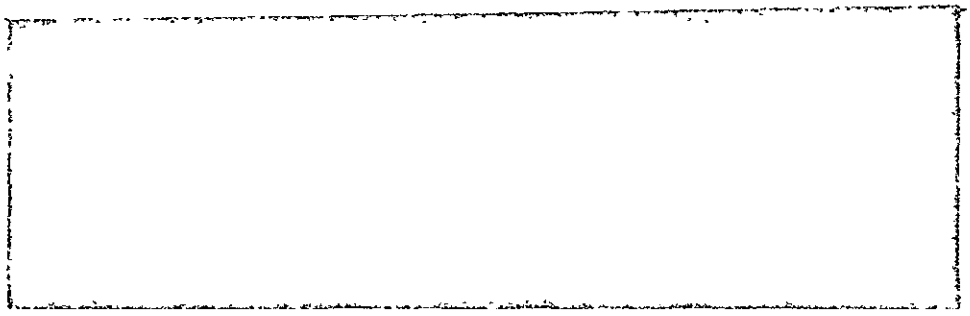

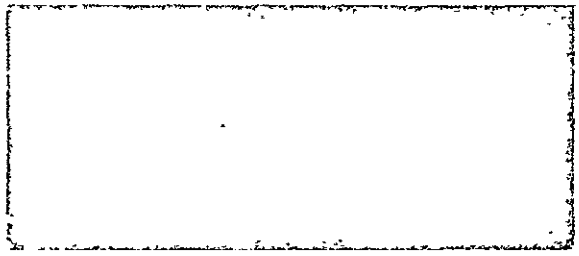

The Pennsylvania State University
Institute for Science and Engineering
APPLIED RESEARCH LABORATORY
Post Office Box 30
State College, Pa. 16801

NAVY DEPARTMENT

NAVAL SEA SYSTEMS COMMAND

THE EFFECTS OF DESIGN AND OPERATING VARIABLES ON THE RESPONSE OF AN AXIAL FLOW FAN TO INLET FLOW DISTORTIONS

Adam M. Yocum, II

Technical Memorandum
File No. TM 78-178
June 14, 1978
Contract No. N00017-73-C-1418

Copy No. 44

The Pennsylvania State University
Institute for Science and Engineering
APPLIED RESEARCH LABORATORY
Post Office Box 30
State College, PA 16801

NAVY DEPARTMENT

NAVAL SEA SYSTEMS COMMAND

UNCLASSIFIED

SECURITY CLASSIFICATION OF THIS PAGE *(When Data Entered)*

REPORT DOCUMENTATION PAGE		READ INSTRUCTIONS BEFORE COMPLETING FORM
1. REPORT NUMBER TM 78-178	2. GOVT ACCESSION NO.	3 RECIPIENT'S CATALOG NUMBER
4. TITLE *(and Subtitle)* The Effects of Design and Operating Variables on the Response of an Axial Flow Fan to Inlet Flow Distortions		5 TYPE OF REPORT & PERIOD COVERED Technical Memorandum 6. PERFORMING ORG. REPORT NUMBER
7. AUTHOR(s) Adam M. Yocum, II		8. CONTRACT OR GRANT NUMBER(s) NASA Grant NSG-3031; N00017-73-C-1418
9. PERFORMING ORGANIZATION NAME AND ADDRESS Applied Research Laboratory Post Office Box 30 State College, PA 16801		10. PROGRAM ELEMENT, PROJECT, TASK AREA & WORK UNIT NUMBERS
11. CONTROLLING OFFICE NAME AND ADDRESS NASA-Lewis Research Center – Naval Sea Systems Command Cleveland, OH 44138 Washington, DC		12. REPORT DATE June 14, 1978 13. NUMBER OF PAGES 224
14. MONITORING AGENCY NAME & ADDRESS*(if different from Controlling Office)*		15. SECURITY CLASS. *(of this report)* Unclassified, Unlimited 15a. DECLASSIFICATION/DOWNGRADING SCHEDULE

16. DISTRIBUTION STATEMENT *(of this Report)*

Approved for public release. Distribution unlimited.
Per NAVSEA - July 6, 1978.

17. DISTRIBUTION STATEMENT *(of the abstract entered in Block 20, if different from Report)*

18. SUPPLEMENTARY NOTES

Submitted in partial fulfillment of the requirements for the degree of Master of Science, Department of Mechanical Engineering, The Pennsylvania State University, August 1978.

19. KEY WORDS *(Continue on reverse side if necessary and identify by block number)*

turbomachinery
distorted flow
rotors
inlet flow

20. ABSTRACT *(Continue on reverse side if necessary and identify by block number)*

This thesis presents the results of a study of total-pressure and velocity circumferential distortions in an axial-flow fan. Distorted inlet flow is an important problem to the turbomachine designer because nonuniform and distorted flows cause noise, vibration, a reduction in efficiency, and also a reduction in the stability limits for a multistage compressor. Some of the sources of a nonuniform flow which are often unavoidable are wakes from upstream struts, sharp bends in the inlet ducting, flow separation in the inlet,

DD FORM 1 JAN 73 1473 EDITION OF 1 NOV 65 IS OBSOLETE

UNCLASSIFIED

SECURITY CLASSIFICATION OF THIS PAGE *(When Data Entered)*

and vortices created by ingesting fluid from a boundary layer.

The present study was conducted to provide some of the fundamental experimental data needed to understand distorted flow phenomena as affected by design and operating variables. The flow through an isolated rotor was examined at various operating conditions with six different distortions and three different blade stagger angles. Circumferential surveys were conducted upstream and downstream of the rotor using five-hole probes in the non-nulling mode. The measurements with the five-hole probes yielded the axial, circumferential, and radial components of velocity, and the total and static pressure.

The total pressure and axial velocity distortion data were analyzed to determine the degree of distortion attenuation as a function of blade stagger angle, mean incidence angle, and reduced frequency. The results indicate that, for the rotors tested, the mean incidence or loading has very little effect on the distortion attenuation. However, the attenuation was influenced by the blade stagger angle and the reduced frequency. The increased attenuation with increased reduced frequency was significantly large, which is an important observation since present day theories do not predict this response. The total pressure losses due to the distorted flow are also briefly presented and discussed.

ABSTRACT

This thesis presents the results of a study of total-pressure and velocity circumferential distortions in an axial-flow fan. Distorted inlet flow is an important problem to the turbomachine designer because nonuniform or distorted flows cause noise, vibration, a reduction in efficiency, and also a reduction in the stability limits for a multistage compressor. Some of the sources of a nonuniform flow which are often unavoidable are wakes from upstream struts, sharp bends in the inlet ducting, flow separation in the inlet, and vortices created by ingesting fluid from a boundary layer.

The present study was conducted to provide some of the fundamental experimental data needed to understand distorted flow phenomena as affected by design and operating variables. The flow through an isolated rotor was examined at various operating conditions with six different distortions and three different blade stagger angles. Circumferential surveys were conducted upstream and downstream of the rotor using five-hole probes in the non-nulling mode. The measurements with the five-hole probes yielded the axial, circumferential, and radial components of velocity, and the total and static pressure.

The total pressure and axial velocity distortion data were analyzed to determine the degree of distortion attenuation as a function of blade stagger angle, mean incidence angle, and reduced frequency. The results indicate that, for the rotors tested, the mean incidence or loading has very little effect on the distortion attenuation. However, the attenuation was influenced by the blade stagger angle and the reduced frequency. The increased attenuation with increased reduced frequency was

significantly large, which is an important observation since present day theories do not predict this response. The total pressure losses due to the distorted flow are also briefly presented and discussed.

TABLE OF CONTENTS

TABLE OF CONTENTS (Continued)

LIST OF TABLES

LIST OF FIGURES

NOMENCLATURE

Symbol	
A	amplitude of square distortion, $\frac{v_{x\ max} - v_{x\ min}}{v_{x\ avg}}$ or $\frac{p_{T\ max} - p_{T\ min}}{\frac{1}{2}\rho v_{x\ avg}^2}$
A_n	harmonic amplitude
A_{1_n}, A_{2_n}, A_{3_n}	complex constants used in actuator disc analysis
a	$\bar{v}_\theta/\bar{v}_x$
b	intercept of tan β_2 vs tan β_1 line
c	blade chord length
d	diameter of five-hole probe at the tip
f, f_1, f_2	functions
i	incidence angle
ℓ	wavelength of the distortion, $\frac{2\pi\bar{r}}{n}$
m	slope of tan β_2 vs tan β_1 line
n	harmonic number
P_T	dimensionless total pressure
p_T	total pressure
P_s	dimensionless static pressure
p_s	static pressure
r	radial coordinate
$\bar{r}$	mean radius, 7.75 inches (19.69 cm)
r_h'	first radial measurement location and lower limit for mass average integration, r_h' = hub radius + 0.25 in.

NOMENCLATURE (Continued)

Symbol	
r_t'	last radial measurement location and upper limit for mass average integration, r_t' = casing inside radius -0.25 in.
Re	Reynolds number
R_n, S_n, T_n	function of X used in actuator disc analysis as defined by Equations (14), (15), and (16)
s/c	space-to-chord ratio
t	time
U	blade speed at the mean radius
V_x	dimensionless axial component of velocity
V_θ	dimensionless circumferential component of velocity
V_R	dimensionless radial component of velocity
v_x	axial component of velocity
v_θ	circumferential component of velocity
v_R	radial component of velocity
$v_{x\,avg}$	average axial velocity measured at Location 1-D
W	relative velocity
W_θ	circumferential component of relative velocity
W_m	mean relative velocity
X	dimensionless axial coordinate, x/r
x	axial coordinate
y	distance from probe tip to the flat plate

NOMENCLATURE (Continued)

Greek Symbols

α_1	absolute flow angle at the inlet to a blade row
α_2	absolute flow angle at the exit of a blade row
β_1	relative flow angle at the inlet to a blade row
β_2	relative flow angle at the exit of a blade row
γ	pitch angle
δ	yaw angle
ν	distortion frequency = $2\pi U/\ell$
ξ	stagger angle
Ψ	pressure rise coefficient = $(p_{T\,exit} - p_{T\,inlet})/\frac{1}{2}\rho U^2$
Ψ'	modified pressure rise coefficient used with the parallel compressor model = $(p_{s\,exit} - p_{T\,inlet})/\frac{1}{2}\rho U^2$
$\Delta\Psi'$	$\Psi'_2-\Psi'_1$ where subscripts 1 and 2 refer to the spoiled and unspoiled sectors in the parallel compressor model, respectively
ω	reduced frequency defined by Equation (49)

Subscripts and Superscripts

exit	refers to the exit of the rotor
inlet	refers to the inlet of the rotor
max	maximum value
min	minimum value
0^-	at X = 0 upstream of the actuator disc
0^+	at X = 0 downstream of the actuator disc
1-D	refers to Location 1-D in the Axial Flow Research Fan, defined in Figure 14

NOMENCLATURE (Continued)

Subscripts and Superscripts

15	refers to Location 15 in the Axial Flow Research Fan, defined in Figure 14
1	refers to the spoiled sector in the parallel compressor model unless specified otherwise in the nomenclature
2	refers to the unspoiled sector in the parallel compressor model unless specified otherwise in the nomenclature
$\bar{(\ )}$	circumferential average value used in the actuator disc analysis
$(\ )'$	perturbation quantity in the actuator disc analysis

ACKNOWLEDGMENTS

The author would like to express his sincere appreciation to his research advisor, Dr. Robert E. Henderson, both for his technical guidance and also his encouragement throughout the project. The assistance given by Mr. Edgar P. Bruce in the operation of the Axial Flow Research Fan is also appreciated.

This project was conducted at the Garfield Thomas Water Tunnel of the Applied Research Laboratory at The Pennsylvania State University. The work was sponsored by the National Aeronautics and Space Administration under Research Grant NSG 3031. Mr. Nelson L. Sanger of the NASA-Lewis Research Center was the technical advisor for the grant.

CHAPTER I

INTRODUCTION

1.1 Significance of Flow Distortions in Turbomachinery

A turbomachine is a device which transfers energy to or from a moving fluid by means of rotating vanes or blades. Small fans and pumps are common types of turbomachines found in many applications. Pumps, compressors, and turbines are also involved in many industrial processes as well as in propulsion and electric power generation. As the need and use of turbomachines has increased to the present-day level, a tremendous amount of engineering development has accompanied this increase so that today's turbomachines are relatively efficient and reliable. As this development continues, one problem, which is important to the designer and currently being investigated by many organizations, is the problem of nonuniform flow entering the turbomachine. One aspect of this problem, specifically, the response of an axial flow fan subjected to circumferentially distorted inlet flow, is examined in this study as a function of rotor design variables. This type of information is hoped to be of particular value to the jet aircraft engine designer, to whom the problem of distorted inlet flow is very serious, because many of the conditions under which the aircraft engine must operate will result in distorted inlet flow.

The sources of distorted inlet flow are numerous. Wakes from upstream blade rows or struts are one form of distortion. This type of distortion, however, can be minimized by proper design of the upstream struts. If the inlet duct is curved, distorted flow can also be created by induced secondary flow as the fluid traverses the bend,

or if the curve is sharp enough, flow separation may occur, which will create a severe velocity defect. This type of distortion can usually be avoided or minimized at the design operating condition by proper inlet design considerations. However, many types of distortions which cannot be avoided are encountered with jet aircraft engines due to the many different conditions under which the engine must operate.

When an aircraft performs a maneuver with large angles of attack or large yaw angles, severe flow distortions may result from either flow separation in the engine inlet, or simply from flow interaction between the engine and the aircraft itself. At low speed and high power, the engines of supersonic aircraft may also be subjected to a severe flow distortion caused by flow separation from the sharp edged entrance which is designed for supersonic flight. In addition to these, all types of jet aircraft can encounter distorted inlet flow when on the ground by ingesting large vortices which are created by the engine as it ingests air from the boundary layer near the ground. When the wind is blowing, a large boundary layer is present near the ground, and the vorticity in this boundary layer is concentrated into a large vortex at the engine inlet. A similar type of vortex can be generated by aircraft with aft-mounted engines such as the DC-9 or Boeing 727. During takeoff when the plane is moving slowly, the boundary layer on the body is large and this air is drawn to the engine creating a vortex [1]*.

All of the possible sources of distorted flow were not discussed above. However, from the ones mentioned, it is obvious that although

---

*Numbers in brackets refer to entries in the List of References.

uniform flow might be preferred, it is not obtainable in all situations. Some of the problems associated with nonuniform flow can be examined by referring to Figure 1. This figure shows a two-dimensional view of a blade row with sinusoidally varying inlet flow. Also shown on the figure are velocity triangles drawn at regions of high and low velocity. From these velocity triangles, it is readily seen that the flow relative to the blades is continuously changing in both magnitude and direction. When analyzing the effects of the fluctuating velocity from a simple quasi-steady viewpoint, it is seen that the changes in the relative velocity will result in fluctuating lift and drag forces on the airfoils. These fluctuating forces will in turn cause vibration and also generate noise. Vibration of the blades may mean the weight of the blades may have to be increased in order to meet endurance stress requirements, while, particularly in aircraft engines, weight should be kept to a minimum. Noise from aircraft engines is also an important problem presently being considered by government and industry. If compressor designs which are more tolerant to distortions or which attenuate the distortion in the early stages of the compressor could be developed, one source of noise in the engine could be reduced. Decreasing the noise at the source would also have the advantage of reducing or eliminating the weight increasing acoustic absorbers which are presently used to lower the radiated noise level.

The preceding quasi-steady approach reveals two of the problems which are associated with inlet distortions--vibration and noise. However, it is also important to realize from an engineering standpoint that predicting the fluctuating forces using a quasi-steady analysis would not be accurate. Since with many distortions the flow relative

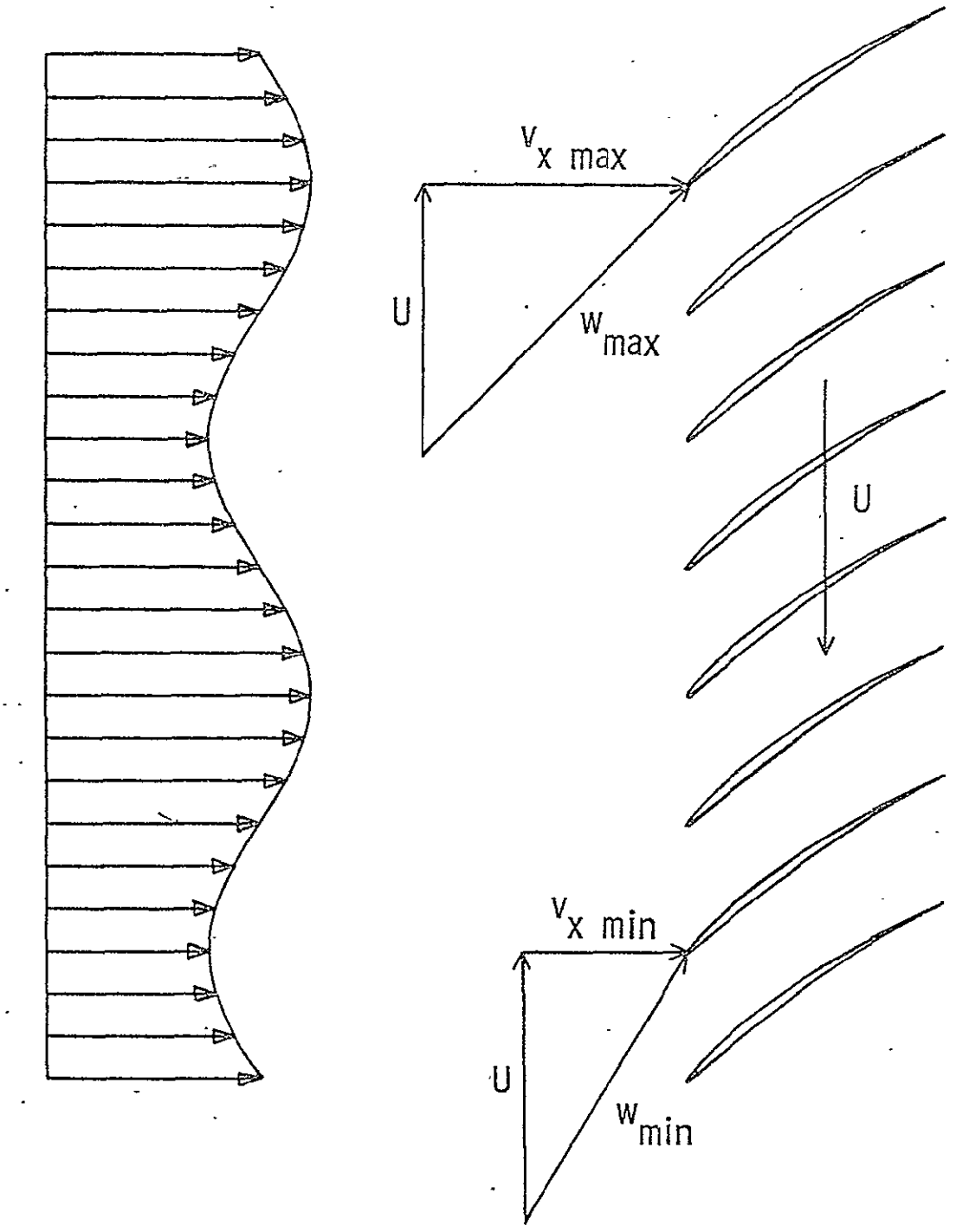

Figure 1. A two-dimensional view of a cascade showing the effect of a sinusoidally varying inlet flow on the relative velocity at the leading edge.

to the blades is changing too rapidly for steady-state conditions to be reached or even approached, the entire flow phenomenon must be considered from an unsteady viewpoint. To further complicate any prediction techniques, the flow around a particular reference blade will have induced effects from the flow around the neighboring blades which is also unsteady and usually out of phase.

Besides the problems encountered because of the fluctuating forces, distorted inlet flow will also have an adverse effect on a compressor or fan's performance. Once again employing a simplified approach, this effect can be studied. The parallel compressor theory, which will be discussed in more detail in Chapter III, will be used for this purpose without going into detail on the assumptions and conditions which must be true for this theory to be valid. Figure 2 is a typical fan performance curve for incompressible flow. In this figure, the non-dimensional pressure rise is plotted versus the non-dimensional flow rate. Considering a square type velocity defect which is present over a 180° circumferential span, the section of the fan which is operating in the retarded flow will operate at Point 1, and the sector of the fan operating in the region of the higher velocity will operate at Point 2 on the curve. The operating point without any distortion, but the same average velocity, can also be plotted and is located at Point 3.

Now, in order for the performance of the fan with distorted and uniform flow to be compared, it will be necessary for an average pressure rise to be computed which will indicate the overall performance of the fan in distorted flow. The circumferential average pressure rise can easily be calculated and in this case will simply

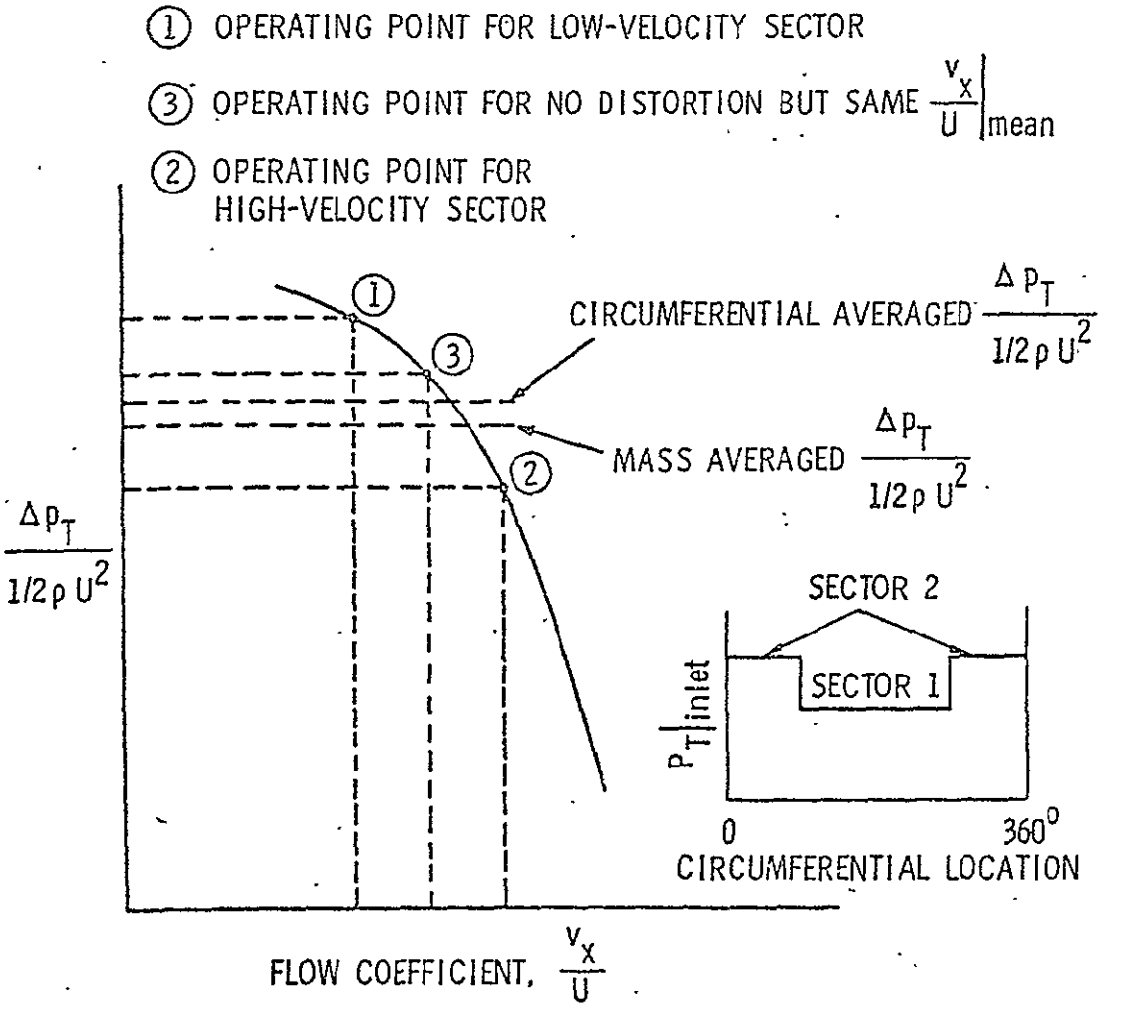

Figure 2. A typical performance curve showing the various operating points with and without flow distortions and the reduction in performance due to the distortion.

be equal to the average pressure rise of Points 1 and 2. When this value is indicated on the figure, it is seen that the average pressure rise for the distorted flow is less than the pressure rise obtained for uniform flow with the same average flow rate, thus indicating a loss in performance due to the distortion. Graphically, this reduction is due to the decreased slope of the performance curve at the lower flow rates. However, since the leveling off is caused by higher losses as the incidence on the blades is increased, the reduction in performance is, therefore, due to the increased losses on the blades when they pass through the distorted sector.

Although the proceeding circumferential average indicates a reduction in performance, since the usefulness of a fan is determined by both pressure rise and mass flow, an even more useful average in indicating the overall performance would take into account the different mass flows in the two sectors. Therefore, defining the mass-averaged pressure rise as:

$$\left.\frac{\Delta p_T}{\frac{1}{2}\rho U^2}\right|_{\text{mass averaged}} = \frac{\int_0^{2\pi} \frac{\Delta p_T}{\frac{1}{2}\rho U^2} V_x \bar{r}\, d\theta}{\int_0^{2\pi} V_x \bar{r}\, d\theta}, \qquad (1)$$

this value for the present case is also computed and indicated on the figure. The mass-averaged pressure rise is seen to lie even further below the pressure rise for uniform flow, and indicates an additional reduction in performance. This reduction is due to the lower mass flow in the distorted sector. Although the reduction is not due to

increased losses, and therefore does not lower the efficiency, it does reduce the performance in terms of average pressure rise for a given mass flow.

The simplified analysis just used, which is a quasi-steady, one-dimensional approach, has demonstrated the degradation of performance caused by distorted inlet flow. Once again, however, it must be realized that the flow cannot accurately be regarded as quasi-steady, and the distortion interaction with the rotor will also induce circumferential and sometimes radial components of velocity making the flow three-dimensional. Despite these factors, however, a significant reduction in performance has already been predicted and the inclusion of unsteady and two- and three-dimensional effects may cause a further reduction in performance.

The final major problem associated with distorted flow is the lowering of the stability limit. It is well known that when the incidence angle and subsequently the loading on an airfoil is increased, a point is reached when the flow will separate from the suction surface of the airfoil. When this occurs in a compressor or fan, however, an unstable condition, either rotating stall or surge, can occur. Both rotating stall and surge will result in very large fluctuating forces on the blades, which may in turn severely damage the machine. In order to prevent this phenomenon from occurring, the stall limit as a function of pressure rise and flow rate is established and controls are designed to prevent the machine from entering the unstable region of its operating range. The problem, therefore, caused by distorted flow is that the stability limit is lowered by the distortion, and unstable conditions will occur at a higher flow rate and lower pressure rise. Since a

margin of safety must be provided if distorted flow will be encountered, the operating range must be further restricted and the peak operating conditions will be lowered.

Although the flow encountered during surge or rotating stall is very complex from an analysis standpoint, it is easy to understand why a distortion would lower the stability limit. If a compressor or fan is operating with its mean flow rate and pressure rise near the stall region, a distortion, which will give rise to even higher incidences and blade loading, could easily cause local stall regions and consequently trigger the unstable flow conditions.

1.2 Previous Work

It has thus been demonstrated that distorted flow is unavoidable and it is also detrimental to the performance of a compressor or fan. However, despite the complications previously mentioned in analyzing the unsteady flow around the blades, in order to design better compressors and fans which are more tolerant to flow distortions, the designers need methods by which they can accurately calculate the unsteady forces on the blades and also the attenuation of the distortion through the blade row. Some of the original work done in unsteady airfoil theory was done by von Karman and Sears [2], so the unsteady forces on a wing subjected to gusts normal to the chord could be calculated. Since this analysis was for an isolated airfoil, Kemp and Sears [3] later extended the original analysis to apply to a turbomachine by including the steady effects of neighboring blades and also the potential interaction with an upstream row of stators. The unsteady contribution of the neighboring blades and velocity perturbations

parallel to the chord were not included in this analysis, since it was felt that these effects would be of second order.

Returning to the analysis of unsteady flow around an isolated airfoil, Horlock [4] demonstrated that for highly loaded airfoils, the unsteady force due to velocity perturbations in the transverse direction could be of the same order as the unsteady forces due to gusts normal to the chord. His analysis, therefore, treated these velocity perturbations and, when combined with the earlier analysis of von Karman and Sears, allowed the generalized gust to be treated. Naumann and Yeh [5] also considered isolated airfoils and were able to include the effect of incidence and camber. This analysis was used to generate design charts which can be used to select design parameters which will minimize the unsteady lift.

Although isolated airfoil theory is valuable in predicting trends associated with design variables, Whitehead [6] has shown that the unsteady effects caused by neighboring blades are significant. Whitehead's analysis, however, which was developed to analysis flutter characteristics, is limited for general use since the airfoils were represented by flat plates at zero mean incidence. Recently, Henderson and Daneshyar [7] were able to include the unsteady contributions of the entire blade row and obtain results for thin, slightly cambered airfoils. The analysis also has the advantage of being of the form which allows it to be applied to design problems. In other words, space-to-chord ratio and camber can be chosen so as to minimize fluctuating lift.

The preceding analyses are primarily intended for predicting the unsteady forces on the blades in compressors or fans. Although these

methods could be used indirectly to determine the attenuation of a distortion through a blade row, when the blade forces are not the primary concern, simpler techniques are available and widely used for predicting distortion attenuation. Two commonly used methods are the parallel compressor model and actuator disc model. Both of these will be discussed in Chapter III with specific emphasis on predicting the flows of this study. For now, however, it is advantageous to briefly discuss their general use. The parallel compressor model, which is the simplest model to employ, is only applicable to square-type circumferential inlet distortions. Other types of distortions cannot be modeled with this theory since they will violate the basic assumptions. Despite the simplicity of the model, it can quite accurately predict the magnitude of the distortion at the exit and also the loss in stall pressure ratio caused by the distortion. Large discrepancies, however, will exist between the predicted and the experimentally observed shape of the distortion.

Actuator disc models are used when the parallel compressor model is invalid and also when the distortion shape and individual blade row attenuation is of primary concern. An actuator disc is a means of representing a blade row by shrinking the chord to zero and concentrating the effects of the blade row at a single axial location. The flow fields upstream and downstream of the blade rows then can be solved either by an analytical solution of linearized equations or by numerical methods. The performance of the blade row represented by the actuator disc can be assumed to be quasi-steady, or unsteady effects may be included. The type of solution and the blade row performance assumed is dependent on the degree of accuracy desired and also the particular

type of distortion phenomenon to be studied. The solution of the linearized inviscid flow equations and the assumption of quasi-steady rotor response is suitable for studying distortion attenuation if the distortion is small. The nonlinear equations and the unsteady response must be used for large distortions and when stall phenomena is investigated. A very good summary of these types of prediction techniques, which basically are used for overall performance and stability studies rather than individual blade performance, is presented by Mokelke in Reference [8].

CHAPTER II

JUSTIFICATION AND OBJECTIVES

As was previously discussed in Chapter I, it is important for the designers of axial flow fans and compressors to know the fluctuating forces on the blades, the attenuation of the distortion through each blade row, the loss in performance, and also any reduction in stability caused by a distortion. Theoretical predictions are valuable in understanding distortion phenomena and also in making some design decisions; however, at the present state-of-the-art, theory has several shortcomings when used in the design process. For example, when trying to predict distortion attenuation, performance loss, or stability limits, methods such as the parallel compressor theory and actuator disc models require the steady performance of the blade row or compressor to be known. Since the performance characteristics are determined by numerous geometric design parameters, these methods give little insight as to what design parameters to select in the design process. Unsteady airfoil theories can be used for selecting design parameters to minimize fluctuating lift, although these methods also suffer limitations since they apply to lightly loaded blades and neglect viscous effects.

To aid in the continual development of theoretical design techniques, and to help bridge the gap between present-day theories and the needs of designers, experimental data of a fundamental nature which demonstrate the effect of various geometric and operating variables are needed. Most of the data available to date are not of this nature. Extensive studies have been made on modern aircraft engines to determine their response to distortions and to identify problem areas. These

studies, however, are usually part of a continuing development program aimed at determining safety limits and suggesting modifications rather than providing the fundamental data needed for designing the next generation of engines.

Some of the basic research which has been performed does examine different operating conditions and different types of distortions; however, the flexibility required to study the effects of design variables was not easily obtained and these data are still not available. The Axial Flow Research Fan (AFRF), a facility of The Pennsylvania State University's Applied Research Laboratory, was designed for the specific purpose of studying unsteady phenomenon and, therefore, possesses the necessary flexibility. Although the possibilities for parametric variation are almost infinite, this investigation has attempted to supply some of the needed information by studying the effects of blade stagger angle for an isolated twelve-bladed rotor (space-to-chord ratio, $s/c = 0.68$ at the mean radius) with different steady loading conditions and various types of circumferential distortions. After changing the number of blades to six ($s/c = 1.35$), a follow-up study will incorporate the same conditions and when combined with the present study will enable the effect of solidity to be determined. Various ways of determining the rotor response are available, but the technique used was to simply measure the flow field upstream and downstream of the rotor. The data thus obtained can be used directly to determine the attenuation by the rotor and the losses caused by the distortion. The unsteady blade circulation can be indirectly obtained by using the analysis of Reference [9].

The attenuation and loss data can be used as a design guide when considering these effects in the design process. It is doubtful, though, whether the data can be used as design charts. Data of this type could lead to design charts, but subsequent studies examining similarity (Reynolds number and Mach number effects) must be made before the data can be used other than for demonstrating trends. Also, although distortion attenuation is desirable since the latter stages of a compressor can operate in a more uniform flow, the attenuation of the distortion may not be compatible with other desirable features. Abrupt attenuation may result in large losses, large fluctuating forces, and an excessive amount of generated noise. This incompatibility is obvious from considering that, if a total pressure deficit is to be made up, there must be higher loading on the blades in the low total pressure region than in the remaining area. It will, therefore, be necessary to simultaneously consider all aspects of the compressor and distorted flow to determine what conditions best meet the design objectives. The data obtained in this investigation could be useful in conducting such a design study.

Although specific uses of the data can be mentioned, one objective of this investigation is to provide a data base to be used for a variety of studies, which will contribute to the development of prediction techniques or improve the basic understanding of distortion phenomena. The data of the present study are readily applicable to such usage, since the number of extraneous variables were minimal and the variables studied were carefully controlled.

With the justification and major objectives of this study presented, it is advantageous to briefly outline specifically the steps taken and the data obtained.

1. As was mentioned earlier, the technique used to determine the rotor response was to measure the flow field upstream and downstream of the rotor. For this purpose, five-hole probes in a non-nulling mode were employed, which enable total and static pressure and the three components of velocity to be determined. The use of five-hole probes in a non-nulling mode requires a detailed calibration of the probes to be performed, and these calibrations may be affected by changes in Reynolds number and the proximity of a solid boundary. The first objective of the study was, therefore, to obtain an accurate calibration of the two probes and determine the Reynolds number and wall proximity effects. The calibration of the probes and the original reasons for selecting this type of probe are discussed in Chapter IV. Additional discussion and data on the probes are presented in Appendix A.
2. To determine the changes brought about by distorted inlet flow, it is obviously necessary to determine the performance of the rotor in uniform flow. The steady performance of the rotor is also needed for making predictions of the distorted flow using the parallel compressor theory and the linear actuator disc model. To determine the overall performance of the rotor, radial surveys of the flow were conducted upstream and downstream of the rotor

enabling mass-averaged performance parameters to be calculated. Since this study is primarily concerned with two-dimensional effects and the distortion data were measured only at the mean radius, the steady performance data for the rotor from the mean radius were used for selecting running conditions and predicting results. Additional measurements at only the mean radius were subsequently made to verify the original results and also to obtain a more detailed performance curve. The steady performance tests were conducted for the three different rotor geometries used in this study.

3. Similar to the requirement of knowing the rotor characteristics with no distortion, the characteristics of the distortion with no rotor is also necessary. Since the rotor will have induced effects on the distorted flow upstream, it is not sufficient to only determine the change of the distortion across the blade row, but also the changes which occurred upstream due to the presence of the rotor. The investigation of this induced change requires the knowledge of how the flow would have existed if no rotor had been present. To provide this information, circumferential flow surveys were made at two axial locations without the rotor installed. The axial locations correspond to those used in measuring the rotor response to the distortions, one upstream and one downstream of the

rotor location. The measurements at the two axial locations without the rotor installed also provide information as to how much the distortion would change between the two locations due to the viscous shear flow. The distortions studied in this phase and through the remainder of the program were 1-, 2-, 4-, and 6-cycle sinusoidal total pressure distortions, and 90° and 180° square total pressure distortions.

4. The final and major phase of the investigation was conducted to determine the rotor response to the six types of distortion listed in Part 3. The effect of blade stagger angle was investigated with stagger angles of 35°, 45°, and 55°. Blade loading was also varied, which in this case, since the blades have zero camber, corresponded to changing the mean angle of incidence. The cases of zero mean incidence and the incidence resulting in zero total pressure rise were tested so the unsteady response of the rotor could be examined without the contribution of steady loading. These cases also provide a good comparison with present day unsteady theories, since most of these theories assume lightly loaded blades. For each stagger angle, two additional mean incidences ranging from 6° to 14° were also tested to investigate the effects of steady loading.

CHAPTER III

THEORETICAL MODELING OF THE FLOW

Before continuing on with the experimental aspects of this program, the parallel compressor and actuator disc models used for comparison with the experimental results are presented in this chapter. The purpose for comparing these models with the results is not to verify the theories, since no new techniques were employed, and the capabilities of the models used are well-known and documented in the literature. The purpose of the comparison is rather to check the experimental results obtained and to explain the trends the data exhibit. The approaches taken are similar to the models described by Mokelke in Reference [8], although, the parallel compressor theory is greatly simplified by the assumption of incompressible flow.

The assumption of incompressible flow, just mentioned, is assumed in both models as well as in the data reduction. This assumption is quite justifiable in the experiments, since both the absolute flow velocity and the velocity relative to the blades are quite low. The average absolute velocity is approximately 67 ft/sec (20.4 m/sec), corresponding to a Mach number of only 0.06. The relative velocity at the mean radius for the maximum rotor speed is 152 ft/sec (46.3 m/sec), resulting in a Mach number relative to the blades of 0.134. Both of these values are far below the value of 0.3, which is usually used as the upper limit for incompressible flow.

3.1 Parallel Compressor Model

The parallel compressor model was chosen for use because of its simplicity. However, despite its simplicity, it explains certain

trends and provides a foundation for subsequent improved models. This model, as is implied from the name, separates the compressor with distorted inlet flow into separate compressors each with uniform flow. This is shown schematically in Figure 3 where a two-dimensional representation of a compressor is shown in which the circumferential direction is once again represented on the vertical axis.

The first fundamental assumption of the parallel compressor model, as is depicted by the schematic, is that there is no cross flow between the compressors. This is not necessarily an accurate assumption, but for circumferential distortions in which the length of the distortion is large compared to the blade spacing, over most of the distorted sector, cross flows can be neglected. The first assumption restricts the use of the parallel compressor model to wide circumferential square distortions.

In addition to dividing the compressor into separate compressors, it is also assumed that the model compressors have the same performance as the real compressor under similar uniform inlet flow conditions. This assumption is nothing more than assuming that the compressor or blade rows respond quasi-steadily to the distortion. The quasi-steady assumption is valid, at least as a first approximation, if the relative velocity at the leading edge of the blades is not changing rapidly. This is obviously not the case at the edges of a square distortion, but steady conditions will be reached near the middle of the distortion if its circumferential width is large compared to the blade spacing.

As a consequence of the assumptions of no cross flow and incompressible flow, it is seen that the axial velocity downstream is identical to the axial velocity upstream. Additionally, since the

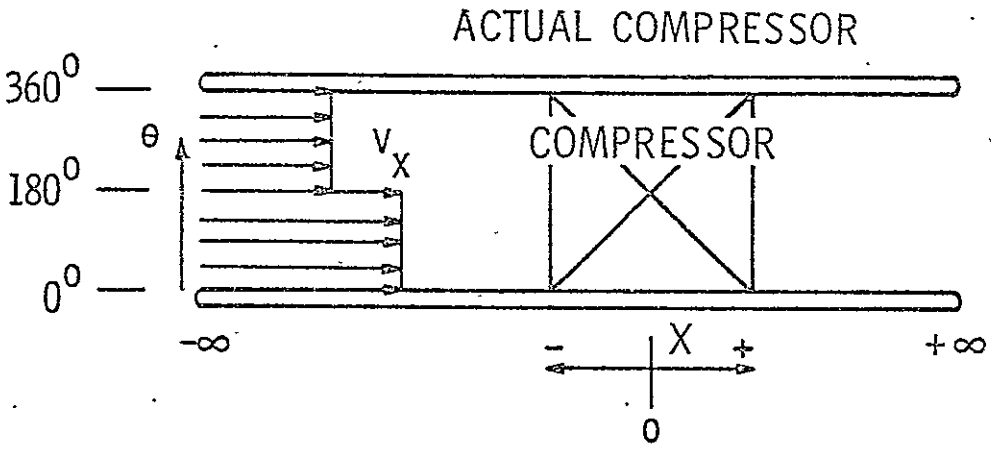

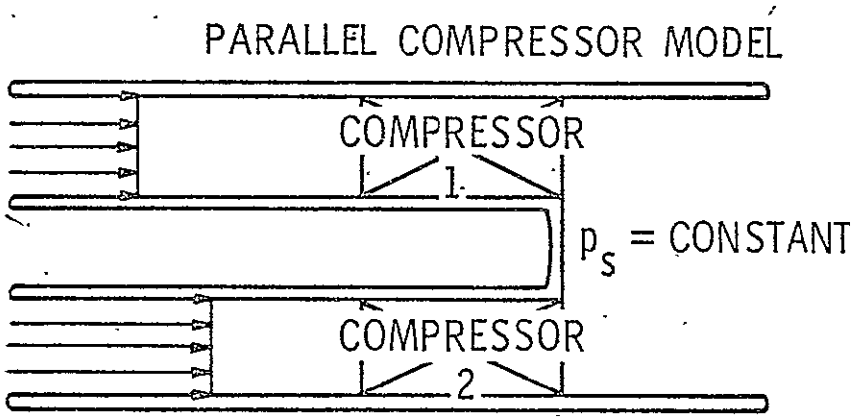

Figure 3. Schematic of a compressor with a 180° circumferential inlet distortion and the parallel compressor model of the compressor.

compressor can modify the velocity, the compressor will cause this modification at the entrance to the flow channels of the model. With this effect on the far upstream flow field, it is impossible to specify an axial velocity at the entrance, and, consequently, only the total pressure at the entrance, which is not affected by the compressor, is known. Without the velocity being known, however, the operating points of the parallel compressors are unknown. To determine the operating points, an additional boundary condition must be specified, and, for this reason, it is assumed that the static pressure at the exit of the compressor is uniform. In terms of the parallel compressor model, this means all parallel compressors exhaust to the same static pressure.

For many types of fans and compressors, the assumption of constant static pressure at the exit of the last blade row is valid. However, as pointed out by Greitzer [10], the validity of the assumption depends on whether the distortion is steady when viewed from a reference frame attached to the last blade row. Also, another component downstream of the compressor may alter the static pressure field and invalidate the assumption. For systems where the distortion is steady with respect to the last blade row and no downstream components exist near the compressor exit, the assumption has been shown both mathematically and experimentally to be valid.

The nature of the static pressure at the exit of a compressor can be understood from a simple physical explanation. For the case where no downstream components are present, it must first be realized that far downstream, the streamlines will be parallel and the static pressure will be constant. It is also known from abundant cascade data that over a fairly wide range of inlet flow angles, the flow will leave a blade

row at approximately the same angle. Therefore, if the flow is steady with respect to the exit blade row, the flow leaving the blades will be at a constant angle and the streamlines will be parallel. The parallel streamlines at the exit and the conditions far downstream imply that the static pressure must also be constant at the blade row exit. Conversely, if the flow is unsteady in the blade row reference frame, the flow angles will not be constant in the reference frame of the distortion. Therefore, the resulting streamline curvature will bring about a change in the static pressure. Since the static pressure far downstream is constant, there must be a nonuniform static pressure distribution at the compressor exit.

The assumption of constant exit static pressure completes the modeling of the compressor, and the performance in distorted flow can now be predicted if the operating characteristics of the fan or compressor are available. Figure 4 is a typical performance curve of a fan for incompressible flow, which will be used for demonstrating the model. The parameter on the vertical axis is slightly different from the conventional $(p_{T\,exit} - p_{T\,inlet})/\frac{1}{2}\rho U^2$ with the static pressure at the exit replacing the total pressure at the exit. A performance curve of this type simplifies the calculations, since the static pressure at the exit is constant, and $\Delta\Psi'$ as defined on the figure is simply equal to the difference in dimensionless pressure between the spoiled and unspoiled sectors at the inlet.

The mean flow coefficient, which must be known, supplies one of the relationships between ϕ_1 and ϕ_2 by its definition:

$$\phi_{mean} = \frac{\phi_1\ \theta + \phi_2\ (2\pi - \theta)}{2\pi}\ , \qquad (2)$$

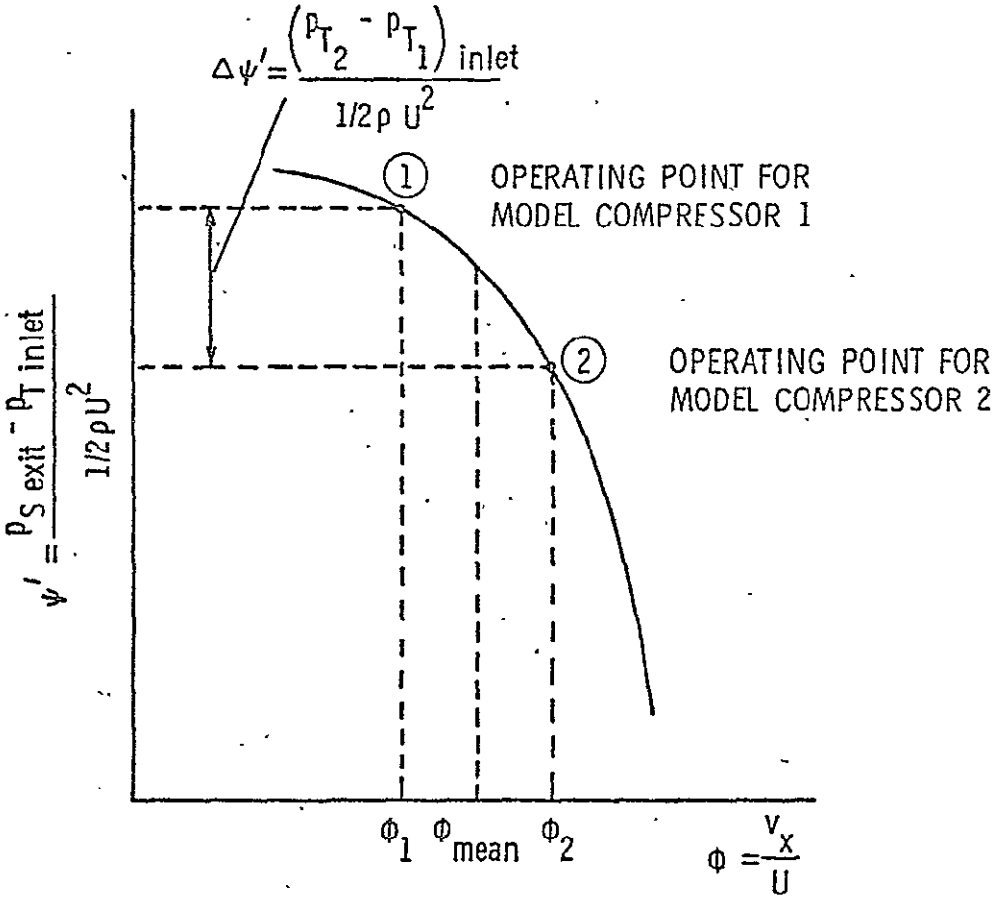

Figure 4. Performance curve for demonstrating the parallel compressor theory.

where θ = angle of the distorted sector (radians), and

$\phi = v_x/U$ = flow coefficient.

Subscripts 1 and 2 refer to the model compressors shown on Figure 3.

An additional relationship is provided by the performance curve which can be mathematically written as:

$$\frac{p_{s\,exit} - p_{T\,inlet}}{\frac{1}{2}\rho U^2} = f(\phi). \tag{3}$$

Equation (3) can be written for both ϕ_1 and ϕ_2, and when the two equations are subtracted, a final equation relating the size of the distortion to ϕ_1 and ϕ_2 is obtained:

$$\Delta\Psi' = \frac{(p_{T_2} - p_{T_1})_{inlet}}{\frac{1}{2}\rho U^2} = f(\phi_1) - f(\phi_2) . \tag{4}$$

Equations (2) and (4) can now be solved simultaneously to determine ϕ_1 and ϕ_2, which will define the operating points of the two model compressors. To determine the functional relationship of Equation (3), the steady data from the Axial Flow Research Fan were represented as a function of the flow coefficient using first and second order polynomials. The total pressure measured upstream and downstream of the rotor was represented by second order polynomials, while the circumferential velocity component downstream was represented as a first order polynomial. The curves were fit using a least squares technique, and the resulting representation of the data was found to be very good.

With the assumptions of the parallel compressor model, it is known that the axial velocity cannot change, the circumferential velocity component upstream of the rotor is zero, and the radial velocity component is zero everywhere. The three polynomials mentioned above, thus, completely describe the steady uniform flow upstream and downstream of the rotor. The reason only the total pressure and circumferential velocity component were used to represent the performance was to obtain performance curves which are consistent with both the Bernoulli equation and the restrictions of the parallel compressor model. In the experimental data, slight changes in the axial velocity did occur across the rotor, and small radial velocity components were present.

The coefficients from the three polynomials can be combined to obtain an equation for Ψ'. This equation is then used to obtain an explicit form of Equation (4). ϕ_1 and ϕ_2 are then solved for algebraically.

With the operating points known, the static pressure at the exit is determined from calculated values of Ψ' and the known inlet total pressure. The total pressure at the exit is determined from data of $(p_{T\,exit} - p_{T\,inlet})\frac{1}{2}\rho U^2$ vs ϕ. The two remaining quantities, $p_{s\,inlet}$ and $v_{\theta\,exit}$, are calculated from known quantities using the Bernoulli equation, thus completely specifying the flow field upstream and downstream of the rotor.

It is well-known and documented in the literature that the parallel compressor model predicts the amplitude of a distortion at the exit of a compressor quite accurately. However, large discrepancies usually exist between the predicted and measured shape of the distortion. This is due to the flow redistribution which occurs in the real situation

which cannot be accounted for by the parallel compressor model, since no cross flow can exist between the parallel compressors.

It is seen from the parallel compressor analysis that the axial velocity is determined by the performance characteristics of the rotor, as well as the mean flow coefficient and the size of the total pressure distortion at the inlet. The axial velocity, except under very special circumstances, will be modified by the presence of the rotor. The parallel compressor model requires this modification to occur at the inlet as was previously discussed in regard to the boundary conditions. In reality, however, the modification will occur near the rotor. For an incompressible fluid, a change in axial velocity will require the stream tube to converge or diverge depending on whether the flow decelerates or accelerates. The resulting streamline curvature will result in induced circumferential components of velocity which will alter the flow incidence on the blades in a asymmetric manner. The parallel compressor model cannot account for this variation and, hence, the poor prediction of the distortion shape results. Near the center portion of the distortion, the circumferential components are negligible and the amplitude is accurately predicted in this region.

3.2 Actuator Disc Model

To overcome the restrictions of the parallel compressor model and to obtain a more accurate prediction of the distortion shape, it is necessary to model the flow upstream and downstream of a blade row without any artificial restrictions imposed. The approach taken with this model is to solve the basic flow equations involved after a few simplifying assumptions have been made and the equations have been linearized. The blade row is represented by an actuator disc, which

is obtained by assuming the chord length of the blades is zero. The actuator disc, therefore, concentrates the effects of the blade row at a single location, and the changes in the flow field across the blade row are thus represented by a discontinuity. Since a discontinuity cannot exist in a real flow system, the regions divided by the actuator disc must be treated as separate flow fields. The boundary conditions at the actuator disc are specified by the matching conditions for the blade row performance. In this case, it is assumed the blade row responds quasi-steadily, and the response is a continuous function of the local incidence. A list of these and other necessary assumptions is as follows:

1. Incompressible flow.
2. Two-dimensional flow.
3. Steady flow.
4. No body forces.
5. Inviscid flow.
6. The amplitude of the velocity distortion is small compared to the average axial velocity.
7. Blade row is represented as an actuator disc.
8. Quasi-steady blade row response.

The first five assumptions are used to simplify the Navier-Stokes equations to a form which can be linearized and solved analytically. Assumptions 1 through 4 are justified since the flow under consideration approximates these conditions very closely. The fifth assumption is also justifiable, even though a non-uniform flow is a viscous shear flow. Due to the low viscosity of air, the change in the distortion velocity profile caused by viscous effects through the distance

considered is negligibly small compared to the effects caused by the blade row. Therefore, viscous effects upstream and downstream of the blade row can be neglected. Viscous effects are accounted for in the blade row by loss data which are included in the rotor performance.

After applying the first five assumptions, the following three basic equations are obtained:

x-momentum equation

$$\rho\left(\frac{v_\theta}{r}\frac{\partial v_x}{\partial \theta} + v_x \frac{\partial v_x}{\partial x}\right) = -\frac{\partial p_s}{\partial x} \quad . \tag{5}$$

θ-momentum equation

$$\rho\left(\frac{v_\theta}{r}\frac{\partial v_\theta}{\partial \theta} + v_x \frac{\partial v_\theta}{\partial x}\right) = -\frac{1}{r}\frac{\partial p_s}{\partial \theta} \quad . \tag{6}$$

Conservation of mass equation

$$\frac{1}{r}\frac{\partial v_\theta}{\partial \theta} + \frac{\partial v_x}{\partial x} = 0. \tag{7}$$

Using the preceding equations, the necessary non-dimensional linear equations are derived in detail in Appendix B. Therefore, the details will not be repeated here, however, the important steps will be outlined. To linearize the equations, the velocity components and the pressure are first represented as the sum of the circumferential mean value and a perturbation quantity.

$$p_s = \bar{p}_s + p_s' \ , \tag{8}$$

$$v_x = \bar{v}_x + v_x' \tag{9}$$

and

$$v_\theta = \bar{v}_\theta + v_\theta' \,. \tag{10}$$

After introducing Equations (8), (9), and (10) into Equations (5), (6), and (7), each term can be expanded. The key assumption for this linear theory is now applied. Assumption 6, which implies that $v_x' << \bar{v}_x$ and $v_\theta' << \bar{v}_x$, allows second order terms to be ignored. It is also possible to ignore all terms containing derivatives of the average quantities, since the basic equations for the average quantities reveal that these derivatives are zero. After eliminating these terms, linear partial differential equations result. For convenience, the static pressure is then replaced by the total pressure, using a form of the Bernoulli equation written in terms of the average and perturbation quantities. After non-dimensionalizing the equations, the following final equations result:

x-momentum equation

$$2a\left(\frac{\partial v_x'}{\partial \theta} - \frac{\partial v_\theta'}{\partial X}\right) = -\frac{\partial P_T'}{\partial X} \,, \tag{11}$$

where

$$a = \frac{\bar{v}_\theta}{\bar{v}_x} \,.$$

θ-momentum equation

$$2\left(\frac{\partial v_x'}{\partial \theta} - \frac{\partial v_\theta'}{\partial X}\right) = \frac{\partial P_T'}{\partial \theta} \,. \tag{12}$$

Conservation of mass equation

$$\frac{\partial V_\theta'}{\partial \theta} + \frac{\partial V_x'}{\partial X} = 0. \tag{13}$$

Equations (11), (12), and (13) are solved by first assuming the solutions can be represented as a Fourier Series. The solution obtained in this manner is, therefore, essentially a separation of variable approach, since the solution is represented as the product of a function of X and a function of θ. The Fourier Series is expressed in complex notation, where it is understood the real part of the complex number represents the physical quantity. Since the quantities considered are perturbation quantities, the term of the summation for $n = 0$ is zero and can be dropped. This simplifies the manipulation of the equations because division by n is possible. The equations expressing the solution in this form are as follows:

$$P_T' = 2 \sum_{n=1}^{\infty} R_n(X) e^{in\theta}, \tag{14}$$

$$V_x' = \sum_{n=1}^{\infty} S_n(X) e^{in\theta} \tag{15}$$

and

$$V_\theta' = \sum_{n=1}^{\infty} T_n(X) e^{in\theta}. \tag{16}$$

After substituting Equations (14), (15), and (16) into Equations (11), (12), and (13), three ordinary differential equations result which must be solved simultaneously. The summation signs must be dropped from these equations so a solution can be found for particular values of n. The three ordinary differential equations are:

$$\text{in } S_n(X) - \frac{d\ T_n(X)}{dX} = -\frac{1}{a}\frac{d\ R_n(X)}{dX} \quad , \tag{17}$$

$$\text{in } S_n(X) - \frac{d\ T_n(X)}{dX} = \text{in } R_n(X) \tag{18}$$

and

$$\text{in } T_n(X) + \frac{d\ S_n(X)}{dX} = 0 \ . \tag{19}$$

The terms on the left-hand side of Equations (17) and (18) are identical. Thus, subtracting these two equations will eliminate S_n and T_n yielding a simple first order ordinary differential equation of R_n. This equation can be solved easily for R_n.

After R_n is known, $\frac{dT_n}{dX}$ in Equation (18) can be eliminated using Equation (19) and a second order nonhomogeneous ordinary differential equation results. This equation can also be solved using conventional techniques for a solution for S_n. The solution for S_n is then differentiated and substituted back in Equation (19), yielding an equation which can be solved algebraically for T_n, completing the solution of the system of ordinary differential equations. The expressions for

R_n, S_n, and T_n are substituted back into Equations (14), (15), and (16), and after expressing the constants in a convenient manner, the following equations for P_T', V_x', and V_θ' are obtained:

$$P_T' = 2(1 + a^2) \sum_{n=1}^{\infty} A_{3_n} e^{-inax} e^{in\theta} , \tag{20}$$

$$V_x' = \sum_{n=1}^{\infty} (A_{1_n} e^{nx} - A_{2_n} e^{-nx} + A_{3_n} e^{-inax}) e^{in\theta} \tag{21}$$

and

$$V_\theta' = \sum_{n=1}^{\infty} (A_{1_n} ie^{nx} + A_{2_n} ie^{-nx} + A_{3_n} ae^{-inax}) e^{in\theta} . \tag{22}$$

The complex coefficients A_{1_n}, A_{2_n}, and A_{3_n} are determined from the boundary conditions. Since the flow fields upstream and downstream of the disc must be treated separately, there is a total of six coefficients for each n that must be determined. Figure 5 is a schematic of the flow fields with the coordinate system and the boundary conditions labeled, which will be helpful in the description of the boundary conditions.

Two of the constants, $A_{2_n}|x < 0$ and $A_{1_n}|x > 0$, are equal to zero, since the velocity perturbation at plus and minus infinity must be finite. The values for $A_{3_n}|x < 0$ are also known from the specified total pressure distortion. The remaining three constants, therefore, are specified by the matching condition at the actuator disc. The three conditions imposed at the disc are: (1) constant axial velocity, (2) a specified total pressure change which is a function of the local inlet

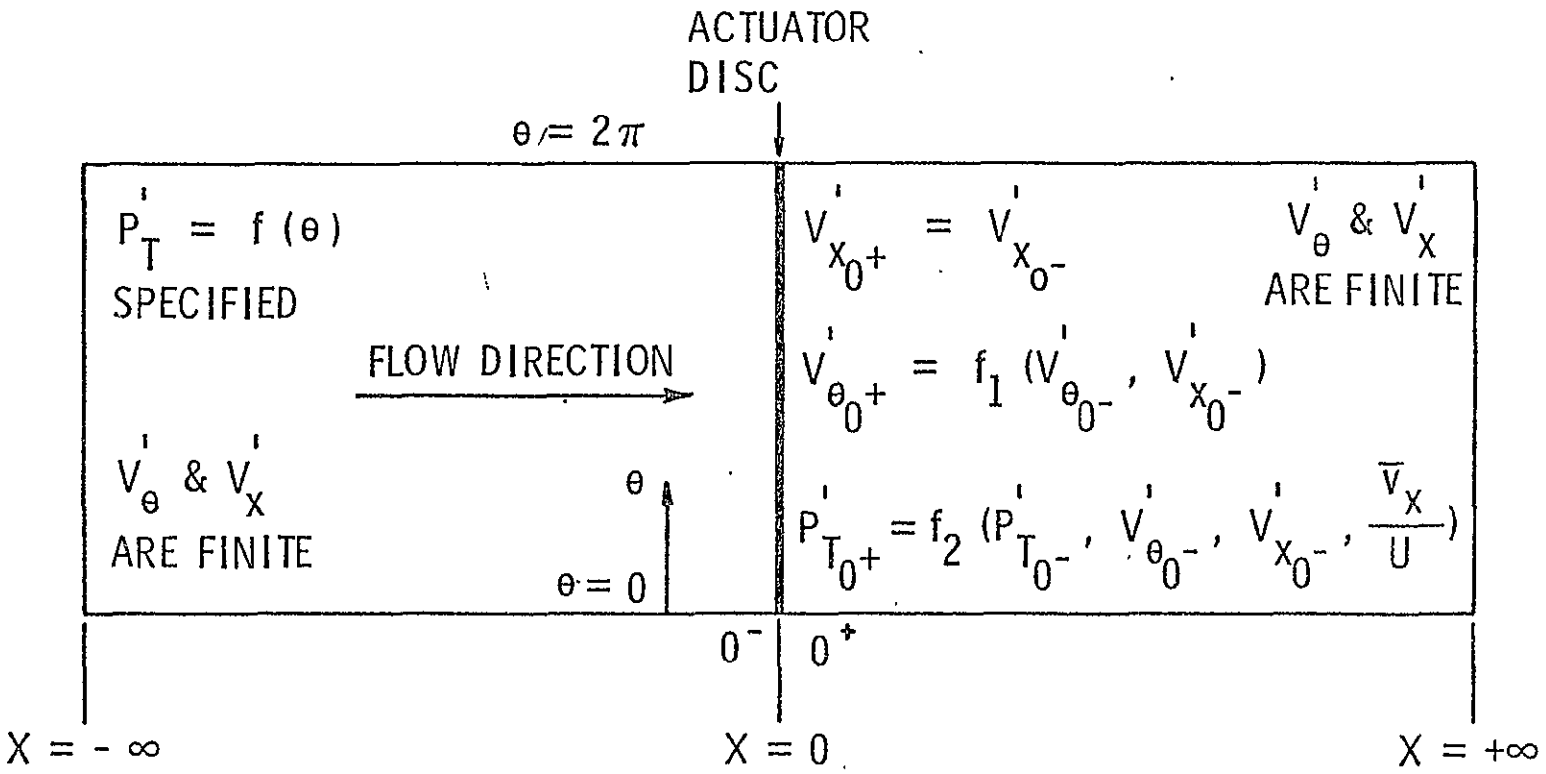

Figure 5. Schematic of the actuator disc and surrounding flow fields, with the boundary conditions indicated.

conditions, and (3) a specified change in V_θ which is also a function of the inlet conditions. The first condition can be expressed simply as $V'_{x_{0^-}} = V'_{x_{0^+}}$ and $\overline{V}_{x_{0^-}} = \overline{V}_{x_{0^+}}$. The other two matching conditions are functions of the inlet flow conditions, with the functional relationship prescribed by the blade row performance. The blade row performance is usually determined from experimental data.

Since the solution to the partial differential equations was made possible by linearizing the equations such that an infinite series type solution was possible, the boundary conditions must also be represented in a linear manner so these conditions can be added in a similar fashion. The performance of the blade row, which was determined experimentally, must therefore be represented in a form such that the equations relating the inlet conditions to the exit conditions are linear relations.

The relationship for the change in the circumferential velocity component is based on the fact that the relative angle of the flow leaving a blade row is approximately constant over small ranges of relative inlet flow angle. In this case, a linear relation is assumed to exist between the tangents of the relative inlet and exit flow angles, with the tangents being used to facilitate the introduction of the velocity components into the equation. The slope and the intercept in the equation is determined from the experimental data. For the data of this study, one line was shown to fit most of the data very well. However, for less linear data, a straight line can be fit through the local region of the performance curve in which the blade row will operate while in the distortion.

Before introducing the necessary equation, Figure 6, which is a two-dimensional representation of a blade row and the velocity triangles,

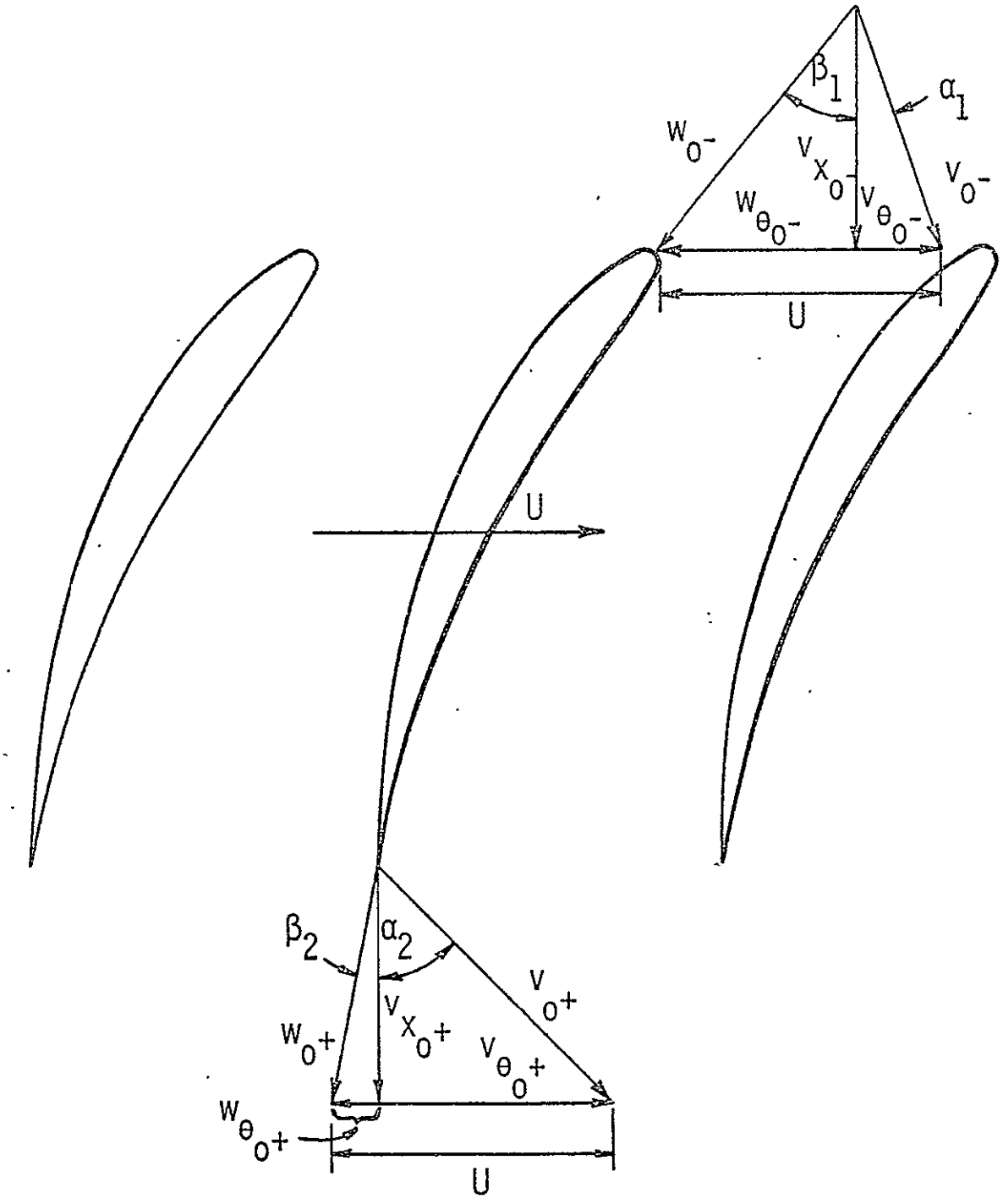

Figure 6. Two-dimensional representation of a blade row with the velocity triangles at the inlet and exit indicated.

is provided to define the angles used and identify the various velocity components involved.

The required relationship relates the tangent of β_2 to the tangent of β_1. This can be written in the following form, where m and b are the slope and intercept of the straight line representing the data:

$$\text{Tan } \beta_2 = m \tan \beta_1 + b \ . \tag{23}$$

Referring to Figure 6, the tangents can now be replaced by the velocity components. It should be noted, that velocity components represented in the figure are total components, the sum of the average and perturbation quantity:

$$\frac{U - v_{\theta_{0^+}}}{v_{x_{0^+}}} = m \left(\frac{U - v_{\theta_{0^-}}}{v_{x_{0^-}}} \right) + b \ . \tag{24}$$

For an incompressible flow, $v_{x_{0^-}} = v_{x_{0^+}} = v_x$; thus, v_x can be removed from the denominator by multiplying through by v_x. The velocity components can also be broken into their average and perturbation quantities. After expanding each term and introducing the dimensionless velocity components, equating constant and fluctuating terms provides the two necessary equations. One equation relates the average swirl (a) to the inlet conditions, and the other specifies the exit condition for V_θ'. The two equations are:

$$a = \frac{U}{\overline{v}_x} (1 - m) - b \tag{25}$$

and

$$V'_{\theta_{0+}} = mV'_{\theta_{0-}} - bV'_{x} \quad (26)$$

Two similar equations must also be found for expressing the change in total pressure across the disc. In this case, it was found convenient to express the change in terms of an ideal total pressure rise calculated from the velocity components using Euler's pump equation and an experimentally determined total pressure loss across the blade row. The total pressure loss is a function of the inlet conditions. However, for the changes in inlet conditions encountered with the distortions of this study, the loss can be assumed constant. An equation expressing the above conditions in terms of the dimensionless variables is as follows:

$$P'_{T_{0+}} = P'_{T_{0-}} + 2\frac{U}{\overline{V}_x}(V_{\theta_{0+}} - V_{\theta_{0-}}) - \Delta P_{Loss} \quad (27)$$

This equation can also be expanded by introducing the average and perturbation quantities. Once again equating constant and fluctuating terms, the two desired equations are obtained. $\overline{V}_{\theta_{0-}}$ has been dropped since, in this case, it is equal to zero:

$$\overline{P}_{T_{0+}} = \overline{P}_{T_{0-}} + 2\frac{U}{\overline{V}_x}a - \Delta P_{Loss} \quad (28)$$

and

$$P'_{T_{0+}} = P'_{T_{0-}} + 2\frac{U}{\overline{V}_x}(V'_{\theta_{0+}} - V'_{\theta_{0-}}) \quad (29)$$

The preceding equations complete the derivation of all the necessary equations. Evaluating Equations (20), (21), and (22) at $x = 0^-$ and $x = 0^+$ for a constant value of n, yields six equations, three for each side of the disc. These six equations can be combined by applying the matching conditions previously derived, resulting in three equations which can be solved simultaneously for the remaining three unknown complex coefficients. With all the coefficients known, the solution is complete.

The only calculations necessary are those required for evaluating the complex coefficients for each harmonic. This requires computing the Fourier coefficients for the known total pressure distortion, and then calculating the other coefficients from the known values of A_{3_n} and the performance parameters.

CHAPTER IV

PROBE SELECTION, CALIBRATION, AND USE

4.1 Probe Selection and Description

The selection of five-hole probes for the measurements of this study was based on several important reasons. A few of these reasons become apparent if the types of measurements made and alternate measuring techniques are considered. To begin with, the flow through the rotor is unavoidably three-dimensional. Although two-dimensional effects are the primary consideration, it is advantageous to measure the three-dimensional characteristics in order to verify the two-dimensional assumption, or to quantify the deviation from two-dimensional behavior. With variations in the flow properties in both the circumferential and radial direction, local measurements of the static pressure, the total pressure and the local flow direction are required. After determining the total and static pressure, the absolute velocity can be calculated, and, with the known flow angles, the velocity can be broken into its three components.

Since only time-averaged flow characteristics at a point are under consideration in this study, fluctuations due to the turbulence in the flow and fluctuations due to the blades passing need not be considered. For this reason, a probe with a slow response can be utilized. Traditionally, the type of probe used for total and static pressure measurements is the pitot-static tube. A probe similar to a pitot-static tube can also be used to sense direction, as well as total and static pressure. Two holes symmetrically located on both sides of the

be measured, are necessary. A schematic of this type of probe is shown in Figure 7.

The holes designated as 2 and 3 in the figure are used for determining the flow direction by rotating the probe until these holes sense equal pressures. When this is accomplished, the probe is aligned with the flow, and the flow angle can be determined by measuring the probe orientation. After the probe is aligned with the flow, total pressure is measured through hole 1, and holes 2 or 3 are used to obtain the static pressure. This method of measuring flow angles can obviously be extended to measuring three-dimensional flow characteristics by using a probe with two additional holes similarly located in the plane perpendicular to the plane of holes 1, 2, and 3, and then also aligning the probe with the flow in this plane. The technique of aligning the probe with the flow is called nulling.

The justification for using five-hole probes for measuring three-dimensional flows is understandable from the preceding considerations. However, nulling a probe is not always practical, especially if nulling is required in both planes. The apparatus necessary for nulling a probe while still maintaining the probe's location can be very complex, and sometimes spatial limitations can make nulling impossible. For these reasons, calibrations were obtained for the probes used in this study, enabling them to be used in a non-nulling mode.

The probes selected for use in the Axial Flow Research Fan were commercially available United Sensor five-hole prism-type probes. A probe of this type has a prism-shaped section cut into the side of a small cylindrical section. This prism-shaped section is used to provide five different surfaces on which to locate the holes, and thus improve

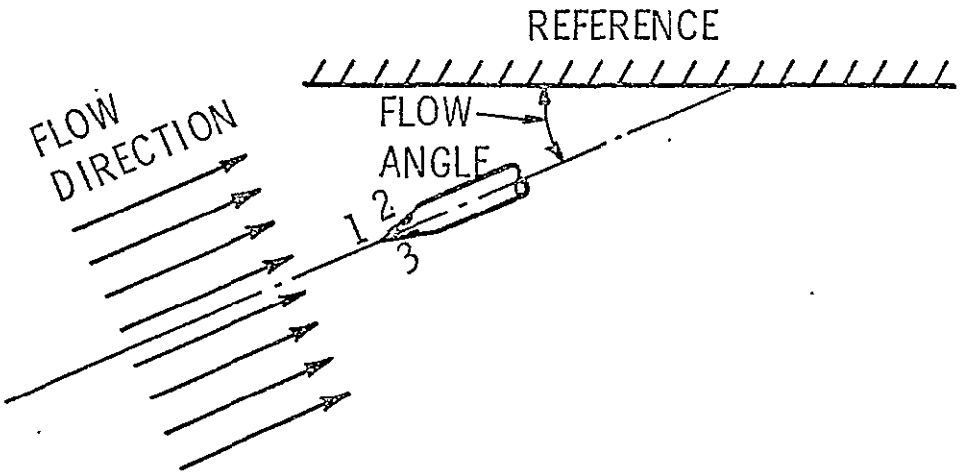

Figure 7. Schematic of a three-hole probe aligned with the flow.

the sensitivity of the device, while still containing the sensing element of the probe within the cylindrical surface around the main axis of the probe. The location of the holes in this manner yields a probe shape which can be inserted easily through a casing wall and used in studies where spatial restrictions are present.

An enlarged sketch of the sensing element of such a probe is shown in Figure 8. This sketch reveals the geometry of the prism section and the location of the five holes. In the figure, the five holes are numbered for identification. These numbers correspond to the numbers inscribed by the manufacturer adjacent to the take-off tubes.

Also included in Figure 8 is a sketch of the entire probe, which is provided to show the overall construction and dimensions of the probes used. It is seen from the figure that the center hole is located 0.25 in. (0.635 cm) from the tip. This distance is necessary to decrease the probe's sensitivity to flow angle, since the flow near the tip will vary greatly with flow direction.

The diameter of the cylindrical section containing the sensing element, as shown by the figure, is 0.125 in. (0.3175 cm). This diameter should be as small as possible to minimize the flow disturbance caused by the probe, but must be large enough to resist bending when in use. To provide a more rigid instrument, the diameter of the probe shaft is increased to 0.25 in. (0.635 cm), 2 in. (5.08 cm) from the tip.

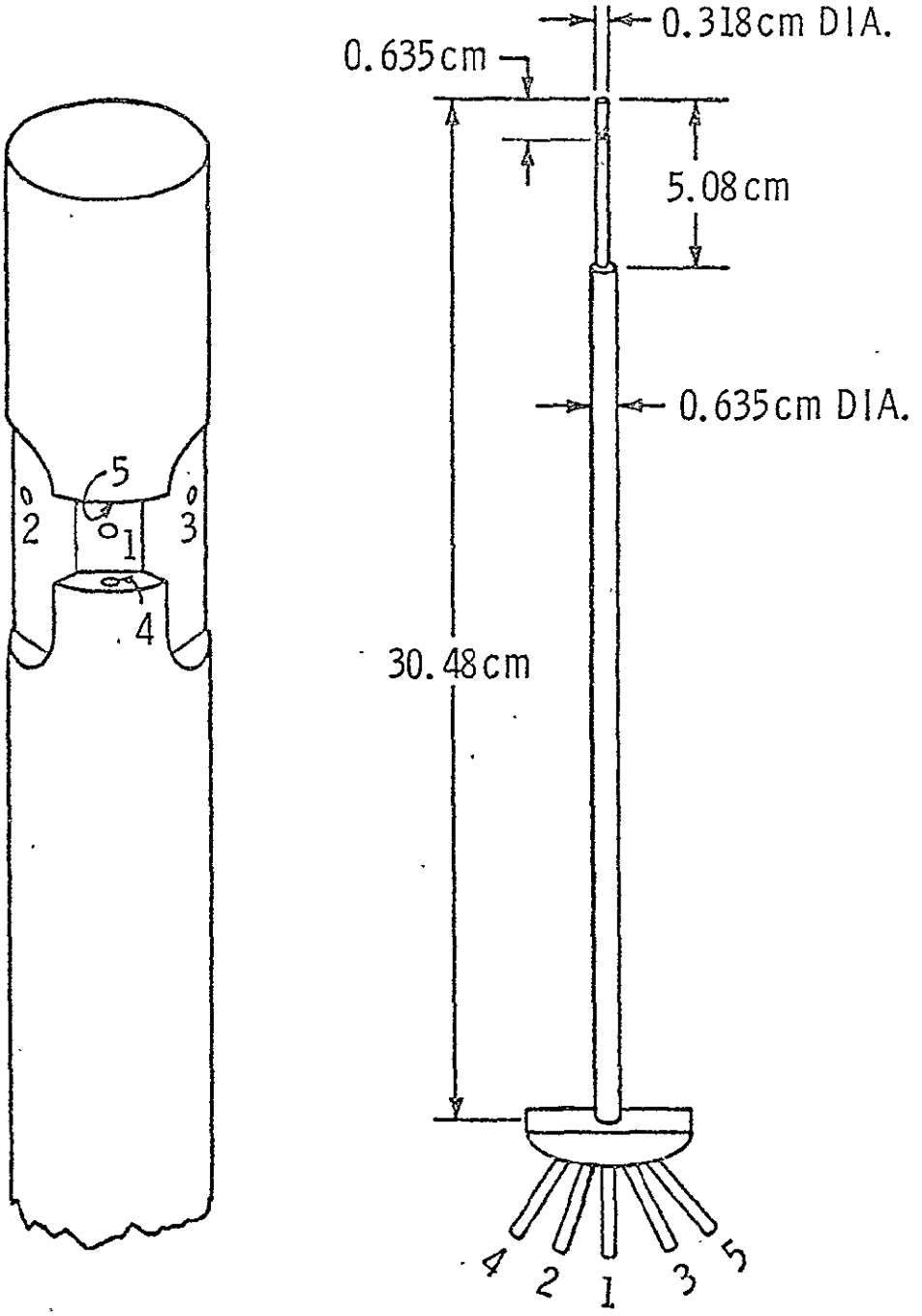

Figure 8. An enlarged sketch of the sensing element and an overall view of a United Sensor five-hole probe, Type DA-125-12-F-10-CD.

4.2 Calibration and Use

It was previously mentioned that the five-hole probes used in this study were used in the non-nulling mode. In this mode, the probe is maintained at a fixed orientation with respect to a certain physical reference, and the flow direction and the total and static pressure are determined from the pressures measured from the five holes. The computation of the flow angles and the total and static pressure, therefore, requires a knowledge of how the pressures sensed by the probe relate to the true fluid pressures and the flow angles. This information is obtained from a calibration process, which consists of placing the probe in a known flow field and recording the probe pressures as a function of flow angularity. The data obtained in this manner are then expressed in dimensionless forms which eliminate the dependence of the data on the absolute values of the pressures of the flow field.

The calibration of five-hole probes for the non-nulling mode is basically simple; however, certain details should be considered. First, consistent physical references on the probe for the angle measurements should be selected, and the orientation of the planes in which the flow angles are measured must be defined. Second, a suitable means of representing the characteristics of the probes and non-dimensionalizing the data must be found. Third, if the type of probe used has not been previously tested in the non-nulling mode, as in this case, more than one calibration is required to prove the repeatability of the probe. Fourth, effects on the calibration data caused by changes in the flow field, such as variations in Reynolds number or Mach number may be important, and also the effects of other operational variables may want to be considered. In this case, changes caused by variations

in Reynolds number, and the interference effect caused by the proximity of a solid boundary were considered important enough to warrant investigation.

It is obvious from the preceding list of considerations that the details of the calibration process could be quite lengthy. For this reason, to avoid excessive deviation from the main topic, Appendix A is devoted to a complete description of the probe calibrations. In this chapter, only a short summary of the basic calibration and its use will be presented.

To begin with, it is necessary to define four pressure coefficients. The yaw coefficient is used to relate the probe pressures to the flow yaw angle, the pitch coefficient is used to relate the probe pressures to the flow pitch angle, and similarly, the total and static pressure coefficients are used to enable the true flow pressures to be calculated from the pressures from the probe. The following four coefficients are therefore defined:

$$C_{p\,yaw} = \frac{p_2 - p_3}{p_1 - 1/4(p_2 + p_3 + p_4 + p_5)}, \tag{30}$$

$$C_{p\,pitch} = \frac{p_5 - p_4}{p_1 - 1/4(p_2 + p_3 + p_4 + p_5)}, \tag{31}$$

$$C_{p\,total} = \frac{p_1 - p_T}{p_1 - 1/4(p_2 + p_3 + p_4 + p_5)} \tag{32}$$

and

$$C_{p\ static} = \frac{1/4(p_2 + p_3 + p_4 + p_5) - p_s}{p_1 - 1/4(p_2 + p_3 + p_4 + p_5)}, \qquad (33)$$

where the subscript numbers refer to the holes as identified in Figure 8, and p_T and p_s are the true total and static pressure, respectively. Physical reasoning and additional justification for defining the pressure coefficients in this manner are described in Appendix A.

With the pressure coefficients defined as in Equations (30) through (33), the purpose of the basic calibration is to evaluate those coefficients as a function of the flow angularity. This was accomplished by locating the probes at various angles in a known flow field (known direction, p_T, and p_s) provided by a 12-in. (30.48 cm) diameter open air jet. Typical results obtained are presented in Figures 9 through 11, where the calibration data for the probe used in the Axial Flow Research Fan upstream of the rotor are given.*

Explanations for the general nature of the curves in Figures 9 through 11 can be obtained by considering basic fluid dynamic concepts. However, this topic is reserved for the discussion of the results in Appendix A. For now, the figures will be used to explain how the calibration data are applied to obtain the desired information when the probes are used in the non-nulling mode.

---

*The serial number of the probe used in the AFRF upstream of the rotor is B-1164-1 and the serial number for the probe used downstream of the rotor is B-1164-2. These numbers are important, since the probe data are identified by these numbers. At subsequent points in this paper, the probes may be referred to as 1 or 2, which correspond to the last digit of the serial number.

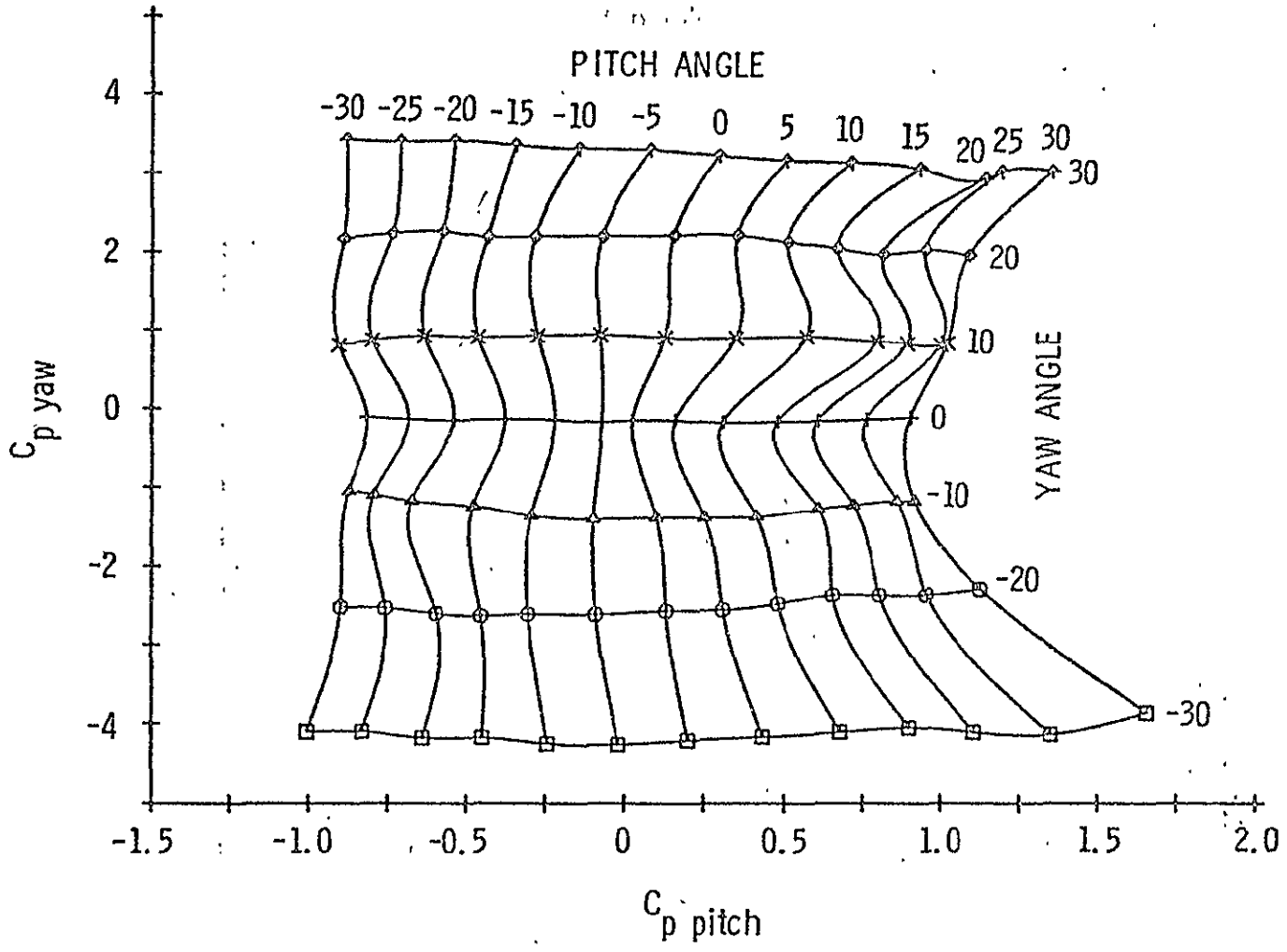

Figure 9. Calibration data for Probe 1, $C_{p\ yaw}$ versus $C_{p\ pitch}$.

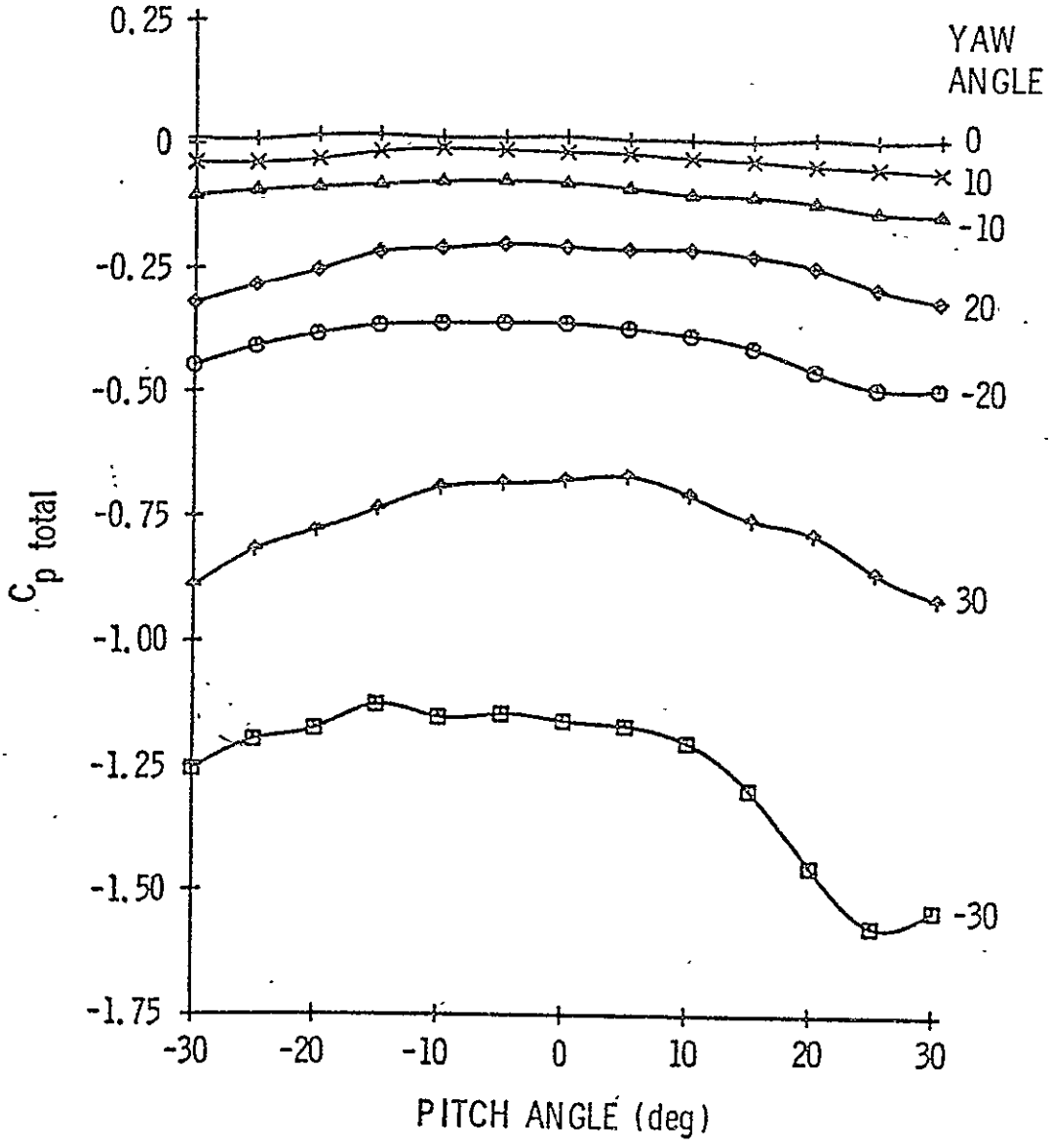

Figure 10. Calibration data for Probe 1, $C_{p\ total}$ versus pitch angle.

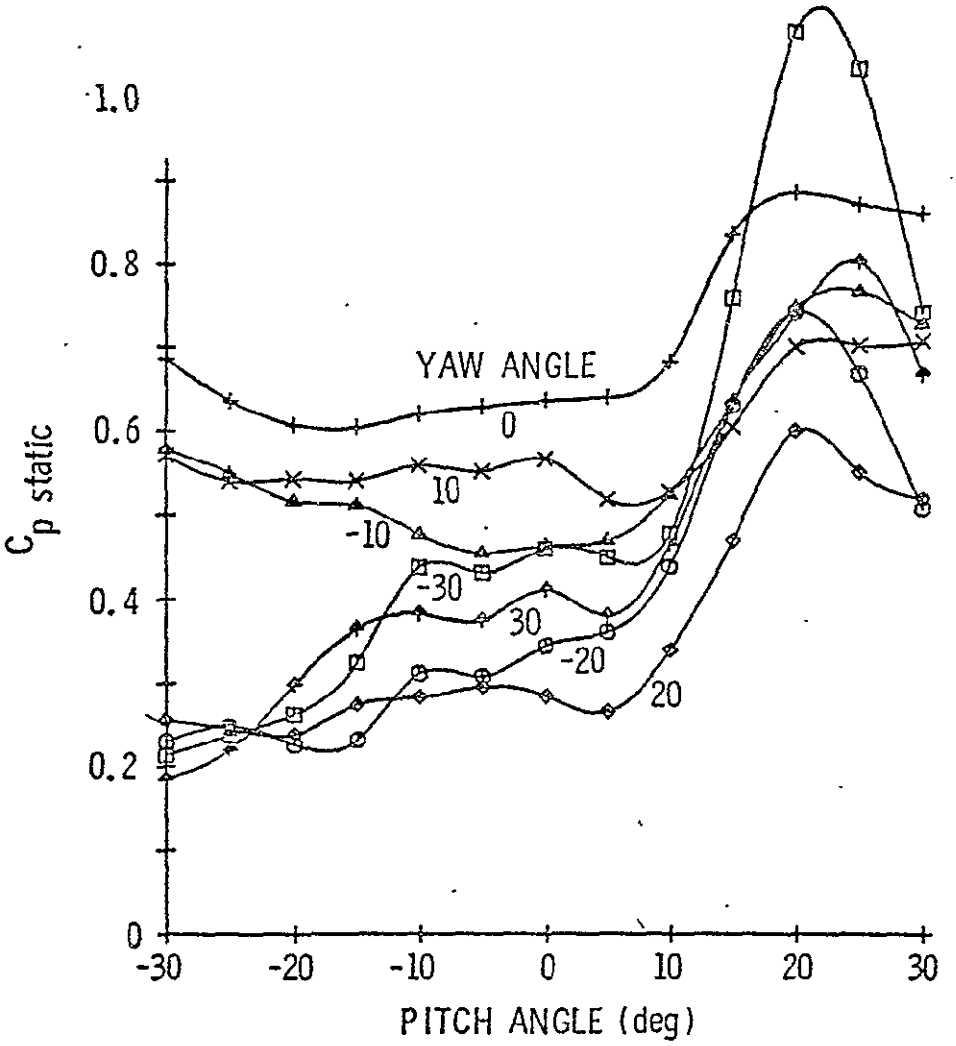

Figure 11. Calibration data for Probe 1, $C_{p\ static}$ versus pitch angle.

Figure 9, which is a plot of the yaw coefficient versus the pitch coefficient, is shown to contain lines of constant pitch angles and lines of constant yaw angles. This figure is easily obtained when calibrating the probes, since the two coefficients are calculated from the five probe pressures and the flow angles are also known. When the probe is being used in an unknown flow field, the data of Figure 9 provide the relation between the probe pressures and the flow angles. After calculating the yaw and pitch coefficients from the probe pressures, entering Figure 9 with these coefficients enables the yaw and pitch angle to be calculated by interpolating for the precise values using the grid lines of constant pitch and yaw angles.

The interpolation procedure for determining the flow angles can be easily performed on the digital computer using spline curve functions. The characteristics of these functions are demonstrated by the curves in Figures 9 through 11, which were generated using the spline functions to obtain closely spaced values of intermediate points. It is realized, however, that the quantities to be determined from the calibration data are a function of two independent variables, and thus a double interpolation procedure is required. Using the calculation for the yaw angle as an example, the first step is to enter Figure 9 with the calculated value of $C_{p\ pitch}$ and, for each line of constant yaw angle, interpolate, using the spline function, the corresponding value of $C_{p\ yaw}$. This step produces data of yaw angle versus $C_{p\ yaw}$. The data obtained from the first step can then be mathematically fitted with a spline curve, and, using the known value of $C_{p\ yaw}$, the yaw angle can be calculated. The procedure for determining the pitch angle is similar.

Since the flow angles are determined from the data of Figure 9, it is convenient to express the total and static pressure coefficients as functions of these angles. Figures 10 and 11 represent the results where $C_{p\ total}$ and $C_{p\ static}$ are plotted versus pitch angle with lines of constant yaw angle. The total and static pressure coefficients can be interpolated from these curves using the flow angles, and the total and static pressure can be calculated. The interpolation procedure is the same as the one previously described. A more detailed description of the entire interpolation procedure can be found in Reference [11].

CHAPTER V

EXPERIMENTAL FACILITIES AND PROCEDURES

5.1 Axial Flow Research Fan Description

The Axial Flow Research Fan (AFRF), which is housed in the Garfield Thomas Water Tunnel building at The Pennsylvania State University, was specifically designed for studying unsteady flow phenomena in turbomachinery. The overall dimensions of the test rotor and the facility were made sufficiently large, so that the blades can be instrumented or flow surveys can be made with few spacial limitations. Figure 12 is a sketch of the facility, which shows the key components of the system and a few overall dimensions.

Basically, the AFRF is an open wind tunnel, with an annular cross section, consisting of four major sections. The first section, which is the entrance section, was designed to provide steady uniform flow to the annulus. This section consists of a bellmouth-shaped entrance and an elliptical-shaped nose on the hub. The entire entrance is enclosed by a wooden framework, which is covered by a layer of foam backed by an insect screen. This inlet enclosure was found to be necessary to eliminate velocity fluctuations in the annulus, which were probably caused by disturbances in the room where the AFRF is housed [14].

Immediately downstream of the entrance is the section where the flow distortions are generated. Here, screens for producing distortions of the various types are placed against the inlet struts, as shown in Figure 12. Downstream of the screen, a section of annulus is then provided to allow small velocity variations and any static pressure

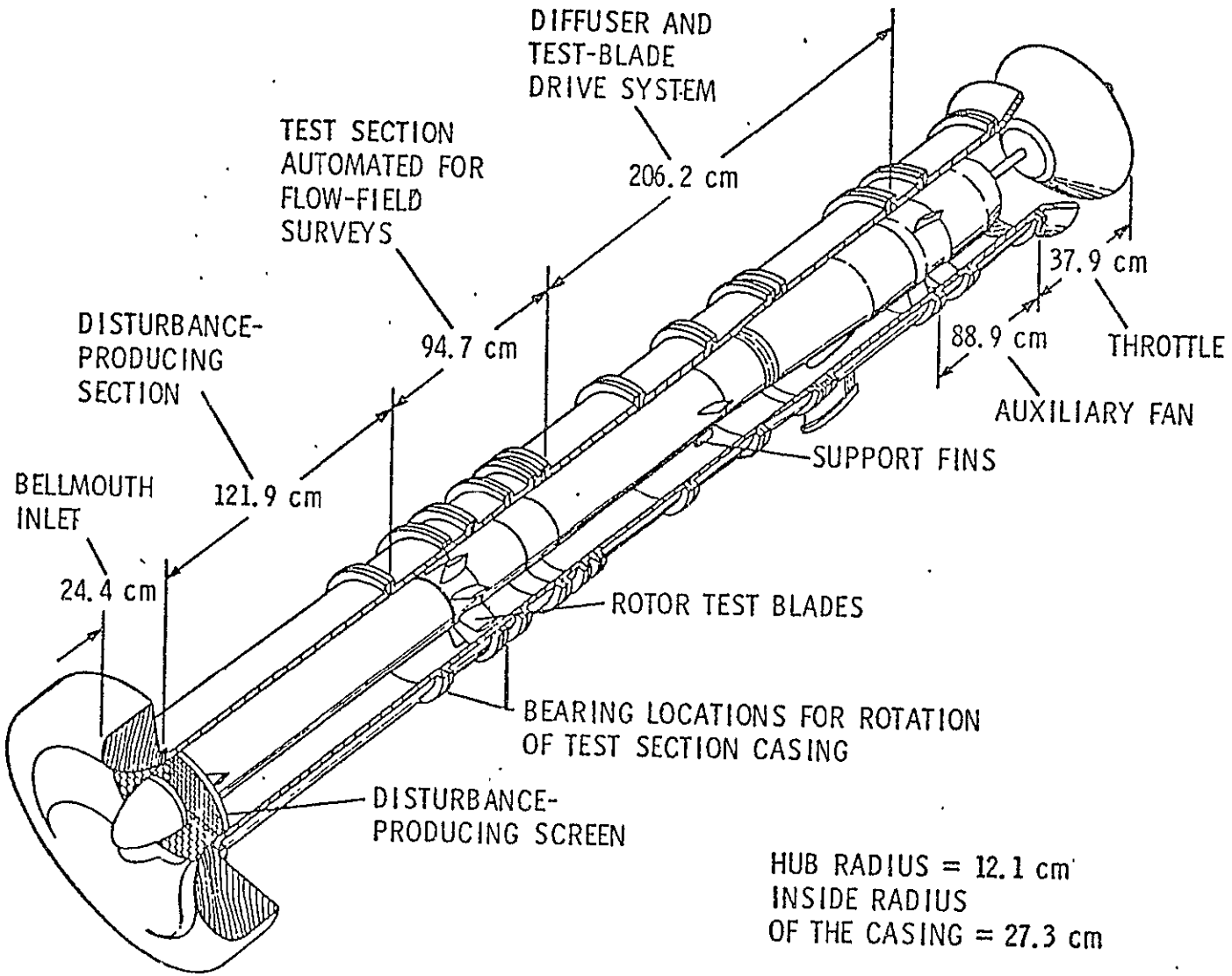

Figure 12. Sketch of the Axial Flow Research Fan revealing the key components and the overall dimensions.

gradients to decrease, thus providing a smooth velocity profile of the desired shape to the test rotor. The section between the screen and the rotor is also necessary to eliminate any interaction which might exist between the rotor and the screen, since it is well known that the rotor will alter the upstream flow if the inlet flow is nonuniform.

The next section is designated as the test section in Figure 12, since it is here that the test rotor is located. This section contains numerous access ports at different axial locations, through which probes can be inserted to measure the characteristics of the flow field. The entire casing surrounding this section is also free to rotate, thus allowing circumferential surveys of the flow to be made. The casing is driven through a worm gear by an 1800 in-ounce torque Slo-Syn motor which is controlled by a Slo-Syn Preset Indexer. The controller allows the casing to be rotated in increments as small as 1/80 of a degree and can be indexed either manually or by an automated data acquisition system.

In the final section downstream of the test section, the drive system for the test rotor, an auxiliary fan, and a throttle are located. The 70 horsepower motor for the test rotor is located at a sufficient distance downstream, such that the noise from the motor can be isolated from the rotor for studies of this nature. This length also provides a sufficient distance between the auxiliary fan and the test rotor, such that no interaction will occur between these components for studies involving flow distortions.

The auxiliary fan is necessary to provide the mean flow, since the test rotor is designed for zero steady loading. Although the test rotor is often operated with a steady load, the auxiliary fan is usually

necessary to provide the flexibility to obtain the desired operating conditions. Either the speed of the auxiliary fan or the throttle setting can be used to control the average throughflow velocity. Sufficient control, however, can be obtained using only the auxiliary fan and, therefore, the throttle is usually maintained in the completely open position. Both the speed of the test rotor and the auxiliary fan are controlled by Borg-Warner variable frequency power supplies.

The entire facility revealed in Figure 12 is mounted on a system of movable trusses. These trusses, which have wheels containing "V" grooves, can be moved on the "V" shaped track, thus allowing certain sections of the facility to be separated to make configuration changes. Particularly in this study, the facility could be easily separated just upstream of the rotor, allowing the rotor to be removed for changing the stagger of the blades.

An additional purpose served by the trusses is that they raise the fan above the supporting stand, thus allowing sufficient clearance for instrumentation to be rotated with the test-section casing. The trusses and supporting stand together also elevate the fan to a sufficient distance above the floor, such that an inlet vortex will not be created. The inlet is four diameters above the floor, while an inlet vortex will be created if the separation between the floor and the inlet is on the order of 2.0 to 2.5 inlet diameters [14].

5.2 Rotor Design

The test rotor, as mentioned earlier, was designed to produce zero steady lift. This was done for several reasons, one of which is that many of the presently available theories apply to zero or lightly-loaded

blades. Therefore, with the rotor designed for zero steady loading, direct comparisons of the experimental results can be made with the theories. Another reason for designing the rotor in this manner is that it is initially desirable to study the unsteady flow effects without the influence of steady loading. This reduces the number of variables. A third reason is that it reduces three-dimensional effects. With the rotor operating with a mean loading of zero, the average energy change across the rotor is also zero, and, therefore, no forces exist to cause a radial component of velocity. This fact greatly simplifies a study of unsteady phenomenon both experimentally and analytically, since it allows the flow to be assumed two-dimensional.

For a zero steady lift rotor, the blades will have no camber. Therefore, neglecting blade thickness and viscous effects, the design reduces to simply specifying the blade stagger angle as a function of radius which yields a zero incidence. The following equation expresses this relationship:

$$\xi = \mathrm{Tan}^{-1}\left[\frac{U}{v_{x_{avg}}}\right], \tag{34}$$

where ξ = blade stagger angle as a function of radius,

U = the blade speed, which is a function of radius, and

$v_{x_{avg}}$ = average axial velocity assumed constant at all radii.

The design condition was selected such that $\xi = 45°$ at the mean radius of 7.75 in. (19.685 cm). The blades have a C1 profile with 10% thickness, a 6 in. (15.24 cm) chord, and a 5.9 in. (14.99 cm) span.

Since the blades are individually mounted on the hub, the rotor, therefore, has the flexibility of being assembled with 2, 3, 4, 6, or 12 blades. Only the 12-bladed configuration, however, which results in a space-to-chord ratio of 0.68 at the mean radius, was used in this study.

Besides being able to mount different numbers of blades, the blades can also be rotated in the hub, and different filler blocks can be used to obtain other blade stagger angles. In addition to the 45° stagger angle for which the blades are designed, stagger angles of 35° and 55° at the mean radius can also be obtained. Although, in these configurations, the blades are at an off-design condition which will result in three-dimensional flows, the deviation of the blade angle from a design based on that particular stagger angle is not large. Therefore, the three-dimensional effects should be small, and the flow can still justifiably be considered two-dimensional.

Although the rotor is designed for zero steady load, the rotor can be operated with a steady load by setting the operating conditions such that the flow has an average incidence which is non-zero. Once again, this will result in three-dimensional flows, with the magnitude dependent upon the amount of blade loading. Under these conditions, the flow cannot accurately be considered two-dimensional, although the radial velocity will be sufficiently small such that the two-dimensional assumption will not cause significant errors.

5.3 Distortion Screen Design

In order to obtain useful experimental information about the response of a rotor to flow distortions, it is necessary to be able to produce distortions which have a specific size and shape. Sinusoidal

velocity distortions are of particular interest because they are easily represented mathematically and, therefore, are convenient for analyzing or for comparing with theoretical predictions. Sinusoidal distortions of various frequencies are also very important because they demonstrate how the response of the rotor is affected by the distortion frequency. As previously mentioned, sinusoidal distortions with 1, 2, 4, and 6 cycles were employed in this study.

The other type of distortion most commonly used in experimental work is the square distortion. This type of distortion is important because it more closely represents the type of flow distortion encountered in practice. One of the primary variables of interest when considering square distortions is the circumferential extent of the distorted flow. This is important because the response of the rotor is strongly dependent on the time a blade spends in the distorted sector. The circumferential extent of a distortion also affects the stability of a compressor subjected to distorted flow. In this study, 90° and 180° circumferential square distortions were investigated.

For both sinusoidal and square distortions, the amplitude of the distortion is an important parameter. All the screens used in this study were designed to create a velocity distortion with a magnitude equal to 20% of the mean flow velocity. This level of distortion was selected because it is a significant distortion, but is still small enough such that linearized theories can be used to predict the rotor's response.

The basic concept involved in manufacturing a screen to produce a specified velocity distribution is illustrated in Figure 13 which is a photograph of the four-cycle screen. The screen consists of several

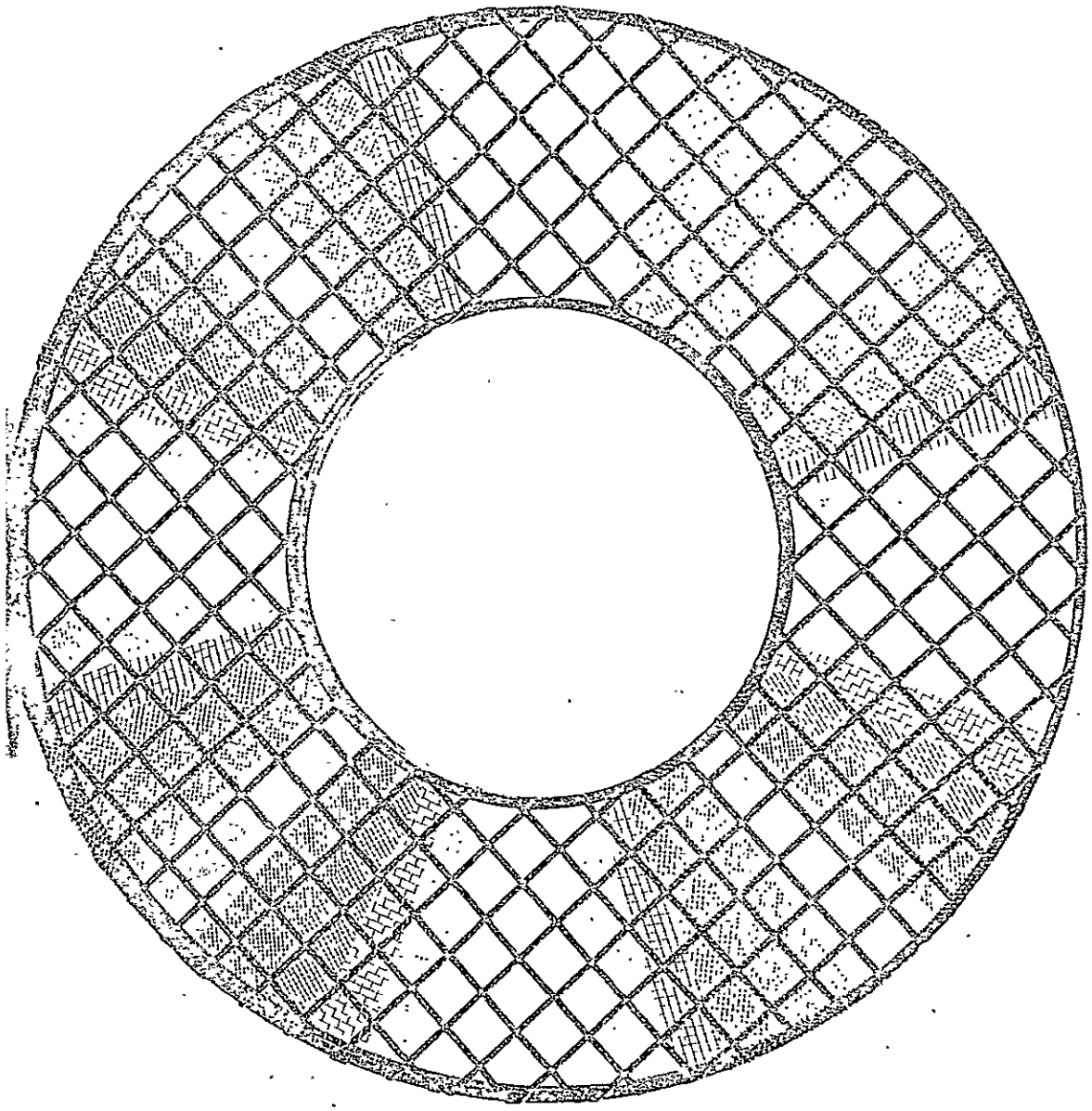

Figure 13. Photograph of a four-cycle distortion screen.

segments of wire screen with different solidities attached to a screen with a much smaller solidity for support. The various segments of the screen present different amounts of resistance to the flow, resulting in the desired velocity profile.

Although the basic idea for a distortion producing screen is simple, the design process is somewhat complicated by the fact that the flow will tend to avoid the high resistance sections, and, consequently, a one-dimensional approach cannot be used. For this reason, an analytical solution developed by McCarthy [16] for a steady, moderately-sheared, three-dimensional flow past wire screens was used to determine the type of screen segments needed. This solution expresses the velocity downstream of the screen as a function of a flow resistance coefficient which is a function of the screen solidity and weakly dependent on the Reynolds number. Thus, for a prescribed velocity distribution, the necessary variation of the resistance coefficient can be calculated. Screen segments can then be selected which will approximate the calculated resistance variation.

The design details for the screens used in the AFRF are presented in Reference [17]. This reference also describes the characteristics of the velocity profiles obtained during tests conducted to evaluate the screen performance. These tests indicate that a high degree of success was achieved in meeting the design criterion. The sinusoidal distortions, which were Fourier analyzed, were shown to be dominated by the fundamental harmonic, and the amplitudes were approximately 20% of the mean velocity. Reference [17] also presents experimental data on the effects of the average axial velocity, the distance from the screen, and the radial position on the velocity profile measured.

This reference may, therefore, be consulted for more details on the screen characteristics. Velocity profiles obtained from the screens used in this study will also be presented in the following chapter on experimental results.

5.4 Instrumentation

The basic instrumentation for the measurements made in the Axial Flow Research Fan is shown schematically in Figure 14. Only small variations in the system shown were made for each of the different types of experiments conducted. The two, five-hole probe positions are identified in the figure, and a table is included which indicates the distance between the probes and the blades at the mean radius. A cross-sectional view of the rotor is also provided, which indicates the direction of the rotor rotation and the convention used for the angular location of the probes.

For all the tests conducted, the two probes were circumferentially offset 45° from each other so that the downstream probe would not be in the wake of the upstream probe. During the radial surveys and the rotor steady-performance measurements made only at the mean radius, the circumferential locations of the probes were fixed at 292.5° and 247.5°. These locations centered the two probes between two of the three support struts located at the inlet, thus assuring the probes would not be in the wakes of these struts.

The radial surveys were conducted using two United Sensor manual traversing devices. These devices have a vernier scale which enables accurate placement of the probes within one-hundredth of an inch. For the other tests conducted, the probes were rigidly attached to the casing with the center hole of the probes at the mean radius of the

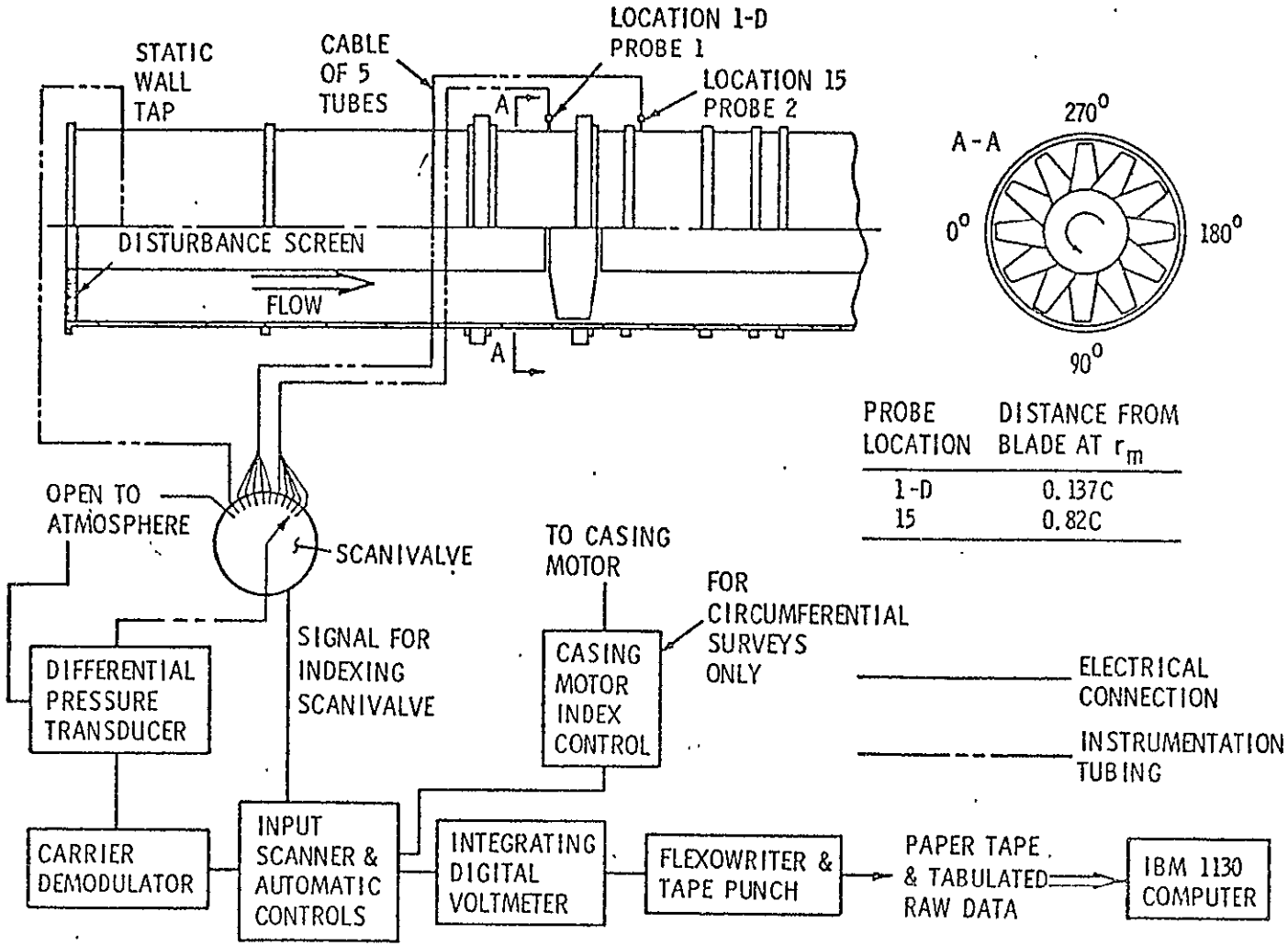

Figure 14. Schematic of probe positions and instrumentation.

annulus. The circumferential surveys were conducted in 2° increments, and the casing was rotated in either direction. The data were then put in the conventional order by the data-reduction program.

The pressures from the five-hole probes were the primary pressure measurements made. Besides these measurements, however, two static pressure wall taps were also used at various points throughout the tests. Since it is not convenient to use the five-hole probes and the calibration curves when setting the flow velocity, a simpler approach was taken. The initial approach employed a static pressure wall tap located at Station 1-D to measure the static pressure and the center hole of Probe 1 to sense the total pressure. These two pressures, when applied to the opposite sides of a differential pressure transducer, enable a voltage proportional to the dynamic head to be read directly on the digital voltmeter. Monitoring the voltage output, the velocity can be set at the desired value. The static-pressure wall tap and the additional transducer and carrier demodulator are not indicated in the schematic of Figure 14, since they were not used for many of the tests.

The technique described in the preceding paragraph was only used for setting the velocity for the radial surveys and for the screen performance measurements which were made with no rotor present. Under both these conditions, the static-pressure gradients at Location 1-D should be negligible; thus, little error is involved when measuring the static pressure from a wall tap. The velocity at Location 1-D under the above conditions should be approximately axial and, therefore, the center hole of the five-hole probe will read very near the true value of total pressure. The wall tap and the center hole of the probe

thus provide an accurate and convenient means for setting the velocity in the initial tests. It should be emphasized, however, that only the five-hole probes were used for making the actual flow field measurements.

During the initial tests, when the flow velocity was set using the wall tap and the center hole of Probe 1, the static pressure measured from a tap just downstream of the inlet was also recorded. This tap is shown in the schematic of Figure 14. As shown by the schematic, the tap is located far upstream from the rotor location. Therefore, the pressure sensed by the tap for all test conditions will depend only on the velocity and the type of screen present, if any. With this relationship, the pressure can be correlated with the velocity at the mean radius or the circumferential mean velocity and subsequently used for setting the operating conditions of other tests. The pressure measurements from the inlet tap were, therefore, used for setting the flow velocity for the circumferential surveys involving the rotor and the screens and also for the steady-performance measurements of the rotor which were made at the mean radius.

All pressure measurements were made with a single transducer through the use of a scanivalve, except for the additional transducer which was used when setting the velocity with the differential pressure between the center hole of Probe 1 and the static pressure wall tap at Location 1-D. A scanivalve is simply a switching valve capable of connecting any one of several pressure tubes to a single tube leading to the transducer. The use of a scanivalve simplified the data acquisition considerably, since only one transducer and its calibration constant need to be considered.

The type of pressure transducers used were variable reluctance differential pressure transducers. This type of transducer consists of a magnetically-permeable, stainless-steel diaphragm clamped between two blocks each containing a coil. A pressure difference applied to the diaphragm, resulting in a deflection of the diaphragm, causes a change in the magnetic reluctance and a corresponding change in inductance of the two coils. The coil inductance ratio is converted to a DC output employing a simple bridge circuit and a filter. These electronic components are housed in the unit identified as the carrier demodulator in the schematic of Figure 14.

The DC output from the carrier demodulator goes into the input scanner. The purpose of an input scanner in many applications is to direct the electrical signals from many sources into a single voltmeter. In this case, however, since only one transducer was employed, all the input channels used were connected to the same transducer. The scanner, therefore, only served as a control system which indexed the scanivalve, reset the scanivalve at the end of a set of readings, and also sent a signal to index the casing for the circumferential surveys. The voltage channeled through the scanner was then read by an integrating digital voltmeter with the digital output punched on paper tape and, in some cases, printed on paper sheets. The paper tape could be fed into the IBM 1130 computer for reduction of the data.

In addition to the pressure measurements made, it was also necessary to measure the angular velocity of the rotor. This was accomplished using a conventional setup involving a slotted disk which rotates with the rotor, a light source, a photocell, and an electronic counter. With sixty slots in the disk and a one-second sample period,

the output from the counter reads directly in RPM. The operating speed of the rotor was set at the beginning of a test and monitored throughout the run to assure that the speed of the rotor did not drift.

5.5 Experimental Procedures

The experimental procedures for all of the tests conducted were approximately the same. The atmospheric conditions were measured and recorded, the initial run conditions were set, and the 10 probe pressures and the transducer zero were recorded for each probe position or running condition. Because of the similarity, a detailed explanation of each experiment is not necessary, but a short explanation of the tests pointing out some of the important considerations will be given.

For all of the tests, except those specifically investigating the effect of flow rate, the mean flow velocity in the AFRF was maintained at approximately 67 ft/sec (20.4 m/sec). This velocity results in the rotor operating at its design condition for the rotor turning at 1000 RPM. To obtain variations in incidence, the rotor speed was changed instead of the flow rate and, in this way, the probes were always operating in approximately the same Reynolds number range.

The first tests conducted were the radial surveys, which were aimed at determining the overall mass-averaged steady rotor performance and also the radial variations of the pressure and velocity. These tests were conducted for the three rotor blade stagger angles and six values of incidence. At the beginning of the tests the barometric pressure and the ambient temperature were recorded. Probe 1 was then set at the mean radius so that the dynamic pressure at this point could be monitored while adjusting the flow rate and rotor speed to obtain the desired incidence. With the desired conditions obtained. the static

pressure read from the tap at the inlet was recorded and the probes were moved to their initial positions. The input scanner was then activated, resulting in the 11 voltages being automatically read and recorded. At the end of a set of readings, the two probes were manually moved to the next position and the process was repeated until the annulus was spanned. The radial increments used in positioning the probes were smaller near the hub and casing to obtain a more detailed survey of the boundary layer. Within one in. of the hub or casing, 0.25-in. increments were used, while 0.5-in. increments were used in the remaining region.

The next tests which were conducted were the measurements of the velocity field produced by the disturbance screens in the absence of the rotor. For these surveys, the probes were fixed at the mean radius. At the beginning of the tests, the atmospheric conditions were again recorded as they were for the radial surveys. The ambient temperature was also recorded at the end of the tests, since some change occurs during these tests of longer duration. The velocity was set by rotating the casing and probes until a maximum or minimum velocity point was located. This was done, since it is much easier to locate a maximum or minimum instead of the mean velocity. The flow rate was then adjusted to obtain a mean velocity of 67 ft/sec, assuming that a 20% velocity variation existed. With the velocity set, the static pressure from the inlet wall tap was recorded, and Probe 1 was located at 0° where the measurements were initiated. For the circumferential surveys, the entire data acquisition was automated, with the scanivalve reset and the test section casing indexed at the end of each set of readings. These surveys were made for the six screens employed in this study.

The circumferential surveys of the distorted flow upstream and downstream of the rotor were the next measurements made. These experiments were conducted with the same procedure as were the screen performance measurements, except the velocity was set by adjusting the flow rate until the same static pressure at the inlet wall tap was achieved that was recorded for the screen performance measurements. The mean velocity which had been calculated from the reduced data of the previous surveys could then be assumed to exist.

The distortion surveys were conducted for the three stagger angles, six different screens, and four values of incidence. For the rotor configuration with a 55° blade stagger angle, a large amount of mean swirl is put into the flow at the higher values of incidence. This large amount of swirl, therefore, required that the probe downstream of the rotor be rotated to decrease the relative flow angle and remain in the calibration range of the probes. For the two conditions of higher incidence, Probe 2 was mounted at a 20° angle to the axial direction.

The final type of measurements made were again steady performance measurements of the rotor. Since only mean radius measurements were made of the distorted flow, the rotor performance at the mean radius is of primary concern. Therefore, steady performance measurements were repeated with greater detail, employing smaller increments of incidence. The flow velocity was maintained at a constant value by monitoring the static pressure wall tap at the inlet, and the rotor RPM was varied to obtain different loading conditions. The RPM was selected to obtain increments in incidence of 2°. The incidence was varied from a value of -10.0° up to values where either the flow exit angles were out of the probe calibration range or stall occurred.

CHAPTER VI

RESULTS AND DISCUSSION

6.1 Rotor Steady Performance

The main performance characteristic of interest when describing the steady performance of a fan or compressor is the relationship between the pressure rise and the inlet flow conditions and rotor speed. For an incompressible flow, the desired information is adequately described by a relationship between a total pressure rise coefficient, Ψ, defined as $(p_{T\,exit} - p_{T\,inlet})/\frac{1}{2}\rho U^2$, and a flow coefficient, ϕ, defined as v_x/U. The pressure rise coefficient is often referred to as a loading coefficient, since it is related to the load on the blades.

For a flow with a zero circumferential velocity component upstream, and assuming there are no losses, a relationship between Ψ and ϕ, which is obtained from Euler's pump equation, is as follows:

$$\Psi = 2 - 2\phi\tan\beta_2 \quad . \tag{35}$$

From Equation (35), it is seen that Ψ is directly related to ϕ. For a given rotor configuration, β_2 will depend on the flow incidence and thus will also be related to ϕ. Furthermore, the losses through the blade row, which are not contained in Equation (35), will depend primarily on the incidence or ϕ. For these reasons, Ψ is expected to be a function of ϕ alone, which justifies expressing the rotor performance in terms of these two parameters.

The experimental data of Ψ versus ϕ measured at the mean radius is plotted in Figure 15 for the rotor configurations having blade stagger angles of 35°, 45°, and 55°. It is seen from the figure that there are two sets of data for the rotors with 35° and 55° staggers. The crosses, triangles, and octagons represent the data measured at the mean radius during the radial surveys. The remaining data for the 35° and 55° stagger angles were obtained in subsequent tests made at the mean radius only, with the purpose of providing more detail of the performance characteristics and also to demonstrate the repeatability of the data. The data show that the repeatability is quite good, with both sets of data falling on the same curve. During the test at the mean radius with the 45° stagger, an equipment malfunction caused one set of data to be invalid.

For most of the data taken in determining the steady performance of the rotor, the flow rate was set to give an average axial velocity of 67 ft/sec (20.4 m/sec). As previously mentioned, this was done to enable the probes to be operating in approximately the same Reynolds number range at all times. For each of the rotor configurations, however, a radial survey was also conducted with an average velocity of approximately 55 ft/sec (16.8 m/sec) to check if the non-dimensional parameters properly described the rotor performance by reducing the data to a single curve. For the 35° stagger configuration, at $\phi \approx 1.2$, the two x's demonstrate the largest deviation caused by the change in flow rate, and the difference is seen to be quite small. Directly across from these data, the data for the 45° and 55° staggers show that the difference due to the flow rate is almost indistinguishable. Although only one point was checked, from these results and the previous

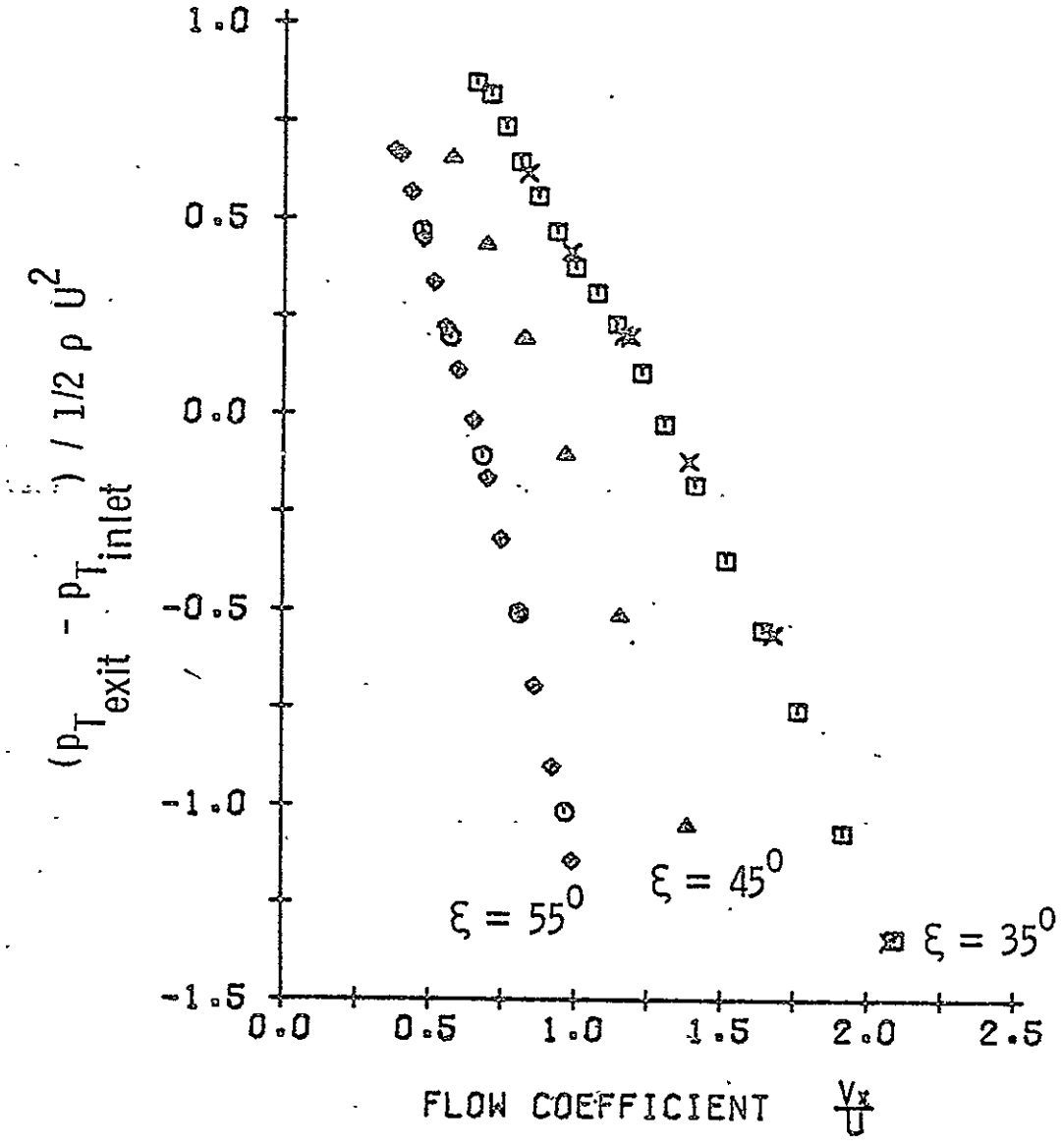

Figure 15. Rotor steady performance data measured at the mean radius.

$$\Psi_{\text{mass avg}} = \frac{\int_{r'_h}^{r'_t} \Psi_{\text{local}} V_x \, r \, dr}{\int_{r'_h}^{r'_t} V_x \, r \, dr} \tag{37}$$

The pressure rise coefficient was mass averaged, since the energy put into the fluid not only depends on the pressure rise, but also the amount of mass given a particular pressure rise. $\Psi_{\text{mass avg}}$ thus represents an average obtained by weighting the pressure rise, which varies radially, according to the flow rate at a particular radial location. The integration limits employed were taken as 0.25 in. (0.635 cm) from the hub and casing walls, since these were the last measurement stations. The integrals were evaluated numerically using Simpson's 1/3 rule and a mathematical spline representation of the data.

The average performance data are presented in Figure 16, where it is represented by the symbols, along with the performance measured at the mean radius, which is represented by the lines. It is seen in all cases that the average performance data are slightly lower than the mean radius data, but apart from this difference, the data are quite similar. The lower performance is expected when the data are averaged because these data include the losses in the hub and casing boundary layers, higher losses due to the higher blade loading in the boundary layers, and also losses due to secondary flow. The fact that the difference is small, however, does further justify the two-dimensional flow assumption made throughout this study.

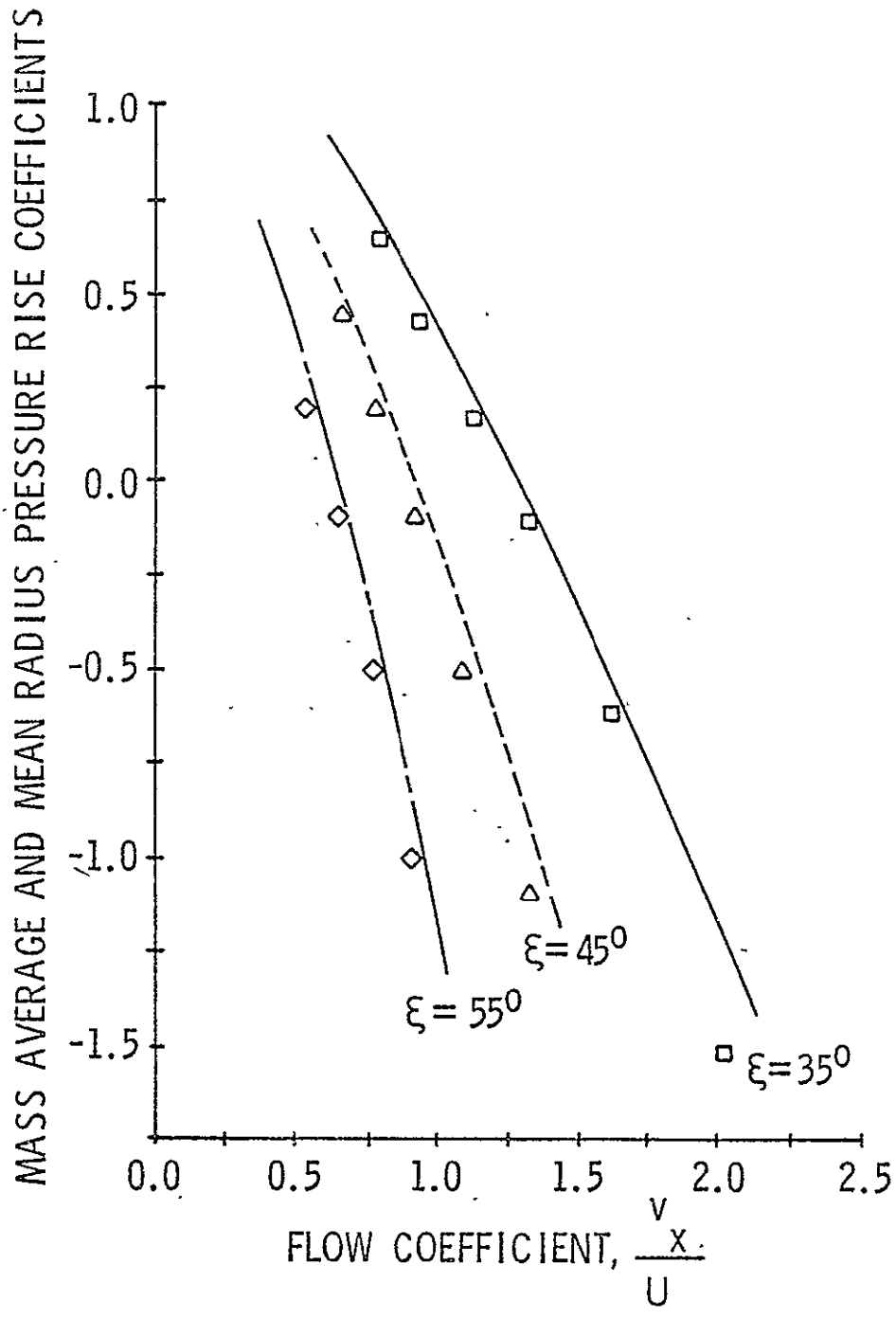

Figure 16. A comparison of the rotor steady performance measured at the mean radius and the average performance determined from radial surveys of the flow. The lines represent the data at $\bar{r}$, while the symbols represent the average data.

Figures 15 and 16 presented the performance of the rotor in the most common manner. In this study, additional performance characteristics, such as the static pressure at the exit and the circumferential velocity component at the exit, are necessary for the parallel compressor and actuator disc theories to be used. The losses across the rotor operating in uniform flow are also important in order to predict the average total pressure rise in conjunction with the actuator disc model and to evaluate the unsteady losses from the experimental data. For these reasons, the data measured at the mean radius with uniform flow will be presented in several other forms, and the characteristics of these data and their expected influence on the response of the rotor in nonuniform flow will be discussed.

Figure 17 presents the data of the modified pressure coefficient, Ψ', versus the flow coefficient. Ψ' was previously defined in Chapter III with regard to the parallel compressor theory. The first thing noticed about these data are the way the curves become increasingly shorter with increased stagger angle. This characteristic can be explained by examining the nature of the flow assuming it behaves ideally. By combining the Euler pump equation with the Bernoulli equations written for both the upstream and downstream conditions, and assuming the flow upstream of the rotor is purely axial, the following equation is obtained:

$$\Psi' = \frac{p_{s\,exit} - p_{T\,inlet}}{\frac{1}{2}\rho U^2} = \frac{2\,v_{\theta\,exit}}{U} - \frac{(v_x^2 + v_{\theta\,exit}^2)}{U^2} \qquad (38)$$

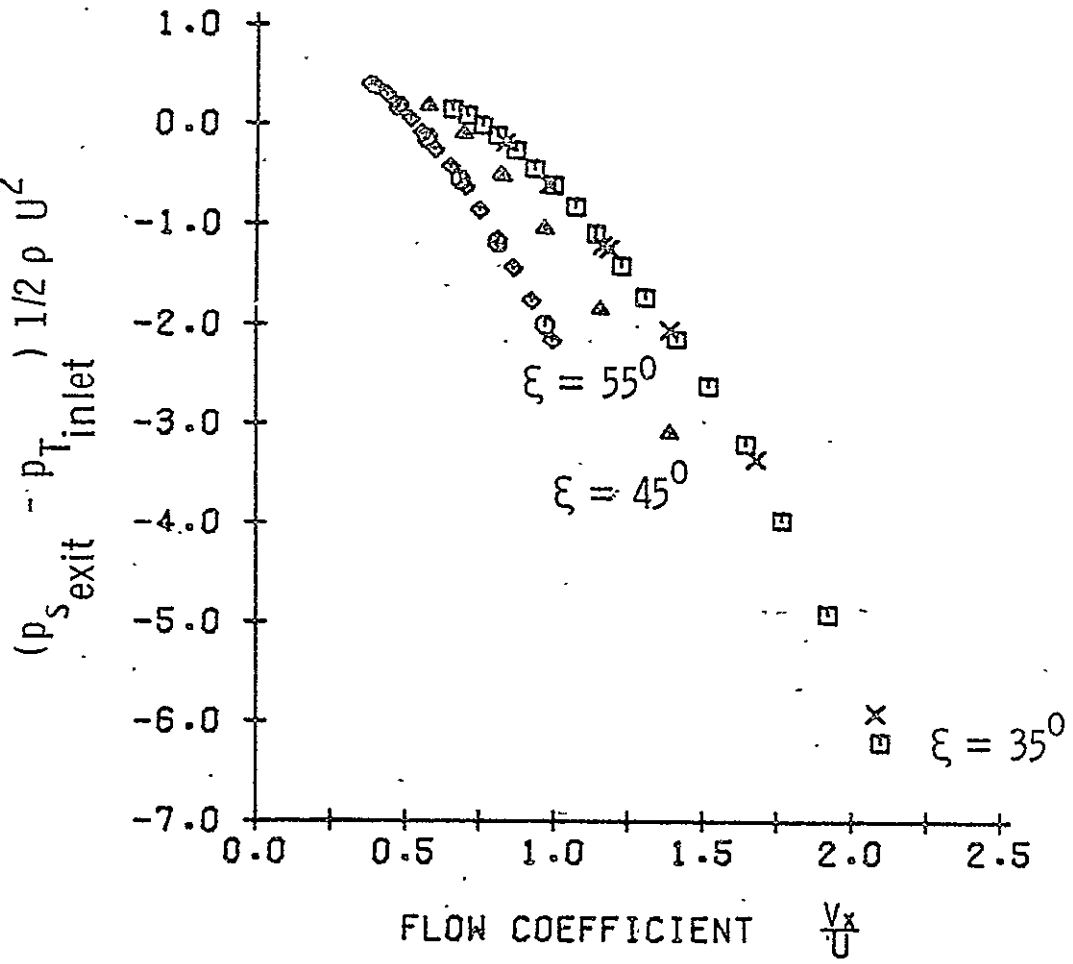

Figure 17. Data of the modified pressure coefficient versus flow coefficient used in predicting distortion attenuation with the parallel compressor model.

Equation (38) can be further reduced by expressing the velocities in terms of the relative velocity and then introducing the relative flow angle, β_2:

$$\Psi' = 1 - \frac{w_{exit}^2}{v_x^2} \quad \phi^2 = 1 - \frac{\phi^2}{\cos^2\beta_2} \quad . \tag{39}$$

Since β_2 will deviate only slightly from the blade stagger angle, it is seen from Equation (39) that as the stagger is increased, Ψ' will have a greater change for the same ϕ^2 change. However, as the stagger is increased, the rotor must be operated at lower values of ϕ in order to maintain the same incidence on the blades. Thus, with the higher stagger angles, Ψ' is found to vary less with ϕ, since Ψ' is dependent on the square of ϕ.

The discussion on the extent of Ψ' was presented to simply explain the peculiar nature of the data and to assure that the results do not deviate from what one would roughly predicted from a theoretical analysis. The extent of Ψ', however, is unimportant when predicting the attenuation of a distortion using the parallel compressor model, since it is the slope of the curve which determines the influence the rotor has on the flow. As discussed in Chapter III, a curve of Ψ' versus ϕ is used to determine the operating points (ϕ values) of the rotor in the spoiled and unspoiled sectors. Rotors with curves of Ψ' versus ϕ with steep slopes will attenuate the axial velocity more than rotors with performance curves which are less steep.

Differentiating Equation (39), assuming β_2 is equal to the stagger angle and thus constant, yields the following equation:

$$\frac{d\Psi'}{d\phi} = - \frac{2\phi}{\cos^2 \xi} \quad . \tag{40}$$

Equation (40) can be used to investigate the effects stagger angle and the flow coefficient will have on the slope of the Ψ' versus ϕ curves. From Equation (40), it is seen that both large values of stagger and high flow coefficients will result in a steeper slope (more negative), and from the parallel compressor model will result in larger attenuations of the axial velocity. The general slope characteristics of the data presented in Figure 17 agree well with those predicted from Equation (40).

The next performance data which are important are the amounts of swirl put into the flow by the rotor. This circumferential component of velocity, or swirl, is important because it allows the energy added to the flow by the rotor or the ideal total-pressure rise to be calculated. The ideal total-pressure rise is required to determine the losses across the rotor, which are needed to analyze the distortion data. In the actuator disc theory, the circumferential velocity component at the exit of the rotor must also be known and related to the inlet condition. This relationship is derived from experimental data.

In Figure 18, values of $v_{\theta\ exit}/U$ measured at the mean radius are presented as a function of flow coefficient, with the symbols representing the individual data points. The straight lines in the figure are the linear representations of the data used in the actuator disc theory.

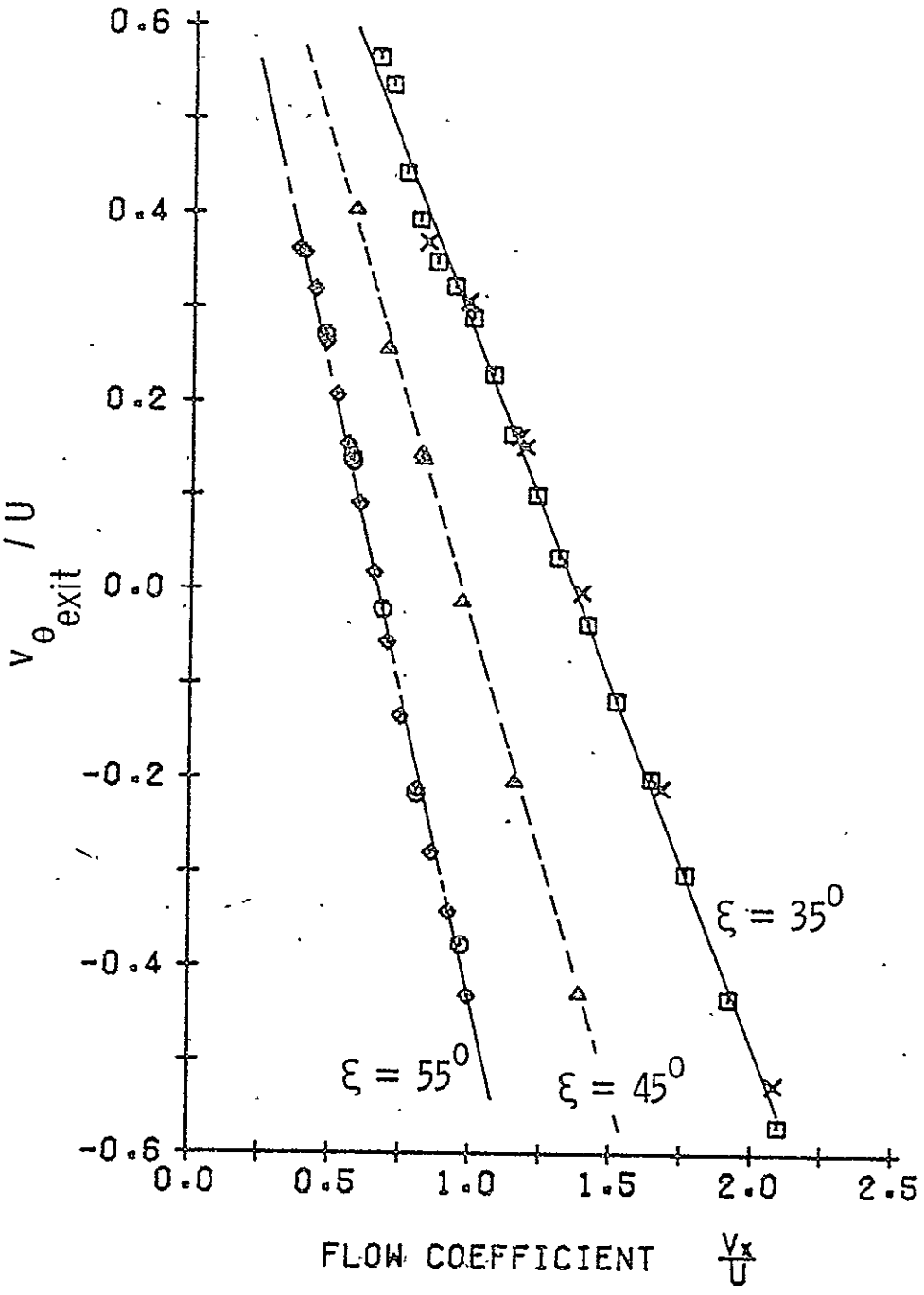

Figure 18. A comparison of $v_{\theta\ exit}/U$ versus v_x/U obtained experimentally and the straight line representation of the data used in the actuator disc analysis.

The near perfect linearity of the data in Figure 18 is the first thing noticed when examining the figure. This linear nature is not surprising, however, since it is well-known that the flow through a blade row usually leaves nearly tangent to the blade trailing edge (except for a small deviation angle), unless large blade loadings cause flow separation. With the flow leaving the blades at a constant relative angle, it is easy to show that the swirl should vary linearly with flow coefficient.

With the linear behavior of the swirl data, a means of representing this performance for use in the actuator disc theory is easily obtained. It is recalled from Chapter III that it was assumed that the swirl added to the flow could be represented by a linear relation between the trigonometric tangent of the rotor inlet and exit relative flow angles [Equation (23)]. Equation (23) was then rewritten in terms of the velocity components to obtain Equation (24). Since the circumferential velocity component upstream is approximately zero with uniform inlet flow, and assuming the axial velocity is constant, Equation (24) can be rewritten in terms of the parameters m and b as:

$$\frac{V_{\theta\,exit}}{U} = (1-m) - b\theta^{*} . \qquad (41)$$

---

*Note: In Chapter III, the inlet and exit conditions were denoted by the subscripts 0^{-} and 0^{+}, respectively, since this nomenclature refers to the coordinate system used in the mathematical model. For the more general case of the data measured upstream and downstream of the rotor in the AFRF, the subscripts inlet and exit are used, respectively.

The parameters m and b were originally calculated from the complete experimental data expressed in terms of $\tan\beta_2$ versus $\tan\beta_1$. To find the best line through the data, a least squares technique was employed. It was found, however, that these parameters when used in Equation (41) did not accurately represent the experimental data. The observed difference was found to be due to the measured change in axial velocity across the rotor, which cannot be accounted for in Equation (41). It is, therefore, necessary to set $v_{x\,exit} = v_{x\,inlet}$ when calculating the tangent of β_1 and β_2 from which m and b are obtained. When this modification is made, the values of m and b accurately represent the $v_{\theta\,exit}/U$ data, as shown by the lines in Figure 18 which are obtained from Equation (41).

The final set of steady performance data, which is needed in this study, is the data of the ideal and actual total pressure rise. From these data, the total pressure losses are also obtained. The steady losses are needed for a reference to evaluate the losses associated with the distorted flow. The ideal total pressure rise is obtained from Euler's pump equation, which when expressed non-dimensionally, is as follows:

$$\Psi_{ideal} = \frac{\Delta P_{T\,ideal}}{\frac{1}{2}\rho U^2} = \frac{2\,(v_{\theta\,exit} - v_{\theta\,inlet})}{U} \quad . \qquad (42)$$

The actual pressure rise coefficient, Ψ, is simply the difference between the total pressure measured upstream and downstream of the rotor expressed non-dimensionally as defined in the beginning of this chapter. The difference between the ideal and actual pressure rise, thus, represents the losses across the rotor. A loss coefficient,

C-2

$C_{P_{T\,loss}}$, is defined in this manner as it is expressed in the following equation:

$$C_{P_{T\,loss}} = \frac{\Delta P_{T\,ideal} - \Delta P_{T\,actual}}{\frac{1}{2}\rho U^2} = \Psi_{ideal} - \Psi . \qquad (43)$$

In Figures 19, 20, and 21, the three pressure coefficients just defined are presented as a function of incidence, for the three rotor configurations having blade stagger angles of 35°, 45°, and 55°, respectively. Figure 20, which presents the data for the 45° stagger configuration, has a loss curve which most exemplifies the characteristics which are expected. For this case, the losses are lowest at the low values of incidence (meaning absolute values of incidence) and increase as the incidence becomes larger in both the positive and negative directions. The loss data for the 35° stagger configuration has similar trends, but has a slight dip in the curve at approximately 15° incidence. For the 55° stagger configuration, the data also has a dip near the end of the curve at approximately 15° incidence.

The dip in the loss data for the 35° and 55° stagger configurations was not considered important enough for the present study to warrant the additional experimentation which would be required to find the cause. However, several possible causes will be briefly discussed. First of all, the question must be answered as to whether the dip in the loss curve at high incidences is a real phenomenon or an experimental error. It is seen from Figures 19 and 21 that most of the sudden decrease in losses can be contributed to a sudden change in the ideal pressure rise, which is calculated from the measured circumferential velocity components. Referring to Figure 18, where the measured

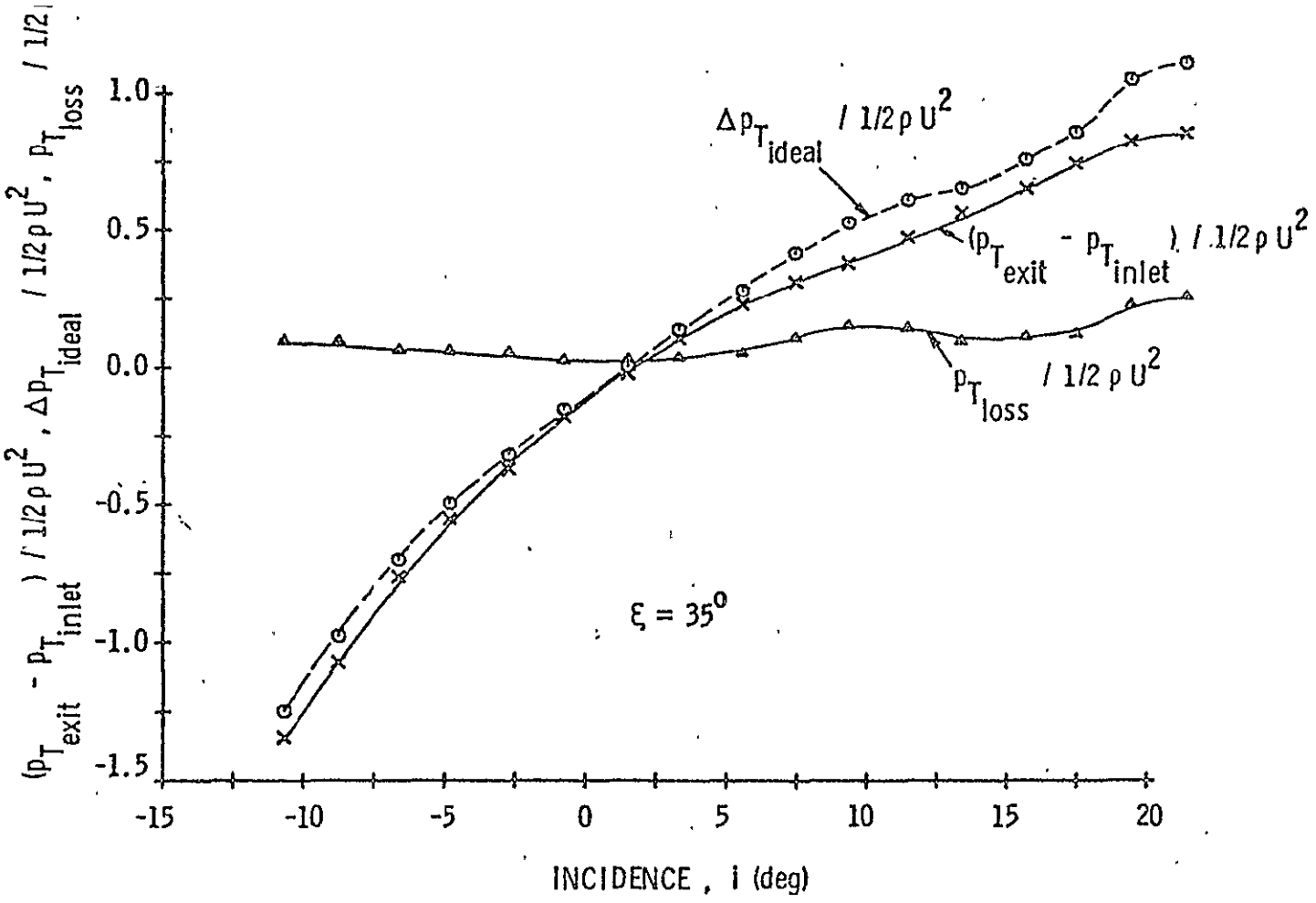

Figure 19. The ideal and actual total pressure rise coefficient and the total pressure loss coefficient as a function of incidence for the rotor with a blade stagger angle of 35°.

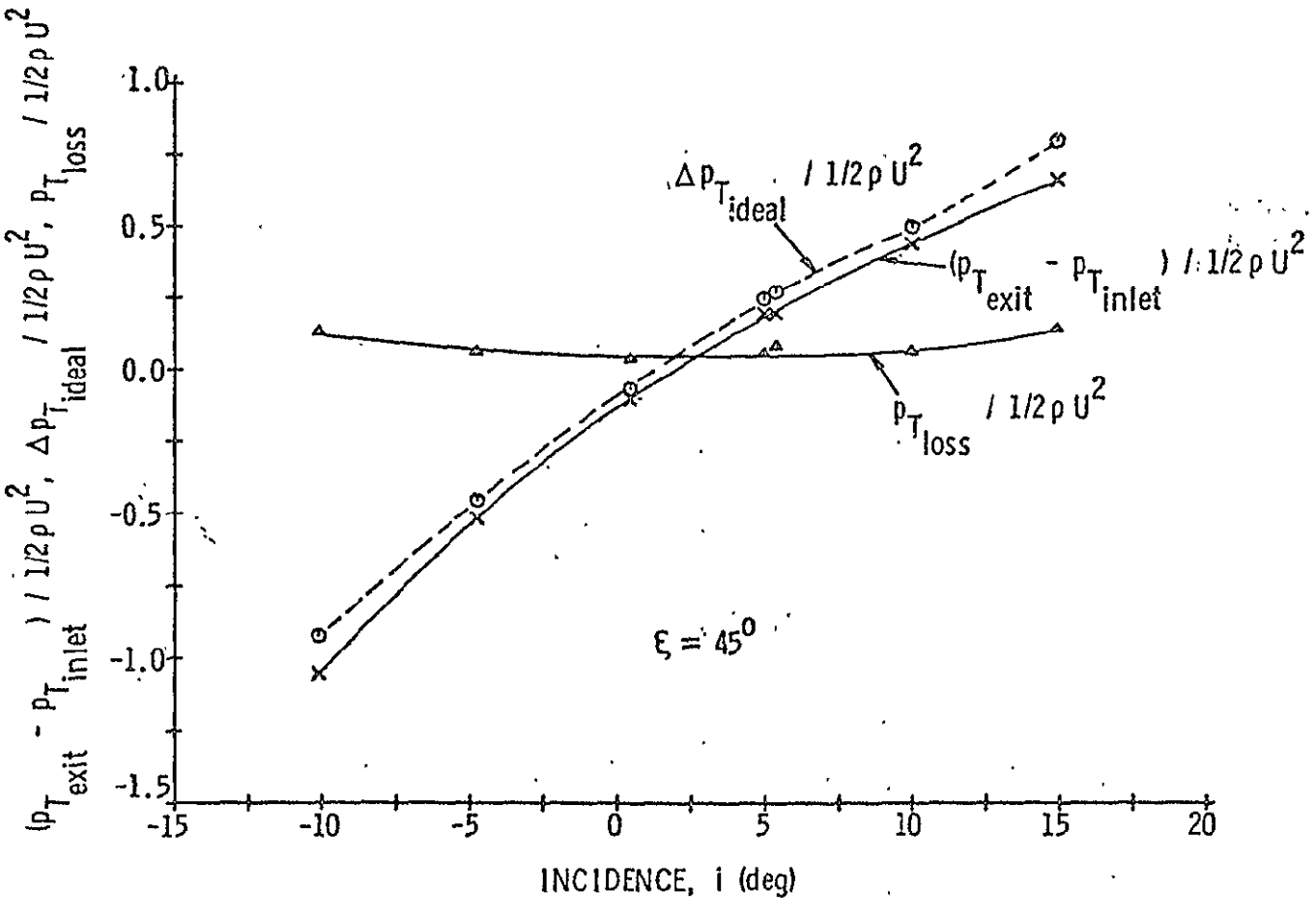

Figure 20. The ideal and actual total pressure rise coefficient and the total pressure loss coefficient as a function of incidence for the rotor with a blade stagger angle of 45°.

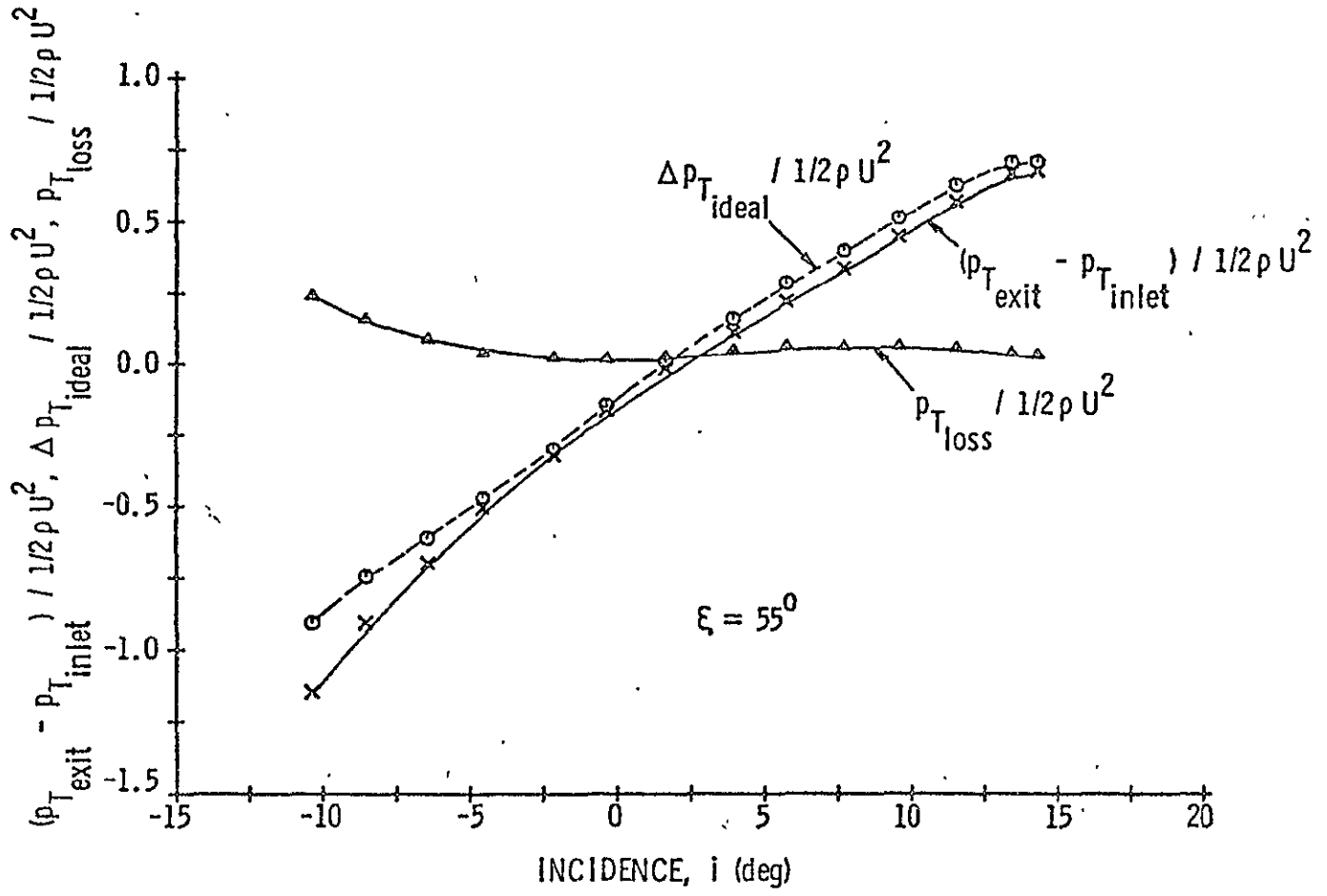

Figure 21. The ideal and actual total pressure rise coefficient and the total pressure loss coefficient as a function of incidence for the rotor with a blade stagger angle of 55°.

circumferential velocity components at the exit of the rotor are plotted, a small dip is evident in the data of $v_{\theta\ exit}/U$ versus ϕ at the values of ϕ corresponding to the incidences where the dip is found in the loss curves. In Figure 18, however, the variation does not appear to be very significant and could easily be contributed to experimental scatter. Apart from experimental scatter, it is also possible a particular characteristic of the five-hole probe at these operating conditions could cause an experimental error.

Although an erroneous change in the v_θ component could be quite small and still cause the observed dip in the loss curves, the fact that the dip is observed for both the 35° and 55° stagger configurations and is also present in additional data not presented here leads to the conclusion that the observed phenomenon is not an experimental error. In this case, several other explanations are possible causes of the unexpected characteristic of the loss curves.

It is well understood that the reason the losses increase with increased incidence is the larger losses in the boundary layer on the blades as the pressure gradient becomes more adverse. This trend will eventually lead to flow separation and a very rapid increase in the losses. With this in mind, one explanation for the observed behavior in this study is that the flow initially undergoes a laminar separation causing an increase in losses, but at higher incidence, the flow either reattaches or the laminar separation is eliminated completely due to the increased turbulence with the larger relative velocities at higher rotor speeds. If the flow separates and reattaches downstream on the airfoil, the effective shape of the airfoil will be changed which could

result in the decrease in losses. If the flow no longer separates at all at higher incidence, the losses would also decrease.

Reference [18] gives the lower Reynolds number limit where laminar separation may occur as between 3×10^5 and 2×10^5, where the Reynolds number is based on the chord length of the blades and the relative flow velocity. In Figure 19, the losses first become large at an incidence of approximately 9.5°. The Reynolds number corresponding to this operating condition is 2.9×10^5, which, according to Reference [18], suggests that laminar separation is not likely to have occurred. For the 55° stagger configuration, the losses become larger at an incidence of approximately 7.5°, where the Reynolds number is 4.5×10^5. Laminar separation would also not be expected in this case.

Since laminar separation probably does not occur, another possible cause for the inflection in the loss curve is turbulent separation. Verification of turbulent separation would require additional experimentation. When considering separation phenomena, it should also be realized that the auxiliary fan in the AFRF may alter the stall characteristics of the airfoils. This influence would be due to the relatively constant mass flow it draws through the system, regardless of the operating conditions of the test rotor.

6.2 Distortion Measurements Without the Rotor Installed

The next phase of the experiments consisted of measuring the distortion produced by the screens when the rotor was removed. As previously mentioned, these circumferential flow surveys were conducted at the same axial locations as the experiments when the rotor was installed, thus providing a direct reference with which to determine the changes caused by the rotor. This phase of the experiments is a step not easily

conducted in many experimental apparatus because a mean through flow often cannot be obtained without the rotor. However, the determination of the flow field characteristics without the rotor is very important, since the rotor will alter both the inlet and exit flows. Thus, a true measure of the velocity distortion attenuation requires a knowledge of the flow when the rotor is not installed. The auxiliary fan of the AFRF provided the through flow for conducting this phase of the program.

Typical results from this phase of the experiments are presented in Figures 22 through 26. In these figures, the three dimensionless velocity components, total pressure, and static pressure are plotted as a function of the circumferential location for the four-cycle sinusoidal distortion. Data are presented for the two axial locations considered in this study. As previously specified in Figure 14, Location 1-D is upstream of the rotor and Location 15 is downstream of the rotor. The data for the 90° square distortion are also presented in this thesis in Appendix C, while a complete set of all data can be found in Reference [19]. Using the four-cycle distortion as an example, it is seen from Figures 22 through 26 that no changes occur in any of the flow properties between the two axial locations. The static pressure is also found to be circumferentially uniform at both locations, as shown by Figure 26. For these two reasons, it can be concluded that any flow redistribution caused by the screen occurs upstream of the measurement locations, and the viscous effects due to the shearing nature of the flow are not important over the short distance between the two locations. Therefore, any changes observed when the rotor was installed were due to the influences of the rotor alone. The fact that the velocity and

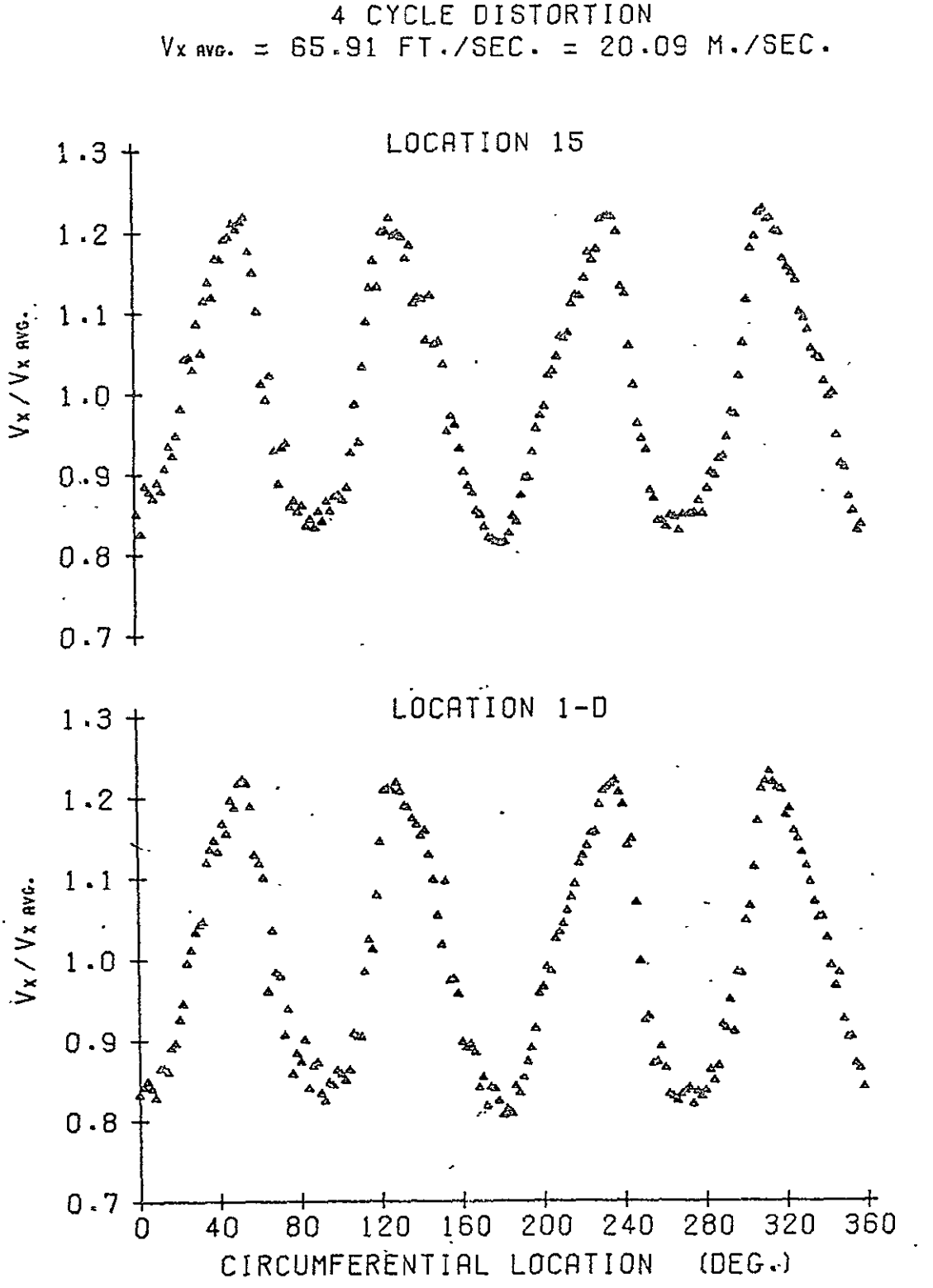

Figure 22. Dimensionless axial velocity variation for the four-cycle distortion without the rotor installed.

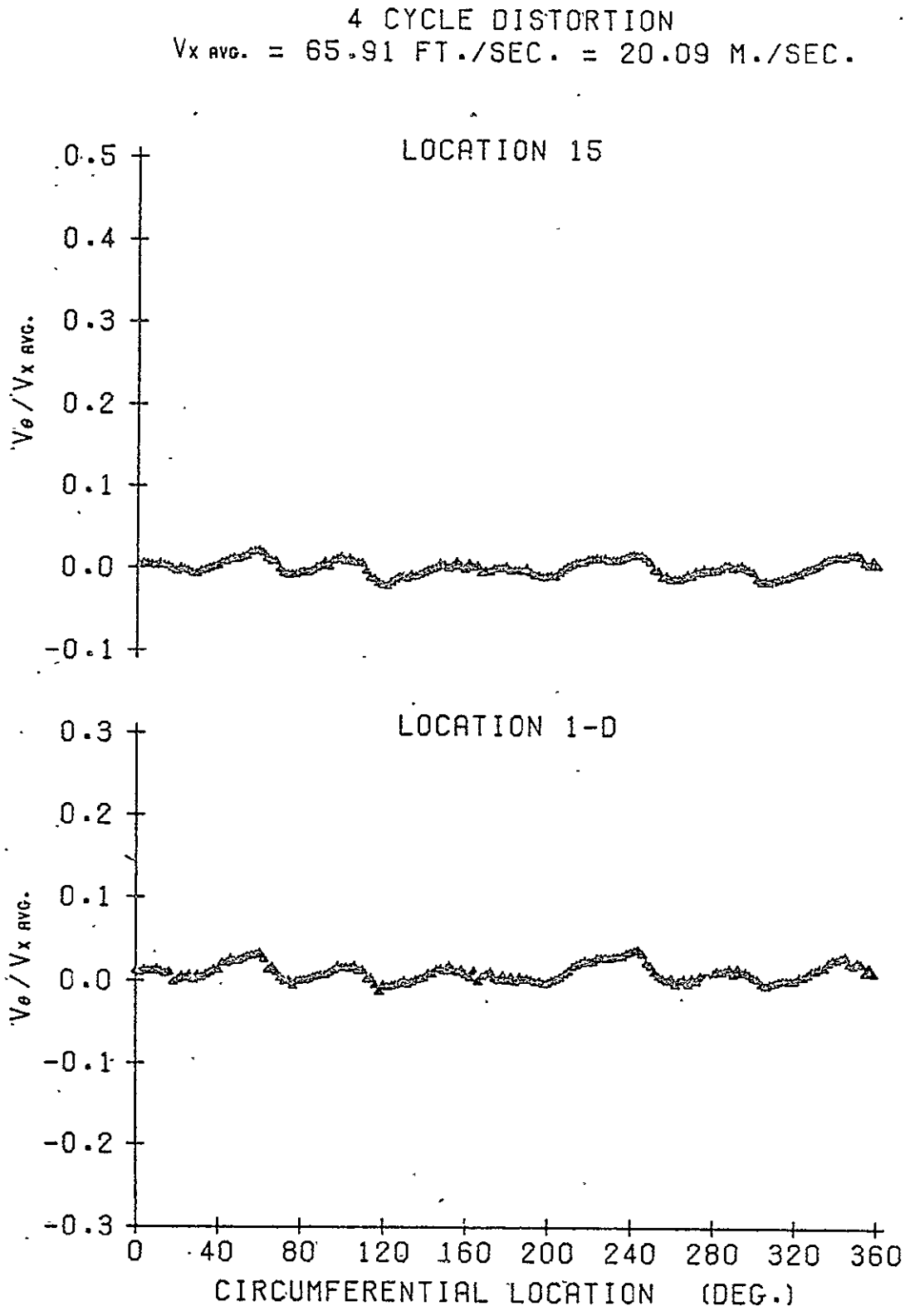

Figure 23. Dimensionless circumferential velocity variation for the four-cycle distortion without the rotor installed.

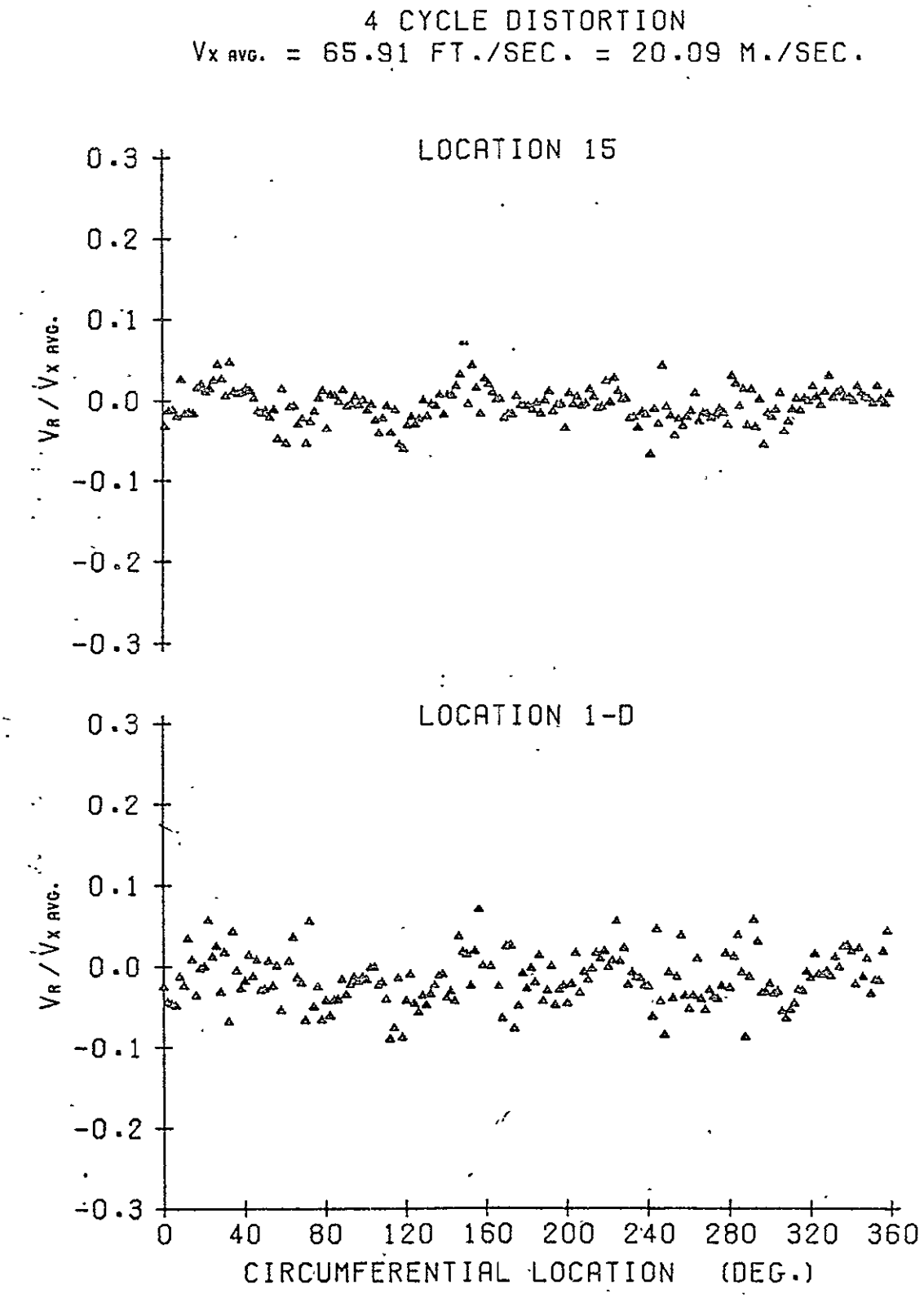

Figure 24. Dimensionless radial velocity variation for the four-cycle distortion without the rotor installed.

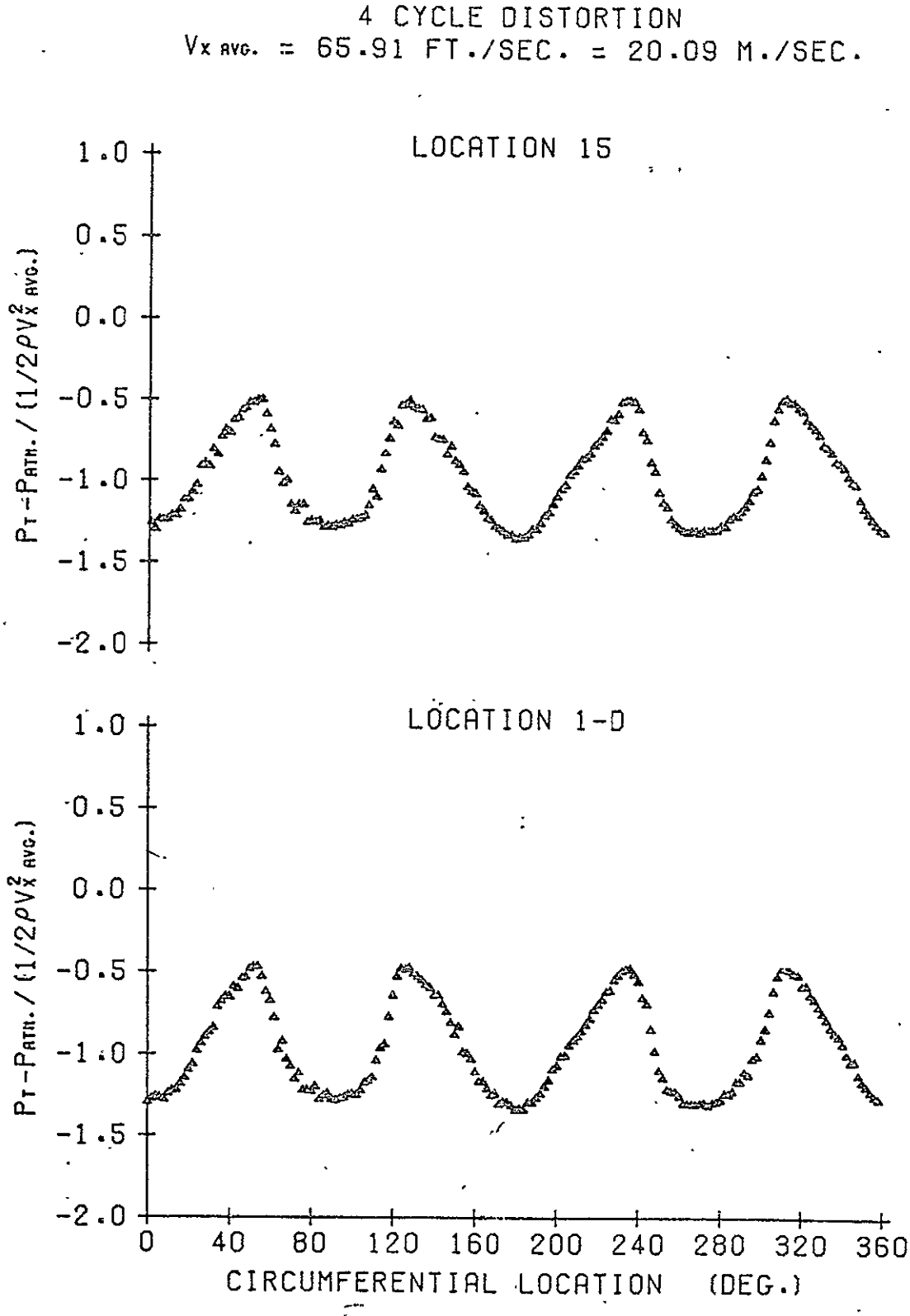

Figure 25. Dimensionless total pressure variation for the four-cycle distortion without the rotor installed.

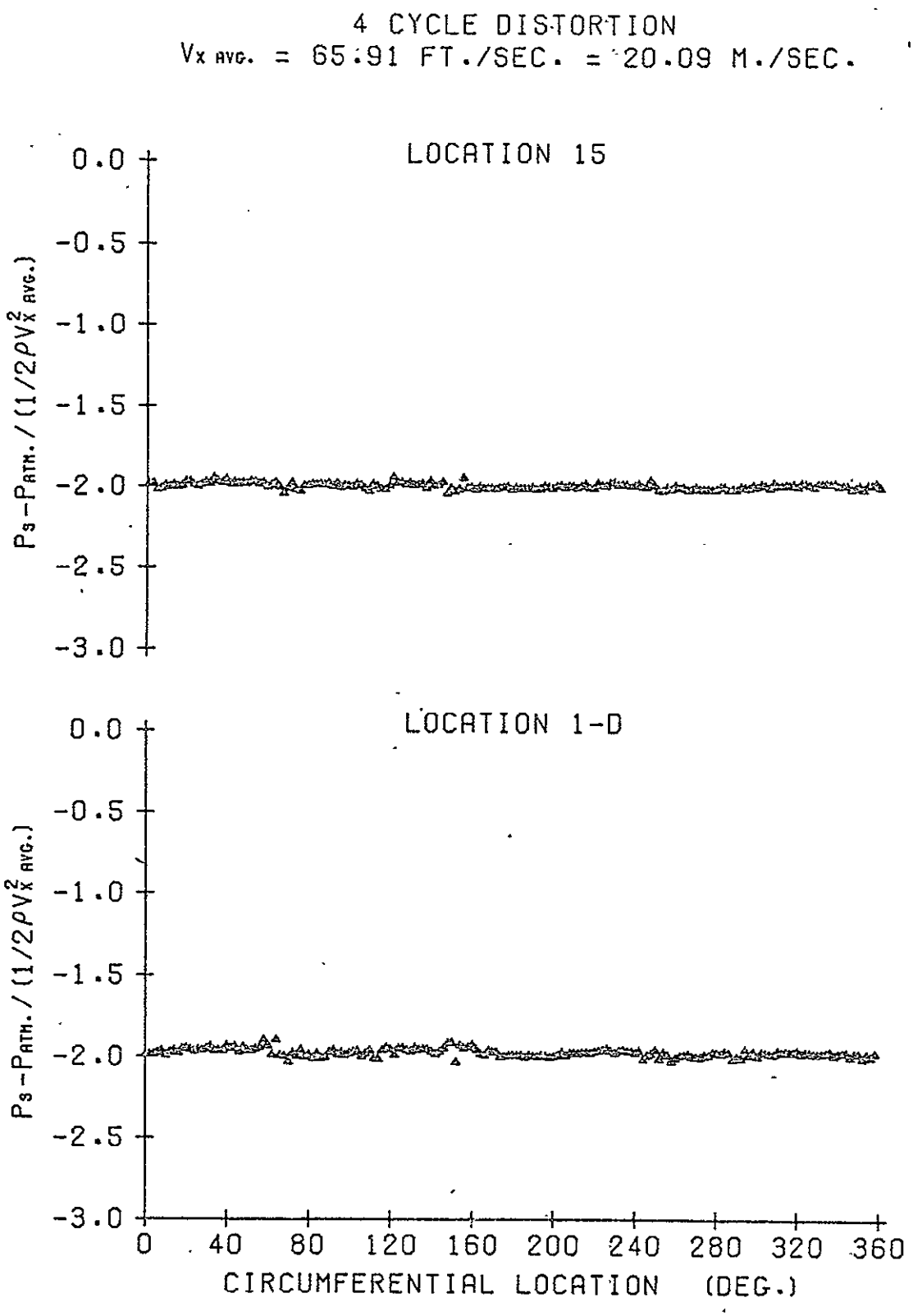

Figure 26. Dimensionless static pressure variation for the four-cycle distortion without the rotor installed.

pressure profiles at the two locations are identical also indicate the precision of the probe calibrations and the instrumentation employed.

6.3 Distortion Measurements with the Rotor Installed and Comparisons with Theory

This section presents sample distortion data from the circumferential surveys conducted upstream and downstream of the operating rotor. The data are presented in the form of the three dimensionless velocity components, dimensionless total pressure, and the dimensionless static pressure as a function of circumferential location for the two axial measurement locations. The data for the two axial locations are presented on the same figure, similar to the manner in which the screen performance data were given. This enables easy comparisons with the data obtained without the rotor installed, and also clearly shows the changes occurring across the rotor. The local incidence on the blades as a function of circumferential location is also presented, since from a quasi-steady viewpoint it determines the fluctuating forces on the blades.

In Section 6.4, some of the overall trends observed, such as the attenuation and losses as a function of design parameters, will be presented. The purpose of this section is to demonstrate the type of data which was obtained and to explain some of the more noticeable characteristics of the distortion shapes both upstream and downstream of the rotor. To aid in the explanation of the distortion characteristics, results from the parallel compressor model and the actuator disc model will be compared with the data. It is again pointed out that the theories employed here have already been thoroughly evaluated and are documented in the literature. Their present usage is simply

as an aid in understanding the present data and is not an attempt to evaluate their accuracy.

Since one purpose of this study is to provide a data base for subsequent studies, it was necessary to document all of the data. However, due to the very large amount of data, it was not practical to document all of the data in this thesis. Therefore, a complete set of data can be found in Reference [19], which includes both the screen performance data without the rotor installed and the distortion data with the rotor installed. In Appendix C of this thesis, the data for the 90° square distortion, without the rotor installed, are presented to enable comparisons to be made with the data presented in this section. In Appendix D, a table of the run conditions for all the tests conducted in this study is presented.

Sample data for the 90° square distortion are presented in Figures 27 through 32.* The square distortion is discussed first because the two distinct sectors of the flow are convenient for making a physical interpretation of the flow phenomena occurring. The changes in the flow expected from examining data and theories in the literature are:

1. An attenuation of the axial velocity distortion upstream of the rotor.
2. Induced circumferential velocity components and a circumferential static pressure gradient upstream.
3. No changes in p_t upstream of the rotor but an attenuation of the total pressure distortion across the rotor.

---

*The average total pressure rise coefficient listed at the top of each figure is nondimensionalized by $\frac{1}{2}\rho v_{x\,avg}^2$. This definition is consistent with the manner by which the pressure data were nondimensionalized, but it differs from the coefficient used for the rotor steady performance data where $\frac{1}{2}\rho U^2$ was employed.

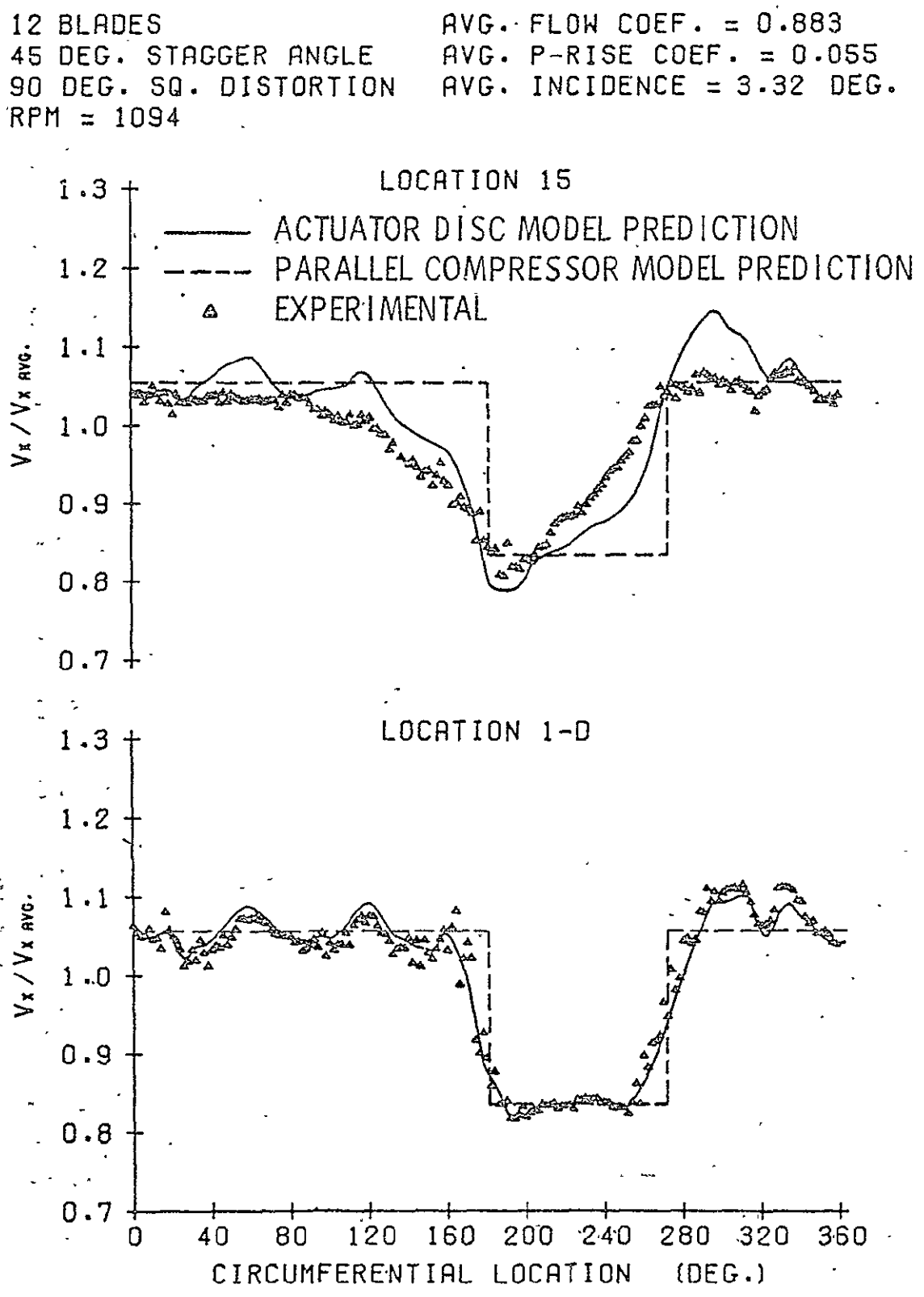

Figure 27. Sample square axial velocity distortion data and the parallel compressor and actuator disc model predictions.

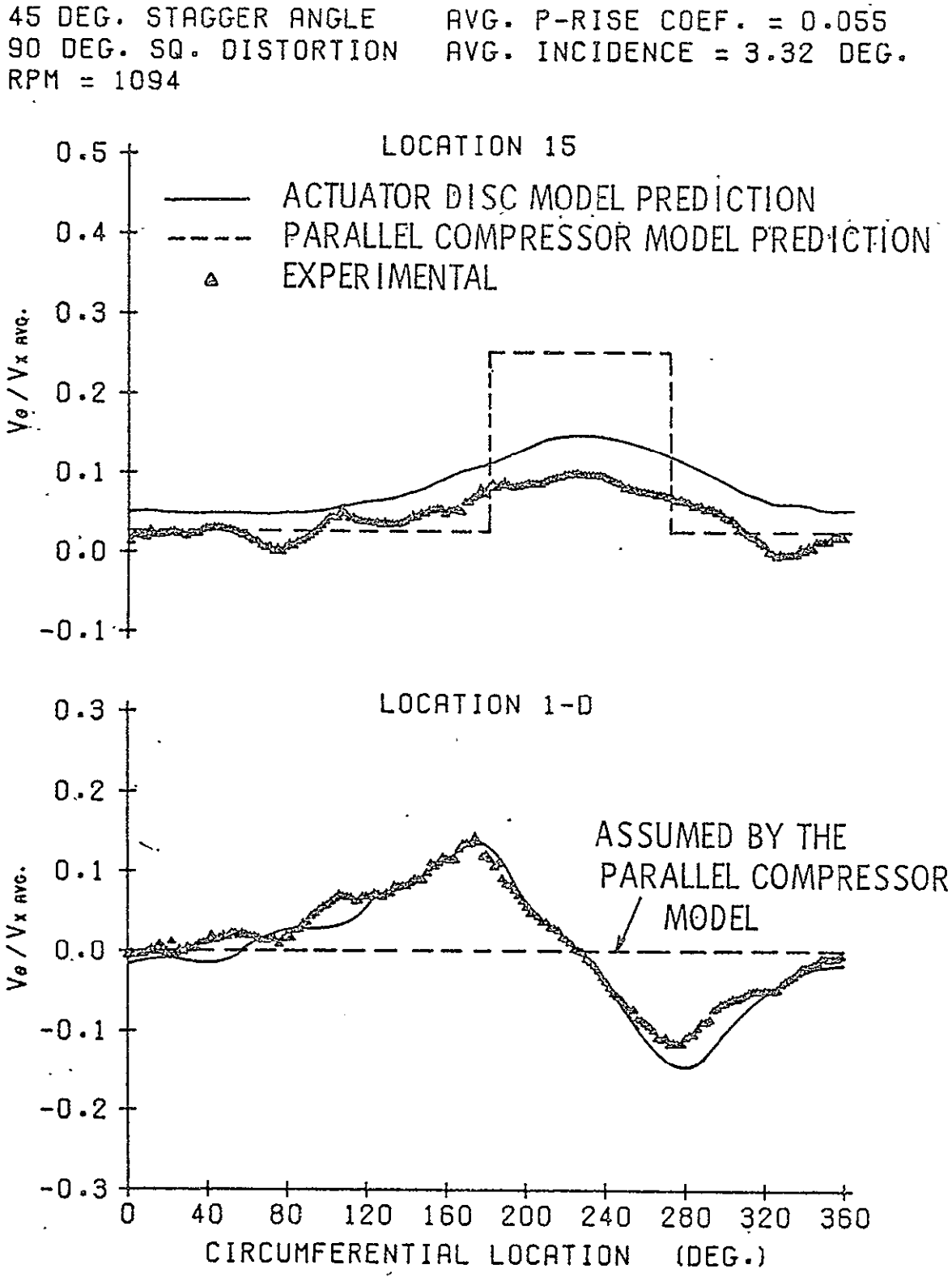

Figure 28. Sample V_θ distribution data and the parallel compressor and actuator disc model predictions.

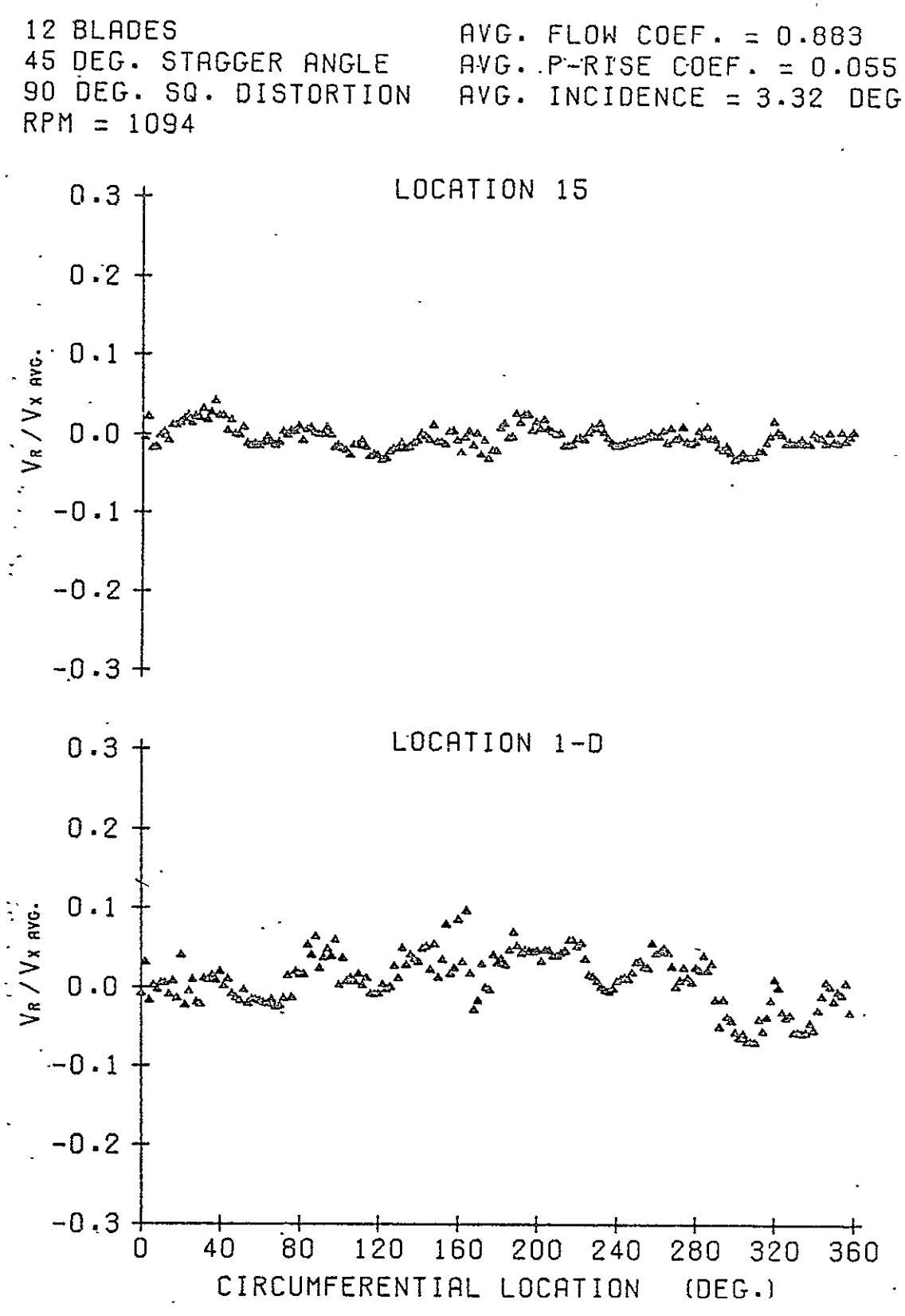

Figure 29. Sample V_R distribution demonstrating the radial component of velocity is small, as implied in the two-dimensional flow field assumption.

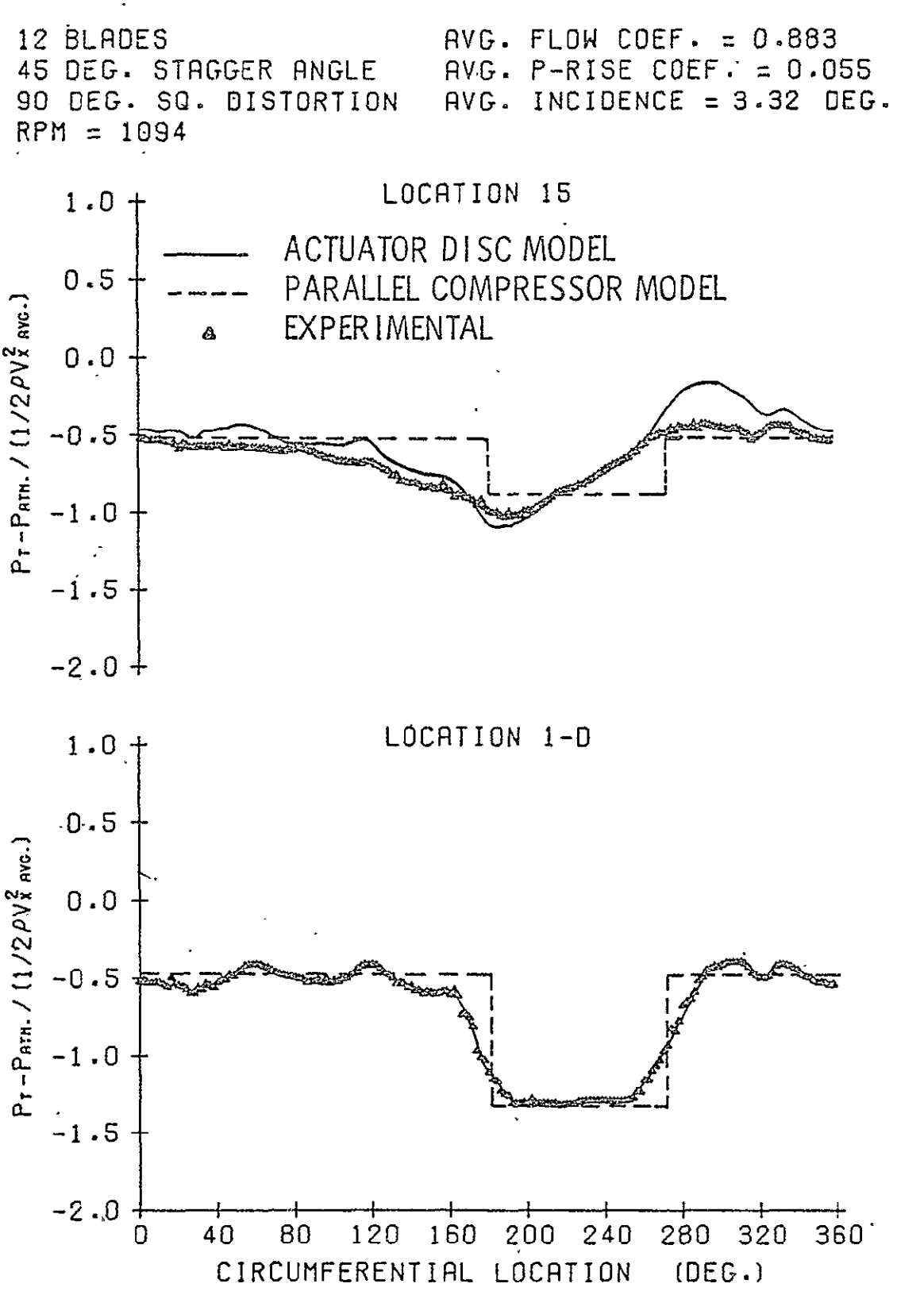

Figure 30. Sample square total pressure distortion data. The solid and dashed lines at Location 1-D are the input to the actuator disc and parallel compressor models, respectively. The lines at Location 15 are predicted.

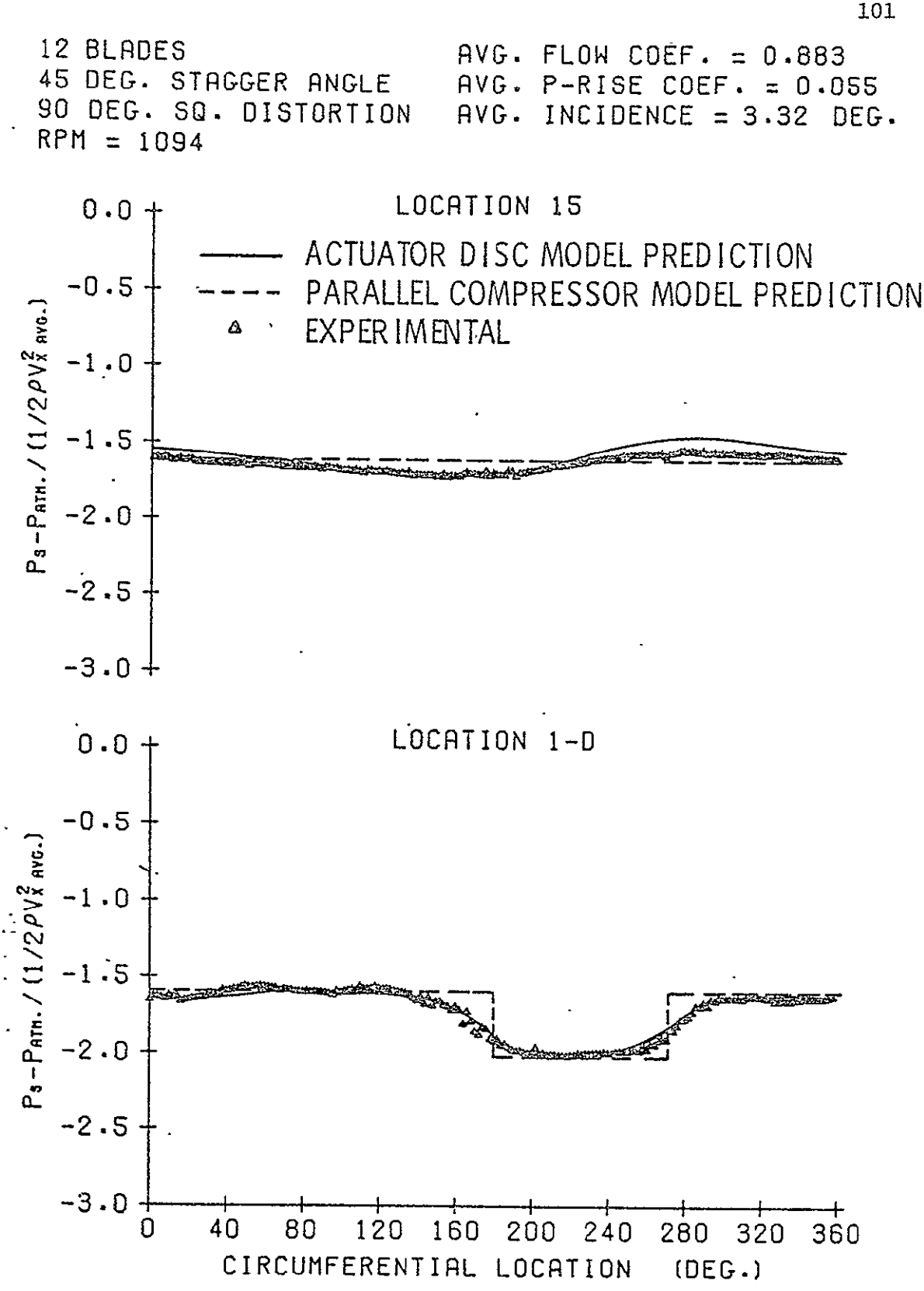

Figure 31. Sample static pressure distribution data for a 90° square distortion and the distributions predicted by the parallel compressor and actuator disc models.

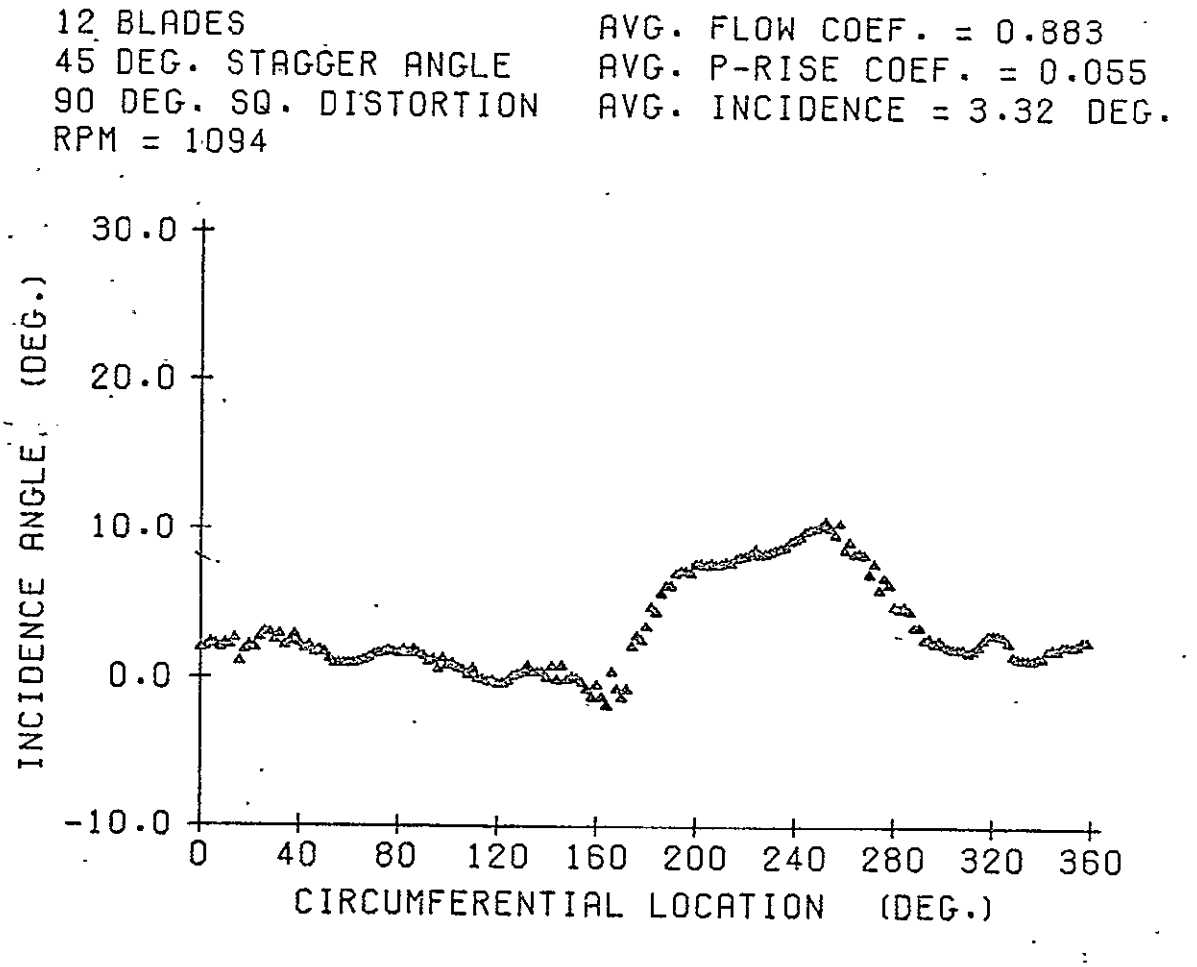

Figure 32. Circumferential variation of the flow incidence on the blades for a 90° square distortion.

A comparison of Figure 27 with Figure C.1 shows that the axial velocity is indeed significantly attenuated upstream of the rotor. Similarly, comparisons of Figures 28 and C.2 and Figures 31 and C.5 show that a nonuniform distribution of V_θ and p_s have arisen at Location 1-D.

The total pressure distortion does not behave exactly as expected, since it is found from a comparison of Figures 30 and C.4 that the magnitude of the distortion at Location 1-D has increased. Although the change is small, no change was expected because, from a two-dimensional viewpoint, the total pressure at the mean radius can only be changed by doing work on the fluid or if a change in the mixing losses occurs. The rotor obviously cannot do work on the fluid (or remove energy) upstream of itself. The mixing losses possibly could increase due to the flow redistribution which takes place. However, the symmetry of the distortion and the magnitude of the change seems to dispel this idea. The most likely cause of the observed change in the total pressure distortion amplitude is a radial total pressure gradient produced by the screens, followed by a radial shift in the streamlines due to the flow redistribution which takes place near the rotor. Although the radial shift would negate the two-dimensional flow assumption made throughout this study, the change in the total pressure distortion is sufficiently small so that it should not have a major effect on the conclusions drawn. The magnitude of the change in the total pressure distortion upstream of the rotor, as compared to the change occurring across the rotor, can be more easily evaluated in Section 6.4. In Section 6.4, the ratios of the distortion amplitude with and without

the rotor are plotted for the two locations. Future experimentation should be conducted to clarify the cause of this discrepancy.

Returning now to an explanation of why the circumferential distributions of V_x, V_θ, P_T, and P_s have the observed shapes, the most suitable place to start is with the explanation given by the simple parallel compressor model. This model will be applied to the test conditions of the data in Figures 27 through 32. It is recalled from Chapter III that the parallel compressor model requires the assumption of constant static pressure at the exit of the compressor. Although this assumption is not completely legitimate for an isolated rotor [10], the assumption of constant exit static pressure will be made initially, and the ramifications of the assumption will be clarified at a latter point.

The most important quantity to be determined in the parallel compressor model is the axial velocity, since it determines all of the remaining quantities. As discussed in Chapter III, the axial velocities in the two sectors of the flow are uniquely determined by satisfying the exit boundary condition for a given mean flow rate, rotor performance characteristic and distortion size. Thus, for any given rotor or compressor operating at specified conditions, the exit boundary condition is the factor controlling the changes occurring in the distortion. In other words, the flow will redistribute in any manner necessary, such that upon passing through the rotor, the exit boundary condition is satisfied.

The total pressure distortion which was input to the model is represented by the dashed line at Location 1-D in Figure 30. The quantities predicted by the model are similarly represented by dashed lines in Figures 27, 28, 30, and 31. Comparing the predicted results

with the experimental data reveals that the magnitudes of the axial velocity, total pressure, and static pressure distortions are fairly accurately predicted by the parallel compressor model. A major discrepancy exists, however, between the predicted shapes of the distortions and those measured in the AFRF. This discrepancy is primarily due to the circumferential cross flows which exist in the real situation but which are ignored by the parallel compressor model. The severity of this restriction placed on the flow by the model is exemplified in Figure 28, where it is shown that the circumferential velocity component measured at Location 1-D is quite significant. The parallel compressor model, however, assumes this component is zero.

Although the parallel compressor model restricts circumferential cross flows and, therefore, does not accurately predict the distortion shapes, two very important points come out of this model. The first point it reveals is that the axial velocity is controlled by the exit boundary condition, and, in this case, the predicted axial velocity distortion magnitude is found to be reduced from what was measured in the absence of the rotor. In other words, the axial velocity distortion is attenuated upstream of the rotor. Secondly, the occurrence of a static pressure gradient upstream of the rotor is explained by the model because a change in the static pressure must accompany the change in axial velocity in order that the same total pressure is maintained.

To get a more accurate prediction of the distortion shapes and thus a better understanding of the flow phenomena occurring, a less restrictive model must be employed. For this reason, the actuator disc analysis was programmed, and the results obtained are represented as the solid lines in Figures 27, 28, 30, and 31. The input to the model

was the Fourier coefficients of the total pressure distortion shown for Location 1-D in Figure 30. As seen from the figures, this model predicts most of the qualities of the distortions very well, including the asymmetry* of the axial velocity and total pressure distortions at Location 15. The shape and magnitude of the circumferential velocity and static pressure distributions upstream of the rotor are also well-predicted.

The actuator disc analysis has thus verified that the factor controlling the shape of the distortions is the flow redistribution which takes place both upstream and downstream of the rotor, but which was ignored by the parallel compressor model. Starting with the conclusions drawn from the parallel compressor model, however, a physical explanation of the flow redistribution which takes place can be made. The parallel compressor model has shown that the axial velocity is altered upstream of the rotor. Because of the assumption of no cross flow between the model compressors, this modification of the axial velocity must occur at the entrance to the system. Otherwise, with the assumptions of the model, a change within the system would violate conservation of mass. Without the artificial restriction imposed by the parallel compressor model, however, it would be expected that the rotor could only influence the flow a short distance upstream. Therefore, beyond a short distance, the flow would exist as it was measured at Locations 1-D and 15 without the rotor installed. This implies that the axial velocity is only changed as it nears the rotor. Conservation

---

*The term asymmetry (or symmetry) as it is used here and throughout the remainder of this section is with respect to the center of the spoiled sector and not $\theta = 0$.

of mass for an incompressible flow requires that accompanying the change in axial velocity must be a convergence of the streamlines in the region where the flow is accelerated and a divergence of the streamlines where the flow is decelerated. It is this convergence and divergence of the streamlines which results in the nonuniform V_θ distribution which is measured and predicted at Location 1-D.

The formation of the nonuniform distribution of V_θ upstream of the rotor is more than just an interesting phenomena because the V_θ distributions upstream of the rotor will strongly influence the flow downstream of the rotor. It is observed from Figure 28 that the circumferential component of velocity is not symmetrical with respect to the center of the spoiled sector. At the entrance of the spoiled sector, a positive V_θ is present, while at the exit of the spoiled sector, V_θ is negative. This asymmetry in V_θ in turn causes a decrease in incidence on the blades as they enter the spoiled sector and an increase in incidence as the blades exit the spoiled sector. Assuming a quasi-steady response of the blades, the asymmetry in the incidence will result in an asymmetrical distribution of p_T and p_s at the exit of the rotor. This explanation is supported by the total pressure data in Figure 30. However, the static pressure as plotted for Location 15 in Figure 31 is almost uniform, and these data do not give much supporting evidence to the explanation. It should be remembered that Location 15 is 0.82 chord lengths downstream of the rotor, and, therefore, some changes in the static pressure may occur before the flow reaches that measurement location.

The possibility of flow redistribution and static pressure changes occurring between the exit of the rotor and Location 15 were investigated

with the aid of the actuator disc analysis. With this analysis, the properties of the flow were predicted at three locations upstream of the rotor and four locations downstream of the rotor, including Locations 1-D and 15. The results are presented in Figure 33 along with the perturbation components of the experimental results previously presented in Figures 27 through 32. The scale marking on the diagrams in Figure 33 represents the same magnitude as the scale in the previous figures. With the high degree of agreement between the predicted and experimental results for Locations 1-D and 15, strong support is given for the accuracy of the predictions at the other locations. It is, therefore, felt that some conclusions can be drawn from the predicted results.

Examination of the diagrams in Figure 33 reveals that the flow upstream of the rotor behaves exactly as has been explained. Furthermore, the static pressure distribution at the exit of the rotor does exhibit a large nonuniformity as expected from the asymmetrical incidence on the blades. However, the static pressure gradient is almost completely eliminated by the time the flow reaches Location 15, which agrees very well with the experimental data. In addition to the asymmetrical static pressure distribution at the exit, it is also seen from Figure 33 that a large V_θ distortion is predicted. The V_θ distortion is significantly reduced at Location 15, and the reduction in the V_θ and p_s distortions have given rise to an asymmetric axial velocity distortion. This asymmetric V_x distribution was previously observed to have differed from the parallel compressor model prediction, and the redistribution of the flow which takes place is found to account for the observed shape of the distortion. All of the distortion shapes

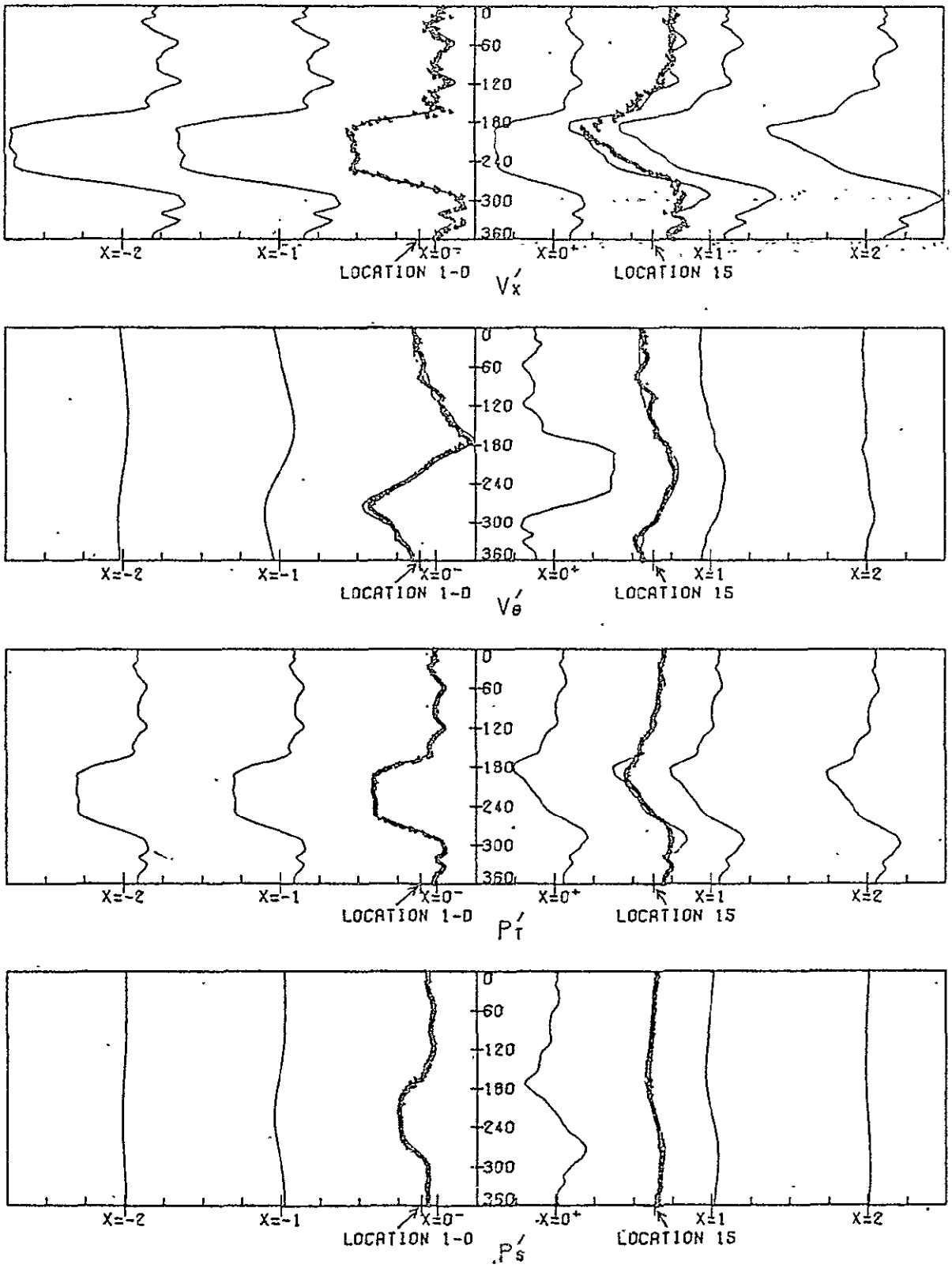

Figure 33. Variation of the perturbation quantities as the flow approaches and leaves the rotor as predicted by the actuator disc analysis. The experimental data are plotted at Locations 1-D and 15 for comparison.

are thus largely accounted for by employing simple fluid dynamic concepts. The small discrepancies which exist between the actuator disc model and the experimental results can be contributed either to a minor unsteady response of the blades, a local blade stall, or increased turbulent mixing caused by the blades.

In light of the new understanding of the flow phenomena occurring, the point made about the validity of the assumption of constant exit static pressure in the parallel compressor model can be clarified. In the AFRF, sufficient distance is available between the test rotor and any downstream component, such that the static pressure will become uniform regardless of the condition at the exit of the rotor. Under these conditions, the assumption of constant exit static pressure is valid, since the only effect of the exit static pressure nonuniformity is to cause a flow redistribution downstream of the rotor. The parallel compressor model ignores this redistribution anyway. The conclusion can thus be made that constant exit static pressure is a valid assumption even for the cases where the static pressure at the exit is not uniform, provided sufficient distance is available downstream to allow the static pressure to equalize. This conclusion is validated by the good agreement achieved by the parallel compressor model in predicting the magnitude of the axial velocity distortion, as shown in Figure 27.

An interesting sideline to the point about the exit boundary condition is the flow response expected if the static pressure was constant at the exit of the blade row. This would be approximately the case if a stator was located downstream of the rotor. Under such circumstances, the flow redistribution, which for the present case took place downstream of the rotor, would be forced to occur upstream of the

stator in order that the exit boundary condition could be obtained. An asymmetrical distribution of P_s' and V_x' upstream would result. Some of the flow redistribution may take place between the rotor and stator, and the remainder would have to occur upstream of the rotor. Thus, P_s' and V_x' profiles representing some combination of the profiles shown for Locations 1-D and 15 for the present case would be expected upstream of the rotor of a single stage.

Before concluding this section on the distortion measurements, sample data for a sinusoidal distortion will be presented and briefly discussed. The data for a four-cycle sinusoidal distortion are plotted in Figures 34 through 39; and included in Figures 34, 35, 37, and 38 are the results from the actuator disc analysis. The same type of flow redistribution and distortion attenuation occurs for the sinusoidal distortion as was noted for the square distortion. For a sinusoidal distortion, however, linear theories predict that the shape of the distortion will remain sinusoidal and not become asymmetrical as occurred for the square distortion. The nonuniform distributions of P_s and V_θ which arise are also expected to be sinusoidal. This sinusoidal nature is predominately what is found in the figures, although the imperfections in the original distortion does yield some asymmetry. The conclusion that the asymmetry is due to the inability to produce a perfect sinusoidal distortion, rather than a nonlinear effect, is substantiated by the linear actuator disc theory which predicts a similar asymmetry.

Another interesting feature to note for the sinusoidal distortions is the phase relationships of $V_{\theta\ 1\text{-}D}$ and $P_{s\ 1\text{-}D}$ with the axial velocity. It is found that V_θ lags the axial velocity by ¼ cycle, while the static pressure distribution and V_x are in phase. These phase relationships

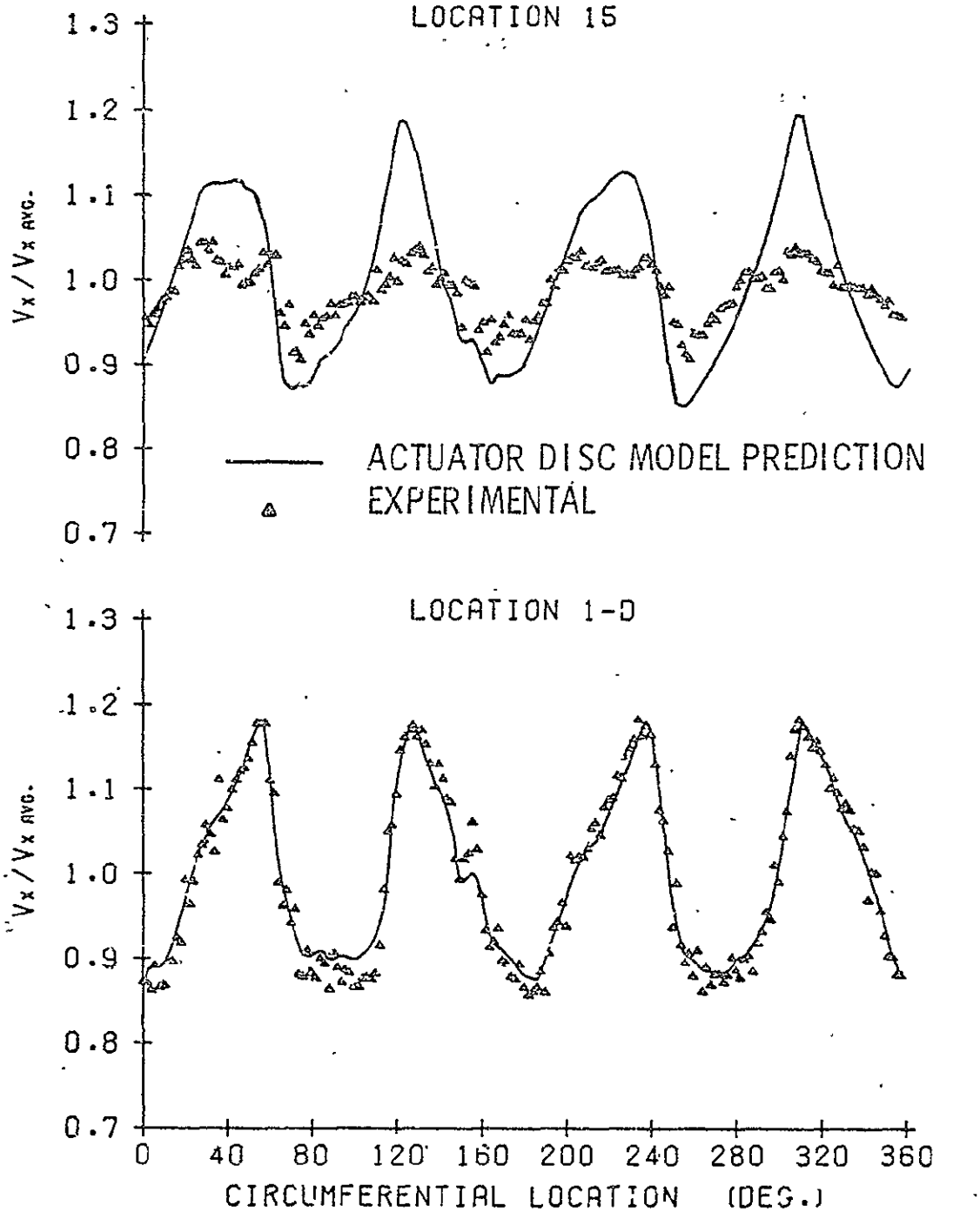

Figure 34. Sample sinusoidal axial velocity distortion data and the actuator disc model predictions.

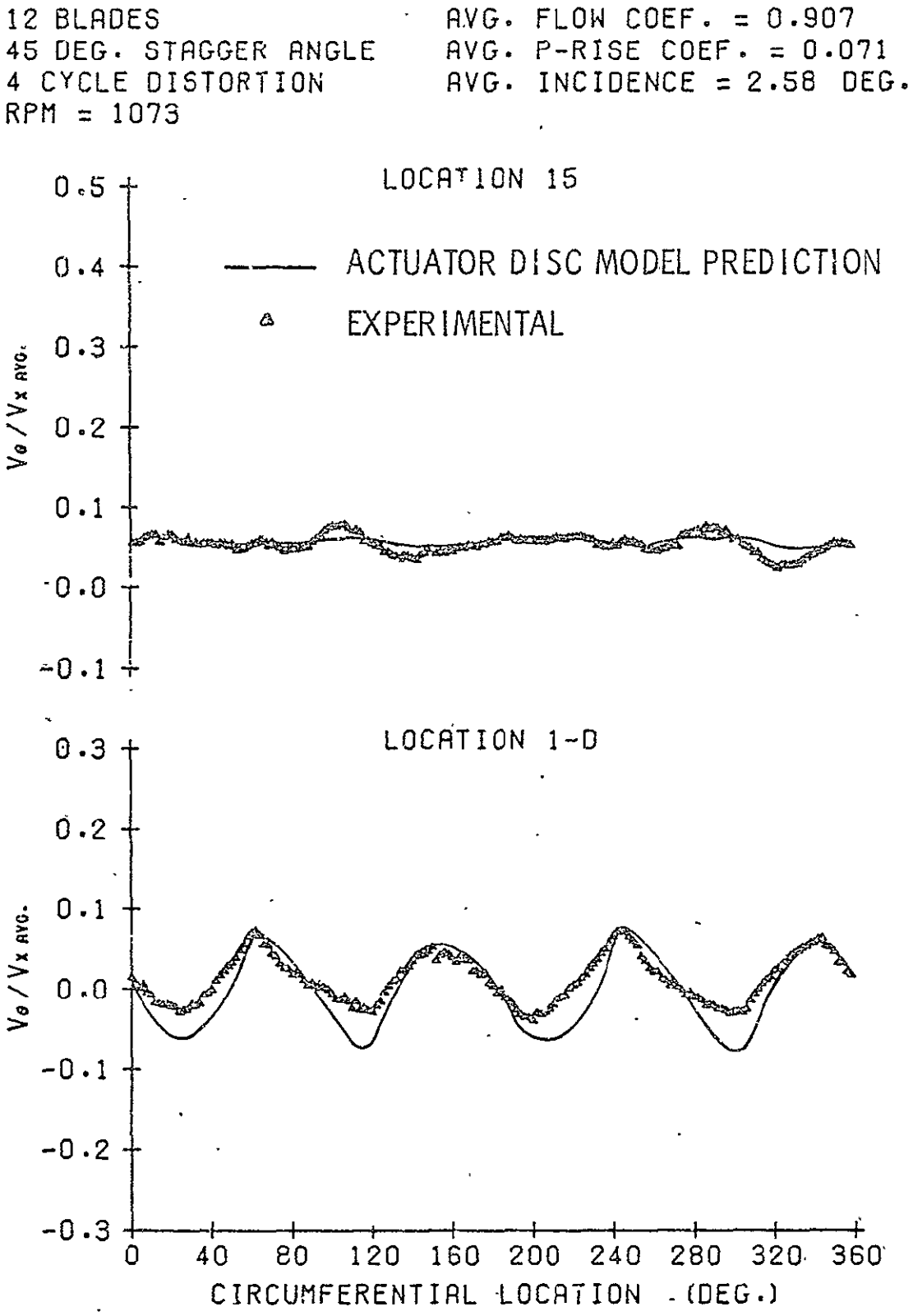

Figure 35. Sample V_θ distribution data and the actuator disc model predictions for a four-cycle sinusoidal distortion.

12 BLADES
45 DEG. STAGGER ANGLE
4 CYCLE DISTORTION
RPM = 1073

AVG. FLOW COEF. = 0.907
AVG. P-RISE COEF. = 0.071
AVG. INCIDENCE = 2.58 DEG.

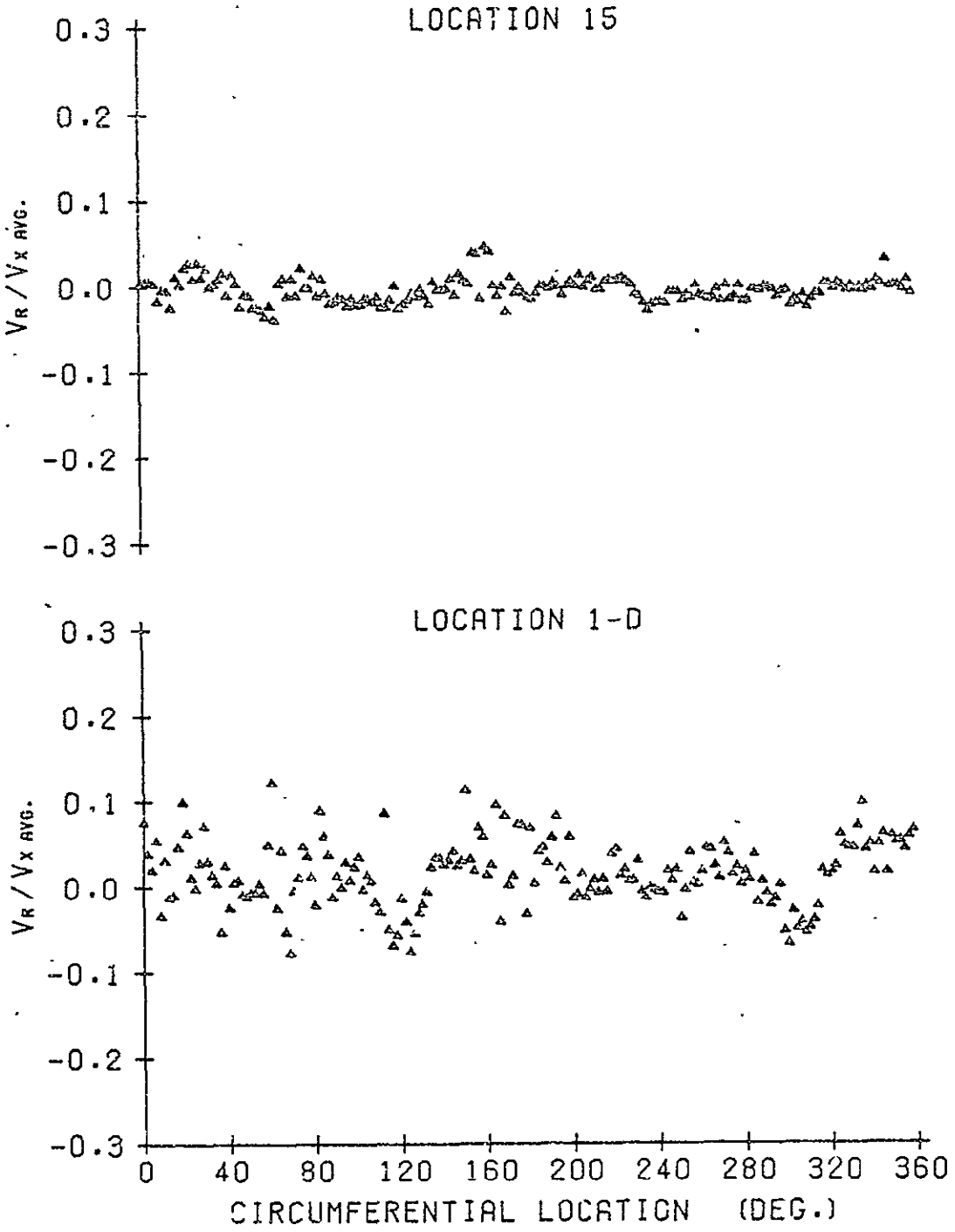

Figure 36. Sample V_R distribution for a sinusoidal distortion.

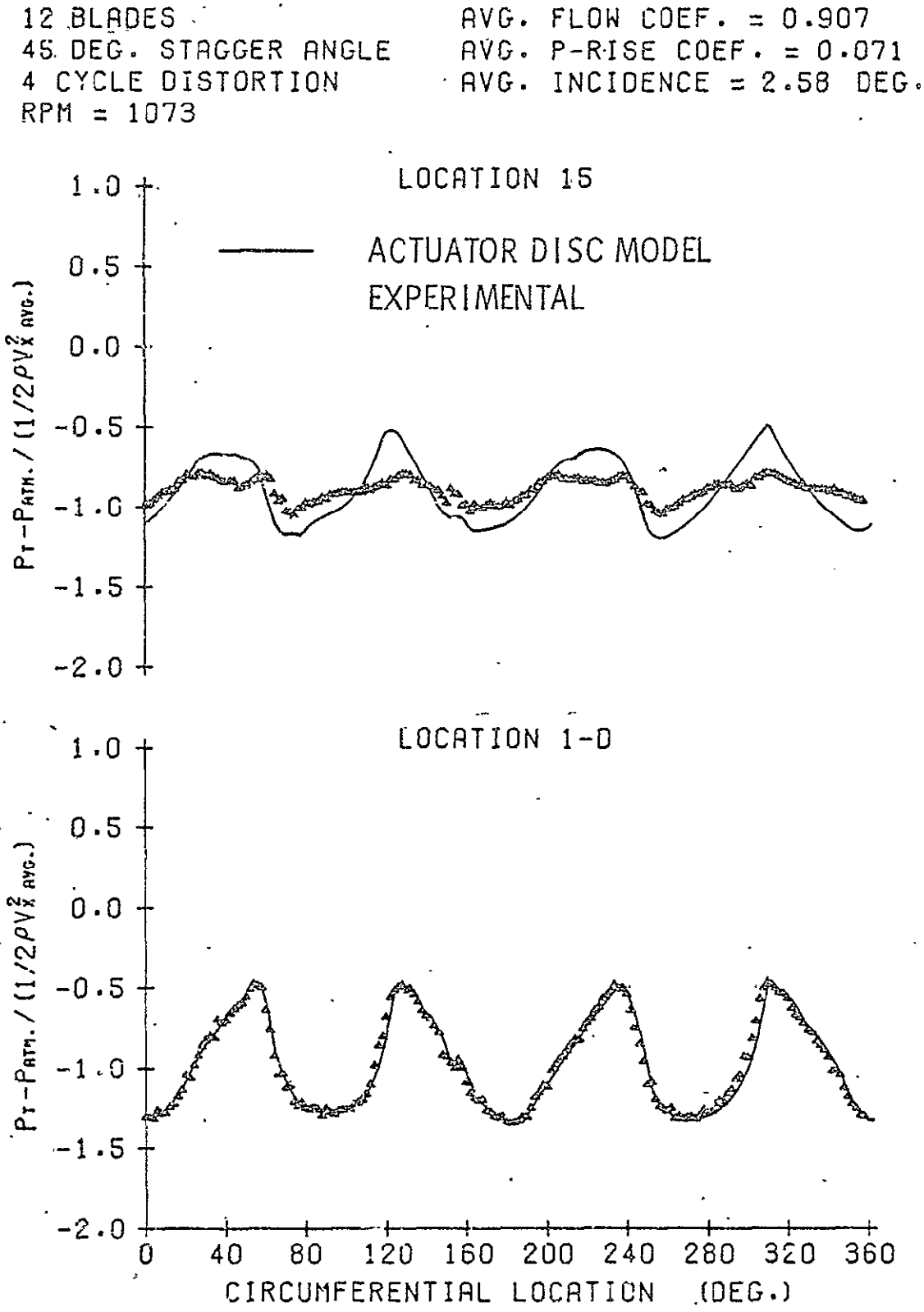

Figure 37. Sample sinusoidal total pressure distortion data. The solid line at Location 1-D is the input to the actuator disc analysis. The line at Location 15 is predicted.

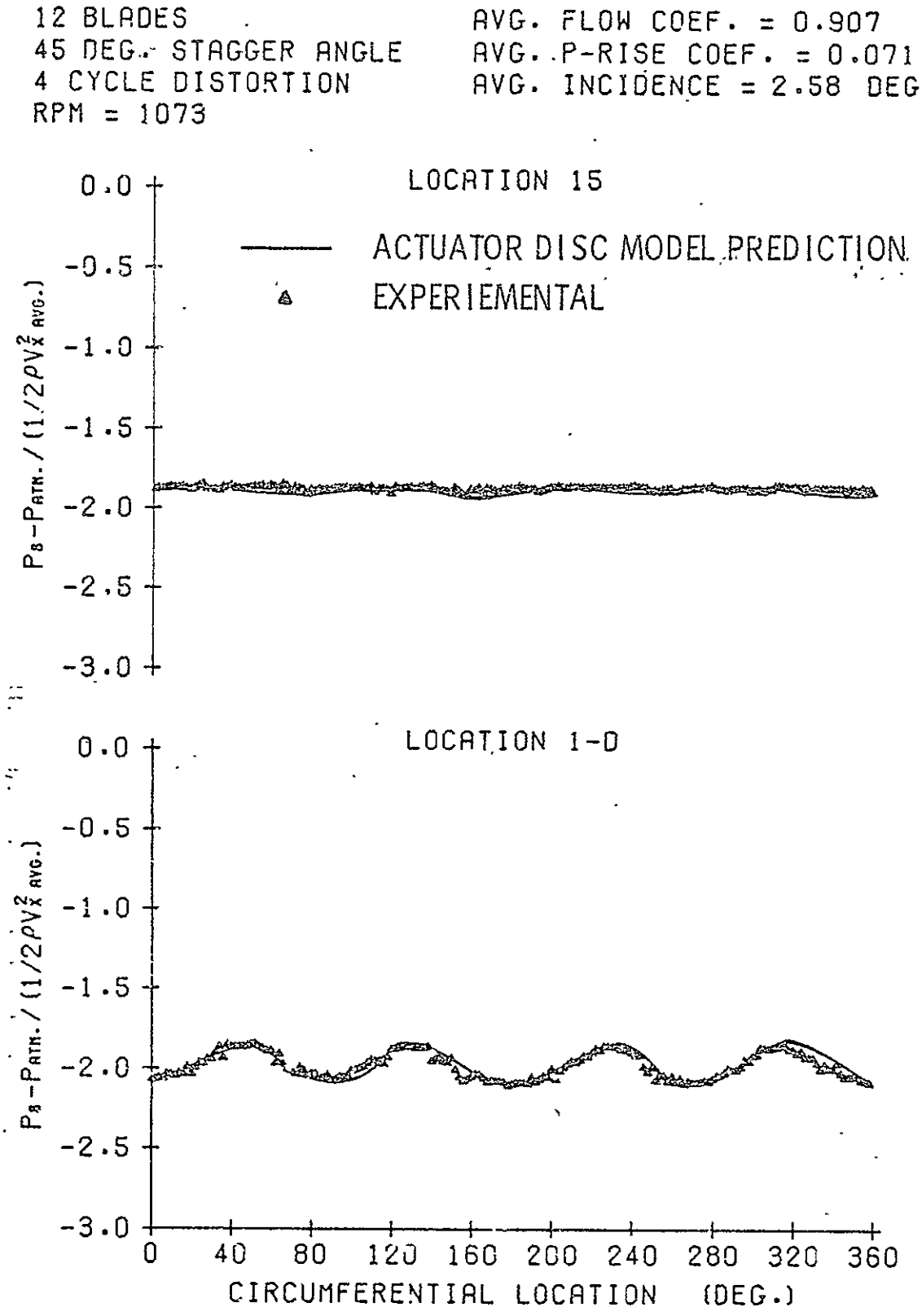

Figure 38. Sample static pressure distribution data for a four-cycle sinusoidal distortion and the distributions predicted by the actuator disc model.

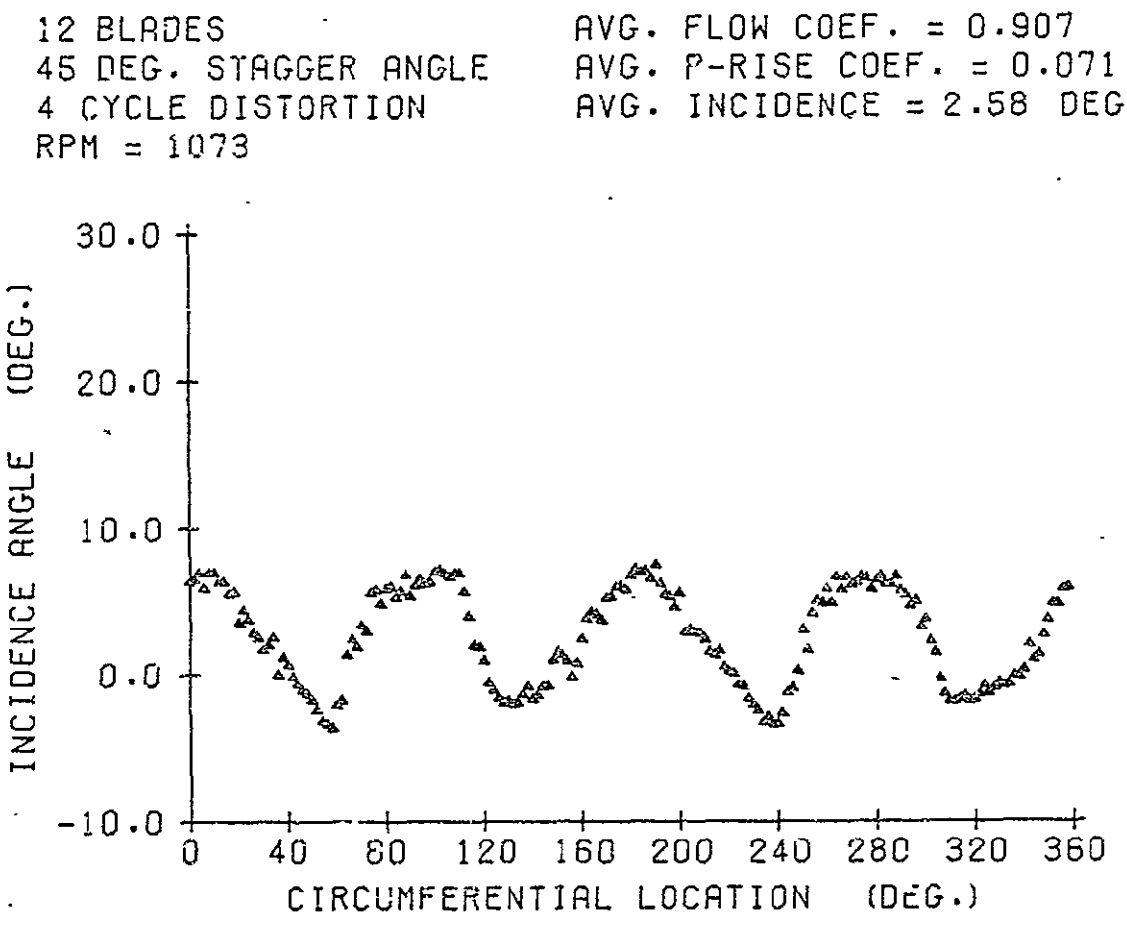

Figure 39. Circumferential variation of the flow incidence on the blades for a four-cycle sinusoidal distortion.

are exactly as would be expected by following the same physical reasoning used to explain the flow redistribution occurring for the square distortions. Similar conclusions are drawn by examining the equations for the linear actuator disc model.

The final characteristics of the data requiring further consideration are the discrepancies between the results from the actuator disc analysis and the experimental V_x and P_T distributions at Location 15. Figures 34 and 37 show that the predicted amplitudes of the V_x and P_T distortions remaining downstream of the rotor are significantly larger than those found experimentally. Similar discrepancies between the results from a quasi-steady linear actuator disc analysis and sinusoidal distortion data measured in a four-stage, low-speed compressor were investigated by Mokelke [20]. For this investigation, he developed two additional actuator disc models, one including the unsteady blade response and the other including turbulent mixing. Using these models, Mokelke concluded that the main reason for the discrepancy was due to turbulent mixing and not an unsteady blade response. It is felt a similar conclusion can be made for the present data; however, it is pointed out that no decay in the distortion amplitude was found between Locations 1-D and 15 when the rotor was not installed. Therefore, additional turbulent mixing must be caused by the rotor, which is most likely to be due to the turbulence in the blade wakes.

6.4 Distortion Attenuation and Unsteady Losses

The purpose of this section is to examine some of the overall trends observed in the distortion data as a function of the screen type and rotor operating parameters. However, because of the large amount of data associated with the objective of providing a data base for

subsequent studies, it is not possible to examine all of the distortion characteristics in this thesis. For this reason, only the attenuation (or amplification) of the axial velocity and total pressure will be discussed, and the total pressure losses caused by the distorted flow will be presented. An attempt has been made to point out the most significant parameters involved, which should be an aid in conducting future studies in these areas. Additional analytical and experimental studies will probably be required to explain some of the characteristics of the data and to obtain a full understanding of the flow processes occurring. A full understanding of the data is needed if the data are to be used in a practical application. For the attenuation data given, comparisons are made with predicted results from the actuator disc model. The discrepancies between this theory and the data give an insight as to what flow or rotor characteristics should be investigated in the future to fully understand the distorted flow phenomena.

Beginning with the topic of distortion attenuation, it is first realized that in order to quantify the attenuation, a means of representing the distortion amplitude must be selected. One method of quantifying the size of a distortion is to represent the data as a Fourier series, so that the amplitudes of the various harmonics can be examined and compared. Following this approach, the dimensionless axial velocity and total pressure data were Fourier analyzed by computing the coefficients of a conventional Fourier series using a numerical integration scheme. The coefficients of the series were then converted to an amplitude and phase so that the data could be represented in the following form:

$$\frac{p_T}{\frac{1}{2}\rho v_{x\,avg}^2} \text{ or } \frac{v_x}{v_{x\,avg}} = \frac{A_o}{2} + \sum_{n=1}^{\infty} A_n \sin(n\theta - \phi_n). \tag{44}$$

Figure 40 contains plots of the amplitudes, A_n, of the dimensionless total pressure and axial velocity distortions versus the harmonic number, n, for a four-cycle distortion. Three sets of data are presented on each graph, one set describes the distortion without the rotor installed, while the other two describe the distortions at Locations 1-D and 15 when the rotor is operating. This type of plot is useful for demonstrating the harmonic content of the distortion and for identifying the dominate harmonics. The figure also shows how each harmonic is affected by the presence of the rotor. As expected for the four-cycle distortion, Figure 40 shows that the fourth harmonic is very dominate, and, thus, the amplitudes of the fourth harmonics can be used to describe the distortion size. Similarly, the furdamental harmonic of the one-, two-, and six-cycle sinusoidal distortions can be used to represent their distortion amplitudes.

Plots similar to those in Figure 40 are presented for a 90° distortion in Figure 41. In this case, it is found that the first two harmonics are significant. Although both of these harmonics could be used to analyze the attenuation of the square distortion, no single parameter from the Fourier series can be used to properly represent the distortion size. For this reason, the amplitudes of the square distortions were defined in terms of the maximum and minimum values, as represented by Equations (45) and (46):

$$A_{p_T} = \frac{p_{T\,max} - p_{T\,min}}{\frac{1}{2}\rho v_{x\,avg}^2} \tag{45}$$

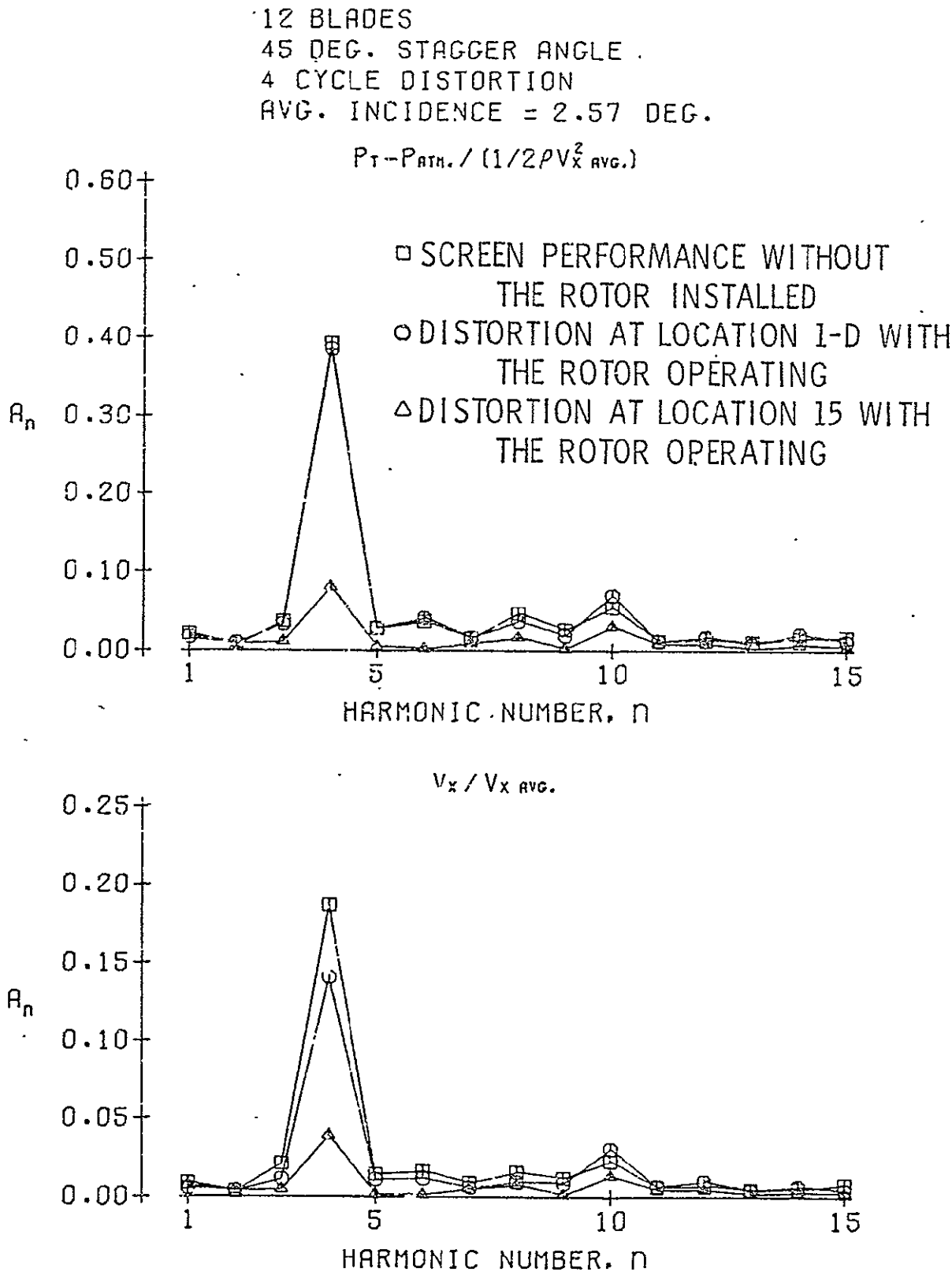

Figure 40. Dimensionless total pressure and axial velocity harmonic amplitudes as a function of the harmonic number, n, for a four-cycle distortion.

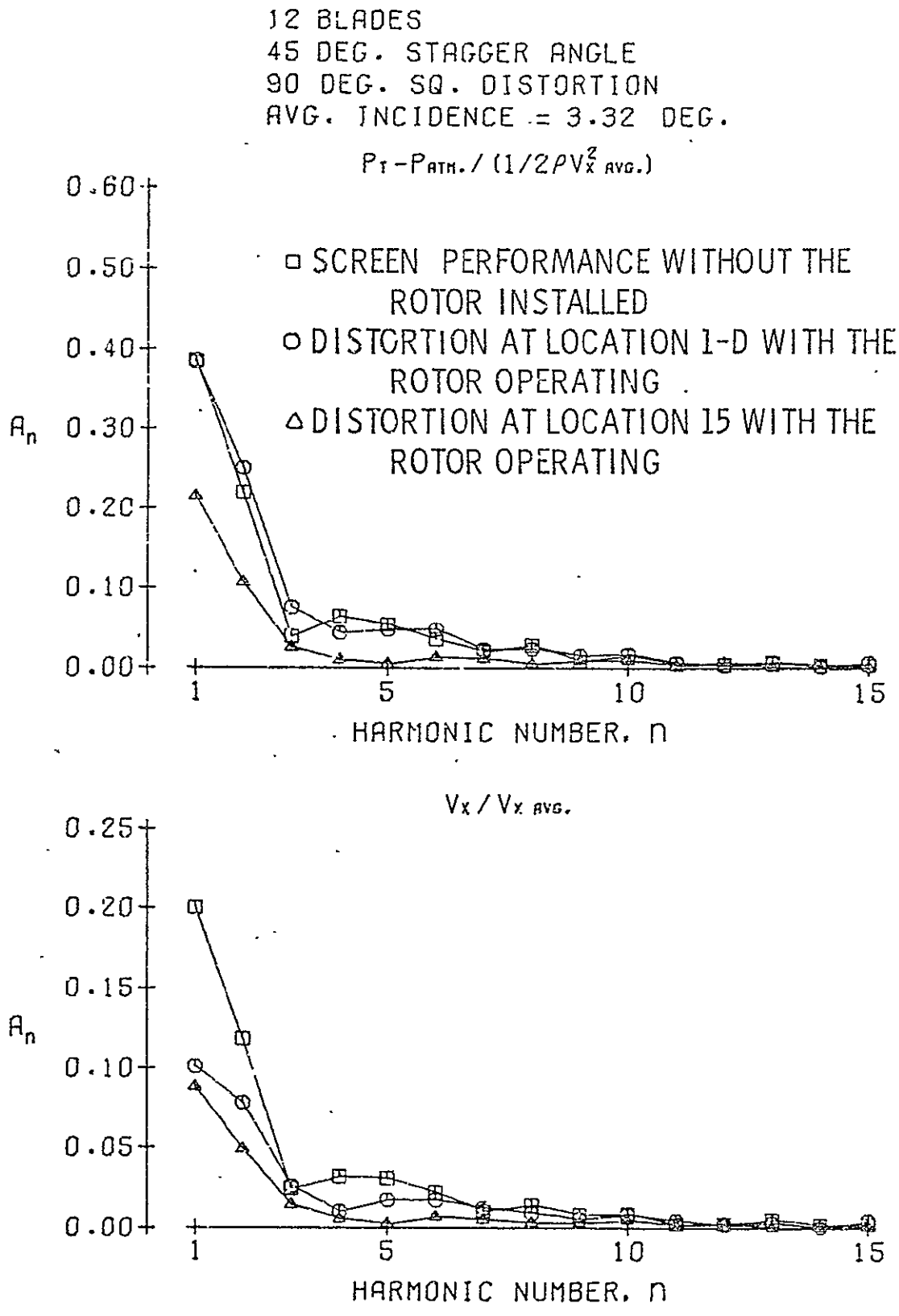

Figure 41. Dimensionless total pressure and axial velocity harmonic amplitudes as a function of the harmonic number, n, for a 90° square distortion.

and

$$A_{v_x} = \frac{v_{x\,max} - v_{x\,min}}{v_{x\,avg}} \quad . \tag{46}$$

These definitions may appear to be an obvious choice, since for a perfect square distortion, the amplitude, A, is simply the difference in magnitude between the unspoiled and spoiled sectors. However, it is necessary to define "A" with the maximum and minimum values because downstream of the rotor, the distortion is no longer square. This fact is exemplified in Figures 27 and 30 of the preceding section, where it is found that the data at Location 15 no longer resemble a square distortion.

For both the sinusoidal and the square distortions, the attenuation is represented as a ratio of the distortion amplitude with the rotor operating to the amplitude of the distortion without the rotor installed.* With the data presented in this manner, this ratio normally ranges from a value of 1, indicating no attenuation, to a value of 0, indicating the distortion was completely eliminated. Values greater than 1 mean that the distortion was amplified.

Figure 42 presents the attenuation for the four-cycle distortion in the form of the amplitude ratio of the fourth harmonic versus the circumferential average incidence. Both the axial velocity and total pressure amplitude ratios are presented for both locations, with the

---

*The distortion measured without the rotor installed theoretically represents the distortion which would exist far upstream of the rotor or at negative infinity. Therefore, the nomenclature employed uses the subscript $-\infty$ to identify this distortion amplitude.

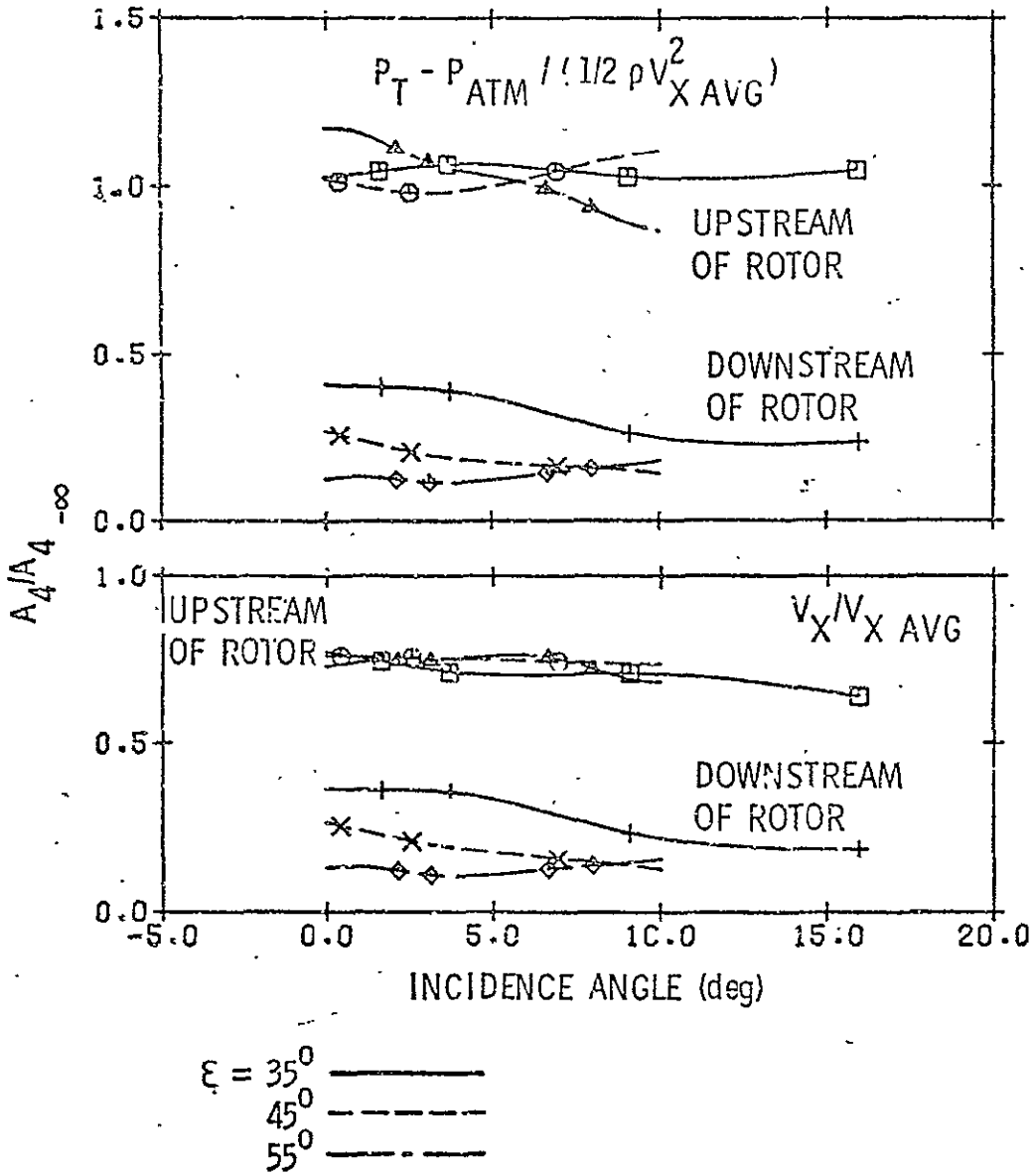

Figure 42. Measured axial velocity and total pressure distortion attenuation versus incidence angle for a four-cycle sinusoidal distortion.

three lines for each location indicating various blade stagger angles. It is seen from the figure that both the total pressure and axial velocity attenuation are not strongly influenced by a change in incidence, or mean blade loading. This independence is probably because the performance characteristics of the rotor are very nearly linear. There is a slight increase in attenuation with increased incidence for the rotor configurations having 35° and 45° blade stagger angles, but a slight decrease in attenuation with increased incidence is observed for the 55° stagger angle.

The most important characteristic of the data revealed in Figure 42 is that the blade stagger angle has an important influence on the amount of attenuation realized downstream of the rotor. The rotor configurations with the higher blade stagger angles produce a larger attenuation of both the total pressure and axial velocity. The increase in attenuation of the total pressure distortion with increased stagger angle is partially a quasi-steady response due to the steepening of the pressure rise versus incidence performance curve which occurs for the higher stagger angles.

To help obtain a better understanding of the data in Figure 42, the amplitude ratios of a four-cycle distortion, as predicted by the actuator disc model, are presented in Figure 43. For the axial velocity, Figure 43 shows that the attenuation is largely independent of incidence, and the effect of an increase in stagger is an increase in the amount of attenuation. These general characteristics are the same as those observed in the experimental data; however, there is a large difference between the magnitudes of the attenuation predicted and that which was

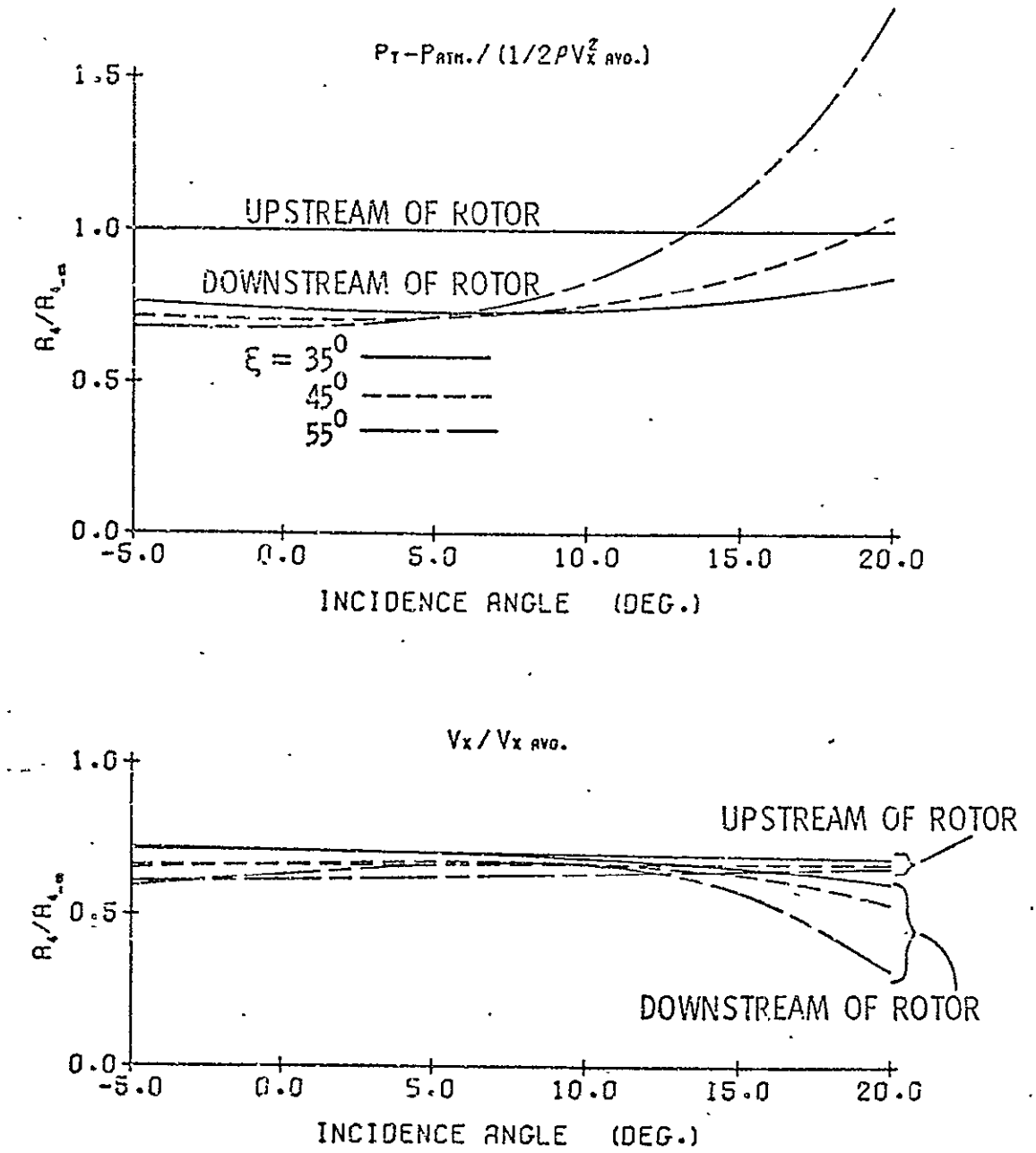

Figure 43. Distortion amplitude ratio versus incidence predicted by the actuator disc model for a four-cycle distortion.

measured. The effect of stagger angle is also much less significant in the predicted axial velocity attenuation.

The most noticeable characteristic of the predicted data is the response of the total pressure. In this case, the amplitude ratio is found to increase at the higher incidence, and the effect of increased stagger is reversed from the effect it causes at the lower incidences. For the 55° stagger, a significant amount of amplification is even predicted. From a quasi-steady, inviscid, one-dimensional approach, this amplification seems unrealistic because the higher incidences in the lower axial velocity regions will result in a larger total pressure rise in these regions. Thus, the total pressure defect should be reduced. However, the actuator disc analysis is a two-dimensional model and, therefore, it is concluded that the induced circumferential velocity component has a dominating role at higher incidence and stagger angles.

The reason for the dominating role of $V_{\theta_{0^-}}$ can be understood by examining the matching conditions across the actuator disc. In Chapter III, Equation (26) expresses the exit condition of V_θ', and Equation (29) expresses the change in P_t' across the rotor. Combining these two equations, it is found that:

$$P_{T_{0^+}}' - P_{T_{0^-}}' = 2 \frac{U}{\bar{v}_x} [(m-1) V_{\theta_{0^-}}' - b V_{x_0}'] . \qquad (47).$$

Substituting the numerical values of m and b for the 55° stagger configuration into Equation (47) yields:

$$P_{T_0}'_{+} - P_{T_0}'_{-} = 2 \frac{U}{\bar{v}_x} [-0.88376\ V_{\theta_0}'_{-} - 1.34096\ V_{x_0}'] \quad . \tag{48}$$

It is initially not apparent from Equation (48) why $V_{\theta_0}'_{-}$ should cause an amplification of the total pressure distortion. It must first be realized, however, that V_{x_0}' and $V_{\theta_0}'_{-}$ are ¼-cycle out of phase, and V_{x_0}' and $P_{T_0}'_{-}$ are in phase. For this reason, the effect of V_{x_0}' is to decrease the amplitude of the total pressure distortion, as expected, from a one-dimensional, quasi-steady approach, while the effect of $V_{\theta_0}'_{-}$ is to create a new distortion ¼ cycle out of phase with the original distortion. At the higher incidence and blade stagger angles, where $U/\bar{v}_x$ is large, the total pressure distortion created by $V_{\theta_0}'_{-}$ is larger than the original distortion, resulting in an apparent amplification of the distortion. Although the experimental data do not reveal any amplification of the distortion downstream of the rotor, it is seen from Figure 42 that the attenuation decreases (an increase in the amplitude ratio) with increased incidence for the 55° stagger configuration. It is also observed that the attenuation for the 35° stagger configuration levels off at the higher incidences. Therefore, it is felt that the convergence of the attenuation lines for the three different stagger angles is explained by the actuator disc theory.

Thus far, the trends in the experimental data have been explained by a quasi-steady, two-dimensional, inviscid approach. The discrepancies between the magnitudes of the predicted and measured results can, therefore, be contributed to either an unsteady blade response or a viscous effect. Although Mokelke [20] concluded for this test configuration that turbulent mixing was the cause for the additional observed attenuation, future experimental work should be conducted to verify the

point. As mentioned in the previous section, it is felt that the tubulent mixing must be a result of the blade wakes, since no significant mixing was observed between Locations 1-D and 15 without the rotor installed.

Another discrepancy observed for both the axial velocity and total pressure distortions is that the lines of constant stagger angle are farther apart in the experimental data than in the predicted results. This occurrence does appear to be consistent with the possible causes of the magnitude discrepancy because, at higher stagger angles, the distortion frequency increases with respect to the blades, and also, higher blade loading will result in larger wakes. Thus, at higher stagger angles, both the contribution from the unsteady blade response and turbulent mixing could increase.

The final thing to be pointed out in Figure 42 is the change in the total pressure distortion amplitude upstream of the rotor. Possible causes for this phenomenon were suggested in the preceding section. For the sinusoidal distortions, the variation is not significantly large and the mean amplitude ratio is approximately 1.0. Therefore, the variation in p_T should not alter the validity of these results.

From the data from the four different sinusoidal distortions, the variation in the attenuation was found to be much greater as a function of distortion frequency than the variation observed with changes in incidence angle. Therefore, the remaining data for the sinusoidal distortions will be presented as a function of the reduced frequency, which is a dimensionless frequency parameter defined as:

$$\omega = \frac{\nu c}{2W_m} = \frac{2\pi}{\ell} \cdot \frac{c}{2} \cdot \frac{U}{W_m} \simeq \frac{\pi c}{\ell} \sin\xi \ . \qquad (49)$$

This definition stems from unsteady aerodynamic theory and is seen to consist of the distortion frequency, ν, the blade chord, c, and the mean relative velocity, W_m. As was done in Equation (49), ν can be replaced by $2\pi U/\ell$ resulting in the term U/W_m. For lightly loaded blades, W_m is parallel to the blade chord, and U/W_m can then be approximated by the sine of the blade stagger angle. Although the blades are not always lightly loaded, ω is defined as $\pi c/\ell \cdot \sin\xi$ throughout this study. As a physical interpretation of ω, it can be shown that the reduced frequency represents the number of distortion cycles across the blade chord.

Figures 44 and 45 present the amplitude ratio of the total pressure and axial velocity distortions versus ω for two constant values of incidence, $i = 0°$ and $i = 10°$, respectively. Similar to Figure 42, data for the two axial locations and the three stagger angles appear on each graph. It is seen from both Figures 44 and 45 that an increase in reduced frequency increases the attenuation of the total pressure and axial velocity distortions downstream of the rotor.

The current actuator disc analysis can give very little insight into the attenuation changes observed with increases in reduced frequency, since a quasi-steady blade response is assumed. With the quasi-steady assumption, no variation in the total pressure amplitude ratio with ω would be predicted. However, the analysis does predict a variation of $A_n/A_{n_{-\infty}}$ for the axial velocity because the axial velocity changes with x and the rate of change is a function of n or ω. The predicted magnitude and slope of $A_n/A_{n_{-\infty}}$ for the axial velocity upstream of the rotor does agree very well with the experimental results. However, this is the only characteristic of the data explained by the actuator disc theory. The

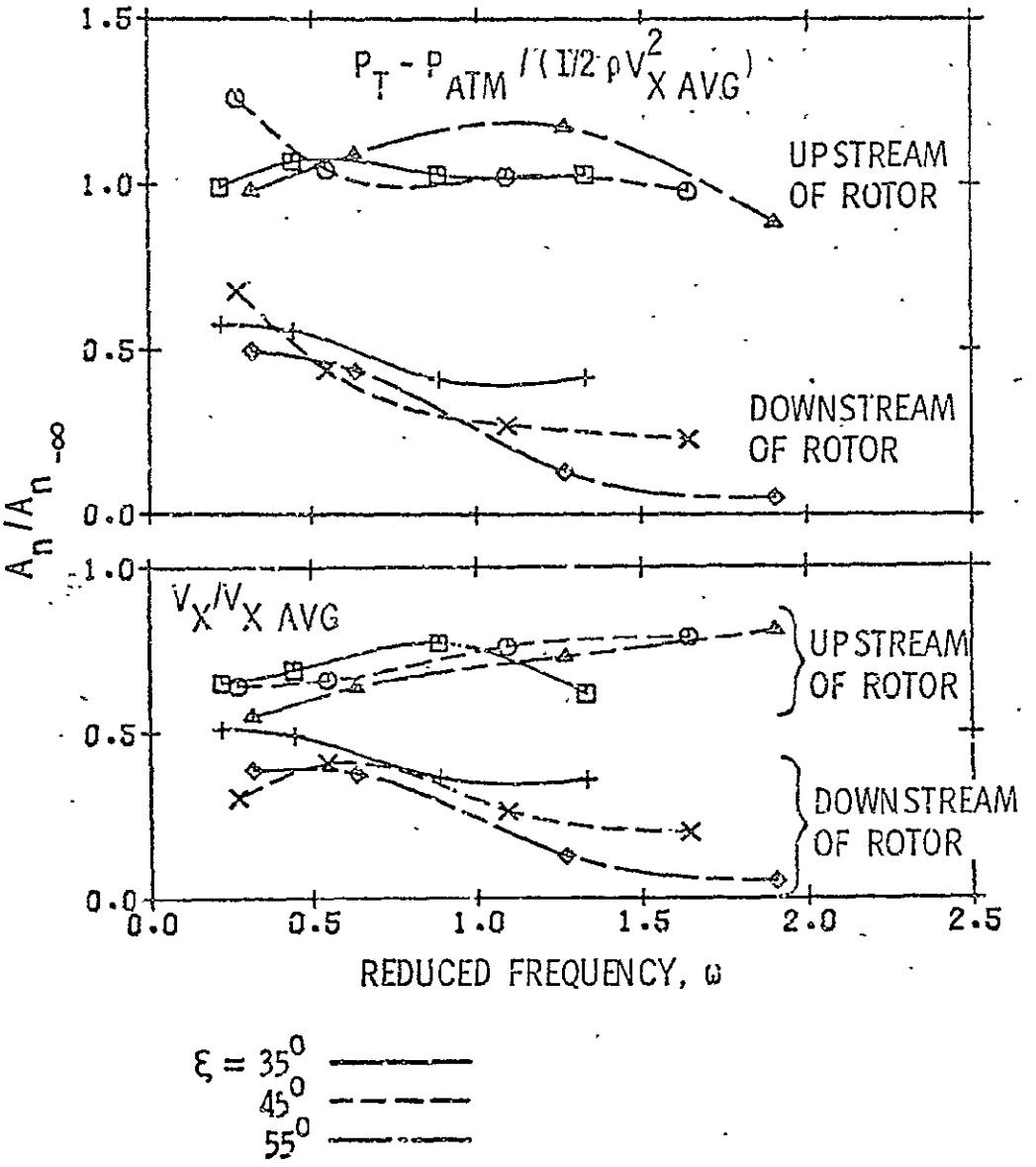

Figure 44. Amplitude ratio versus reduced frequency for a constant 0° mean incidence angle.

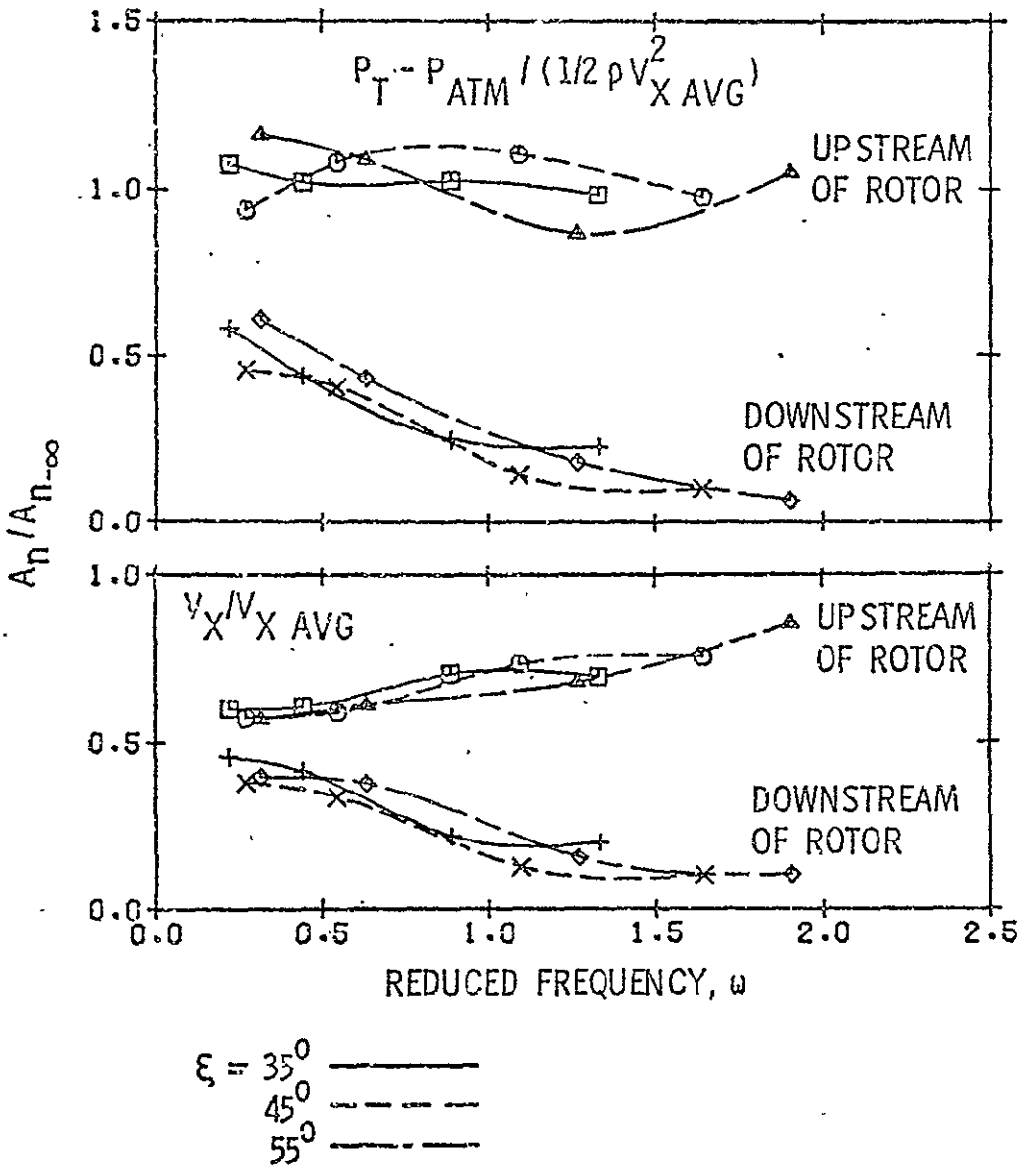

Figure 45. Amplitude ratio versus reduced frequency for a 10° mean incidence angle.

large increase in the distortion attenuation with ω is, once again, contributed to unsteady effects or turbulent mixing. The fact that the attenuation is very strongly dependent on ω is an important conclusion of this study, since no current theoretical analyses can predict this response. It should be noted that at the highest value of ω for the 55° stagger angle the distortion has been almost completely eliminated.

The stagger angle is found to have a significant effect on the distortion attenuation for $i = 0°$, as shown in Figure 44. For $i = 10°$, however, the effect of stagger has been diminished. The decreased effect of stagger is associated with the convergence of the constant stagger angle lines in Figure 42, which was previously explained using the actuator disc analysis. For this rotor, the higher incidence angles negate the difference associated with the stagger angle.

The last set of attenuation data to be presented is the amplitude ratios of the total pressure and axial velocity distortions for the two square-shaped inlet distortions tested. These data are presented in Figures 46 and 47 for the 90° and 180° distortions, respectively. The total pressure distortion amplitude is defined by Equation (45), and the velocity distortion amplitude is defined by Equation (46). The data on the figures are presented with the lines representing the same parameters as they previously represented for the sinusoidal distortions.

Similar to the data for the sinusoidal distortions, the effects of incidence on the attenuation are very small. It is also found that the stagger angle does not significantly affect the attenuation. However, the main observation which can be made from Figures 46 and 47 is the influence of the circumferential extent of the distortion. It is seen that the magnitudes of the axial velocity amplitude ratios are quite

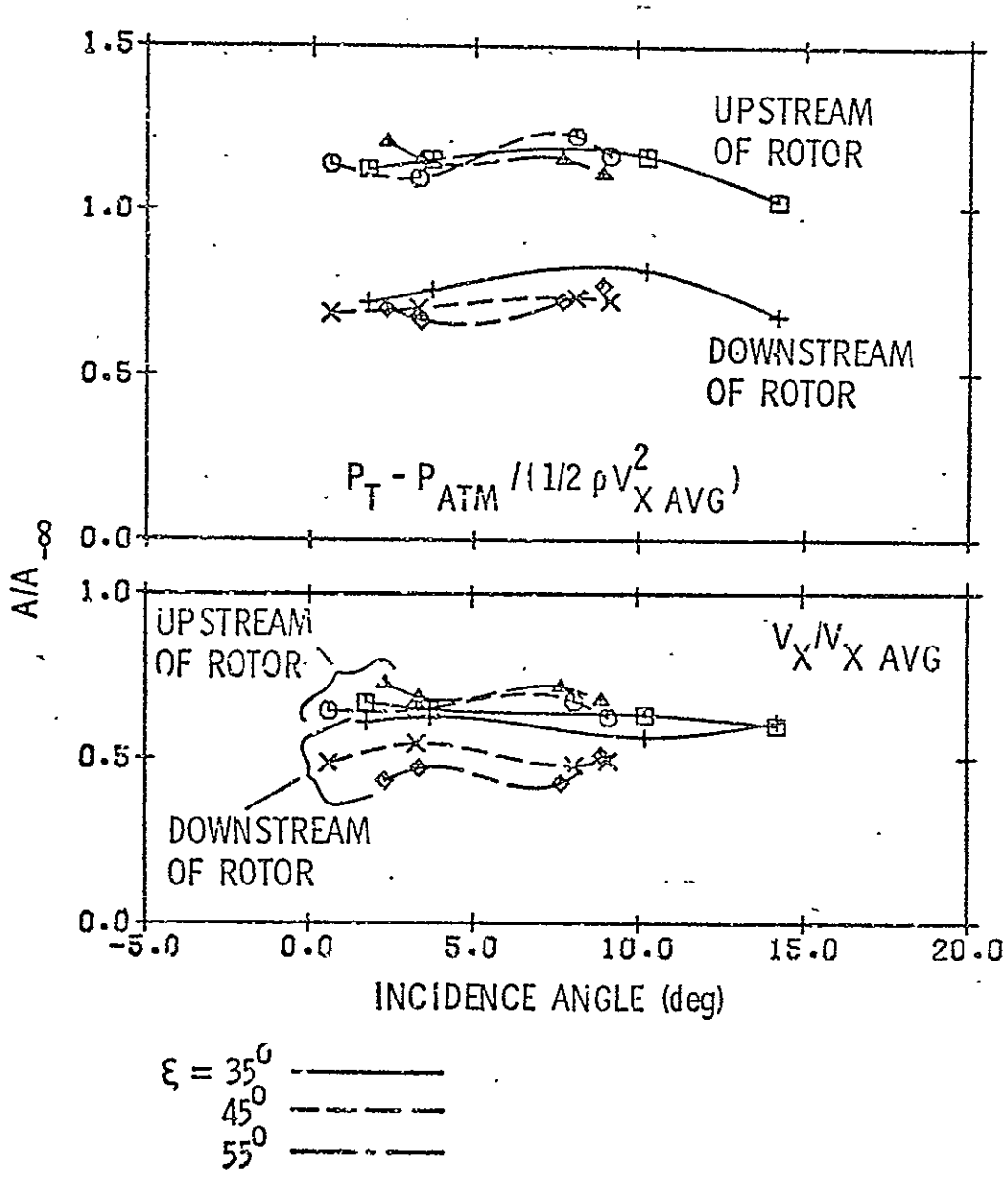

Figure 46. Amplitude ratio versus incidence for a 90° square distortion.

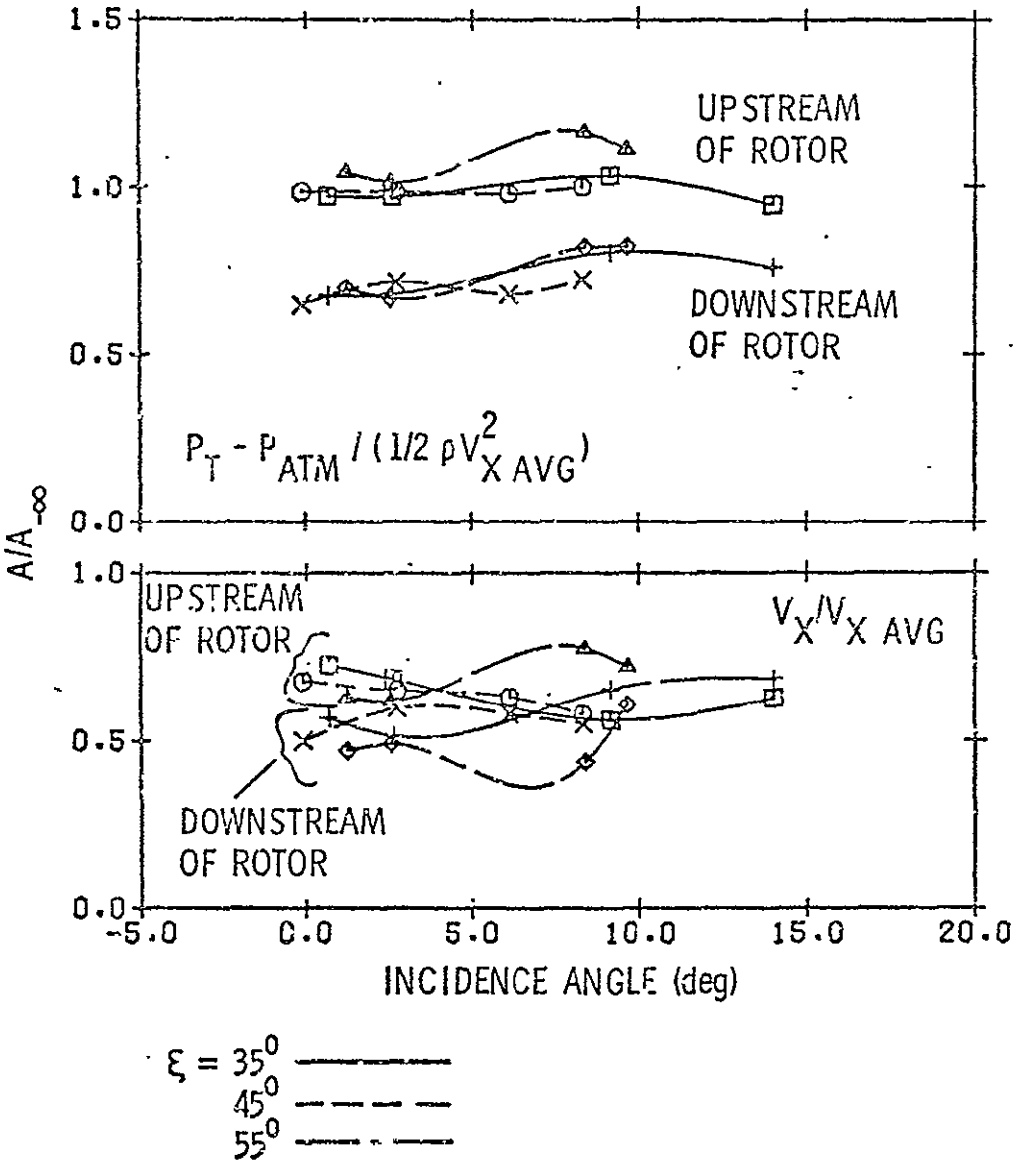

Figure 47. Amplitude ratio versus incidence for a 180° square distortion.

similar for both the 90° and 180° square distortions. The total pressure amplitude ratios downstream of the rotor also have approximately the same magnitude. However, it does appear from the figures that the 90° total pressure distortion was attenuated more than 180° distortion because the amplitude of the 90° distortion upstream of the rotor has been amplified. Due to the hypothesized three-dimensional flows involved in amplifying the inlet distortion, it cannot be inferred from these data, however, that a larger attenuation will always be observed for smaller width distortions.

The last data to be presented describe the total pressure losses which are caused by the nonuniformity of the inlet flow. This study was not primarily intended to obtain this type of data; thus, an explanation for the losses cannot be made. The data will simply be presented for a future reference. From the data given, however, the importance of the unsteady losses is apparent, and additional research in this area is warranted.

For steady uniform flow, the losses across a blade row have been thoroughly investigated and are well-documented in the literature [18]. These losses can be contributed to skin friction and pressure drag on the blades, skin friction on the casing walls, secondary flows caused by turning a flow with velocity gradients, and losses due to tip clearance effects. For unsteady flow, however, very little loss data exists. References [21], [22], and [23], which investigated unsteady losses in a turbine cascade, have shown that the losses due to the unsteadiness can be very significant. In some cases, the losses in unsteady flow were twice as large as the losses measured in steady flow.

From a quasi-steady viewpoint, higher losses are expected with a nonuniform inlet flow because of the higher incidence angles experienced by the blades in the low velocity regions. Local regions of flow separation may even be caused by the rapidly changing relative flow angles near the leading edge or the blades. From an unsteady viewpoint, additional losses may be caused by the vortex shedding associated with the unsteady circulation on the blades. The unsteady pressure distribution on the blades will also affect the growth and stability of the boundary layer. It is expected that the effect of the unsteadiness on the boundary layer will be frequency dependent.

In Section 6.1, the total pressure loss coefficient for steady flow was defined by Equation (43). The same definition will be used to represent the unsteady losses in this section, except that the circumferential average values of p_T and v_θ are used. A ratio is then formed from the unsteady loss coefficient and the steady loss coefficient at the same mean incidence. This ratio calculated from the data for the sinusoidal distortions is presented in Figure 48 as a function of reduced frequency. It should be noted that the reduced frequency for steady uniform flow is zero.

In Figure 48, it is found that the unsteady losses are highly dependent on the reduced frequency. It is also observed that the unsteady losses reach a maximum at low values of reduced frequency and, in some cases, the peak unsteady losses are greater than three times the losses in steady flow. Kirillov et al. [22] observed a similar peak at low frequencies, but in their case, part of the change with respect to frequency was due to a change in the flow nonuniformity as the frequency changed. Additional experimental and analytical work is required to

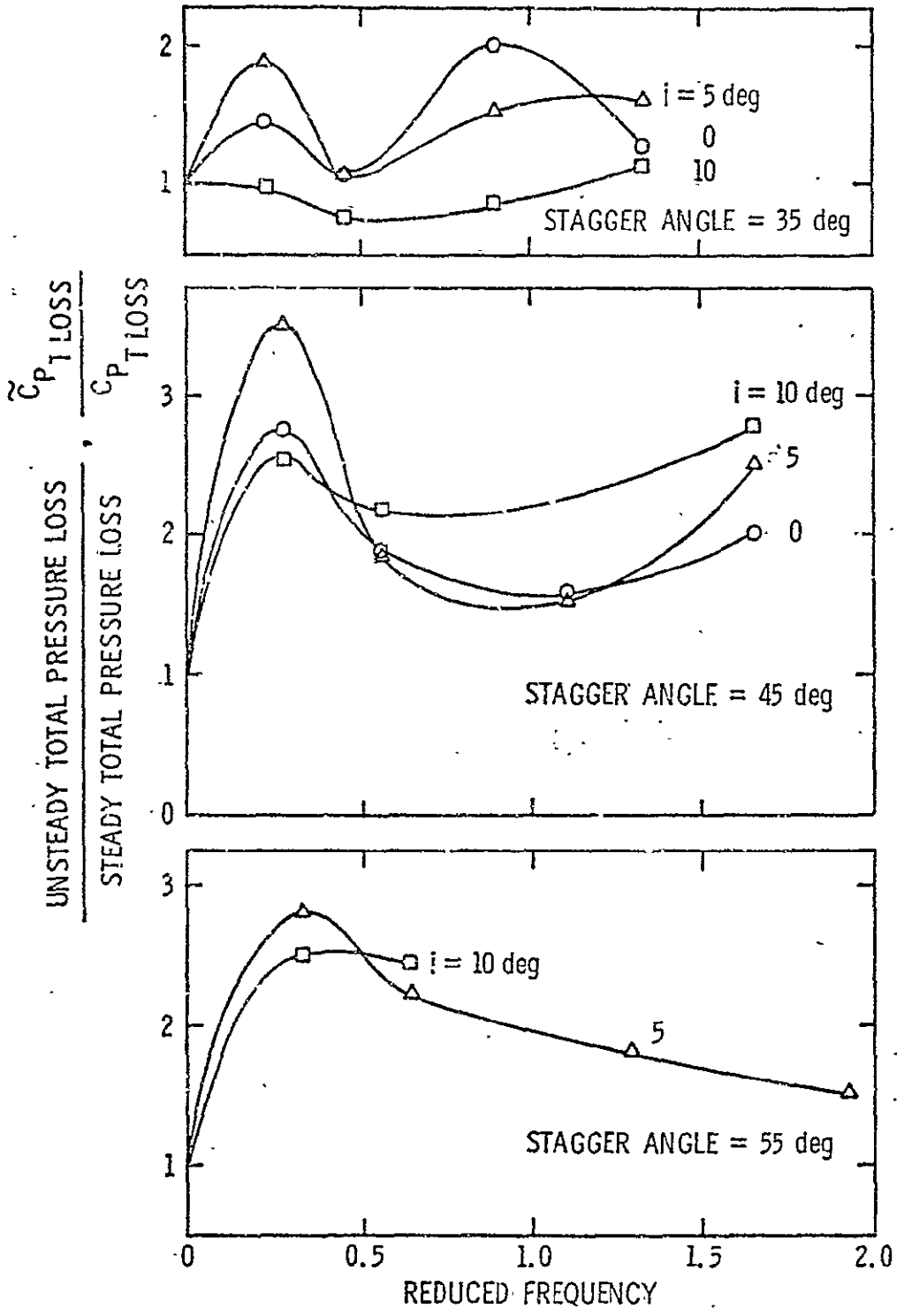

Figure 48. Ratio of unsteady loss to steady loss versus reduced frequency.

identify the causes of the unsteady losses and to explain the dependency on frequency.

For the square distortions, the unsteady losses in most cases were found to be much greater than the losses in steady flow. However, no consistent trends in the losses were observed with respect to changes in blade loading, width of the distortion, or stagger angle. Because there are no observable trends, the validity of the loss data for the square distortions is questioned. A radial shift in streamlines, which is suspected in causing the amplification of the square distortion upstream of the rotor, could seriously affect the loss measurement made at only one radius and, thus, yield misleading results. In a flow where a radial shift in the streamlines occurs, radial and circumferential surveys of the flow are required, and the data should then be energy or mass averaged. A mass average could have been used in calculating the unsteady losses for the sinusoidal distortions, but with the radial variations unknown, the additional complexity in the calculation was not justified. Future studies with regard to the proper averaging technique should be conducted.

CHAPTER VII

SUMMARY, CONCLUSIONS, AND RECOMMENDATIONS FOR FUTURE RESEARCH

7.1 Summary and Conclusions

A systematic study of the effects of blade stagger angle, mean loading, and distortion characteristics on the flow fields upstream and downstream of an isolated rotor has been conducted. One objective of this study was to provide a data base which demonstrates the effects of the above parameters. The data base is to be used in future studies conducted to obtain better understanding of distortion phenomena and to improve current prediction techniques. This objective has been met, and a complete set of the data can be found in Reference [19]. The study has also revealed several key parameters affecting distortion attenuation and unsteady losses, which should provide guidance for conducting future experimental and analytical studies where they will yield the most beneficial results.

The following specific conclusions can also be made from the research conducted with the isolated rotor:

1. The incidence or mean loading was found to have very little effect on the distortion attenuation. This is probably partially due to the linearity of the steady performance characteristics of the rotor. For a rotor with a non-linear performance curve, the influence of blade loading would probably be more significant.
2. Increasing the blade stagger angle (ξ) or increasing the reduced frequency (ω) were both found to result in an increased attenuation of the sinusoidal

distortions. At the higher values of incidence, however, the effects of stagger angle are minimal. It should also be noted that the stagger angle is contained in the definition of ω, and an increase in ξ will increase ω. The stagger angle, therefore, appears to play a double role, and it may be a very important parameter influencing the attenuation of a distortion. It is not known from the present study, however, whether ξ is a governing factor in the influence ω was shown to have on the attenuation.

3. The measured attenuation of the sinusoidal distortions was found to be much greater than the attenuation predicted by an inviscid, quasi-steady, linear actuator disc model. As previously noted, the attenuation was also found to increase with ω, and, thus, the additional attenuation can be contributed to either an unsteady blade response or turbulent mixing which is frequency dependent. Since the additional attenuation above that which is predicted is of the same order of magnitude as the prediction, this additional attenuation is very important and the mechanism causing it should be found. A very important observation from the present study is that no significant amount of turbulent mixing is present between Locations 1-D and 15 without the rotor installed. Therefore, if turbulent mixing is causing the increased attenuation, the turbulence is introduced by the rotor.

4. The most significant characteristic of the square distortion data is the appearance that the 90° distortion is attenuated more than the 180° distortion. However, before this conclusion is valid, the amplification of the total pressure distortion upstream of the rotor must be investigated.

5. The operation of a rotor in a distorted flow field was found to result in total pressure losses greater than those measured with the rotor operating in a uniform flow. The magnitudes of these unsteady losses were in some cases found to be twice as large as the steady losses. The unsteady losses were also found to be highly dependent on the reduced frequency and, in most cases, a maximum occurred at low values of ω. However, in the present study, the flow was assumed to be two-dimensional. Since radial shifts in the streamlines could yield misleading results, the unsteady loss data from the present study should be interpreted with care. If future studies, which include or completely eliminate three-dimensional effects (not neglect them), should verify a peak in the losses at low values of ω, high attenuation and low unsteady losses would not be incompatible. In other words, a distortion could be greatly attenuated without suffering severely from unsteady losses.

similar analysis could be used as a starting point for a study of the observed phenomena in the AFRF. However, Mokelke's turbulent model did not include the turbulence introduced by the blades. In this study, it is known that no significant turbulent mixing occurs without the rotor installed; thus, if turbulent mixing is significant, it must be caused by the rotor. Experimentally, the effect of turbulent mixing could be studied by artificially changing the size of the blade wakes, and then correlating the size of the wakes and the turbulence intensity with the attenuation observed. Wake size and turbulence measurements would be made with hot-wire anemometers. For a study of the effects of unsteady blade response, experimental unsteady force and moment data, which exists for the blades of the AFRF, could perhaps be included in a model of the flow. The contribution of the unsteady blade response on the attenuation could then be evaluated.

The third recommendation for future study is an investigation of the effects the parameters in the reduced frequency have on the distortion attenuation. From the definition of the reduced frequency, it is seen that ω contains the blade chord length, the distortion wave length, and the blade stagger angle. A designer who may want to apply the attenuation data, however, only has control over the blade chord length and stagger angle. If the dominate variable determining the attenuation is the distortion wave length, the large increase of attenuation with ω cannot be advantageously employed. Therefore, the question arises as to what effects the chord length and stagger angle have on the distortion attenuation. The present study has shown that the influence of stagger angle is dependent on blade loading, but in most cases, larger stagger angles resulted in greater attenuation. The effect of chord length still needs to be evaluated.

The final topic where extensive research is needed is the area of unsteady losses. The present study has revealed that the losses associated with nonuniform inlet flow are quite significant. Since turbomachines usually operate in nonuniform flow, the minimization of the unsteady losses could improve the efficiency of the machine. However, considerable research determining the sources of the losses and research evaluating the effect design variables have on the losses are required. Part of the unsteady losses may be due to the turbulent mixing in the distorted flow. Other possible sources of losses are local regions of flow separation and vortex shedding due to the unsteady blade circulation. The contributions of these sources should be evaluated.

The ideal way to study unsteady losses would be to conduct tests in a two-dimensional cascade. However, a means of producing a distorted flow which correctly models the flow in a rotating machine is required. Data could then be obtained similar to the massive amount of cascade data currently available and used for steady designs of turbomachines. If a proper method of producing an unsteady flow in a two-dimensional cascade cannot be found, circumferential surveys in a rotating blade row will be required at several radial locations both upstream and downstream of the blade row. With the complete flow field known, mass averaged data can be used to evaluate the unsteady losses. For studies conducted in the AFRF, it may be necessary to eliminate the auxiliary fan, since it is suspected that the auxiliary fan may alter the stall characteristics of the test rotor.

As a closing remark, in general, the long range goals of future research in the field of distorted inlet flow and unsteady aerodynamics

is to provide data and an understanding of compressor stability, noise, distortion attenuation, unsteady losses, and the unsteady blade forces. When sufficient knowledge is gained, all of the above factors can be combined in an optimum unsteady design of a turbomachine. Studies will also be required in determining the compatibility of an optimum unsteady design and the optimum steady design.

REFERENCES

1. Fuhs, A. E., "Introduction to Distortion Induced Engine Instability," Advisory Group for Aerospace Research and Development, AGARD-LS-72, National Technical Information Service No. AD-A008-587, 1974, pp. 1-1 to 1-19.

2. von Karman, T. and W. R. Sears, "Airfoil Theory for Non-Uniform Motion," Journal of Aeronautical Sciences, Vol. 5, No. 10, Aug. 1938, pp. 379-390.

3. Kemp, N. H. and W. R. Sears, "Aerodynamic Interference Between Moving Blade Rows," Journal of Aeronautical Sciences, Vol. 20, No. 9, Sept. 1953, pp. 585-597.

4. Horlock, J. H., "Fluctuating Lift Forces on Aerofoils Moving Through Transverse and Chordwise Gusts," Transactions of ASME, Journal of Basic Engineering, Dec. 1968, pp. 494-500.

5. Naumann, H. and H. Yeh, "Lift and Pressure Fluctuations of a Cambered Airfoil Under Periodic Gusts and Application in Turbomachinery," ASME Transactions, Journal of Engineering for Power, Vol. 95A, 1973, pp. 1-10.

6. Whitehead, D. S., "Force and Moment Coefficients for Vibrating Aerofoils in Cascade," Aeronautical Research Council, ARC R&M 3254, Feb. 1960.

7. Henderson, R. E. and H. Daneshyar, "Theoretical Analysis of Fluctuating Lift on the Rotor of an Axial Turbomachine," Aeronautical Resarch Council, ARC R&M 3684, Sept. 1971.

8. Mokelke, H., "Prediction Techniques," Advisory Group for Aerospace Research and Development, AGARD-LS-72, National Technical Information Service No. AD-A008-587, 1974, pp. 5-1 to 5-32.

9. Henderson, R. E., "The Unsteady Response of a Blade Row from Measurements of the Time-Mean Total Pressure," Presented at ASME Gas Turbine Conference, ASME Paper 73-GT-94, Apr. 1973.

10. Greitzer, E. M., "A Note on Compressor Exit Static Pressure Maldistributions in Asymmetric Flow," University of Cambridge Department of Engineering, CUED/A-Turbo/TR 79, 1976.

11. Treaster, A. L., "The Calibration of Six Probes for Sensing Three-Dimensional Fluid Flow Properties," Applied Research Laboratory TM 74-282, The Pennsylvania State University, Oct. 1974.

12. Hale, M. R. and D. H. Norrie, "The Analysis and Calibration of the Five-Hole Spherical Pitot," Presented at the ASME Winter Annual Meeting and Energy Systems Exposition, ASME Paper No. 67-WA/FE-24, Nov. 1967.

13. Krause, L. N. and T. J. Dudzinski, "Flow-Direction Measurement with Fixed-Position Probes in Subsonic Flows over a Range of Reynolds Numbers," NASA TM X-52576, May 1969.

14. Nilsen, A. W., "Analysis of the Unsteady-Pressures in a Turbulent Jet," A Thesis in Aerospace Engineering, The Pennsylvania State University, Sept. 1969.

15. Bruce, E. P., "The ARL Axial-Flow Research Fan--A New Facility for Investigation of Time-Dependent Turbomachinery Flows," Paper presented at the Joint Fluids Engineering & CSME Conference, Montreal, Quebec, Canada, ASCE Paper No. 74-FE-27, May 1974.

16. McCarthy, J. H., "Steady Flow Past Non-Uniform Wire Grids," Journal of Fluid Mechanics, Vol. 19, 1964, pp. 491-512.

17. Bruce, E. P., "Design and Evaluation of Screens to Produce Multi-Cycle ±20% Amplitude Sinusoidal Velocity Profiles," Paper presented at the AIAA 8th Aerodynamic Testing Conference, Bethesda, Md., AIAA Paper No. 74-623, July 1974.

18. Horlock, J. H., Axial Flow Compressors, Fluid Mechanics and Thermodynamics, Huntington, N.Y.: Robert E. Krieger Publishing Co., 1973.

19. Yocum, A. M., "Measurements of Flow Distortions in an Axial Flow Fan," Applied Research Laboratory TM 78-193, The Pennsylvania State University, July 1978.

20. Mokelke, H., "Circumferential Inlet Flow Distortions in Multi-Stage Axial Compressors," Ph.D. Thesis, University of Cambridge, 1974.

21. Yurinskiy, V. T. and I. Ya. Shestachenko, "Losses in an Impulse Turbine Cascade in an Unsteady Flow," Fluid Mechanics-Soviet Research, Vol. 3, No. 1, 1974.

22. Kirillov, I. I., A. S. Laskin, and G. G. Shpenzer, "Influence of Unsteadiness of the Flow in Efficiency of Turbine Stages," Teploenergetika, Vol. 17, No. 10, 1970.

23. Samoilovich, G. S. and L. D. Yablokov, "Profile Losses with Unsteady Flow Through Turbomachine Cascades," Teploenergetika, Vol. 18, No. 4, 1971.

APPENDIX A

PROBE CALIBRATION

The purpose of this appendix is to present the details of the calibrations which were performed for the two United Sensor five-hole probes. The reasons for selecting this type of probe, a description of the probe geometry, and a brief outline of the probe calibration and its use were given in Chapter IV. This appendix will go into more detail of the preliminary analysis, describe the apparatus and procedures used for calibrating the probes, and will discuss the nature of the results in more detail. The methods used for applying the data obtained from the Reynolds number and wall interference studies are also presented.

A.1 Calibration Analysis

The five-hole probes employed in this study were used in a non-nulling mode. This means that relationships must be found between the pressures from the five holes and the true total and static pressure or velocity. The desired relationships are usually expressed as dimensionless pressure coefficients, which will be a function of the flow angularity. Since, when in use, the flow angles are unknown, relationships between the probe pressure and the flow direction are also required.

The determination of the necessary relationships by analytical techniques would be worthwhile; however, in most cases, the use of analytical techniques is not possible. For probes of spherical geometry, a potential flow solution can predict the pressure distribution and, thus, the probes' characteristics quite reasonably.

However, due to manufacturing inaccuracies, and also to obtain the desired operating range and accuracy required in the laboratory, calibrations are necessary even for probes of this simple geometry. For the more complex geometry of a prism probe with which viscous effects will play a significant role, analytical techniques of any value are impossible. For this reason, the only mathematical considerations which must be made at this stage are the ways in which to best represent the probe's characteristics.

In some previous studies, coefficients have been formed which contain the velocity; thus, with additional coefficients relating the flow angles to the probe pressures, the velocity and its components can be calculated directly [12]. However, in this study, as in many situations, the total and static pressure are also of interest. Therefore, the approach was taken to determine the total and static pressure through the probe calibration, and then, after calculating the velocity by using the Bernoulli equation, the velocity components are determined from the known flow angles which were also obtained through the calibration data. Since there are four unknown quantities, four pressure coefficients will be necessary to relate the total and static pressure and the two flow angles to the measured probe pressures.

Before defining the necessary pressure coefficients, the references used for measuring the flow angles and the terminology employed should be described. The two reference planes referred to as the yaw and pitch planes are sketched in Figure A.1, with their orientation with respect to the probe shown. The pitch plane contains the axis of the probe. In the pitch plane, the reference line from which the pitch angle (γ) is measured was chosen to be perpendicular to the planes

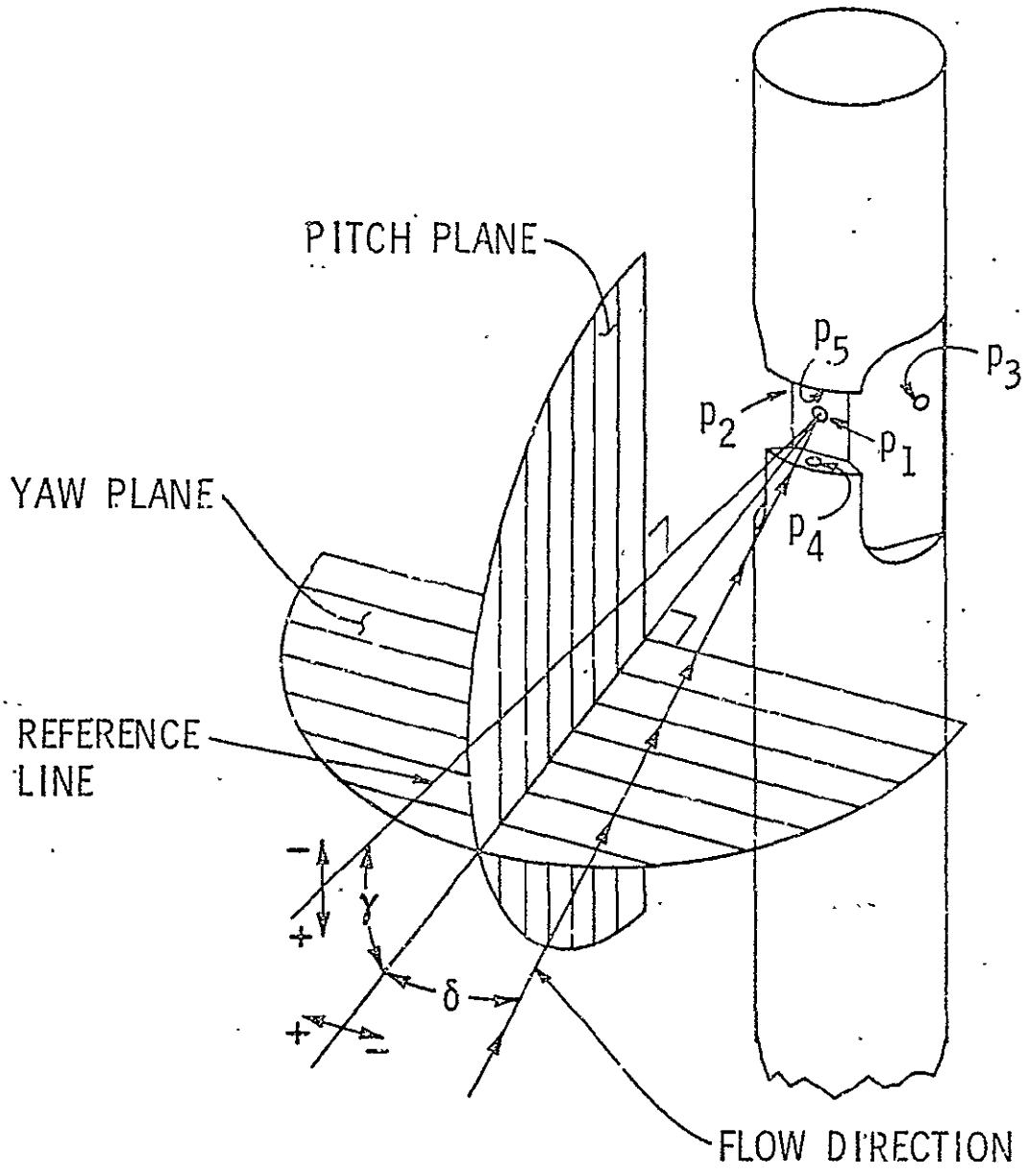

Figure A.1. A schematic of the probe tip defining the reference planes and the flow angles measured.

containing the sides of the circular block at the end of the probe. These surfaces and the axis of the probe thus serve as a physical reference for aligning the probe and measuring the flow angles. The yaw angle (δ) is measured in a plane aligned with the flow in the pitch direction and perpendicular to the pitch plane.

The orientation of the two planes with respect to each other was necessitated by the type of device which was used for positioning the probes when they were calibrated. This device was used in a uniform flow field and was capable of rotating the probe about its axis, corresponding to a change in yaw angle, and then tilting the probe forward or backward, corresponding to a change in pitch angle. Obviously, using the same device in the reverse order would yield the same probe orientation. However, in this case, after tilting the probe, the rotation is no longer around the probe's axis Thus, the other possible type of device would have to tilt the probe and still rotate the probe about its axis. This type of device would result in a different probe orientation with the flow and would yield the only other possible orientation of the reference planes.

It should be mentioned that the selection of the probe axis and the block on which the take-off tubes are mounted as alignment references was based primarily on convenience. It may be thought that a more accurate reference could be obtained by first balancing the pressures from Holes 2 and 3, and Holes 4 and 5. Although the balanced condition could be used as a reference, this reference would require in each experimental setup a flow of known direction in order to determine the relation between the measured flow angles and the physical boundaries of the system. Since a condition of known flow cannot be obtained in

every experimental situation, it is far better to use a consistent physical reference on the probe for both calibration and usage. The references selected in this case will differ from the balanced condition only by the pressure differences caused by manufacturing inaccuracies in the location of the holes and the probe construction.

With the angular references chosen, and the pressure from each hole identified as shown in Figure A.1, the pressure coefficients can be defined. For the total and static pressure, the purpose of the pressure coefficients is to relate the true pressures to the total and static pressure indicated by the probe. The center hole, or Hole 1, senses the true total pressure if the probe is aligned with flow but deviates slightly from the true value for non-zero flow angles. For this reason, the pressure sensed by the center hole is defined as the indicated total pressure when calibrating five-hole probes.

Unlike the ability of the center hole to accurately indicate total pressure, the pressures sensed by the surrounding four holes vary greatly with flow angle, and no single hole will indicate true static pressure. The pressure from these holes may be much less than the local static pressure, due to the acceleration of the flow around the probe, or may be much larger than the local static pressure if the holes are partially aligned with the flow. Due to the large amount of variation sensed by each individual hole, the arithmetic average pressure from Holes 2, 3, 4, and 5 is used as the indicated static pressure.

Static and total pressure coefficients are formed by normalizing the difference between the indicated and true values of pressure by a suitable parameter, such that the resulting coefficient is approximately independent of velocity or Reynolds number. Since the normalizing

parameter must be formed from quantities which are known when the probe is in use, the pressures from the probe must be used. With the indicated total and static pressure already defined, the difference between these values will provide an indicated dynamic pressure which is similar to the conventional $\frac{1}{2}\rho v^2$ commonly used to non-dimensionalize pressure quantities. With this in mind, the following definitions for the total and static pressure coefficients are given:

$$C_{p\ total} = \frac{p_1 - p_T}{p_1 - 1/4(p_2 + p_3 + p_4 + p_5)} \qquad (A.1)$$

and

$$C_{p\ static} = \frac{1/4(p_2 + p_3 + p_4 + p_5) - p_s}{p_1 - 1/4(p_2 + p_3 + p_4 + p_5)}, \qquad (A.2)$$

where p_T and p_s are the true values of total and static pressure, respectively.

The physical reasoning for using the difference between the indicated total and static pressure as a normalizing parameters was given above. It should also be mentioned that the authors of Reference [13] found that this normalizing quantity reduced the random scatter of the data they obtained for probes of an angle tube design. This serves as additional justification for normalizing the data in this manner.

In addition to the previously defined coefficients, two other pressure coefficients are necessary to relate the flow angles to the probe pressures. When considering the manner in which three-dimensional probes are used in the nulling mode, instead of balancing the pressures from the two holes in the pitch and yaw planes, it becomes apparent

that a pressure coefficient based on the pressure difference between the two holes could be formed. Normalizing these pressure differences with the same quantity as above results in the following definitions for the yaw and pitch pressure coefficients:

$$C_{p\,yaw} = \frac{p_2 - p_3}{p_1 - 1/4(p_2 + p_3 + p_4 + p_5)} \tag{A.3}$$

and

$$C_{p\,pitch} = \frac{p_5 - p_4}{p_1 - 1/4(p_2 + p_3 + p_4 + p_5)} \tag{A.4}$$

It is worthwhile to note, at this point, that three coefficients similar to the ones defined for the five-hole probes can be defined for two-dimensional, three-hole probes. However, a previous study has found that the static pressure coefficient will vary significantly with flow variations in the plane in which no measurements are taken [13]. Therefore, it may be advantageous to employ five-hole probes, even if only the two-dimensional characteristics are of concern, in order to improve the accuracy of the static pressure measurements.

Before concluding this section on the calibration analysis, two problems which can be encountered with five-hole probes will be mentioned. It has been found that the pressure coefficients defined by Equations (A.1), (A.2), (A.3), and (A.4), and particularly the static pressure coefficient, will vary with changes in Reynolds number. If the velocity or Reynolds number variation is small, this effect usually can be neglected. However, for larger changes, it may be necessary to obtain several calibrations at various Reynolds numbers. The effect

of varying Reynolds number was investigated in this study by obtaining calibrations at several free-stream velocities. With these data, average corrections could be calculated and applied to the results.

One other problem, not necessarily unique with five-hole probes, is the interference effect caused when the probe approaches a solid boundary. For the case of a five-hole probe, the shift in streamlines caused by a wall could result in errors in the flow direction as well as the pressure measurements. The effect of a solid boundary was investigated by mounting a flat plate in the calibration facility and obtaining calibration data as a function of the distance between the probe tip and the plate. The data obtained in this manner can be used to make corrections, which will be discussed at a later point in this appendix.

A.2 Apparatus and Procedure

The two United Sensor five-hole probes were calibrated in the 12-in. (30.48 cm) open air jet facility at the Applied Research Laboratory of The Pennsylvania State University. This facility is shown schematically in Figure A.2 along with the instrumentation used in the calibration. The jet facility consists of a 21.25-in. (53.975 cm) diameter axial flow fan, a circular to square transition section, a wide-angle screened diffuser, a plenum chamber, and a nozzle [14]. The velocity of the flow can be varied between approximately 20 to 120 ft/sec (6.1 to 36.6 m/sec) by changing the fan speed, which is controlled by a Borg-Warner variable frequency power supply.

The facility and the flow characteristics of the jet are described in Reference [14]. Of particular concern in the calibration process is the uniformity of the flow and the ranges where uniform flow exists.

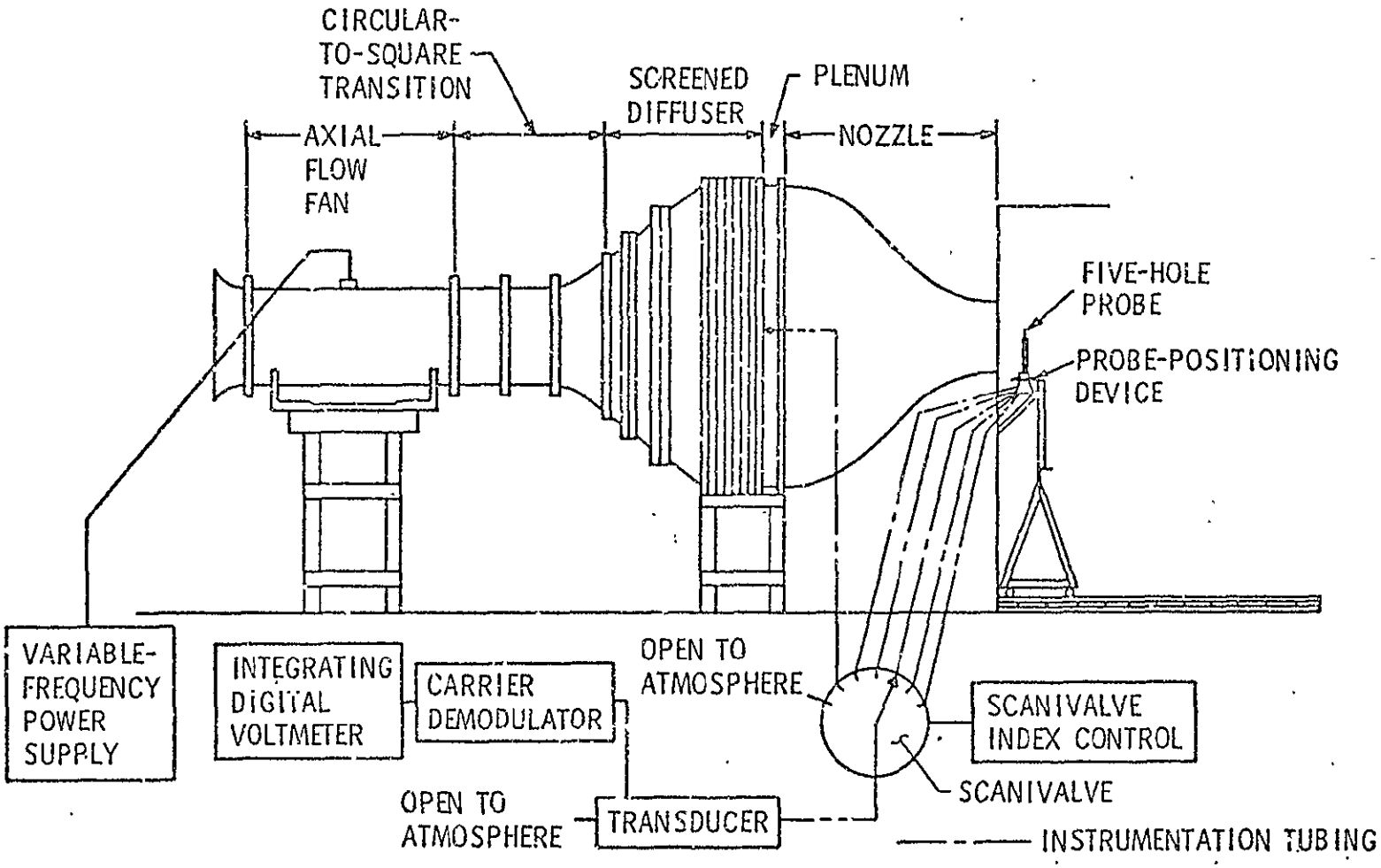

Figure A.2. A schematic of the open air jet facility and the instrumentation used for calibrating the five-hole probes.

Uniform flow is necessary, since, with the type of probe positioning device used, the probe will change locations in the flow field. The information in Reference [14] verifies that the flow is symmetrical about the jet axis and uniform within the potential core. With this knowledge, it was made certain that the probe was always located within the potential core of the jet during the calibrations.

A sketch of the probe positioning device used for the calibrations is shown in Figure A.3. This device is capable of providing variations in both the yaw and pitch angles within the range of ±30°. Yaw variation is obtained by rotating the entire device relative to the rectangular support member shown in the figure. The pitch angle can be changed by tilting the probe support tube in which the probe is mounted.

The measurements necessary for the calibration of the probes are the true total and static pressure in the jet and the five pressures from the probe. As shown in Figure A.2, all pressure measurements were made with a single variable reluctance pressure transducer through the use of a scanivalve. Since this type of transducer can only measure a pressure difference, another pressure must serve as a reference, and the ambient pressure was, therefore, used for this purpose. The voltage output from the transducer system was measured with an integrating digital voltmeter.

The total pressure was measured from a static wall tap in the plenum section where the velocity is almost zero. It was found, however, that this pressure was approximately 1.58% higher than the true total pressure measured in the jet with a pitot tube. Since the neglected dynamic pressure in the plenum section would result in the opposite trend being observed, the reduction in the measured pressure between

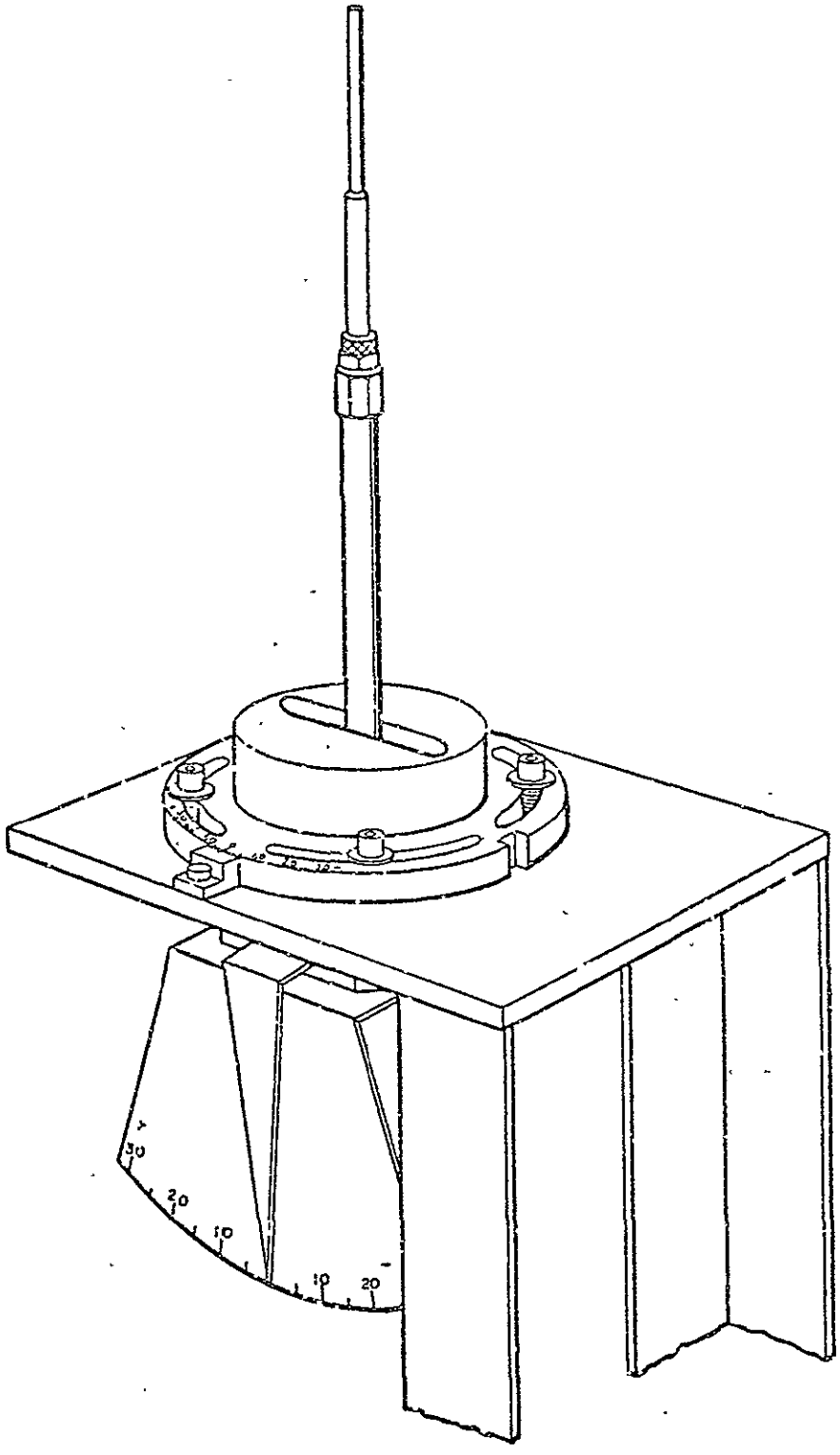

Figure A.3. A sketch of the probe calibration positioning device.

the plenum and the exit must be due to turbulent mixing losses. The measurement made at the plenum was, therefore, corrected for this effect.

The true static pressure in the jet is equal to atmospheric pressure, since the pressure ratio for the nozzle is far below the critical pressure ratio. The static pressure was, therefore, measured through an open tube on the scanivalve, and, since the ambient pressure is used as a reference, the static pressure measurement corresponded to the transducer zero. This voltage output was periodically modified to assure that the proper transducer zero was being maintained.

At the beginning of each calibration, the probe was mounted in the positioning device in a vertical position, with the previously mentioned probe references parallel to the exit plane of the nozzle. The ambient temperature and pressure were then measured before the start of the test. These values were used to obtain the air density and viscosity and, thus, enable the Reynolds number to be calculated. It should be noted that the absolute pressure is not needed for the calibration pressure coefficients, since it is apparent from the definitions of the coefficients that any reference pressure will cancel out of the equations.

With the probe properly mounted and the preliminary measurements taken, the procedure followed for the general calibration consisted simply of positioning the probe and recording the seven pressures. The yaw angle was varied in 10° increments and the pitch angle in 5° increments between plus and minus 30°, thus yielding 91 calibration points. The 5° pitch angle increment was selected since the static pressure coefficient was found to exhibit sharp variations and,

therefore, more points were necessary to describe the probe's characteristics. For this same reason, a smaller yaw angle increment might also have been used, but this would have resulted in an excessive amount of data to obtain and also to use in subsequent data reduction programs.

The two probes were each calibrated, with the previous procedure, three times to verify the data and also to help eliminate some of the experimental errors by averaging the results. For these tests, the jet velocity was approximately 110 ft/sec (33.5 m/sec), resulting in a Reynolds number based on the probe tip diameter of approximately 7000.

In addition to the general calibrations, five calibrations for each probe examining the effect of Reynolds number variation were also performed. These tests were conducted with jet velocities which yielded Reynolds numbers of approximately 2000, 3000, 4000, 5000, and 6000. The procedure was similar to the general calibrations, except that the pitch angle increment was also chosen at 10°.

One other phenomenon was also investigated at this stage, so the characteristics of the probe could be understood under all operating conditions. The effect of the proximity of a solid boundary was investigated by mounting a flat plate across the exit of the jet and recording the probe's response as a function of distance to the plate and the yaw angle. The two configurations tested are shown schematically in Figure A.4.

It is obvious from the schematic of the probe through the plate that pitch angle variation was not possible with the present apparatus. Although the pitch angle could be varied with the probe approaching the

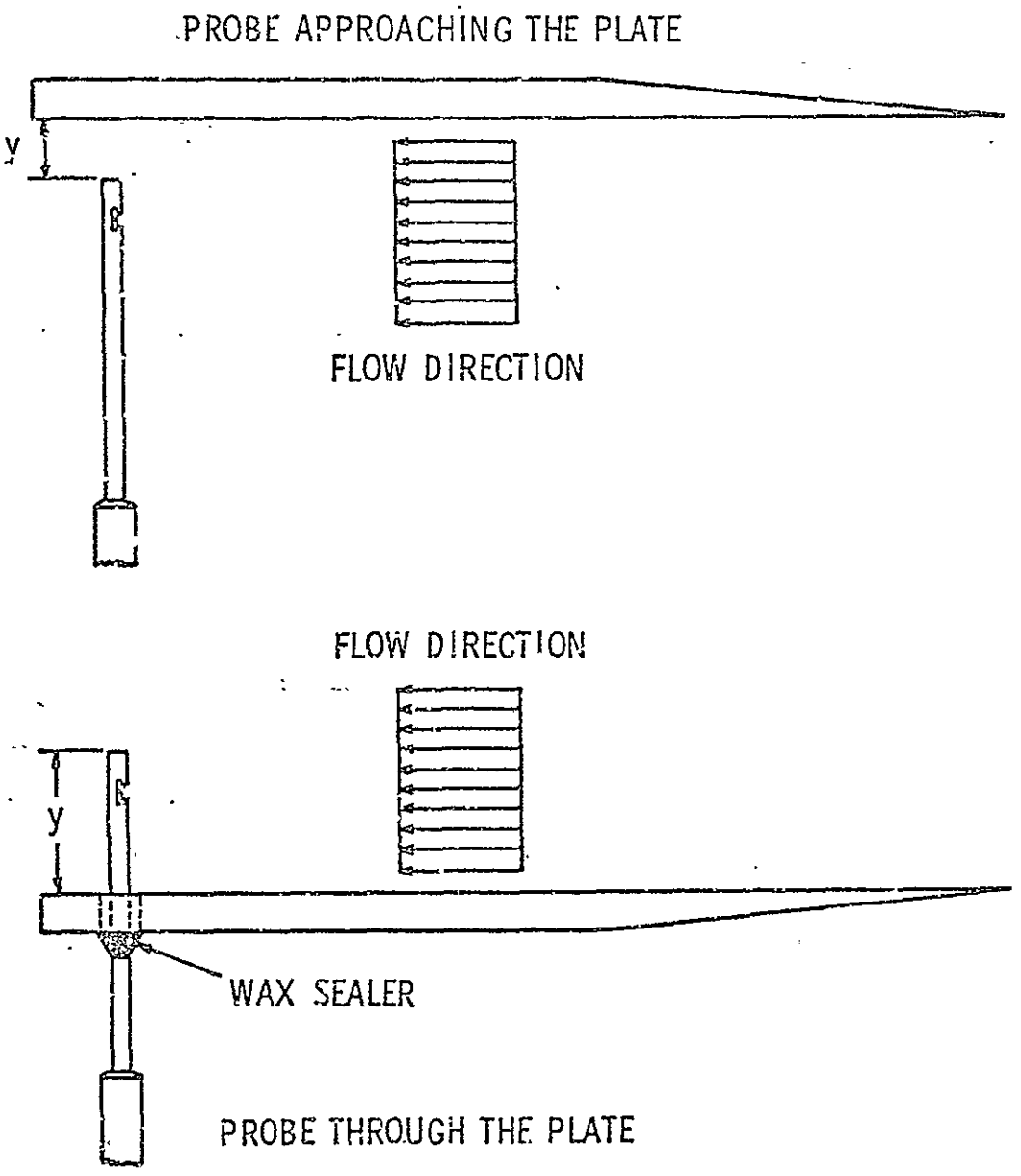

Figure A.4. A schematic of the two test configurations tested to determine the effect of a solid boundary on the probe's response.

wall, the orientation of the probe with respect to the plate would also change, thus introducing another variable into the test. For these reasons, only the yaw angle was varied.

The procedure followed for the calibrations with the plate consisted first of mounting the probe at a given distance from the plate, with the probe aligned in the same manner as for the previous tests. The increments for the change in the distance were selected so that the measurement stations were closer together near the plate. The yaw angle was then varied between ±30° in 10° increments, and the seven pressures were recorded for each position. The jet velocity for these tests was approximately the same as for the general calibrations, 110 ft/sec (33.5 m/sec).

A.3 Results and Discussion

The calibration results for the probe used downstream of the rotor are presented in Figures A.5 through A.7 and will serve as a reference for further discussion. Similar results for the other probe were presented in Chapter IV. Since three basic calibrations were performed for each probe, the results plotted in the figures are the arithmetic average of the three calibrations. These are the results which were used for reducing data from the fan.

Since the calibration data have no purpose other than enabling the flow angles and total and static pressure to be calculated, the primary requirement of the data is that it be repeatable. Initially, after examining the irregular nature of the static pressure coefficient, the repeatability of the data was questioned, since it was not known whether the observed nature of the static pressure coefficient was due to random scatter or the actual steady response of the probe. It was for this

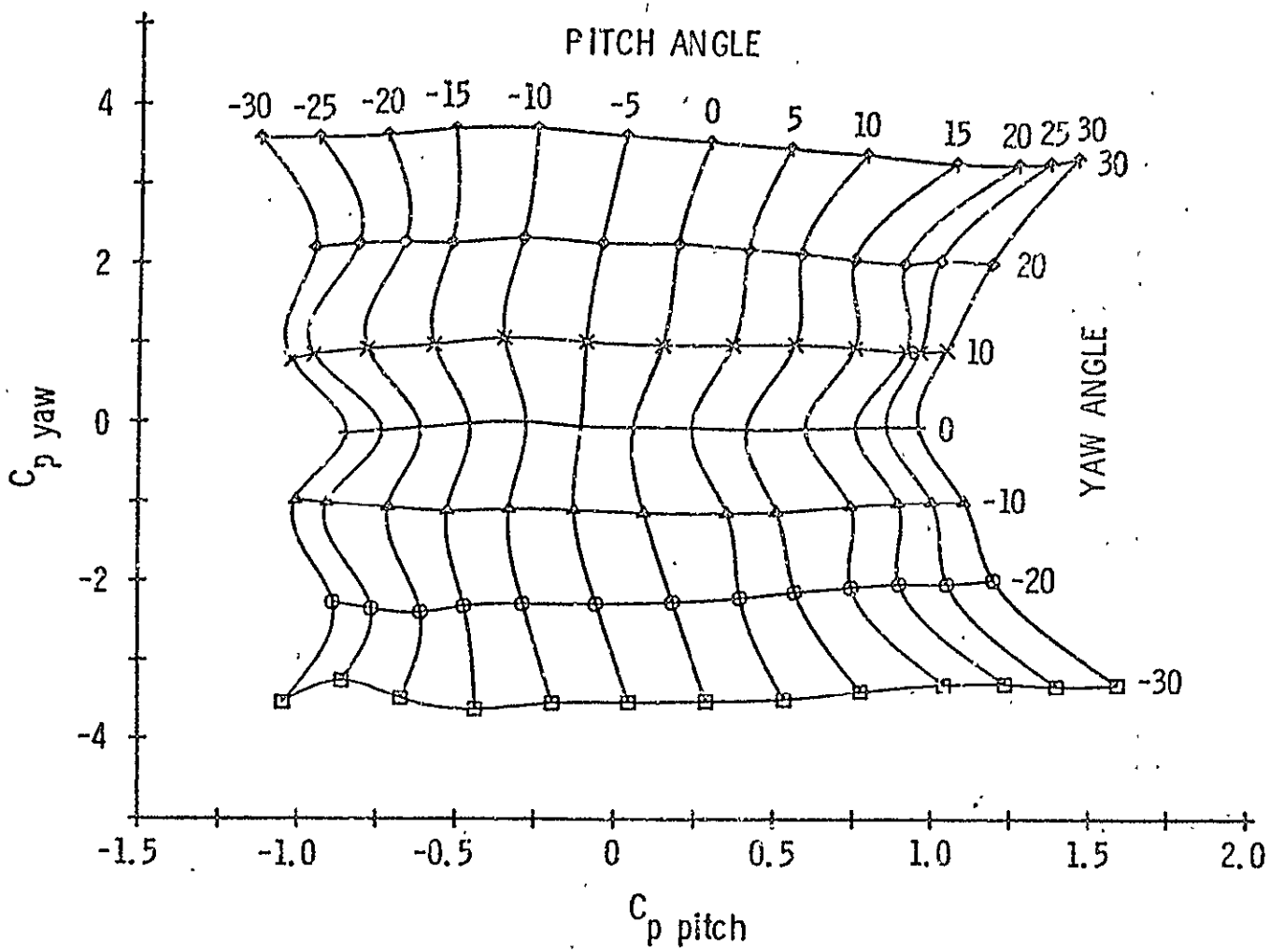

Figure A.5. Calibration data for Probe 2, $C_{p\ yaw}$ versus $C_{p\ pitch}$.

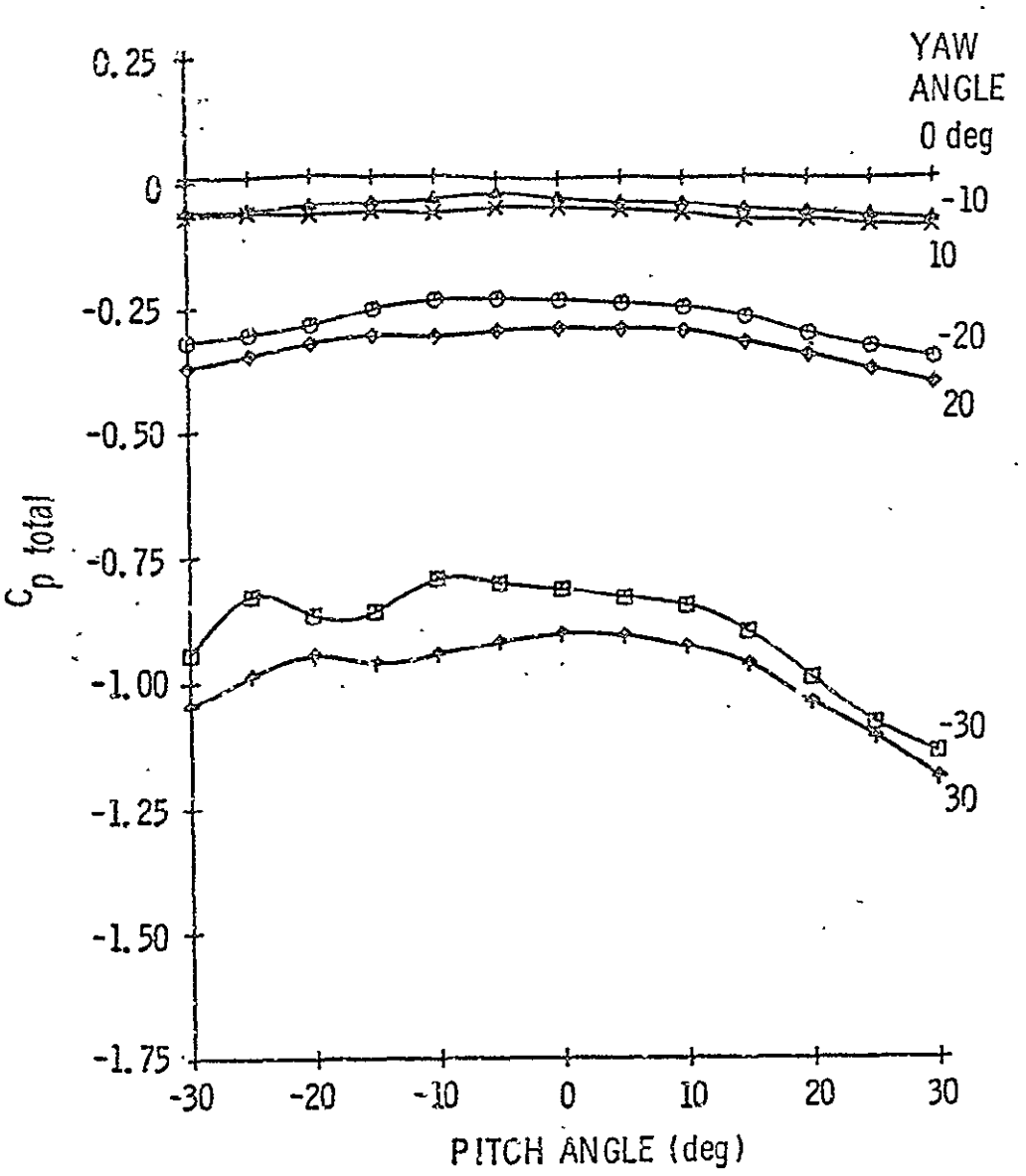

Figure A.6. Calibration data for Probe 2, $C_{p\ total}$ versus pitch angle.

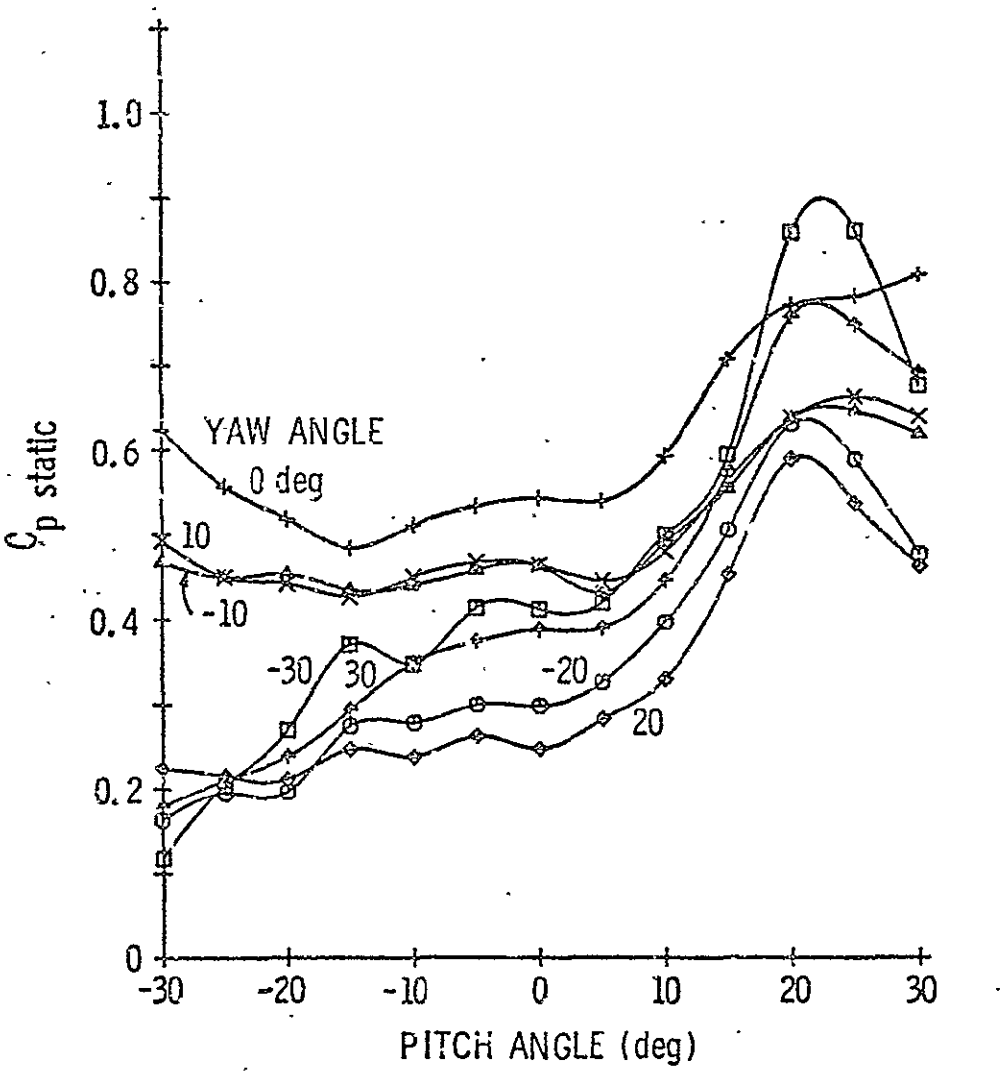

Figure A.7. Calibration data for Probe 2, $C_{p\ static}$ versus pitch angle.

reason, and also to eliminate some of the experimental error, that the probes were calibrated three times.

The results from the three calibrations revealed that the data were quite repeatable. To quantitatively demonstrate this repeatability, the difference between the coefficients for a particular test and the average values were calculated and expressed as a percentage of the maximum absolute value of that particular coefficient. For example, the percent deviation in the static pressure coefficient can be written as:

$$\text{Percent deviation} = \frac{C_{p\,\text{static}} - C_{p\,\text{static}_{\text{average}}}}{\text{Maximum} \left| C_{p\,\text{static}_{\text{average}}} \right|} \times 100\% \,. \qquad \text{(A.5)}$$

The preceding approach was taken since insufficient data existed for a statistical analysis. However, with the deviation defined in this manner, the scatter of the data was usually found to be less than 1%. Presenting the worst case, which occurred for the static pressure coefficient of Probe 2*, only 19% of the data deviated from their respective averages by more than 1%, less than 2% of the data deviated by more than 3%, and no data deviated by more than 5%. This high degree of repeatability demonstrates that this type of probe can be used quite accurately in the nonnulling mode and also demonstrates the degree of precision in the experimental procedure.

With the data found to be quite repeatable, the shapes of the calibration curves are not important. However, it is worthwhile to

---

*The number 2 refers to the last number of the probe serial number.

examine the characteristics of the curves to obtain some insight into what to expect when using the probes and also to assure that sufficient data exists to adequately describe the probe's response. Referring to Figure A.5, one obvious characteristic of the yaw and pitch coefficient data is the different ranges in the values of these coefficients. It is seen, by noting the different scales in Figure A.5, that the pitch coefficient has only about half the range that the yaw coefficient has. When using the probes, the smaller range for the pitch coefficient means that slight variations in the pitch coefficient due to flow turbulence or measurement inaccuracies will result in a significant change in the calculated pitch angle. For this reason, the probe can be expected to be very sensitive to flow variations in the pitch plane, and scatter in the resulting velocity component will probably be observed.

The reason for the difference in the range of the pitch and yaw coefficients is due to the different types of surfaces on which the holes in the pitch and yaw planes are located. Holes 4 and 5 in the pitch plane are located on surfaces perpendicular to the axis of the probe. Therefore, when large pitch angles exist, one hole will be located in a region of flow which has separated from the outer edge of the prism, while the other hole will be more aligned with the flow sensing a pressure nearer the free-stream total pressure. Since some pressure recovery occurs in a separated region, the hole in this zone will sense a pressure greater than the free-stream static pressure, and the resulting pressure difference between Holes 4 and 5 will be less than the dynamic pressure of the flow.

Holes 2 and 3 in the yaw plane have a different response. For large yaw angles, once again one hole is approximately aligned with

the flow and senses a pressure near the free-stream total pressure. However, the other hole is positioned around the side of the probe and, therefore, senses a pressure less than the free-stream static pressure, since a static pressure drop occurs as the flow accelerates around the probe. For this reason, the pressure difference between Holes 2 and 3 will be greater than the dynamic pressure of the flow, and the absolute value of the resulting yaw coefficient based on this pressure difference will be much greater than the pitch coefficient obtained for an equivalent pitch angle. Although the small range in pitch coefficient is undesirable, the present probes were selected for their convenience in inserting the probes into the Axial Flow Research Fan, which necessitated the particular probe geometry used. The expected scatter in the calculated pitch angle should not be a serious drawback, since the radial velocity component in the AFRF is not of primary concern.

Other characteristics to note on Figure A.5 are the symmetry of the lines of constant yaw angle and their relative independence on the pitch angle. The symmetry with regard to positive and negative yaw angles is expected, since the probe is symmetrical in the yaw planes. The independence of $C_{p\,yaw}$ on pitch angle, however, is a consequence of the definition of $C_{p\,yaw}$. It is found that Holes 2 and 3 respond differently with positive and negative pitch angles, either due to the nonsymmetry of the prism or the nonsymmetry caused by the sensing element being located a short distance from the probe tip. The denominator of $C_{p\,yaw}$ varies in a manner which negates the nonsymmetrical response of Holes 2 and 3 and yields a yaw coefficient which is approximately constant for a particular yaw angle. The greater range of the

yaw coefficient also contributes to the straight nature of the lines, since small pressure fluctuations will not significantly alter the yaw coefficient.

The lines of constant pitch angle in Figure A.5 do not have characteristics similar to the lines of constant yaw angle. These lines demonstrate a strong dependence on yaw angle and nonsymmetry with respect to positive and negative pitch angles. The wiggles in these lines are due primarily to the changes in the amount of pressure recovery in the separated regions, where either Hole 4 or 5 is located. The yaw angle strongly influences this pressure recovery, since it changes the distance in the direction of the flow from the prism edge to the hole. The difference in the curves for positive and negative pitch angles can be contributed to the nonsymmetrical geometry of the probe in the probe axial direction. The variations caused by both the nonsymmetry and the flow separation are also amplified by the smaller range of the pitch coefficient.

The next figure, Figure A.6, also exhibits some interesting characteristics. This figure shows that the total pressure coefficient is approximately independent of pitch angle, especially for the smaller yaw angles, but is strongly dependent on the yaw angle. The independence of $C_{p\ total}$ with respect to pitch variations is probably caused by the prism edges perpendicular to the surface of Hole 1, which would tend to direct the flow into Hole 1, causing it to sense a pressure near the true total pressure, regardless of the pitch angle. The center hole, however, will sense larger pressure changes with yaw angle variations, since the pressure will drop due to flow misalignment and also due to the fluid acceleration around the probe. The slight nonsymmetry with

respect to pitch angle can once again be attributed to the probe tip effects or the nonsymmetrical prism.

The final necessary figure for presenting the calibration data is Figure A.7. The curves of the static pressure coefficient in this figure contain many irregularities, which is the reason a 5° increment of pitch angle was used, thus assuring that the curves are adequately described. The dominate characteristic of these curves is the peak which occurs near a pitch angle of 20°. This peak is caused by the average pressure sensed by Holes 2 and 3 being greater for positive pitch angles than it is for negative pitch angles. The only differences in the probe geometry which could cause this effect are the location of sensing element and the nonsymmetrical location of the surfaces on which Holes 2 and 3 are located.

For a positive pitch angle, the body of the probe may turn the flow more than the tip section does for negative pitch angles, perhaps resulting in smoother flow with less losses arriving at Holes 2 and 3. This is one explanation for the pressures of Holes 2 and 3 being greater for positive pitch angles. The nonsymmetrical location of prism edges with respect to the holes could also contribute to the observed behavior. Since the edge of the prism toward the tip of the probe is closer to the holes than the opposite edge, flow separation off the edge could cause the lower pressures which are sensed for negative pitch angles. Although these two effects are the only apparent possible causes, the exact reason for the peak in the static pressure coefficient is unknown due to the complexity of the flow.

Despite the irregularity of the static pressure coefficient curves in Figure A.7, the general trends for the curves of different yaw angles

are similar. It is not apparent from Figure A.7, however, how the static pressure coefficient varies as a function of yaw angle. This relationship should be examined to assure that the 10° increments in yaw angle are adequate to describe the probe's response. For this reason, Figure A.8 presents the same data which are in Figure A.7, as $C_{p\ static}$ versus yaw angle. (Only seven curves of constant pitch angle are presented to avoid confusion.) This figure shows the curves are all similar and symmetrical with respect to the yaw angle. These characteristics and the smoothness of the curves suggest that the 10° increment is adequate.

The "W" shape of the curves can be contributed to two factors. At 0° yaw, the static pressure coefficient is large because the average pressure sensed by Holes 4 and 5 is near the total pressure of the flow. Therefore, the indicated static pressure is much larger than the true static pressure. For positive or negative yaw angles, however, the pressures sensed by these holes begins to drop as the flow near these holes becomes less stagnant. This results in the decrease of the $C_{p\ static}$ curve observed on both sides of the 0° yaw angle. The final rise in the curves at the larger yaw angles is caused by the denominator of the static pressure coefficient becoming small when the pressure sensed by the center hole decreases due to the flow misalignment.

It is seen from the preceding discussions that the characteristics of the calibration data can be explained by considering basic fluid flow concepts. These explanations enable more confidence to be put into the use of the probes, since no peculiar unexplainable characteristics were observed. The repeatability, which was also demonstrated, shows that the five-hole probes can be used accurately in the non-nulling mode.

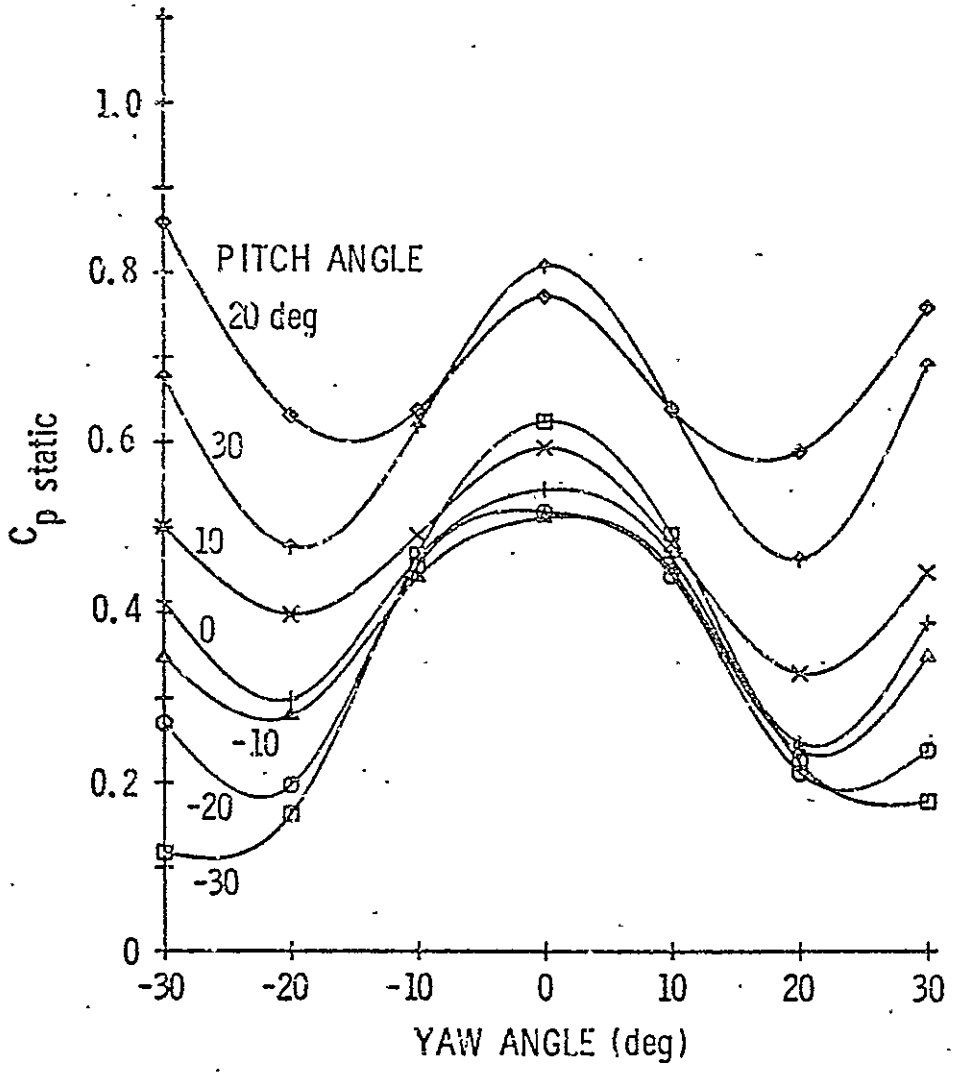

Figure A.8. Calibration data for Probe 2, $C_{p\ static}$ versus yaw angle.

A.4 Reynolds Number Effects

In order for the calibration of five-hole probes to be meaningful, it is necessary that the calibration data be independent, to a large extent, of the measured quantities. Since the velocity is the primary quantity to be measured, the effect of Reynolds number (Re) changes on the calibration data was assessed. A portion of the results obtained in the study are presently in Figures A.9 through A.12. These figures graphically present the four calibration pressure coefficients as a function of Reynolds number for seven pitch angles and a yaw angle of 20°. The symbols differentiating the different pitch angles, which are identified in Figures A.9 and A.12, are similarly used in Figures A.10 and A.11, although they may not be distinguishable due to the overlapping of the lines.

The introduction of the Reynolds number as an additional variable greatly increased the quantity of calibration data, which is the reason only the data for a yaw angle of 20° are presented. This portion of data, however, is sufficient to demonstrate the trends which were discovered and is typical of the remaining data. Examination of Figures A.9 through A.11 reveals that the pitch coefficient, the yaw coefficient, and the total pressure coefficient are independent of Reynolds number over the range tested. Figure A.12, however, does show that the static pressure coefficient is slightly dependent on the Reynolds number. This dependence is unfortunate, since a complete elimination of any error caused by the variation in the static pressure coefficient would require the use of a three-parameter calibration in terms of the yaw angle, pitch angle, and Reynolds number. With the Reynolds number unknown, an iterative computational procedure would be

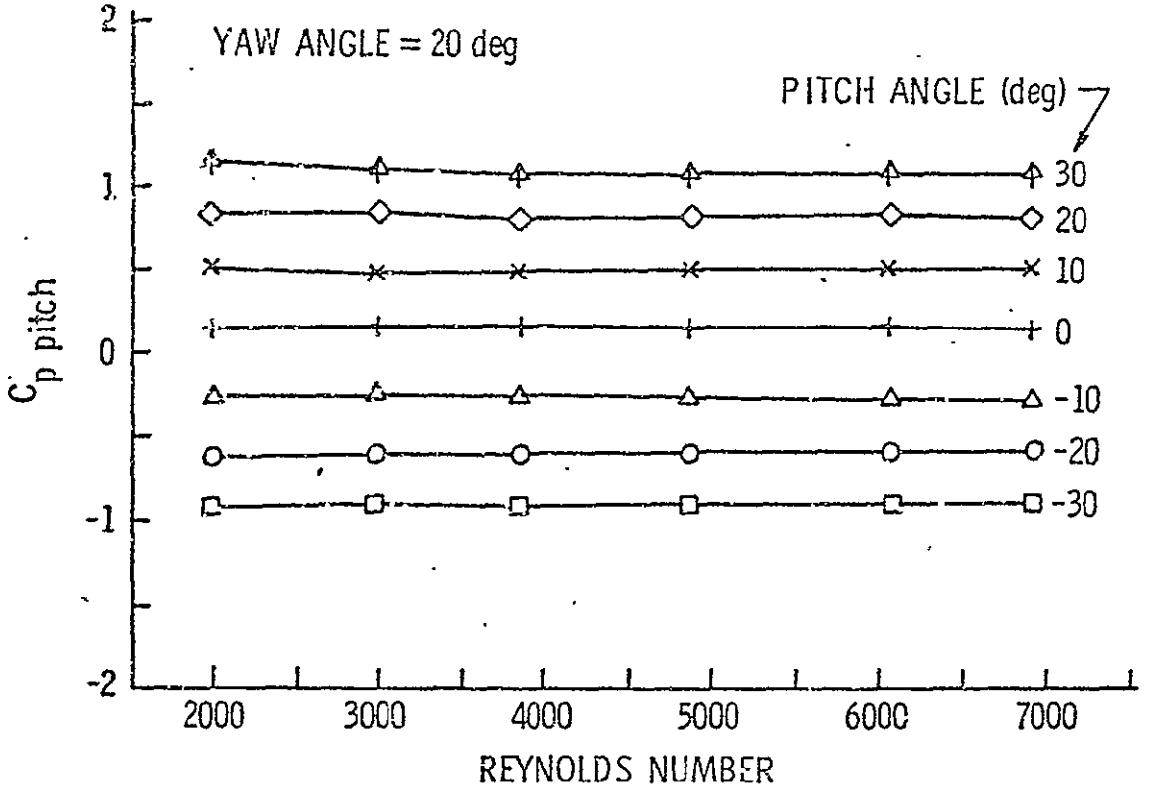

Figure A.9. $C_{p\ pitch}$ versus Reynolds Number for Probe 1 at a 20° yaw angle.

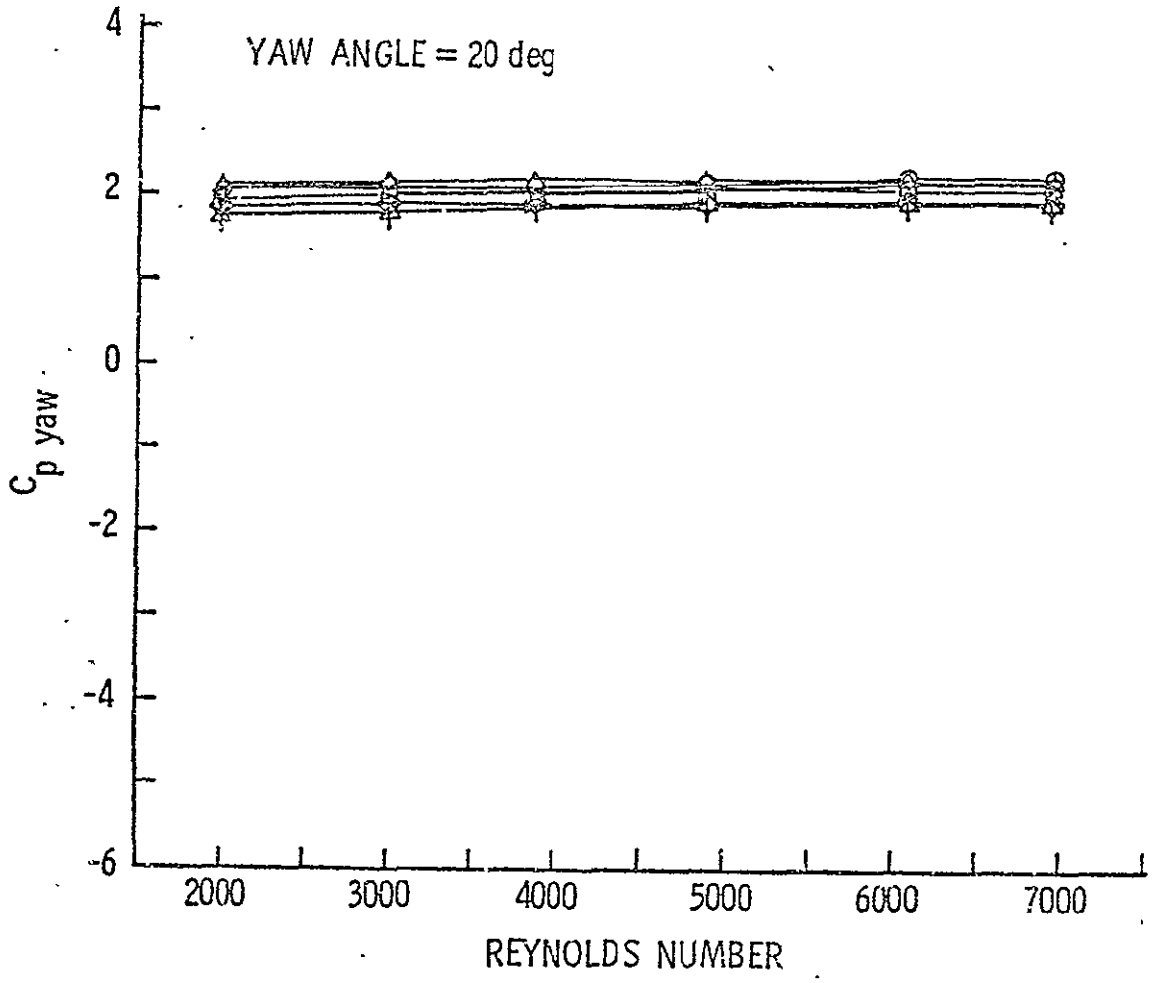

Figure A.10. $C_{p\ yaw}$ versus Reynolds Number for Probe 1 at a 20° yaw angle.

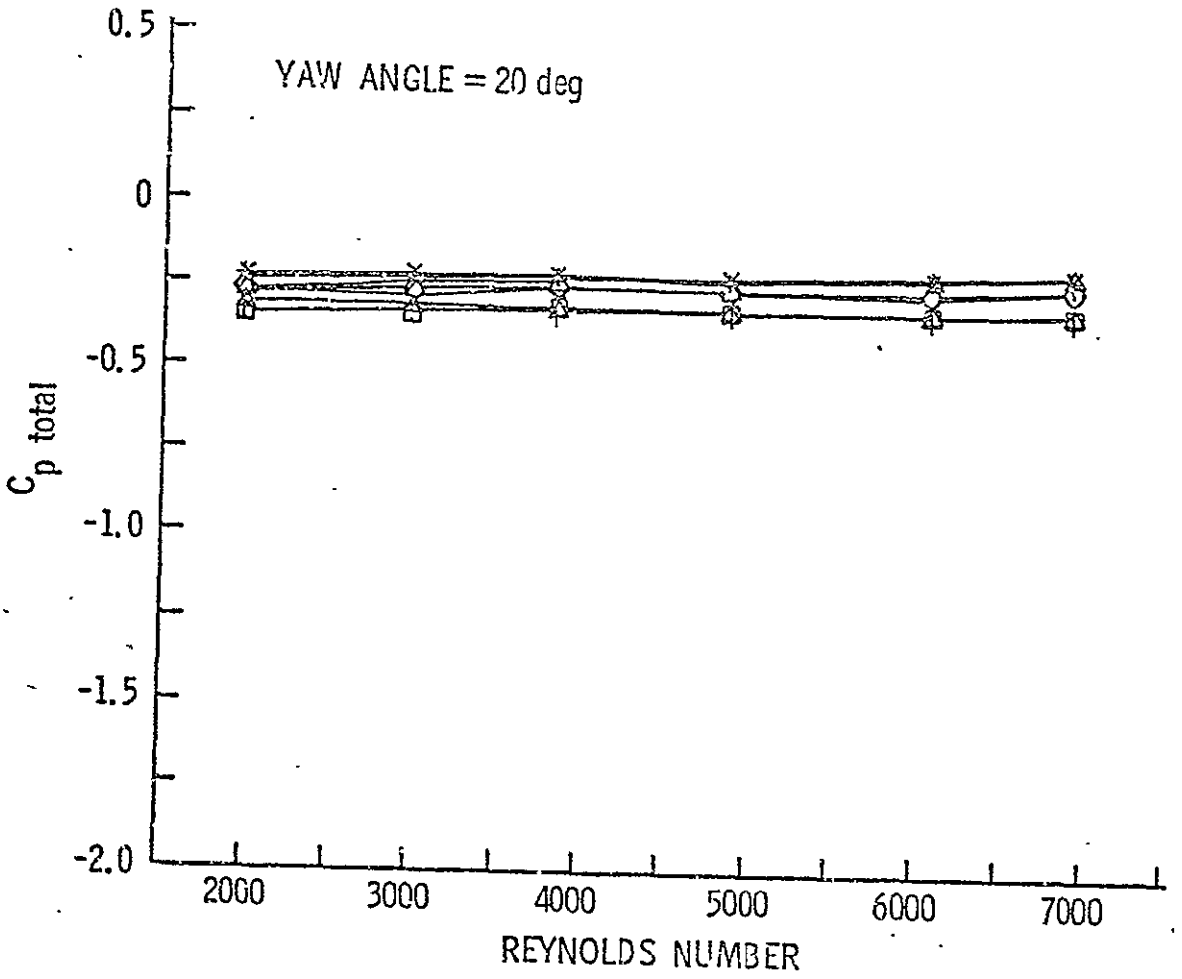

Figure A.11. $C_{p\ total}$ versus Reynolds Number for Probe 1 at a 20° yaw angle.

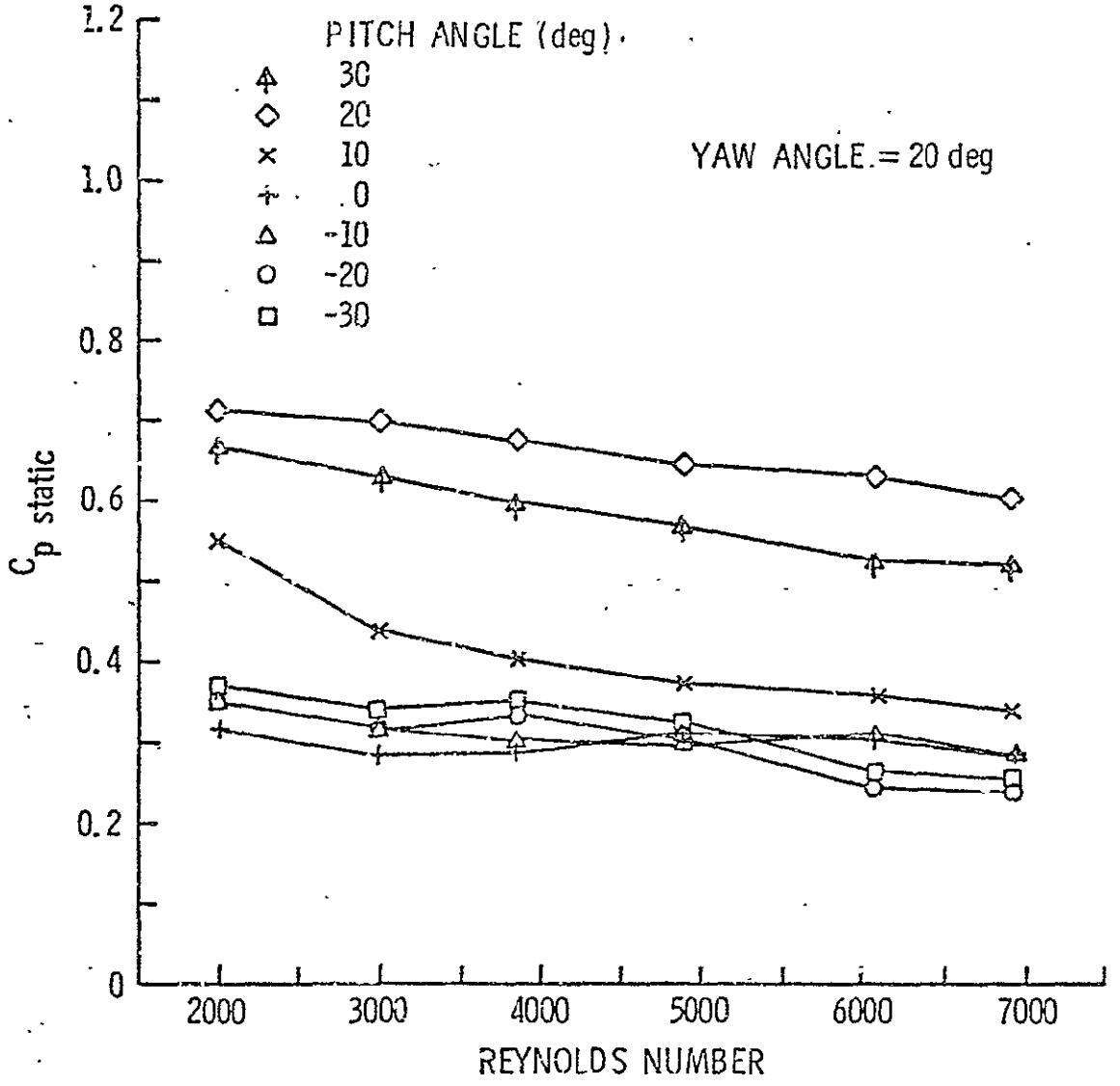

Figure A.12. $C_{p\ static}$ versus Reynolds Number for Probe 1 at a 20° yaw angle.

necessary which would increase the complexity of the data-reduction program and would also increase the required computer time.

Although a definite dependence of the static pressure coefficient on Reynolds number is revealed in Figure A.12, the variation is not extremely large. For this reason, and also to eliminate the need for an iterative computational procedure, approximate means for accounting for the variation in $C_{p\ static}$ were employed. The Reynolds number range in which the probe is operated can be estimated from mean flow conditions or from previously reduced test results. Using this information, average values of $C_{p\ static}$ could be calculated for the estimated Re range. The calculation and use of average values is justifiable, since the variation of the static pressure coefficients within the expected Re range would be very small and cause an insignificant error.

The average static pressure coefficients calculated for a given Reynolds number could have been used directly in a data reduction program. Instead, these values were used to form corrections which could then be applied to the original calibrations conducted at the Reynolds number 7000. This was done, since, in the basic calibration, 5° increments were used for the pitch angle variation. The correction, therefore, enabled the more extensive calibrations to be used throughout the data-reduction program. The following equation defines the correction which was employed:

$$\text{Re Correction} = \frac{(C_{p\ static})_{\text{averaged for a particular Re range}} - (C_{p\ static})_{Re \approx 7000}}{(C_{p\ static})_{\text{maximum for Re} \approx 7000}} \times 100\%.$$

Figure A.13 is a plot of the Reynolds number correction calculated for a Reynolds number range of 2990 to 3010. In this case, the range was made very small for demonstration purposes, so that the change in the static pressure coefficient between Reynolds numbers of 7000 and 3000 could be examined. For most of the data reduced from the AFRF, the changes in the Reynolds number were much larger and usually on the order of 1000 to 2000.

The significance of the magnitude of the correction can be obtained by examining the error which would result in the calculated static pressure and velocity if the correction was not used. For a yaw angle of 20° and a pitch angle of 30°, the correction is found to be 10.0. This value represents one of the larger corrections but, if neglected, will only result in an error in the calculated static pressure which is 5.5% of the dynamic head. The error in the calculated velocity would be even less, with only a 2.8% difference between the calculated and the true velocity. From this example, it is apparent that the Reynolds number effects are not large, although they should be accounted for if accurate measurements are required. The small error which would result from neglecting the correction also demonstrates the adequacy in representing the Reynolds number effects in the approximate manner chosen. Since less than a 3% error in the calculated velocity has been shown to result from the change in $C_{p\ static}$ from a Reynolds number of 7000 to 3000, the error associated with averaging the static pressure coefficient over a small range will be insignificant.

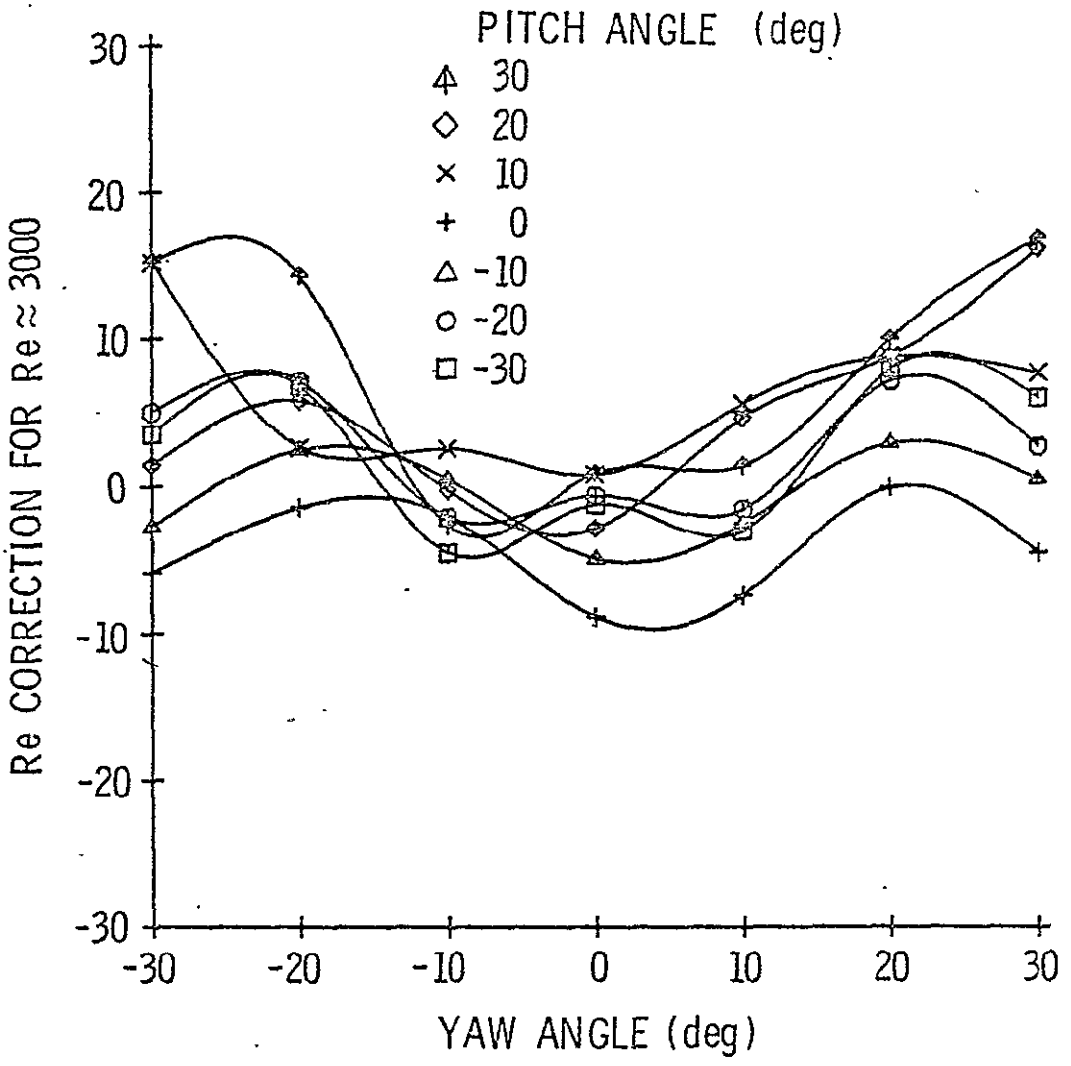

Figure A.13. Reynolds Number correction versus yaw angle for Probe 1 for a Reynolds Number of approximately 3000.

A.5 Effects Caused by the Proximity of a Solid Boundary

As discussed in the section on the experimental procedures, the change in the probe's response due to the proximity of a solid boundary was investigated. This study was initiated so that the probes could be used to conduct radial surveys in the AFRF determining the steady performance of the rotor. When using the probes for radial surveys, both types of wall-probe configurations are encountered, one when the probes are near the hub and the other when measurements are made near the outer casing.

It should be emphasized that the change in the probe's response which was investigated was not due to the boundary layer, but, rather, it was due to the potential interaction with the wall. It is true that errors may result with the use of five-hole probes in a boundary layer because of the velocity gradient which exists. Since the holes are located a finite distance apart, the holes will not only sense different pressures due to flow angularity (for which the probes are calibrated), but also due to the velocity gradient. The magnitude of the error associated with the use of a five-hole probe in a velocity gradient will depend on the relative size of the hole spacing and the change in the velocity between hole locations. With proper probe selection, the error due to the velocity gradient will be reduced to an insignificant level; however, it does not appear possible to eliminate the error through a calibration.

Unlike the error caused by a velocity gradient in a boundary layer, it should be possible to eliminate the error caused by a potential interaction with a wall by obtaining a calibration of the changes induced. Since a change in the probe's response will be caused by a

shifting of the streamlines due to the presence of the wall, the response will depend primarily on the distance between the wall and the probe. A knowledge of the change in the probe's response can, therefore, be used to correct for the wall effects. The experimental setup, which was shown schematically in Figure A.4, allowed the potential interaction to be investigated. With the distance from the leading edge of the plate to the probe less than 6 in., the boundary layer on the plate is very small and would not contribute significantly to the probe response.

Once again, for brevity, only a portion of the experimental results are presented. These results appear in Figures A.14 through A.17, where the first two figures are results from the tests for the probe tip approaching the plate. In Figure A.14, the plot of $C_{p\,yaw}$ versus the distance from the probe tip to the plate shows that the yaw coefficient is not affected by the proximity of the plate. This figure exemplifies the characteristics observed for the pitch coefficient and the total pressure coefficient, which were also not affected by the plate's presence.

The fact that the yaw coefficient is unaffected by the plate is not surprising, since any shift in the streamlines with respect to the probe will be symmetrical in the yaw plane. The total pressure coefficient would also not be expected to change, since streamline curvature will not affect the total pressure of the flow. It is somewhat unexpected, however, to see no change in the pitch coefficient, because a shift in the streamlines caused by the plate could change the local flow angle sensed by the probe. The change in the local flow angle must, therefore, be too small to cause a measurable effect.

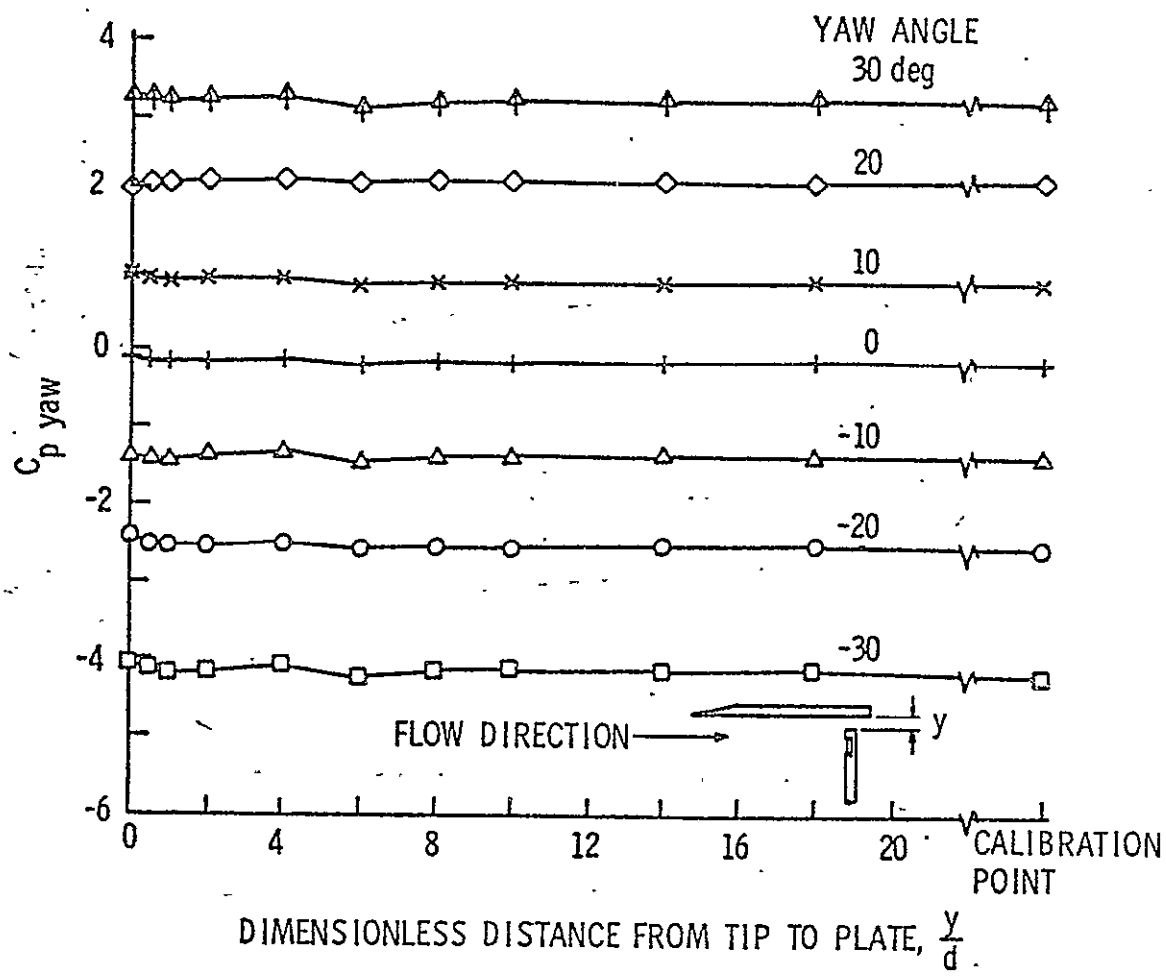

Figure A.14. $C_{p\ yaw}$ versus the dimensionless distance from the probe tip to the plate for Probe 1. The probe is approaching the plate as shown in the accompanying sketch.

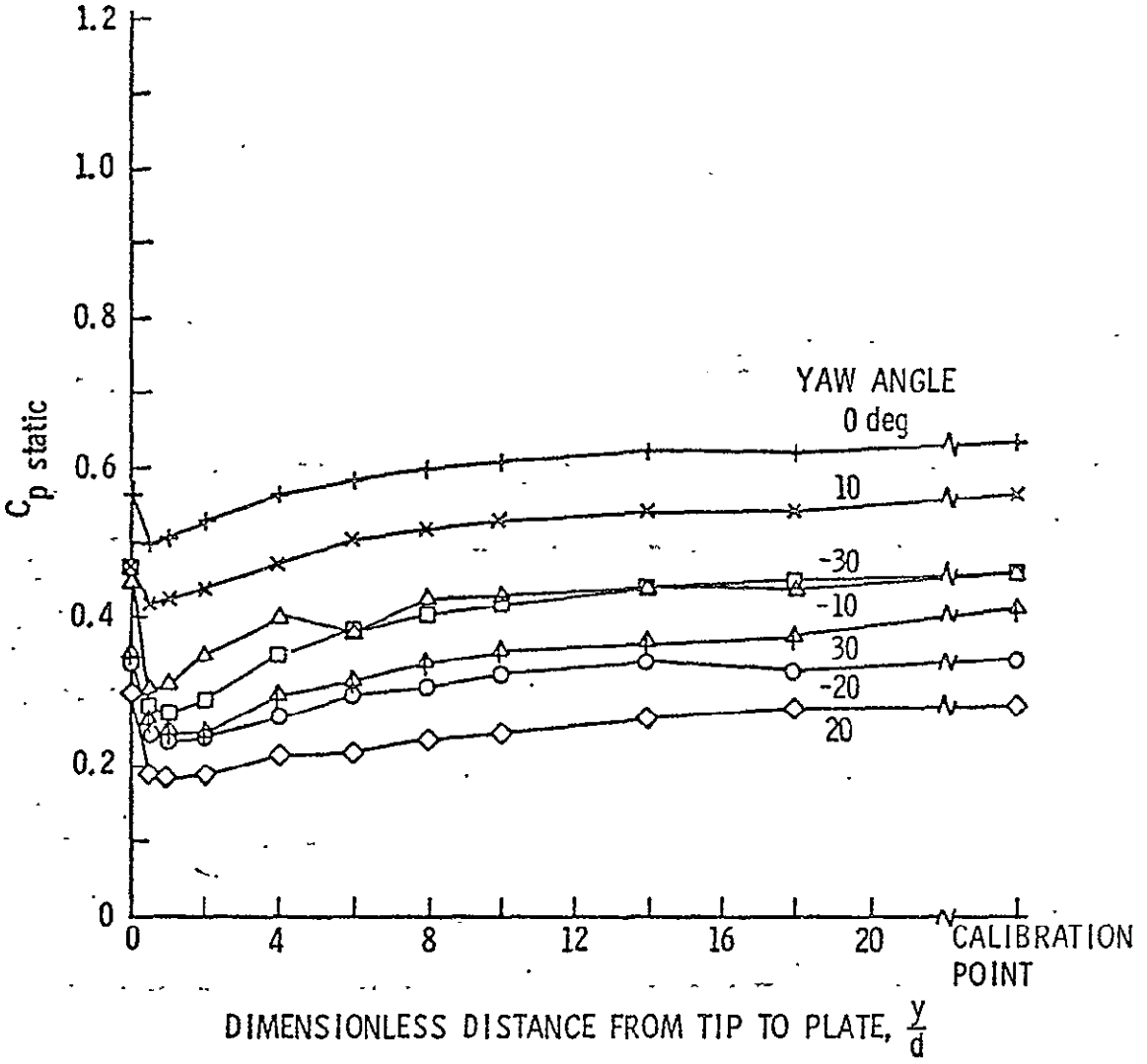

Figure A.15. $C_{p\ static}$ versus the dimensionless distance from the probe tip to the plate for Probe 1. The probe is approaching the plate.

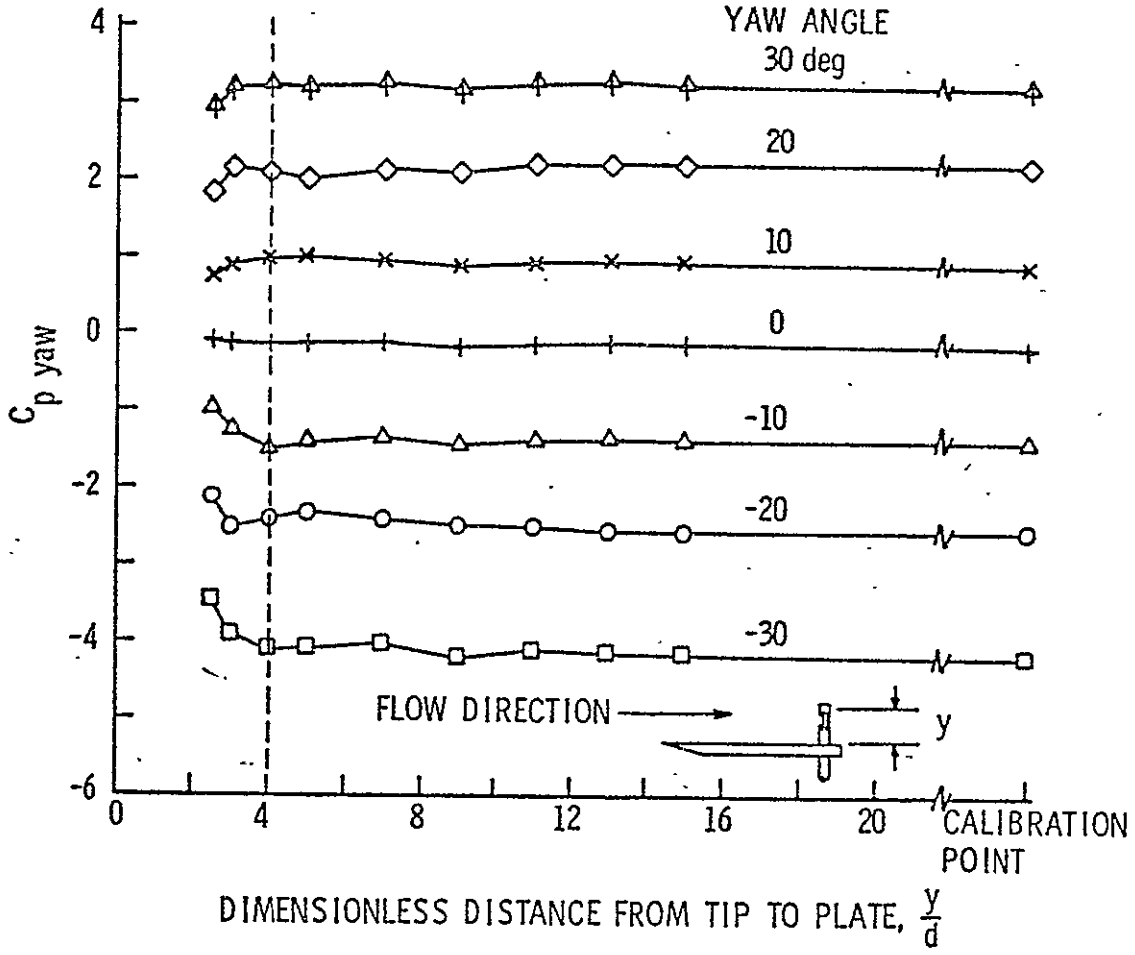

Figure A.16. $C_{p\ yaw}$ versus the dimensionless distance from the probe tip to the plate for Probe 1. The probe is drawn through a hole in the plate as shown by the accompanying sketch.

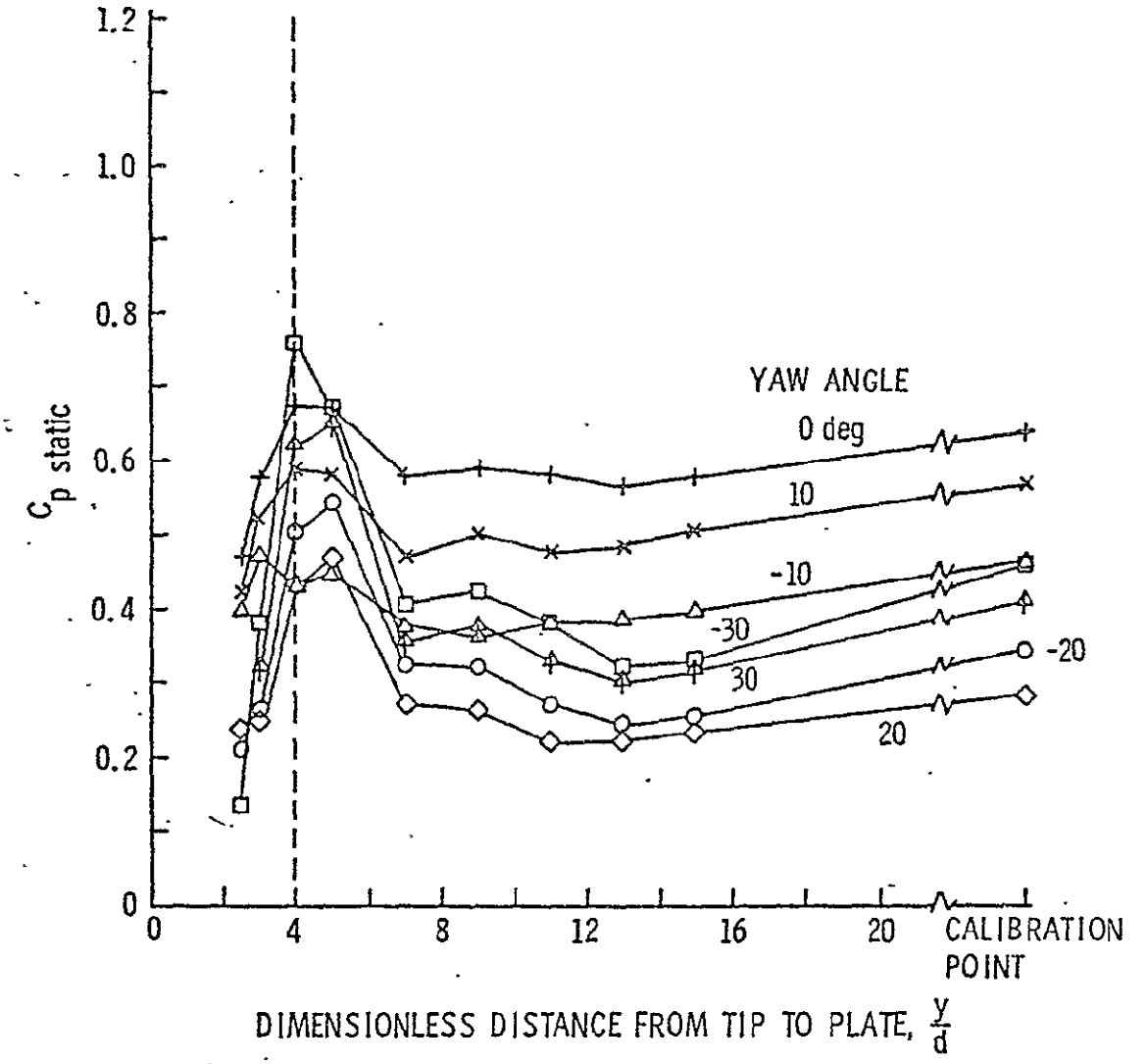

Figure A.17. $C_{p\ static}$ versus the dimensionless distance from the probe tip to the plate for Probe 1. The probe is drawn through a hole in the plate.

For the case where the probe tip is approaching the plate, the only calibration coefficient which is affected by the plate is the static pressure coefficient. Figure A.15, which demonstrates this effect, shows the variation of the static pressure coefficient as a function of the plate-probe spacing. The observed change in the coefficient is due to the change in the local static pressure which is altered by the changing flow patterns.

The remaining two figures show results from the tests where the probe is drawn through a hole in the plate. In Figure A.16, once again the yaw coefficient is plotted versus the distance from the probe tip to the plate. It is seen for this case, however, that the yaw coefficient is affected by the plate if the distance is less than 0.5 in. or four probe tip diameters. Similarly, variations in the other coefficients were also observed in this region.

The variation observed in all the coefficients essentially makes the probes impractical for use when the distance from the tip is less than four tip diameters. It should be pointed out, however, that, when the probe tip is four diameters from the plate, the center hole is only 0.25 in., or two tip diameters, from the plate. This means measurements made with this type of probe would only have to be restricted to distances from a wall greater than two tip diameters. A similar restriction is necessary for the other configuration from probe geometrical limitations only. When the probe tip is against a wall, the center hole is two tip diameters from the wall.

Restricting the use of the probe to distances greater than two probe diameters does not eliminate all of the wall interaction effects. Figure A.17 shows that the static pressure coefficient is still affected

at greater distances. The effects of a wall, when limited to the static pressure coefficient only, however, can easily be accounted for in a data-reduction program. Corrections similar to the Reynolds number correction were formed for both wall configurations and incorporated into the data-reduction program for the radial surveys.

... Before concluding this section on the effects caused by the proximity of a solid boundary, one problem which was encountered should be pointed out. This problem is revealed in Figure A.17, where it is seen that the values of $C_{p\ static}$ do not level off to the free-stream calibration data. It was suspected that the static pressure in the jet was altered by the plate, and atmospheric pressure did not exist as was assumed. Later investigation of the static pressure, using static taps on the plate, did verify that the pressure was altered by the plate. Although the change in the static pressure was not large, it was found that the pressure was very sensitive to the plate alignment. With the new data as a justification, the wall effects data were corrected such that, at large distances, the values were identical to the data obtained with no plate. This correction was made before putting the data into the radial survey reduction program. Future calibrations using a plate should check the static pressure on the plate before initiating the tests.

APPENDIX B

DERIVATION OF DIMENSIONLESS LINEARIZED FLOW EQUATIONS

The non-dimensional linearized flow equations used in Chapter III are derived in detail in this appendix. The assumptions necessary for their derivation, which appear in a complete list of the assumptions for the actuator disk model in Chapter III, are repeated here for clarity.

Assumptions

1. Incompressible flow.
2. Two-dimensional flow ($v_r = 0$, $\frac{\partial}{\partial r} = 0$).
3. Steady Flow ($\frac{\partial}{\partial t} = 0$).
4. No body forces.
5. Inviscid flow.
6. The amplitude of the velocity distortion is small compared to the average axial velocity.

The first five assumptions are used to reduce the Navier-Stokes equations to the following simple form:

x-momentum equation

$$\rho\left(\frac{v_\theta}{r}\frac{\partial v_x}{\partial \theta} + v_x\frac{\partial v_x}{\partial x}\right) = -\frac{\partial p_s}{\partial x} \quad . \tag{B.1}$$

θ-momentum equation

$$\rho\left(\frac{v_\theta}{r}\frac{\partial v_\theta}{\partial \theta} + v_x\frac{\partial v_\theta}{\partial x}\right) = -\frac{1}{r}\frac{\partial p_s}{\partial \theta} \quad . \tag{B.2}$$

Conservation of mass equation

$$\frac{1}{r}\frac{\partial v_\theta}{\partial \theta} + \frac{\partial v_x}{\partial x} = 0 \; . \qquad (B.3)$$

In order to linearize the equations, the velocity and pressure are represented as the sum of a circumferential mean and perturbation quantity, as presented in Equations (B.4) through (B.6) which follow:

$$p_s = \bar{p}_s + p_s' \; , \qquad (B.4)$$

$$v_x = \bar{v}_x + v_x' \qquad (B.5)$$

and

$$v_\theta = \bar{v}_\theta + v_\theta' \; . \qquad (B.6)$$

When Equations (B.4) through (B.6) are substituted into Equations (B.1) through (B.3), after expanding the terms, several simplifications are possible.

The conservation of mass equation and the momentum equations for the average quantities offer numerous simplifications because these equations, upon examination, reveal that all derivatives of average quantities are zero. Since this conclusion has important consequences, these equations are presented below:

Average x-momentum equation

$$\rho\left(\frac{\bar{v}_\theta}{r}\frac{\partial \bar{v}_x}{\partial \theta} + \bar{v}_x \frac{\partial \bar{v}_x}{\partial x}\right) = - \frac{\partial \bar{p}_s}{\partial x} = 0 \; . \qquad (B.7)$$

Average θ-momentum equation

$$\rho\left(\frac{\bar{v}_\theta}{r}\frac{\partial \bar{v}_\theta}{\partial \theta} + \bar{v}_x \frac{\partial \bar{v}_\theta}{\partial x}\right) = -\frac{1}{r}\frac{\partial \bar{p}_s}{\partial \theta} \qquad (B.8)$$

Average conservation of mass equation

$$\frac{1}{r}\frac{\partial \bar{v}_\theta}{\partial \theta} + \frac{\partial \bar{v}_x}{\partial x} = 0 \qquad (B.9)$$

By definition, $\frac{\partial \bar{v}_\theta}{\partial \theta} = \frac{\partial \bar{v}_x}{\partial \theta} = \frac{\partial \bar{p}_s}{\partial \theta} = 0$. It therefore follows directly from the continuing equation that $\frac{\partial \bar{v}_x}{\partial x}$ must equal zero; and also, from Equation (B.8), $\frac{\partial \bar{v}_\theta}{\partial x}$ is equal to zero since $\bar{v}_x$ cannot equal zero. After the previous observations, it is also apparent that $\frac{\partial \bar{p}_s}{\partial x}$ is equal to zero from Equation (B.7).

The preceding results may seem peculiar, since they essentially state that all the average quantities are constant. However, it must be remembered that the equations of motion do not apply at the actuator disc, which represents the blade row response as a discontinuity in the flow. Therefore, $\bar{v}_\theta$ and $\bar{p}_s$ are constant up to the actuator disc, but may undergo an abrupt change at the disc and are once again constant downstream of the disc. $\bar{v}_x$ maintains the same value both upstream and downstream, since conservation of mass for an incompressible flow in a constant area duct requires that $\bar{v}_x$ is a constant everywhere.

In addition to the simplifications obtained by dropping terms containing derivatives of average quantities, Assumption 6, which is

the basis of the linearized theory, must be employed. Assumption 6 implies that $v_\theta' << \bar{v}_x$ and $v_x' << \bar{v}_x$. With this assumption, terms containing products of v_θ', v_x', or their derivatives are eliminated since they will be small and of second order. After all of the previous simplifications are applied, the following linear partial differential equations result:

x-momentum equation

$$\rho\left(\frac{\bar{v}_\theta}{r}\frac{\partial v_x'}{\partial \theta} + \bar{v}_x\frac{\partial v_x'}{\partial x}\right) = -\frac{\partial p_s'}{\partial x} . \tag{B.10}$$

θ-momentum equation

$$\rho\left(\frac{\bar{v}_\theta}{r}\frac{\partial v_\theta'}{\partial \theta} + \bar{v}_x\frac{\partial v_\theta'}{\partial x}\right) = -\frac{1}{r}\frac{\partial p_s'}{\partial \theta} . \tag{B.11}$$

Conservation of mass equation

$$\frac{1}{r}\frac{\partial v_\theta'}{\partial \theta} + \frac{\partial v_x'}{\partial x} = 0 . \tag{B.12}$$

It is advantageous at this point to replace the static pressure which now appears in the x and θ momentum equations by the total pressure. One reason for this is that the distortion is usually represented as a total pressure deficit. Thus, replacing the static pressure with the total pressure allows the inlet boundary condition to be applied directly. Also, the matching conditions for the change of the total pressure across the blade row are more easily applied with the total pressure appearing in the equations. In addition to these reasons, it turns out that the substitution changes the partial

derivatives on the left side of the x and θ momentum equations, so that both equations have identical terms, except for a constant multiplier. This consequence offers an additional advantage, since it simplifies the simultaneous solution of the equations.

For the purpose of replacing the static pressure by the total pressure, a special form of the Bernoulli equation is used. Starting with the basic equation, $p_T - p_s = \frac{1}{2}\rho v^2$, this equation is expanded in terms of the x and θ components of velocity and also the average and fluctuating quantity of each variable. After subtracting the equation for the average quantities, and once again neglecting second order terms, the following form of the Bernoulli equation is obtained:

$$p_s' = p_T' - \rho\bar{v}_x v_x' - \rho\bar{v}_\theta v_\theta' \quad . \qquad (B.13)$$

Using Equation (B.13) to replace p_s' in Equations (B.10) and (B.11), the following new forms of the x and θ momentum equations are obtained:

x-momentum equation

$$\rho\bar{v}_\theta\left(\frac{1}{r}\frac{\partial v_x'}{\partial\theta} - \frac{\partial v_\theta'}{\partial x}\right) = -\frac{\partial p_T'}{\partial x} \quad . \qquad (B.14)$$

θ-momentum equation

$$\rho\bar{v}_x\left(\frac{1}{r}\frac{\partial v_x'}{\partial\theta} - \frac{\partial v_\theta'}{\partial x}\right) = \frac{1}{r}\frac{\partial p_T'}{\partial\theta} \quad . \qquad (B.15)$$

The final modifications of Equations (B.12), (B.14), and (B.15) is to introduce non-dimensional variables. In conventional practice, the rotor speed U is used to non-dimensionalize velocity and $\frac{1}{2}\rho U^2$ is used to non-dimensionalize pressure. However, it was found when reducing the data of this study that the average axial velocity provided a more convenient parameter for non-dimensionalizing the data. This was due to the fact that the average axial velocity was approximately constant for all the tests. Thus, comparing results from different tests at different rotor speeds was greatly simplified when the data was non-dimensionalized by the circumferential average axial velocity. Therefore, to be consistent with the experimental data, the average axial velocity will also be used in the actuator disc model to non-dimensionalize the equations. The following non-dimensional parameters are defined:

$$V_x' = \frac{v_x'}{\bar{v}_x} , \tag{B.16}$$

$$V_\theta' = \frac{v_\theta'}{\bar{v}_x} , \tag{B.17}$$

$$P_T' = \frac{p_T'}{\frac{1}{2}\rho \bar{v}_x^{\,2}} , \tag{B.18}$$

$$a = \bar{v}_\theta / \bar{v}_x \tag{B.19}$$

and

$$X = x/r . \tag{B.20}$$

When the dimensionless parameters are introduced into Equations (B.12), (B.14), and (B.15), the final equations are obtained:

x-momentum equation

$$2a\left(\frac{\partial V_x'}{\partial \theta} - \frac{\partial V_\theta'}{\partial x}\right) = -\frac{\partial P_T'}{\partial x} \quad . \tag{B.21}$$

θ-momentum equation

$$2\left(\frac{\partial V_x'}{\partial \theta} - \frac{\partial V_\theta'}{\partial x}\right) = \frac{\partial P_T'}{\partial \theta} \quad . \tag{B.22}$$

Conservation of mass equation

$$\frac{\partial V_\theta'}{\partial \theta} + \frac{\partial V_x'}{\partial x} = 0 \quad . \tag{B.23}$$

APPENDIX C

90° SQUARE DISTORTION DATA WITHOUT THE ROTOR INSTALLED

This appendix presents the data from the circumferential surveys
›nducted without the rotor installed for the 90° square distortion.
.gures C.1 through C.5 present the three velocity components, total
'essure, and static pressure as a function of circumferential location.
ese data are presented for comparison with the sample 90° distortion
ta obtained with the rotor operating, presented in Chapter VI. The
ta for the four-cycle distortion are similarly presented in Chapter
. The complete data for all of the distortion tests can be found
Reference [19].

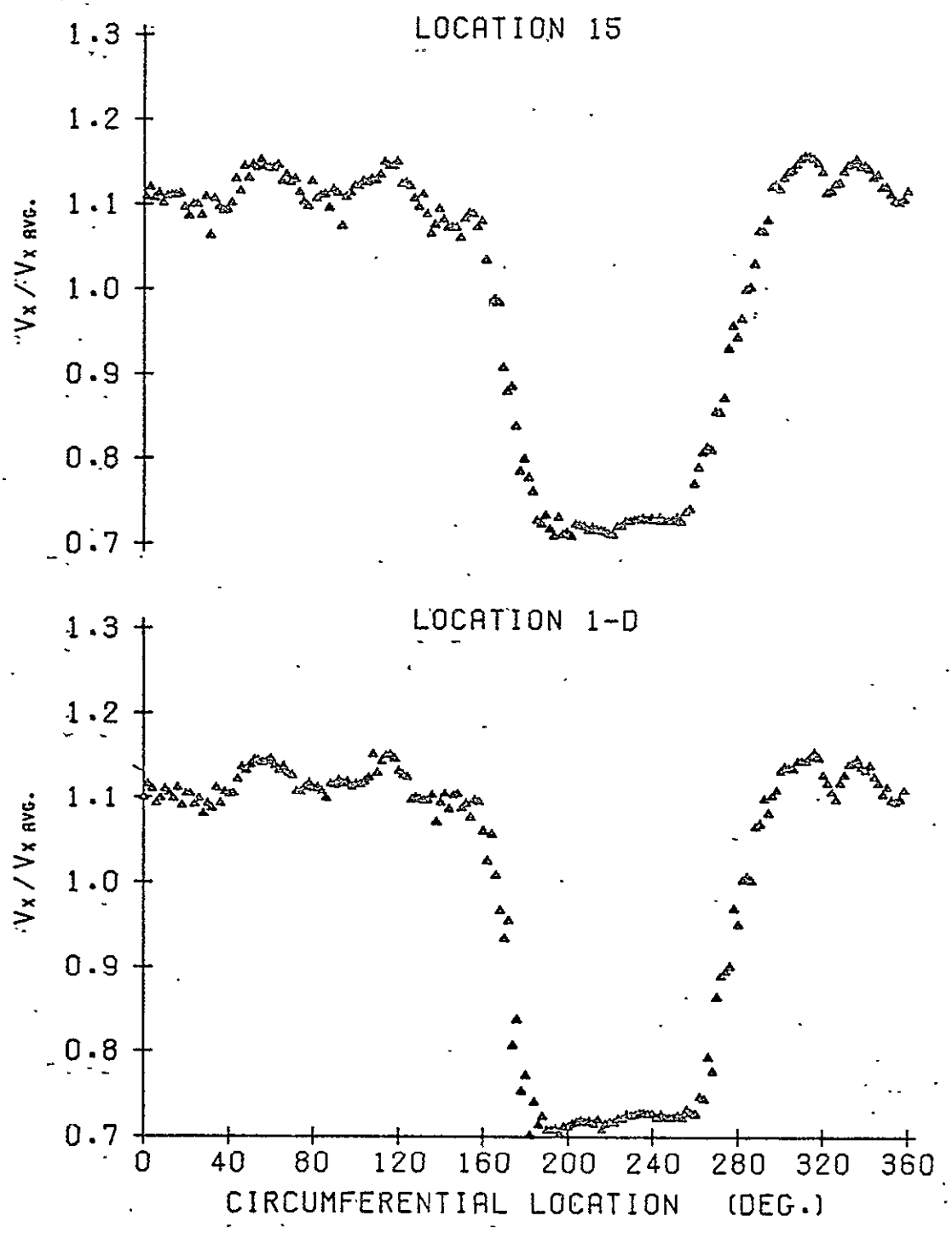

Figure C.1. Axial velocity distribution for the 90° square distortion without the rotor installed.

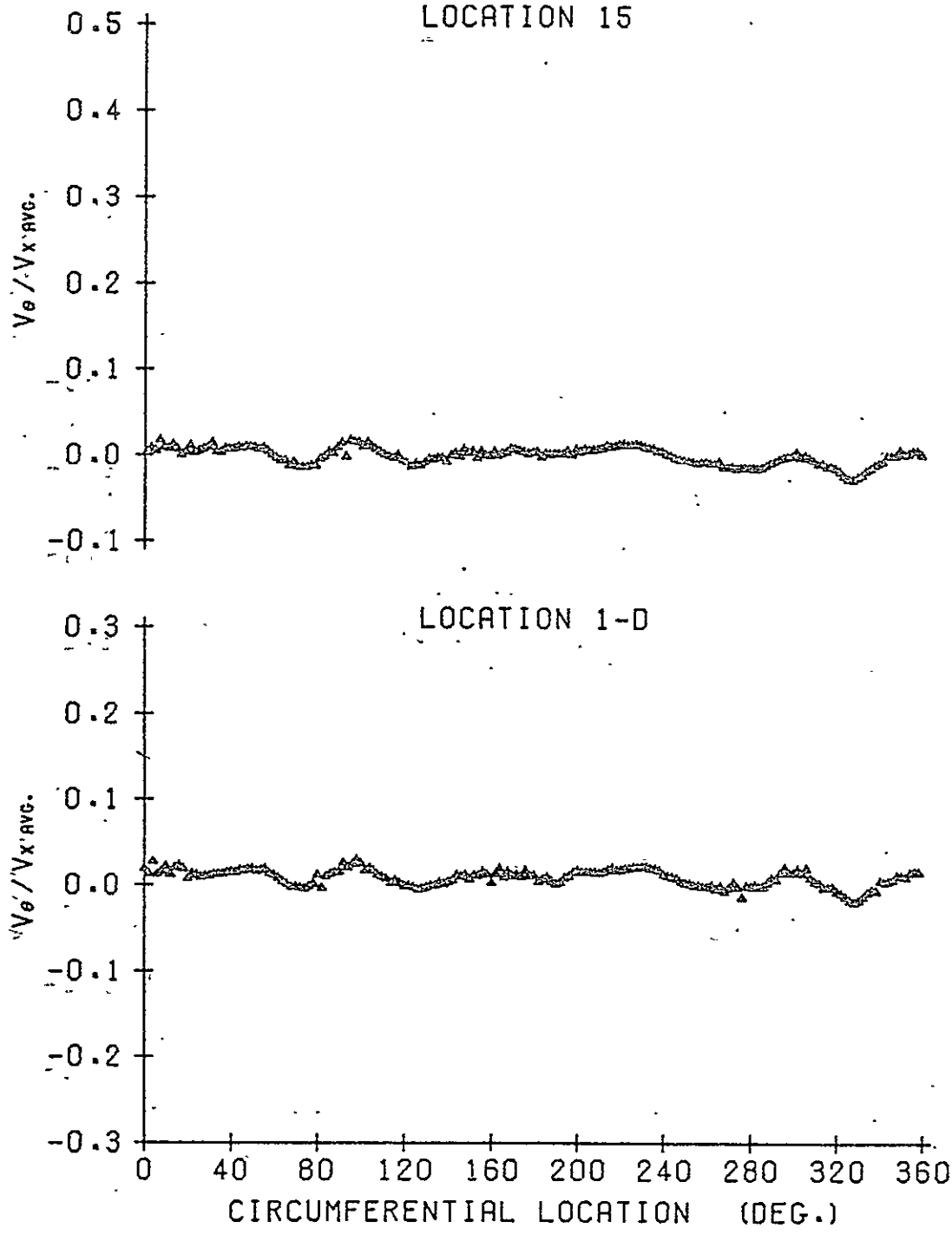

Figure C.2. Circumferential velocity distribution for the 90° square distortion without the rotor installed.

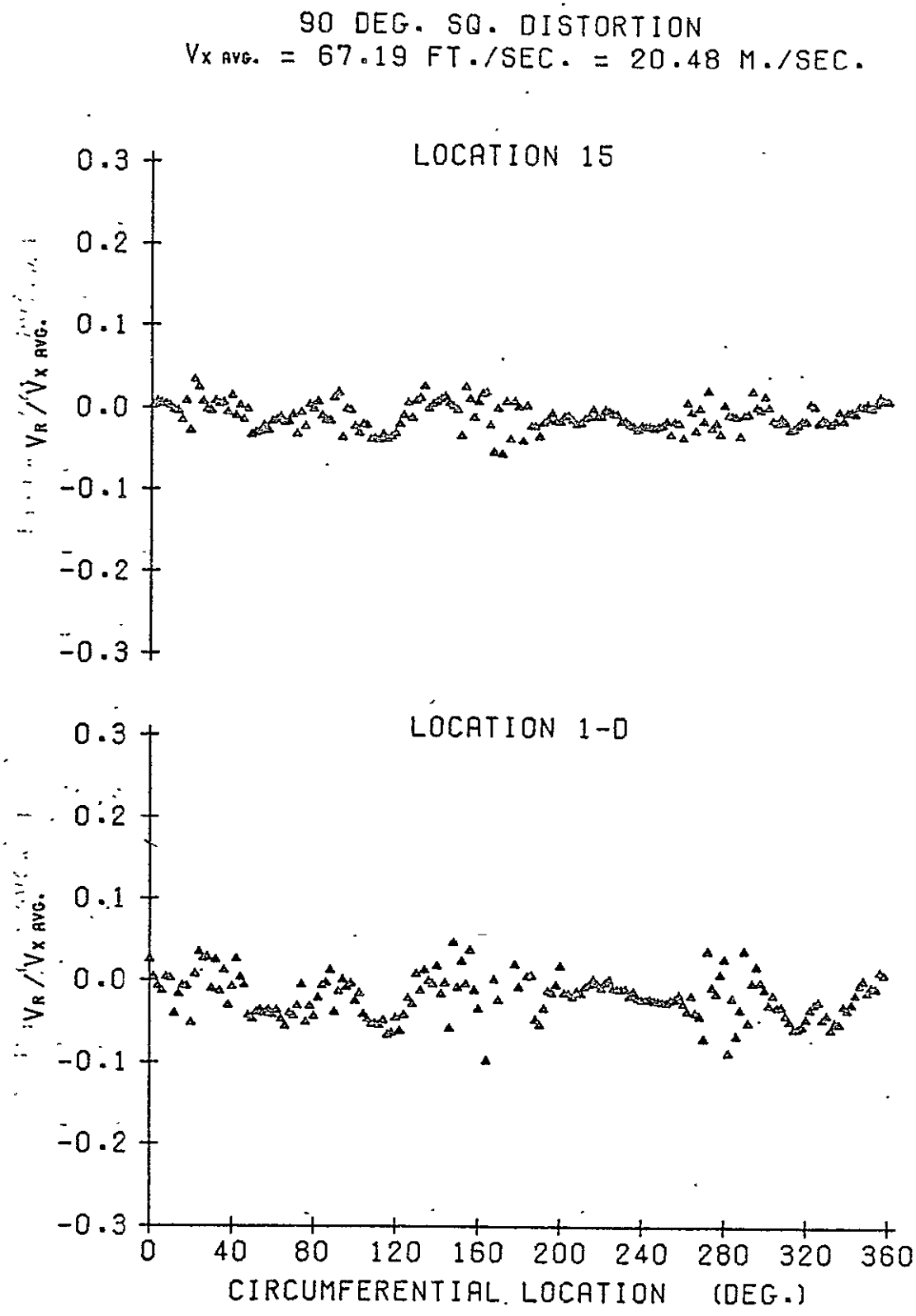

Figure C.3. Radial velocity distribution for the 90° square distortion without the rotor installed.

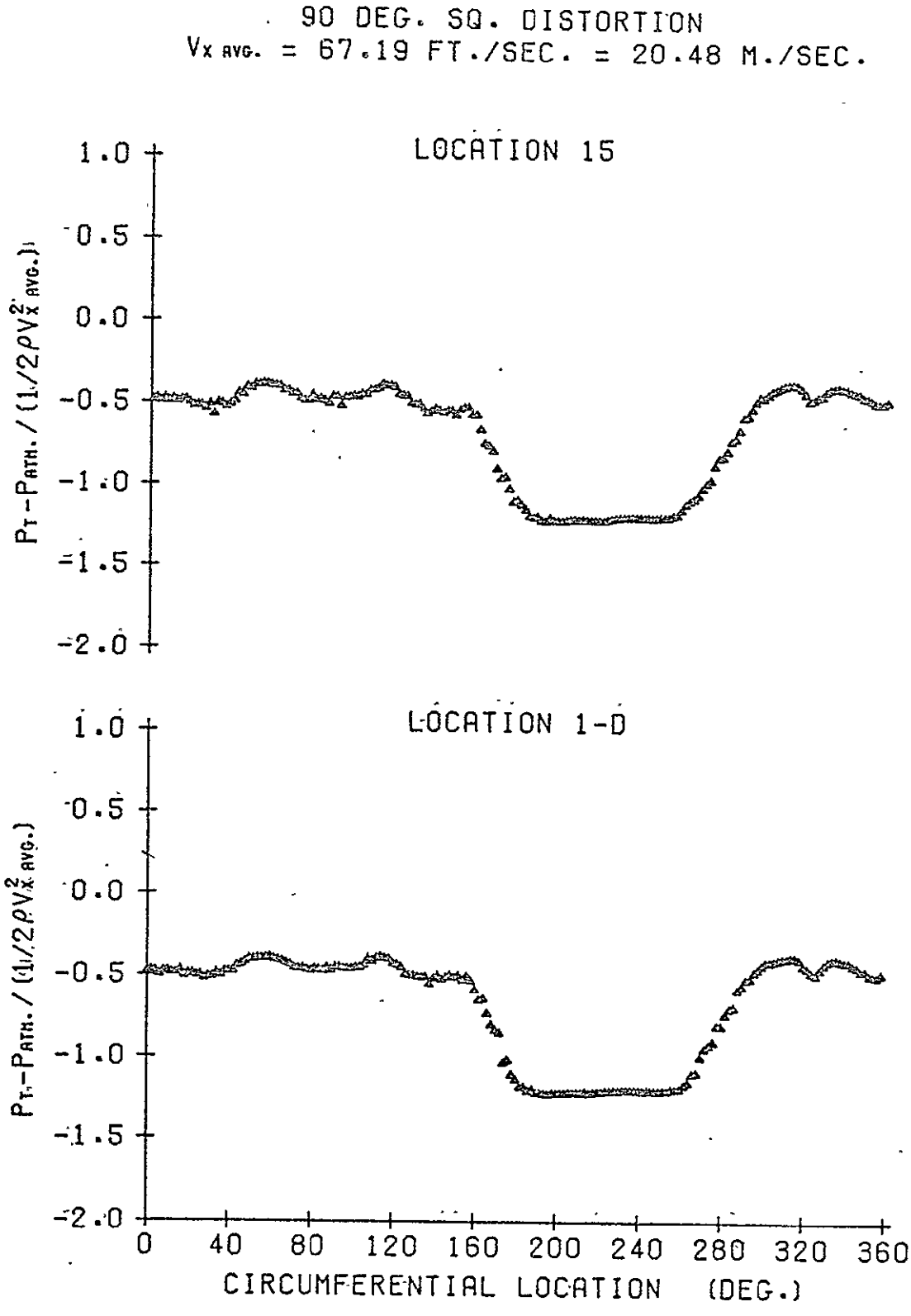

Figure C.4. Total pressure distribution for the 90° square distortion without the rotor installed.

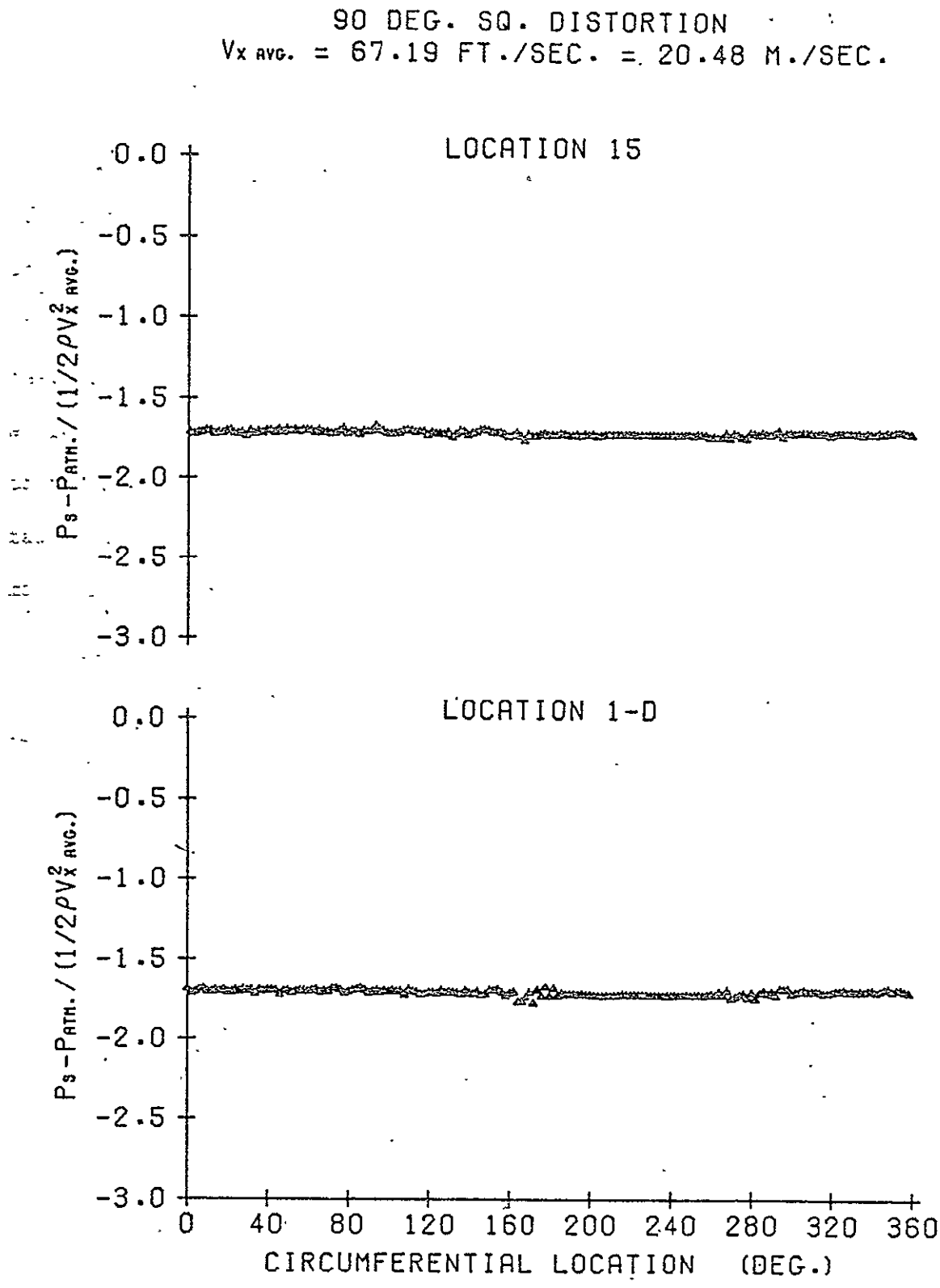

Figure C.5. Static pressure distribution for the 90° square distortion without the rotor installed.

APPENDIX D

RUN CONDITIONS FOR THE DISTORTION TESTS

Table D.1 of this appendix tabulates the run conditions for all of the distortion tests conducted. The first entry for each screen is for the test without the rotor installed, and thus, only the average axial velocities at Locations 1-D and 15 are defined. For the remaining tests in each section, the number of rotor blades, stagger angle, average axial velocities at Locations 1-D and 15, RPM, average flow coefficient, average $\Delta p_T/\frac{1}{2}\rho v_{x\,avg}^2$, and the average incidence are tabulated. The average values presented are computed as the arithmetic mean of the data from the 180 circumferential measurement locations.

Table D.1 Run Conditions for the Distortion Tests

Screen	No. of Blades	Stagger (degrees)	V_x avg 1-D (ft/sec)	V_x avg 15 (ft/sec)	RPM	Avg ϕ	Avg $\Delta p_T/\frac{1}{2}\rho v_{x\,avg}^2$	Avg i (degrees)
1-cycle	—	—	67.34	67.96	———	———	———	———
1-cycle	12	35	66.32	65.78	721	1.360	-0.071	0.91
1-cycle	12	35	65.08	64.76	766	1.256	-0.004	3.17
1-cycle	12	35	64.57	64.06	948	1.007	0.323	9.51
1-cycle	12	35	68.10	67.10	1171	0.860	0.815	14.04
1-cycle	12	45	62.25	60.55	996	0.924	-0.213	1.95
1-cycle	12	45	64.03	63.60	1096	0.864	0.049	3.86
1-cycle	12	45	66.46	65.68	1245	0.789	0.310	6.41
1-cycle	12	45	67.69	65.77	1328	0.754	0.504	7.72
1-cycle	12	55	68.45	66.21	1464	0.691	-0.316	0.04
1-cycle	12	55	61.85	60.83	1556	0.588	-0.102	4.34
1-cycle	12	55	65.70	62.92	1830	0.531	0.877	6.88
1-cycle	12	55	61.74	59.59	1972	0.463	1.610	10.05

Table D.1 Run Conditions for the Distortion Tests (Continued)

Screen	No. of Blades	Stagger (degrees)	V_x avg 1-D (ft/sec)	V_x avg 15 (ft/sec)	RPM	Avg ϕ	Avg $\Delta p_T/\frac{1}{2}\rho v_x^2$ avg	Avg i (degrees)
2-cycle	—	—	67.53	67.88	———	———	———	———
2-cycle	12	35	66.44	65.59	724	1.357	-0.051	1.25
2-cycle	12	35	67.26	66.52	768	1.295	0.014	2.55
2-cycle	12	35	66.77	64.96	951	1.038	0.330	8.75
2-cycle	12	35	68.21	66.37	1175	0.858	0.858	14.21
2-cycle	12	45	67.93	66.64	999	1.005	-0.148	- 0.38
2-cycle	12	45	63.65	62.88	1099	0.856	0.068	4.25
2-cycle	12	45	68.59	67.07	1248	0.813	0.345	5.70
2-cycle	12	45	66.91	65.63	1331	0.743	0.568	8.19
2-cycle	12	55	66.44	63.74	1468	0.669	-0.279	1.03
2-cycle	12	55	67.49	65.74	1560	0.640	-0.034	2.22
2-cycle	12	55	62.87	59.26	1836	0.506	1.007	8.07
2-cycle	12	55	63.99	61.43	1977	0.479	1.584	9.36

Table D.1 Run Conditions for the Distortion Tests (Continued)

Screen	No. of Blades	Stagger (degrees)	V_x avg 1-D (ft/sec) /	V_x avg 15 (ft/sec)	RPM	Avg ϕ	Avg $\Delta p_T/\frac{1}{2}\rho v_x^2$ avg	Avg i (degrees)
4-cycle	—	—	65.91	66.18	———	———	———	———
4-cycle	12	35	63.44	62.74	706	1.329	-0.051	1.65
4-cycle	12	35	62.57	62.13	750	1.233	0.017	3.71
4-cycle	12	35	64.15	63.14	928	1.022	0.343	9.11
4-cycle	12	35	62.57	66.52	1147	0.807	0.978	15.94
4-cycle	12	45	64.40	63.31	975	0.977	-0.119	0.42
4-cycle	12	45	65.80	65.15	1073	0.907	0.071	2.58
4-cycle	12	45	63.97	62.92	1218	0.777	0.411	6.96
4-cycle	12	55	62.14	59.96	1433	0.641	-0.260	2.15
4-cycle	12	55	63.63	62.17	1523	0.618	-0.017	3.12
4-cycle	12	55	65.05	62.68	1791	0.537	0.925	6.66
4-cycle	12	55	66.28	63.70	1930	0.508	1.453	7.97

Table D.1 Run Conditions for the Distortion Tests (Continued)

Screen	No. of Blades	Stagger (degrees)	V_x avg 1-D (ft/sec)	V_x avg 15 (ft/sec)	RPM	Avg ϕ	Avg $\Delta p_T/\frac{1}{2}\rho v_{x\ avg}^2$	Avg i (degrees)
6-cycle	—	—	68.99	69.22	———	———	———	———
6-cycle	12	35	65.66	64.69	739	1.314	-0.045	1.97
6-cycle	12	35	67.57	66.67	785	1.273	0.031	2.82
6-cycle	12	35	64.74	65.32	972	0.985	0.385	10.18
6-cycle	12	35	64.04	69.63	1200	0.789	1.006	16.52
6-cycle	12	45	66.79	64.89	1020	0.968	-0.129	0.69
6-cycle	12	45	67.64	65.71	1123	0.891	0.064	3.10
6-cycle	12	45	64.94	63.78	1275	0.753	0.430	7.84
6-cycle	12	45	65.97	66.50	1360	0.717	0.647	9.18
6-cycle	12	55	69.27	67.03	1500	0.683	-0.135	0.51
6-cycle	12	55	63.79	62.05	1594	0.592	0.122	4.24
6-cycle	12	55	69.33	66.13	1875	0.547	0.949	6.20
6-cycle	12	55	68.45	65.22	2020	0.501	1.517	8.27

Table D.1 Run Conditions for the Distortion Tests (Continued)

Screen	No. of Blades	Stagger (degrees)	V_x avg 1-D (ft/sec)	V_x avg 15 (ft/sec)	RPM	Avg ϕ	Avg $\Delta p_T/\frac{1}{2}\rho v_x^2$ avg	Avg i (degrees)
90° sq.	—	—	67.19	67.38	———	———	———	———
90° sq.	12	35	64.72	64.45	720	1.329	-0.036	1.75
90° sq.	12	35	63.98	63.98	764	1.238	0.024	3.72
90° sq.	12	35	63.12	62.63	946	0.987	0.373	10.23
90° sq.	12	35	67.80	66.85	1169	0.858	0.828	14.19
90° sq.	12	45	65.19	63.80	994	0.970	-0.193	0.63
90° sq.	12	45	65.36	64.46	1094	0.883	0.055	3.32
90° sq.	12	45	62.63	62.32	1242	0.746	0.404	8.10
90° sq.	12	45	64.31	64.41	1325	0.718	0.563	9.14
90° sq.	12	55	62.93	59.85	1461	0.637	-0.321	2.34
90° sq.	12	55	64.20	62.32	1552	0.612	-0.033	3.40
90° sq.	12	55	63.53	60.46	1826	0.514	0.941	7.70
90° sq.	12	55	64.86	62.21	1967	0.488	1.492	8.93

Table D.1 Run Conditions for the Distortion Tests (Continued)

Screen	No. of Blades	Stagger (degrees)	V_x avg 1-D (ft/sec)	V_x avg 15 (ft/sec)	RPM	Avg ϕ	Avg $\Delta p_T/\frac{1}{2}\rho v_{x\ avg}^2$	Avg i (degrees)
180° sq.	—	—	66.89	67.20	—	—	—	—
180° sq.	12	35	67.19	66.12	717	1.386	-0.064	0.71
180° sq.	12	35	66.41	65.56	761	1.290	-0.009	2.66
180° sq.	12	35	65.32	64.01	942	1.025	0.322	9.15
180° sq.	12	35	67.95	67.24	1164	0.863	0.801	14.05
180° sq.	12	45	66.60	65.55	989	0.996	-0.162	- 0.07
180° sq.	12	45	66.33	65.44	1089	0.901	0.064	2.77
180° sq.	12	45	66.86	65.57	1236	0.800	0.349	6.14
180° sq.	12	45	65.96	65.06	1319	0.739	0.577	8.33
180° sq.	12	55	65.15	62.20	1454	0.662	-0.321	1.27
180° sq.	12	55	65.80	63.95	1545	0.630	-0.042	2.59
180° sq.	12	55	61.46	57.52	1818	0.500	1.016	8.40
180° sq.	12	55	62.61	59.62	1958	0.473	1.574	9.65

DISTRIBUTION LIST FOR ARL UNCLASSIFIED TM 78-178 by Adam M. Yocum, June 14, 1978

Commander
Naval Sea Systems Command
Department of the Navy
Washington, DC 20362

Attn: Library, Code NSEA-09G32
(Copy Nos. 1 & 2)
Code NSEA-0342
(Copy Nos. 3 & 4)
T. E. Peirce, Code NSEA-0351
(Copy No. 5)
A. R. Paladino, Code NSEA-0372
(Copy No. 6)

Defense Documentation Center
5010 Duke Street
Cameron Station
Alexandria, VA 22314
(Copy Nos. 7-18)

Commander
Naval Ship Engineering Center
Washington, DC 20362
Attn: D. Burke, Code NSEC-6140B.1
(Copy No. 19)

Commanding Officer
Naval Underwater Systems Center
Newport, RI 02840
Attn: Library, Code 54
(Copy No. 20)

Commanding Officer
Naval Ocean Systems Center
San Diego, CA 92152

Attn: D. Nelson, Code 2542
(Copy No. 21)
Library
(Copy No. 22)
M. Reischman, Code 2542
(Copy No. 23)

Commanding Officer & Director
David W. Taylor Naval Ship R&D Ctr.
Department of the Navy
Bethesda, MD 20084

Attn: W. B. Morgan, Code 154
(Copy No. 24)
R. Cumming, Code 1544
(Copy No. 25)
J. McCarthy, Code 1552
(Copy No. 26)
M. Sevik, Code 19
(Copy No. 27)
W. K. Blake, Code 1942
(Copy No. 28)

Commanding Officer & Director
David W. Taylor Naval Ship R&D Ctr.
Department of the Navy
Annapolis Laboratory
Annapolis, MD 21402
Attn: J. G. Stricker, Code 2721
(Copy No. 29)

Commander
Naval Surface Weapon Center
Silver Spring, MD 20910
Attn: Library
(Copy No. 30)

NASA Lewis Research Center
21000 Brookpark Road
Cleveland, OH 44135

Attn: N. C. Sanger, MS 5-9
(Copy No. 31)
M. J. Hartmann, MS 5-9
(Copy No. 32)
D. M. Sandercock, MS 5-9
(Copy No. 33)
W. M. McNally, MS 5-9
(Copy No. 34)
J. Adamczyk, MS 5-9
(Copy No. 35)
Library
(Copy No. 36)
D. Morris, MS 60-3
(Copy No. 37)

DISTRIBUTION LIST FOR ARL UNCLASSIFIED TM 78-178 by Adam M. Yocum, June 14, 1978 (Cont'd)

General Applied Science Labs.
Merrick and Stewart Avenues
Westbury, NY 11590
(Copy No. 38)

Arnold Air Force Station
Tennessee 37389
Attn: Library
(Copy No. 39)

Air Force Aero Propulsion Laboratory
Wright-Patterson Air Force Base
Ohio 45433
Attn: Library
(Copy No. 40)

Air Force Office of Scientific Research
1400 Wilson Boulevard
Arlington, VA 22209
Attn: Dr. J. F. Masi
(Copy No. 41)

NASA Ames Research Center
Moffett Field, CA 94085

Attn: Library
(Copy No. 42)
Dr. S. Bodapati, MA 227-9
(Copy No. 43)

NASA Langley Research Center
Hampton, VA 23365
Attn: Library
(Copy No. 44)

National Technical Information Service
Department of Commerce
5285 Port Royal Road
Springfield, VA 22151
Attn: Chief, Input Section
(Copy 45)

Naval Postgraduate School
Monterey, CA 93940
Attn: Library, Code 0212
(Copy No. 46)

Office of Naval Research
Department of the Navy
Arlington, VA 22217
Attn: J. Patton
(Copy No. 47)

Calspan Corporation
4455 Genessee Street
Buffalo , NY 14221
Attn: Head Librarian
(Copy No. 48)

Detroit Diesel Allison Division
P. O. Box 894
Indianapolis, Indiana 46206

Attn: Dr. S. Fleeter
(Copy No. 49)
Library
(Copy No. 50)

Garrett Corporation
AiResearch Manufacturing Company
Sky Harbor Airport
402 South 36th Street
Phoenix, Arizona 85034
Attn: Library
(Copy No. 51)

General Electric Company
Cincinnati, Ohio 45215
Attn: Library
(Copy No. 52)

General Electric Company
Corporate Research & Development
P. O. Box 8
Schenectady, NY 12301
Attn: Library
(Copy No. 53)

General Electric Company
1000 Western Avenue
West Lynn, Massachusetts 01910
Attn: Library
(Copy No. 54)

DISTRIBUTION LIST FOR ARL UNCLASSIFIED TM 78-178 by Adam M. Yocum, June 14, 1978 (Cont'd)

LTV Vought Aeronautics Company
P. O. Box 5907
Dallas, Texas 75222
Attn: Library
(Copy No. 55)

Lockheed-Georgia Company
Marietta, Georgia 30060
Attn: Library
(Copy No. 56)

Lockheed Propulsion Company
Scientific and Technical Library
P. O. Box 111
Redlands, CA 92373
Attn: Head Librarian
(Copy No. 57)

McDonnell Aircraft Company
P. O. Box 516
St. Louis, Missouri 63166
Attn: Res. & Eng. Library
Dept. 218 - Bldg. 101
(Copy No. 58)

Nielsen Eng. & Research, Inc.
510 Clyde Avenue
Mountain View, CA 94040
Attn: Dr. J. N. Nielsen
(Copy No. 59)

Pratt and Whitney Aircraft Division
United Aircraft Company
400 S. Main Street
East Hartford, Connecticut 06108

Attn: Library
(Copy No. 60)
R. Mazzaway
(Copy No. 61)

Pratt and Whitney Aircraft
Florida Res. & Dev. Ctr.
P. O. Box 2691
West Palm Beach, Florida 33402
Attn: Library
(Copy No. 62)

United Aircraft Research Laboratory
East Hartford, Connecticut 06108

Attn: Dr. F. Carta
(Copy No. 63)
Librarian
(Copy No. 64)

California Institute of Technology
Jet Propulsion Laboratory
4800 Oak Grove Drive
Pasadena, CA 91130
Attn: Library
(Copy No. 65)

Case Western Reserve University
10900 Euclid Avenue
Cleveland, OH 44106
Attn: Sears Library - Reports Dept.
(Copy No. 66)

Massachusetts Institute of Technology
77 Massachusetts Avenue
Cambridge, Massachusetts 02139

Attn: Dr. E. M. Greitzer
(Copy No. 67)
Technical Reports - MIT Libraries
Room 14 E-210
(Copy No. 68)
Eng. Tech. Repts. - Room 10-408
(Copy No. 69)

Virginia Polytechnic Inst. &
State University
Mechanical Engineering Dept.
Blackburg, Virginia 24061

Attn: Mr. W. F. O'Brien, Jr.
(Copy No. 70)
Library
(Copy No. 71)

Dr. John H. Horlock
Vice Chancellor
University of Salford
Salford, M5 4WT
ENGLAND
(Copy No. 72)

DISTRIBUTION LIST FOR ARL UNCLASSIFIED TM 78-178 by Adam M. Yocum, June 14, 1978 (Cont'd)

Dr. G. K. Serovy
Mechanical Engineering Department
Iowa State University
Ames, Iowa 50010
(Copy No. 73)

Von Karman Inst. for Fluid Dynamics
Turbomachinery Laboratory
Rhode-Saint-Genese
BELGIUM
Annt: Library
(Copy No. 74)

Dr. D. S. Thompson
Turbine Research Department
Rolls Royce Ltd.
P. O. Box 31
Derby, ENGLAND
(Copy No. 75)

Whittle Turbomachinery Laboratory
Madingley Road
Cambridge, England

Attn: Library
(Copy No. 76)
Sir William Hawthorne
(Copy No. 77)

Prof. R. E. Peacock
School of Mechanical Engineering
Cranfield Institute of Technology
Cranfield, Bedford MK430AL
ENGLAND
(Copy No. 78)

Dr. Hans Mokelke
Mut-Munchen GMBLT
8 Munchen 50
Postfach 50 06 40
GERMANY
(Copy No. 79)

Dr. S. N. B. Murthy
Thermal Science & Prop. Center
Purdue University
West Lafayette, Indiana 47907
(Copy No. 80)

Prof. J. P. Gostelow
School of Mechanical Eng.
NSW Institute of Technology
Broadway
Sidney, Australia
(Copy No. 81)

Applied Research Laboratory
Post Office Box 30
State College, PA 16801

Attn: E. P. Bruce
(Copy No. 82)
B. Lakshminarayana
(Copy No. 83)

1. CHANGE NO.	2. DATE ISSUED	3. DOCUMENT AFFECTED NO. / TITLE	4. JOURNAL ISSUE
79-1731	7-11-79	N79-22087	79-17

5 AUTHORITY FOR CHANGE ☒ INPUT ☐ DDC ☐ ERDA ☐ NASA ☐ ORAL ☐ WRITTEN

☐ OTHER NAME-

6. ISSUED BY: LaGarde

7. CHANGES

A. ☒ DUPLICATE OF: AD-A058 959
B ☐ SUPERSEDED BY:
C. ☐ WITHDRAWN FROM NTIS
☐ DESTROY DOCUMENT
☐ RETURN DOCUMENT, MICROFORM & RELATED PAPERS TO:
☐ DDC-T ☐
D. ☐ DISTR/AVAIL CODE:
E. ☐ FILL FROM PC ☐ MN ☐
F. ☐ PUBLIC RELEASABILITY ☐
G. ☐ OTHER

8. ACTION

	DAY	HOUR	INITIAL	REMARKS
1. REPRODUCTION	7/23		mf	
2. MICROFICHE DISTRIBUTION	7/19		mk	
3. WAREHOUSE				
4. INVENTORY 1)				

1) ONLY WHEN STOCK IS TRANSFERRED

9. ☐ ADP TAKE ACTION ON IB TRANSACTION SHEET ☐ ADP TAKE NO ACTION ☐ ADP SCHEDULING TAPE SALES

10 REMARKS

2 ARCHIVES

CHANGE IN DOCUMENT STATUS NTIS 62 (1-78)

U. S. DEPARTMENT OF COMMERCE
National Technical Information Service